Title
The Structure and Dynamics of Jupiter's Magnetosphere

Author
Vogt, Marissa Farland

Publication Date
2012

Peer reviewed|Thesis/dissertation

UNIVERSITY OF CALIFORNIA

Los Angeles

The Structure and Dynamics of Jupiter's Magnetosphere

A dissertation submitted in partial satisfaction of the

requirements for the degree Doctor of Philosophy

in Geophysics and Space Physics

by

Marissa Farland Vogt

2012

ABSTRACT OF THE DISSERTATION

The Structure and Dynamics of Jupiter's Magnetosphere

by

Marissa Farland Vogt

Doctor of Philosophy in Geophysics and Space Physics

University of California, Los Angeles, 2012

Professor Margaret G. Kivelson, Chair

Eight spacecraft have now visited the Jovian system and obtained a wealth of information about Jupiter's magnetosphere and aurora, both of which have proved to be very different from what we observe at the Earth. These differences are due in part to unique features such as large magnetospheric scale sizes, an internal plasma source from the moon Io, and a rapid planetary rotation period. These features have important influences on Jupiter's magnetosphere structure and dynamics, which are the focus of the three studies described in this dissertation. The first study is a survey of magnetometer data from the Jovian magnetotail to search for signatures of magnetic reconnection, an important dynamic process in planetary magnetospheres. Reconnection is thought to be predominantly internally driven at Jupiter. We have identified 249 reconnection events from the magnetometer data, and have analyzed their spatial distribution and periodicity to establish where and how often reconnection occurs at Jupiter. Results, including the location of a statistical separatrix, are compared to previous studies of flow bursts and

particle anisotropies. The second study establishes a new model for relating auroral features to sources in the middle and outer magnetosphere. At Jupiter the polar aurora mapping is highly uncertain because global field models are inaccurate beyond ~30 Jovian radii. The open/closed field line boundary is also not well defined because Jupiter's main auroral emissions are associated with the breakdown of plasma corotation rather than the polar cap. Therefore our mapping model, which uses a flux equivalence calculation rather than tracing global models, provides a more precise mapping of the polar aurora and allows us to identify the size and location of Jupiter's polar cap. In the final study, we use a large scale kinetic simulation to examine the effects of centrifugal forces arising from Jupiter's rapid rotation and non-adiabatic field line stretching in the noon to dusk local time sector. We examine changes to the pitch angle and energy distributions and conclude that the changes arising from the non-adiabatic stretching effects could account for the field dipolarization and plasma sheet thickening observed between noon and dusk.

The dissertation of Marissa Farland Vogt is approved.

Maha Ashour-Abdalla

Vassilis Angelopoulos

Krishan K. Khurana

Raymond J. Walker

Margaret G. Kivelson, Committee Chair

University of California, Los Angeles

2012

For my parents,

Colette Farland-Vogt and Alexander Vogt,

and for my husband, Michael McGraw-Herdeg,

for their selfless and unconditional support

TABLE OF CONTENTS

LIST OF FIGURES

LIST OF TABLES

ACKNOWLEDGMENTS

My family, friends, colleagues, and advisors provided an incredible amount of encouragement, kindness, and understanding while I worked on this dissertation, and I gratefully acknowledge their support and influence on this work.

I would first like to thank my advisor, Margaret Kivelson, for her guidance and support. I am very grateful for the opportunity to work with her and learn from her fascinating perspectives on research, being a woman in science, and everything else in life. In addition to Margy, two other committee members, Krishan Khurana and Raymond Walker, have been intimately involved with the work in this dissertation. I thank them all for their support and encouragement with everything from paper revisions to late-night group meeting discussions. I was very lucky to have such a wonderful core group of advisors. They all have been incredibly generous with their time, and I greatly enjoyed working with them.

All of my committee members have shown an incredible amount of patience, understanding, and flexibility over the past few months, and I thank them sincerely for their close reading, helpful comments, and cheerful support. I gratefully acknowledge many helpful discussions with Maha Ashour-Abdalla regarding the kinetic simulation that formed part of this dissertation, and I thank Vassilis Angelopoulous for his thoughtful questions and interest in my work. I would also like to thank Bob McPherron for serving on the committee for my first qualifying exam.

Fran Bagenal has been an incredible mentor to me over the past six years, and I sincerely thank her for all of the ways she has supported me and my career. Her criticism has always been constructive and thought provoking, and has improved my work. Fran's unwavering enthusiasm has had a great impact on my graduate studies, and I am grateful for her support.

During my time at UCLA I was fortunate to meet two truly kindred spirits: Katherine Ramer and Bertrand Bonfond. These two individuals have greatly enriched my life both personally and professionally, and I am deeply grateful for their friendship. I look forward to many more years of adventures and collaborations with them.

There are many members of the technical and support staff in the ESS and IGPP departments at UCLA who have assisted me over the years by giving cheerful advice, providing computing resources, or processing administrative forms. In particular, I thank Todd King, Steve Joy, Joe Mafi, Jim Nakatsuka, and Rick Fort for their general assistance, and Lauri Holbrook and Kevin McKeegan for help with some important last-minute filing forms. I also thank Vahe Peroomian, Mostafa El-Alaoui, Dave Schriver, and Yingjuan Ma for lending their expertise freely and cheerfully as I developed the simulation used in the last part of my dissertation and ventured into the new world of supercomputing. I also gratefully acknowledge generous computing resources provided by the UCLA Hoffman2 Cluster and NASA Advanced Supercomputing (NAS) Division at Ames Research Center, and the expert help of their staff.

I have been fortunate to meet many new friends beyond UCLA whose support and collaboration have contributed to this dissertation and had a positive influence on my graduate studies and future career path. Among them are Denis Grodent, Katerina Radioti, Jean-Claude Gérard, Norbert Krupp, Elena Kronberg, Peter Delamere, and Licia Ray. I am also grateful to new friends Caitriona Jackman and Chris Arridge for inviting me to participate in their ISSI magnetotails team, which was a wonderful learning experience and has led to exciting collaborations with Mervyn Freeman and Jim Slavin, among others. I thank all of these individuals for their support during the early stages of my career, and I look forward to many more collaborations in the future.

I would also like to acknowledge two fantastic supervisors with whom I have had the privilege to work: Charles Smith at the University of New Hampshire, and Emma Bunce at the University of Leicester. Chuck offered me a summer job while I was an undergraduate, and that job turned out to be a very positive experience and had a tremendous effect on my decision to pursue a Ph.D. at UCLA and a career studying planetary magnetospheres. I am sincerely grateful to him for giving me that opportunity and for his support over the years. I thank Emma for her patience and understanding, which have greatly eased the task of finishing this dissertation.

On a personal level, I am sincerely thankful for the support of my friends and family. They have shared their computing knowledge and other expertise, lent a kind and understanding ear through the highs and lows of the Ph.D., and provided endless encouragement. In particular, I would like to thank my friends Bill Harris, Patrick Cruce, and Jeff Simpson for kindly and happily sharing technical advice and acknowledge the support of my fellow graduate students and friends Jodie Ream, Feifei Jiang, Jenni Kissinger, and Christine Gabrielse with whom I have shared this incredible journey. I would also like to gratefully acknowledge the encouragement of friends and family members Austin Chu, Nick Bushak, Shreyes Seshasai, Melissa Godin, Roberta and Joe Kieronski, David Vogt, Andrew C. Vogt, Doris and Luis Yepez, and my in-laws Sharon McGraw and Paul Herdeg.

My parents have unconditionally supported me through every step of my education, and I am incredibly grateful for their love and encouragement. They have made many sacrifices to provide me with the wonderful opportunities that have led me here.

Finally, and most importantly, I thank my husband, Michael McGraw-Herdeg. He has actively supported me in every way imaginable, from recovering a failing hard drive to

proofreading conference posters and presentation slides. He has been an amazing partner to me during my graduate studies, and I am grateful for his unwavering faith in me. I could not have completed this dissertation without his constant encouragement, love, and understanding.

VITA

2006	S.B. Earth, Atmospheric, and Planetary Sciences
	S.B. Physics
	Massachusetts Institute of Technology
	Cambridge, MA
2006 – 2012	Graduate Student Researcher
	Department of Earth and Space Sciences
	University of California, Los Angeles
2008	Outstanding Student Paper Award
	American Geophysical Union
	Fall Meeting, San Francisco, CA
2009	M.S. Geophysics and Space Physics
	University of California, Los Angeles
2010	Outstanding Student Paper Award
	American Geophysical Union
	Fall Meeting, San Francisco, CA
2010-2011	Young scientist member, ISSI (International Space Science Institute) team
	"Investigating the Dynamics of Planetary Magnetotails"

SELECTED PUBLICATIONS AND PRESENTATIONS

Vogt, M. F., C. M. S. Cohen, P. Puhl-Quinn, V. K. Jordanova, C. W. Smith, and R. M. Skoug (2006), Space weather drivers in the ACE era, *Space Weather, 4*, S09001, doi:10.1029/2005SW000155.

Vogt, M. F., M. G. Kivelson, K. K. Khurana, S. P. Joy, and R. J. Walker (2010), Reconnection and flows in the Jovian magnetotail as inferred from magnetometer observations, *J. Geophys. Res., 115*, A06219, doi:10.1029/2009JA015098.

Bonfond, B., M. F. Vogt, J.‐C. Gérard, D. Grodent, A. Radioti, and V. Coumans (2011), Quasi-periodic polar flares at Jupiter: A signature of pulsed dayside reconnections?, *Geophys. Res. Lett.*, *38*, L02104, doi:10.1029/2010GL045981.

Vogt, M. F., M. G. Kivelson, K. K. Khurana, R. J. Walker, B. Bonfond, D. Grodent, and A. Radioti (2011), Improved mapping of Jupiter's auroral features to magnetospheric sources , *J. Geophys. Res.*, *116* , A03220, doi:10.1029/2010JA016148.

Radioti, A., D. Grodent, J.‐C. Gérard, M. F. Vogt, M. Lystrup, and B. Bonfond (2011), Nightside reconnection at Jupiter: Auroral and magnetic field observations from 26 July 1998, *J. Geophys. Res.*, *116*, A03221, doi:10.1029/2010JA016200.

Jones, B., M. F. Vogt, M. Chaffin, M. Choukroun, N. Ehsan, L. Gibbons, K. Lynch, K. Singer, D. Blackburn, G. Dibraccio, D. Gleeson, A. LeGall, T. McEnulty, E. Rampe, C. Schrader, L. Seward, I. Smith, C. Tsang, P. Williamson, J. Castillo, and C. Budney, Concept for a new frontiers mission to Ganymede: A Planetary Science Summer School study, Aerospace Conference, 2011 IEEE, March 2011.

Vogt, M. F., M. G. Kivelson, K. K. Khurana, and R. J. Walker, Simulating the effect of rapid rotation on the local time dependence of Jupiter’s plasma sheet thickness, Poster presented at the “Magnetospheres of the Outer Planets” meeting, July 2011, Boston, MA.

Jackman, C. M., M. F. Vogt, J. A. Slavin, S. W. Cowley, and S. A. Boardsen, Magnetotail reconnection and flux circulation: Jupiter and Saturn compared, Talk presented at the “Magnetospheres of the Outer Planets” meeting, July 2011, Boston, MA

CHAPTER 1

Introduction

1.1 Introduction to Jupiter's magnetosphere

Jupiter is a planet of superlatives. It has the largest planetary radius (1 R_J = 71,492 km), the most energetic and brightest auroral emissions, the fastest planetary rotation period (~10 hours), and the strongest internal magnetic field in the solar system (magnetic moment ~4.2 Gauss). The strong magnetic field acts as an obstacle to the plasma flowing in the solar wind and forms a cavity in space, called a magnetosphere, in which the planetary magnetic field influences the motion of charged particles. In both absolute and relative (to the planetary radius) terms, Jupiter's magnetosphere is the largest in the solar system. These superlative properties combine to make Jupiter a unique and exciting target for magnetospheric studies.

1.1.1 Observational history

The first measurements indicating a magnetic field at Jupiter were made remotely with the Mills Cross antenna array, which observed radio bursts coming from the planet [*Burke and Franklin*, 1955]. These decametric radio emissions are produced by the cyclotron maser instability, which develops from a resonance between the electronic cyclotron frequency at high magnetic latitudes and the electron plasma frequency. Nearly two decades later, the spacecraft Pioneer 10 flew by Jupiter and collected the first *in situ* plasma and magnetic field data in Jupiter's magnetosphere. Eight spacecraft have now visited the Jovian system and obtained a wealth of information about the magnetosphere and aurora. The spacecraft observations are summarized in Table 1.1, and the trajectories are shown in Figure 1.1.

Table 1.1 Summary of spacecraft observations at Jupiter

	Spacecraft trajectory	Observation interval	Closest approach (R_J)	Local time coverage (hrs) >20 R_J	Latitude coverage (SIII)	Relevant Instrumentation
Pioneer 10	Flyby	Nov. – Dec. 1973	2.8	4.2 –10.9	+/- 13º	Helium vector magnetometer, plasma analyzer, charged particle instrument[1]
Pioneer 11	Flyby	Nov. – Dec. 1974	1.7	8.6 – 12.3	+/- 52º	Helium vector and flux gate magnetometers, plasma analyzer, charged particle instrument
Voyager 1	Flyby	March 1979	4.9	2.6 – 12.0	+/- ~6º	Magnetometer, plasma investigation, plasma wave investigation, low energy charged particle investigation[2]
Voyager 2	Flyby	July 1979	10.1	~0 – 13.0	-10º to +5º	Magnetometer, plasma investigation, plasma wave investigation, low energy charged particle investigation
Ulysses	Flyby	Feb. 1992	6.3	8.9 – 20.2	+/- 35º	Magnetometer, solar wind plasma experiment[3]
Galileo	Orbiter	Dec. 1995 – Sept. 2003	3.6	0 – 24	+/- 5º	Magnetometer, Energetic Particle Detector, plasma investigation, plasma wave subsystem[4]
Cassini	Flyby	Dec. 2000 – Jan. 2001	137	12.1 –19.8	+/- 3º	Magnetometer, plasma spectrometer, radio and plasma wave science, magnetospheric imaging instrument[5]
New Horizons	Flyby	Feb. – March 2007	32	11.3 – 23.4	-8º to +4º	Energetic particle spectrometer, solar wind and plasma spectrometer[6]

[1] http://www.nasa.gov/centers/ames/missions/archive/pioneer.html
[2] http://voyager.jpl.nasa.gov/science/index.html
[3] http://ulysses.jpl.nasa.gov/spacecraft/instruments.html
[4] http://solarsystem.nasa.gov/galileo/facts.cfm
[5] http://saturn.jpl.nasa.gov/mission/quickfacts/
[6] http://pluto.jhuapl.edu/spacecraft/overview.php

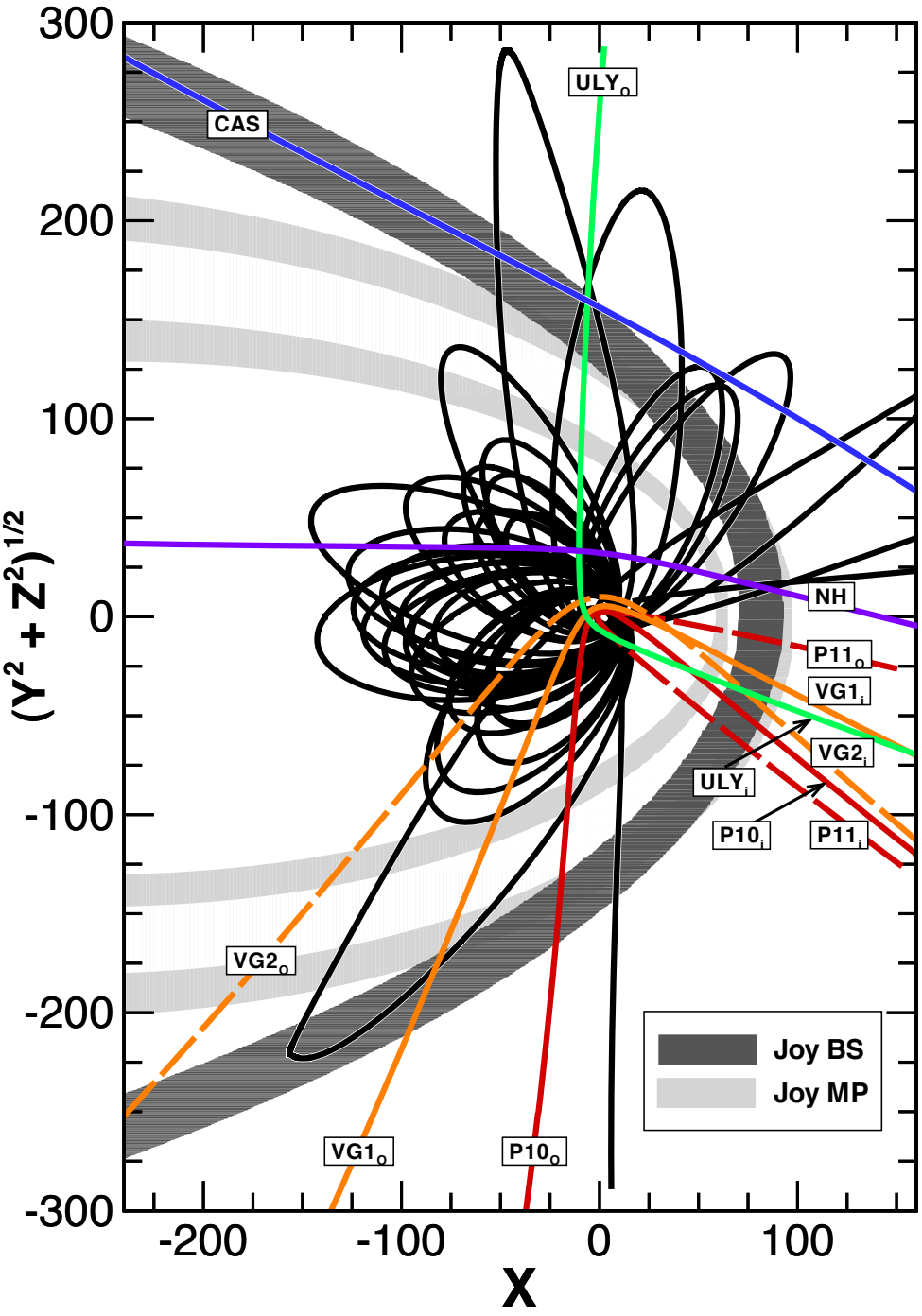

Figure 1.1: Trajectories of the spacecraft which have visited Jupiter's magnetosphere, projected onto the equatorial plane. Figure courtesy Joe Mafi.

The early flybys – Pioneer 10 in 1973, Pioneer 11 in 1974, Voyagers 1 and 2 in 1979 – provided the first clues to the structure of Jupiter's magnetosphere, which is illustrated in Figure 1.2. The Pioneer 10 data showed that in the inner magnetosphere, Jupiter's magnetic field is primarily dipolar, and that the dipole field is offset toward the north from the center of the planet, has a ~10º tilt, and a ~4 Gauss magnetic moment [*Smith et al.*, 1974]. Voyager 1 in early 1979 flew through the Io plasma torus in the inner magnetosphere, collecting *in situ* plasma and magnetic field measurements. Though the Io plasma torus had been discovered several years earlier by ground-based observations [*Brown*, 1974; *Kupo et al.*, 1976], the Voyager spacecraft enabled direct measurement of the torus' spatial extent and plasma energy and density. The Pioneer 10 and Voyager 1 and 2 observations showed that in the middle magnetosphere the magnetic field is swept back in a spiral configuration [*Smith et al.*, 1974; *Khurana and Kivelson*, 1993]. Pioneer 10 data also contributed to the discovery of Jupiter's plasma sheet [*Smith et al.*, 1974], which Voyager 2 observations showed is bent beyond ~40 R_J, after which the plasma sheet becomes parallel to the solar wind (the hinged-magnetodisc model) [*Behannon et al.*, 1981; *Khurana and Kivelson*, 1989]. Finally, the early flybys also probed the structure of the outer magnetosphere, with Voyager 2 observing the Jovian magnetotail as far out as ~9000 R_J – past the orbit of Saturn [*Lepping et al.*, 1983].

Though data from the early spacecraft flybys led to many new discoveries, they were very limited in local time extent. The Pioneer and Voyager spacecraft all entered the magnetosphere in the pre-noon local time sector and, with the exception of Pioneer 11, exited on the pre-dawn to dawn flank. Pioneer 11 exited just before noon local time and had a higher inclination trajectory (maximum 52º SIII latitude) than the other spacecraft, which remained at relatively low latitudes (maximum latitude ~15º). It was not until the Galileo spacecraft, which

entered orbit around Jupiter in December 1995, that more complete local time coverage became available. Galileo's near-equatorial orbit covered local times from post-noon through dawn. The new observations showed significant dawn-dusk local time asymmetries in the magnetic field configuration, plasma sheet thickness, and plasma flow [*Krupp et al.*, 2001; *Kivelson and Khurana*, 2002]. Additional coverage in the afternoon local time sector enabled development of three-dimensional models of Jupiter's bow shock and magnetopause location [*Joy et al.*, 2002]. Those models established that the magnetopause has two probable standoff distances corresponding to different solar wind conditions: ~60 R_J for the compressed magnetosphere case (high solar wind dynamic pressure) and ~90 R_J for the expanded case (low solar wind dynamic pressure).

In addition to providing additional local time coverage, Galileo's trajectory included multiple flybys of Jupiter's four largest moons: Io, Europa, Ganymede, and Callisto. Data collected during those flybys led to exciting discoveries about the Galilean satellites, their interior structure, and the interactions between magnetized moons and Jupiter's magnetic field. It was discovered that Ganymede possesses its own intrinsic magnetic field, which forms a mini-magnetosphere within Jupiter's magnetosphere [*Kivelson et al,* 1996; *Gurnett et al,* 1996]. Magnetometer observations from near Europa and Callisto show that these satellites do not have an intrinsic field but do exhibit a magnetic signature, due to an induced magnetic field, that can be explained by the presence of a salty subsurface ocean [*Khurana et al,* 1998; *Kivelson et al.*, 1999, 2000; *Zimmer et al.*, 2000]. The induced field is formed because the satellites, which are orbiting Jupiter at the jovigraphic equator, experience temporal changes in Jupiter's magnetic field due to the 10º tilt of Jupiter's dipole field. The plasma sheet moves up and down over the satellites during a rotation period and that changing external magnetic field environment induces

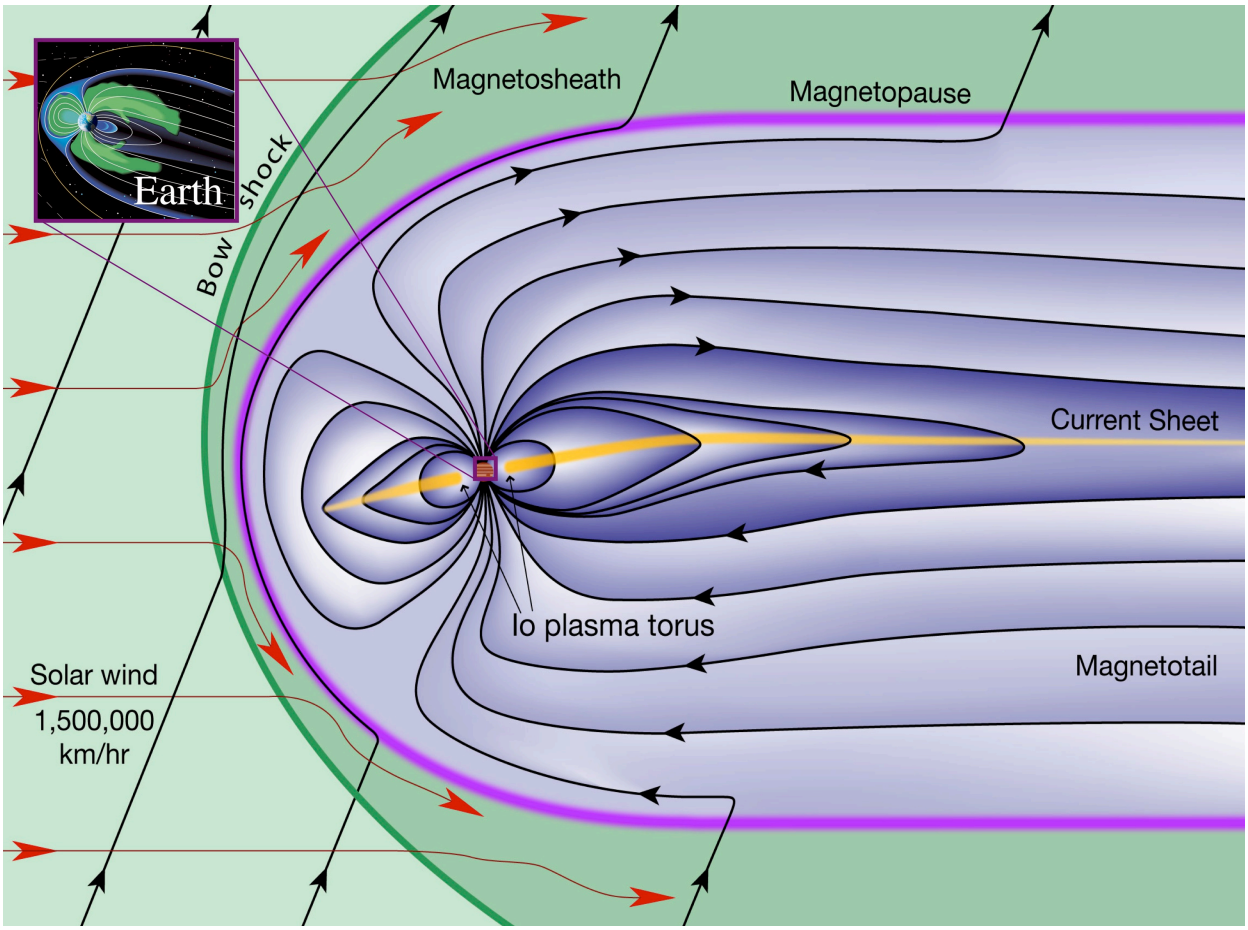

Figure 1.2: Illustration of the main features of Jupiter's magnetosphere, seen here in the noon-midnight meridian plane, including the hinged current sheet, plasma torus, and stretched nightside field configuration. Figure courtesy of Fran Bagenal and Steve Bartlett.

a magnetic field in conducting layers inside the moons. Similarly, the induced magnetic field at Io has been shown to be consistent with a subsurface magma ocean, or a thick conducting layer with a ~20% melt fraction, inside Io that is at least 50 km thick [*Khurana et al.*, 2011].

1.1.2 Magnetospheric structure: brief overview

Many of the properties and processes in Jupiter's magnetosphere are influenced by two unique features: an internal plasma source from the moon Io and the importance of centrifugal

forces due to Jupiter's rapid rotation. Their effects can be seen throughout the magnetosphere, which we traditionally divide into three regions: inner (< 20 R_J), middle (20 to ~60 R_J), and outer (> 60 R_J). In this section we summarize briefly the main features of each region, following the discussion in *Khurana et al.* [2004].

1.1.2.1 Inner magnetosphere

The magnetic field in Jupiter's inner magnetosphere is largely dipolar, and the bulk plasma flow is in the azimuthal direction with speeds at or near corotation. The dominant feature of the inner magnetosphere is the Io plasma torus, a ring of dense plasma whose source is the volcanically active moon. About 1 ton per second of SO_2 is lost from Io's atmosphere through ionization by solar UV photons and magnetospheric electrons and charge exchange with heavy ions from the torus. About 2/3 of the material lost is quickly ejected from the magnetosphere through charge exchange, while the rest stays in the torus on timescales of ~25-80 days and gradually expands into the middle magnetosphere [*Thomas et al.*, 2004]. The torus extends from ~5 R_J to ~10 R_J, and includes a cold (T_i = ~few eV) inner torus and a warm (T_i = ~100eV) outer torus outside of ~6 R_J. The mean density is ~2000 ions/cm^3, with a typical ion mass of 20 m_p.

The other major feature in the inner magnetosphere is the presence of high-energy radiation belts inside of 5 R_J. These inner radiation belts are produced as plasma diffuses radially inward due to dynamo fields generated by ionospheric winds [*Brice and McDonough*, 1973; *Bolton et al.*, 2004]. Because the plasma conserves the first and second adiabatic invariants, it is energized as it moves radially inward.

1.1.2.2 Middle magnetosphere

The plasma in Jupiter's middle magnetosphere is concentrated in a current sheet, or plasma sheet, that is hinged at large distances (see illustration in Figure 1.2). Between 10 and 30 R_J the current sheet is aligned with the magnetic equator tilted 9.6º with respect to the jovigraphic equator) [*Behannon et al.*, 1981], from ~30 to ~60 R_J it is located between the centrifugal and magnetic equators, and beyond ~60 R_J the current sheet is parallel to the solar wind. The thickness varies with local time, being thickest near dusk, where the typical half-thickness is > 6 R_J, and thinnest near dawn, where the typical half-thickness is ~2-3 R_J [*Khurana and Schwarzl*, 2005].

In the middle magnetosphere, between ~20 and ~30 R_J, the plasma angular velocity decreases and begins to lag corotation. This occurs so that angular momentum may be conserved as plasma diffuses radially outward from the Io torus. Because of the frozen-in-flux condition, the magnetic field is fixed to the outflowing plasma, and as the plasma's angular velocity decreases near the equator, the field is swept back into a spiral shape (as seen looking down onto the equatorial plane), and the flux tube lags corotation. In the middle magnetosphere, radial currents provide a $\vec{\mathbf{j}} \times \vec{\mathbf{B}}$ force that acts to speed the plasma back towards corotational speeds and transfers angular momentum from Jupiter's ionosphere to the plasma. These radial corotation enforcement currents are part of the current system which drives Jupiter's main auroral emissions, which we discuss in more detail in Chapter 3.

1.1.2.3 Outer magnetosphere

Jupiter's magnetosphere is much more compressible than the Earth's magnetosphere because the plasma sheet contributes a significant amount of thermal pressure and inflates the

magnetosphere. This is most noticeable in the dayside outer magnetosphere, where the magnetopause standoff distance has two probable values, ~60 R_J and ~90 R_J, corresponding to high and low solar wind dynamic pressure conditions, respectively. However, a simple pressure balance calculation between the average solar wind dynamic pressure and the magnetic pressure from Jupiter's dipole field would place the expected magnetopause distance at ~42 R_J, much closer to the planet. The additional thermal pressure means that, compared to the Earth, Jupiter's magnetopause standoff distance is much more sensitive to changes in solar wind dynamic pressure.

Local time asymmetries in the plasma flow and magnetic field configuration are most pronounced in the outer magnetosphere, due in part to the influence of the solar wind. On the nightside is Jupiter's magnetotail, which includes a thin current sheet located between two lobes that have a stretched (mostly radial) field configuration and low plasma density. In this local time region, the plasma flow is subcorotational and primarily azimuthal, with an outward radial component (see Figure 1.2). The fastest plasma flows are near dawn local time, where the field is most strongly bent back due to interaction with the oppositely-flowing solar wind. An important feature in the pre-noon to afternoon local time sector is the cushion region [*Smith et al.*, 1974], an area of southward-oriented and strongly fluctuating field in the outermost part of the magnetosphere (spanning a distance of ~20 R_J just inside of the magnetopause). The origins of the cushion region are not well-understood, with one theory suggesting that it is associated with empty flux tubes that were emptied by reconnection on the night side [*Kivelson and Southwood*, 2005]. Finally, in the dusk local time sector the magnetic field is swept forward in the outermost regions of the magnetosphere due to interaction with the solar wind. The plasma sheet is thickest

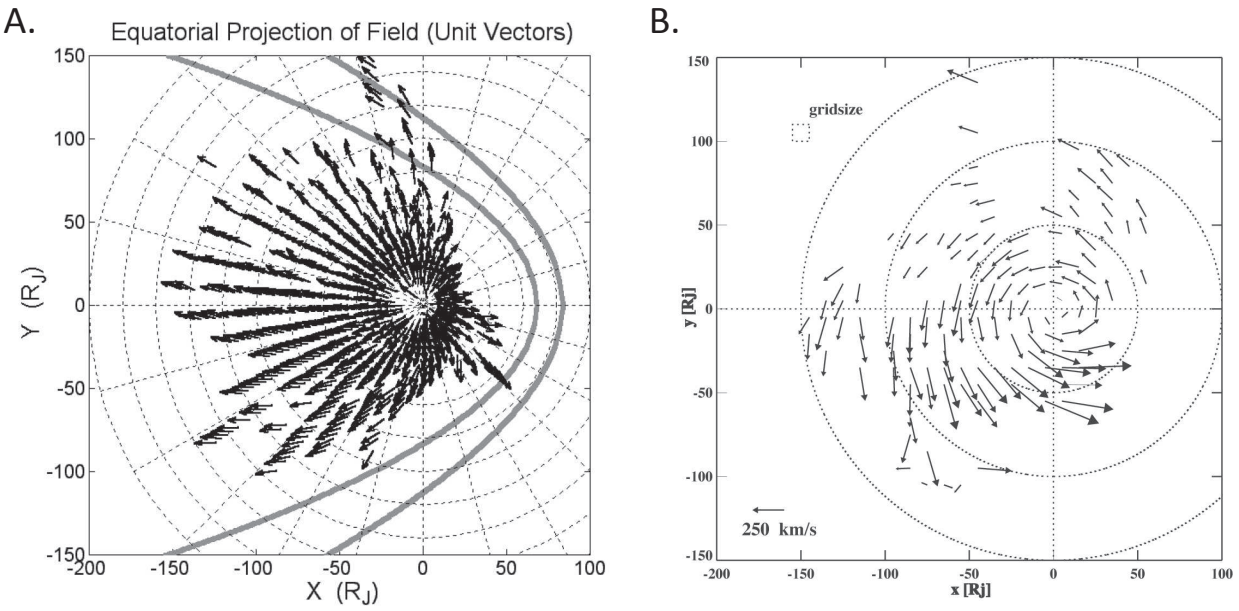

Figure 1.3: Observed (a) magnetic field and (b) plasma flow patterns in Jupiter's magnetosphere, projected onto the equatorial plane. The Sun is to the right. Modified from Figures 24.14 and 24.21 in *Khurana et al.* [2004].

in this region, and in Chapter 4 we explore some of the theories that have tried to explain the plasma sheet thickening between noon and dusk.

1.1.3 Dynamics in a rapidly-rotating magnetosphere

In the previous section we discussed how the structure of Jupiter's magnetosphere is influenced by the internal plasma source from the moon Io and centrifugal forces due to Jupiter's 10 hour rotation period. These two features also heavily influence magnetospheric dynamics at Jupiter, which are thought to be rotationally-driven rather than solar wind-driven as at the Earth.

The Io plasma source is important to magnetospheric dynamics because it produces the mass and energy that must eventually be released from Jupiter's magnetosphere through magnetotail reconnection or other processes. Producing about ~1000 kg/s, Io is by far the most

significant source of plasma; by comparison, the solar wind provides Jupiter's magnetosphere with only an estimated ~20-100 kg/s [*Hill et al.*, 1983]. The influence of centrifugal forces, relative to the solar wind, are much more important at Jupiter than at the Earth. For example, at the Earth, the potential energy from corotation is ~5 times larger than the solar wind induced potential across the polar cap, which is an indicator for the amount of energy available from the solar wind. At Jupiter, because of the fast rotation period and large magnetospheric scale size, the potential energy from corotation is ~50 times more than the solar wind induced cross magnetosphere potential [*Khurana et al.*, 2004]. This suggests that rotational stresses will play an important role in driving dynamics at Jupiter.

In the model of rotationally-driven dynamics first proposed by *Vasyliūnas* [1983], reconnection occurs on mass-loaded flux tubes that are stretched by centrifugal forces, pinch off, and form a plasmoid. This process, which is often referred to as the Vasyliūnas cycle, is illustrated in Figure 1.4. Mass-loaded flux tubes rotate to the night side (1), where they are stretched due to the centrifugal acceleration of rotating particles (2). The stretched flux tubes eventually pinch off, releasing a plasmoid that can escape down the tail (3,4). Also drawn in Figure 1.4 is the magnetic x-line that forms across the tail, beginning just before midnight local time and extending forward in local time and until it encounters the magnetopause. The x-line is accompanied by a magnetic o-line at larger radial distances.

More recently, observations of local time asymmetries in the plasma sheet thickness have been shown to result from rotationally-driven dynamics that are qualitatively similar to the Vasyliūnas model. The plasma sheet is observed to be thinnest at dawn and to thicken as it rotates through the dusk sector, where it is thickest. *Kivelson and* Southwood [2005] attribute the plasma sheet thickening between noon and dusk to the effects of centrifugal forces and field line

stretching that occurs as the magnetopause moves out between noon and dusk. On the night side where the plasma is no longer constrained by the magnetopause and is free to flow down the tail, the plasma-field configuration is unstable and plasma is centrifugally accelerated outward down the tail. As a result, the plasma sheet thins. Flux tubes break and are depleted of plasma then continue to rotate through the nightside to dawn. The empty flux tubes are carried inward via interchange motions as they rotate through the night side, while full flux tubes are carried outward. *Kivelson and Southwood* [2005] suggest that the stretching and pinching-off continues for all nightside local times across the tail, and that the location for the stretching and pinching off moves radially inward as the flux tubes rotate from dusk to dawn.

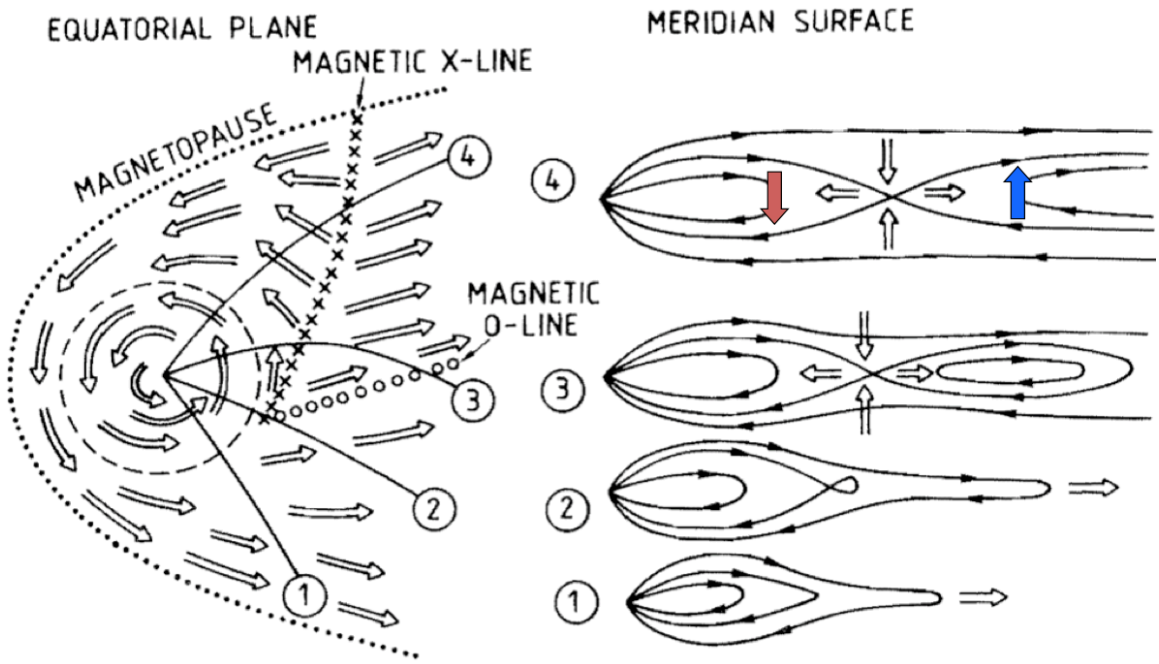

Figure 1.4: Schematic showing the mass loading and release process of the Vasyliūnas cycle describing rotationally-driven magnetospheric dynamics [figure from *Vasyliūnas*, 1983]. Mass-loaded flux tubes: (1) rotate to the night side, (2) stretch due to centrifugal acceleration of rotating particles, and (3 and 4) pinch off, releasing a plasmoid. Colored arrows emphasize the expected north-south direction of the field on either side of the reconnection x-line.

The cause of the magnetic reconnection that drives the dynamics in the Jovian magnetosphere is still under discussion, and there are other models that suggest reconnection at Jupiter is to a significant degree solar wind-driven [e.g., *Cowley et al.*, 2003]. Solar wind-driven reconnection would occur on the dayside low latitude magnetopause for a northward-oriented interplanetary magnetic field (opposite Jupiter's equatorial magnetic field, which is oriented southward). The opened flux would close owing to reconnection at an x-line in the tail, similar to the process in the Dungey cycle at Earth (see section 2.2). However, *Cowley et al.* [2003] propose that the Dungey cycle x-line at Jupiter would likely be restricted to the dawn side because of the strong outward flows, associated with corotation and the Vasyliūnas cycle, that oppose sunward flow in the dusk and midnight sectors. In contrast, the x-line due to Vasyliūnas cycle reconnection is expected to extend across most of the tail (see Figure 1.4).

Finally, there are studies that propose a non-traditional interaction betwen Jupiter's and the solar wind. *Delamere and Bagenal* [2010] suggest that the solar wind drives flows in Jupiter's magnetosphere through viscous interactions with the magnetopause. These interactions allow for the transport of mass and energy between the solar wind and the magnetosphere, and would influence the location of a tail x-line. In another study, *McComas and Bagenal* [2007] argue that at Jupiter the magnetic flux opened via dayside reconnection with the solar wind need not close in the magnetotail as at the Earth. Instead, they propose that the flux closes on the magnetopause, near the polar cusps, rendering tail reconnection unnecessary. They also argue that at Jupiter tail reconnection is an ineffective method of returning flux to the day side, based on calculations of length of time it would take for the return flow of plasma from a distant neutral line, ~750-1,000 hours (~75-100 rotation periods). Therefore, another mechanism must exist for closing and returning the flux that is opened on the day side, rather than return flow

from a distant x-line. However, *Cowley et al.* [2008] point out that substorm-like reconnection could occur much closer to the planet than the distant neutral line, so returning flux to the day side is not as difficult as McComas and Bagenal estimate. Cowley et al. also illustrate the difficulty of getting enough flux to close in the cusp to balance flux opened through reconnection with northward IMF, meaning that open flux would still accumulate in the lobes until it can be closed through tail reconnection.

1.2 Purpose and organization of the dissertation

The subjects of this thesis are the structure and dynamics of Jupiter's magnetosphere. We address these topics and related unanswered questions in three distinct but related studies, each described in one of the following three chapters. The first study is a survey of magnetometer data to identify signatures of reconnection in Jupiter's magnetotail and characterize the spatial distribution, recurrence period, and other properties of these events. The second part of the thesis is an improved mapping, through flux equivalence, of Jupiter's auroral features to their sources in the middle and outer magnetosphere. The final study is a large-scale kinetic simulation that examines the effects of centrifugal forces and field line stretching in Jupiter's rapidly-rotating magnetosphere.

In Chapter 2 we describe the first study, a statistical analysis of the properties and distribution of reconnection events in Jupiter's magnetotail. Reconnection is an important process that allows for the release of mass and energy from the system. The goal of our study was to establish where and how often reconnection occurs at Jupiter, and to use that information to contribute to our understanding of magnetospheric dynamics. For example, the local time distribution of reconnection events provides useful clues to the relative importance of the solar

wind in driving reconnection. The results are also relevant to the current picture of Jupiter's magnetospheric structure because the spatial distribution of reconnection events would indicate the location of a statistical separatrix separating inward and outward flow. The motivating questions behind this study include: What is the spatial distribution of reconnection events in magnetometer data collected in Jupiter's magnetotail? How frequently does reconnection occur? Does reconnection at Jupiter occur with a statistically significant periodicity? Where is the statistical separatrix separating inward and outward flow? What is the typical length scale and duration of Jupiter's reconnection events or plasmoids? How do the events and their properties (duration, frequency, etc.) compare to similar reconnection or reconfiguration events identified from particle data?

Chapter 3 describes a new model for mapping the polar aurora to source regions in the middle and outer magnetosphere. This mapping model uses flux equivalence rather than tracing field lines from a model, which provides a more precise mapping beyond ~30 R_J, where the current global field models become inaccurate. Mapping the polar aurora provides information about magnetospheric dynamics because it allows identification of the size and location of Jupiter's polar cap. Knowing how much flux may be open in the polar cap gives us insight into whether Dungey cycle-like reconnection may be required. The mapping also enables us to identify the source regions of polar dawn spots, auroral signatures which are thought to be associated with the inward flow of tail reconnection, and relate our findings to the location of a statistical separatrix in the tail. The mapping results also contribute to our understanding of Jupiter's magnetospheric structure. The varying nature of the auroral emissions in the polar regions suggests that there are very different processes occurring in the different source regions in the magnetosphere. Additionally, we are able to more precisely identify the magnetospheric

source region of the main oval emissions, which are associated with corotation enforcement currents and are expected to map to ~20-30 R_J, though the distance may vary with local time. Such variations could be explained by a local time dependence of the plasma outflow rate or the current sheet density and thickness. Some of the motivating questions behind this study are: Where, and how big, is Jupiter's polar cap? Where do the polar auroral features map to in radial distance and local time in the equatorial plane? What is the source of the polar dawn and nightside spots, which are through to be associated with tail reconnection? Do the main oval emissions map to similar equatorial radial distances at all longitudes? What are the magnetospheric sources of the multiple auroral arcs? Where do they map, and what processes produce them?

In Chapter 4 we examine the effects of centrifugal forces arising from Jupiter's rapid rotation and the associated effects of field line stretching in the noon to dusk sector and beyond on particle energy and pitch angle distributions. Observations show that Jupiter's plasma sheet is thickest in the afternoon to dusk local time sectors. From noon to dusk, the magnetopause distance increases by ~50 percent, so one might then expect that the plasma sheet would thin in response to the reduced solar wind pressure as the magnetopause distance increases, but observations show that the opposite is true. *Kivelson and Southwood* [2005] offered an explanation in which they attributed the dusk side plasma sheet heating and thickening to centrifugal forces, suggesting that as a result of rotation, low energy particles gain parallel velocity as they move radially outward, and the resulting anisotropy makes the plasma sheet become unstable. It is not immediately apparent that the model provides net heating of the plasma because the particles that remain near the equatorial part of the flux tube cool as the flux tube stretches and the field magnitude decreases. We developed a large-scale kinetic (LSK)

simulation to test the key physical processes in this idea, with the goal of better-understanding the effects of centrifugal forces on plasma sheet and magnetospheric structure. The motivating questions behind this study include: How do centrifugal forces and field line stretching affect the plasma energy distribution and pitch angle distribution? If there is a net gain in energy, is it sufficient to explain the observed plasma sheet thickening from noon to dusk? What are the consequences of nonadiabatic behavior that arises because the time scale for field line stretching is short compared with particle bounce periods?

We end the dissertation with a summary and discussion of future work.

Bibliography

Behannon, K. W., L. F. Burlaga, and N. F. Ness (1981), The Jovian magnetotail and its current sheet, *J. Geophys. Res.*, *86*, 8385-8401.

Bolton, S. J, R. M Thorne, S. Bourdarie, I. DePater, and B. Mauk (2004), Jupiter's Inner Radiation Belts, in *Jupiter: the Planet, Satellites, and Magnetosphere*, edited by F. Bagenal et al., Cambridge Univ. Press, New York.

Burke, B. F. and K. L. Franklin (1955), Observations of a variable radio source associated with the planet Jupiter, *J. Geophys. Res.*, *60*, 213-217.

Brown, R. A. (1974), I. A. U. Symposium No. 65, presented 1973, in *Explo- ration of Planetary Systems,* edited by A.Woszczyk and C. Iwaniszewska, p. 527, International Astronomical Union, Tomn, Poland.

Cowley, S. W. H., E. J. Bunce, T. S. Stallard, and S. Miller (2003), Jupiter's polar ionospheric flows: Theoretical interpretation, *Geophys. Res. Lett.*, *30*(5), 1220.

Cowley, S. W. H., S. V. Badman, S. M. Imber, and S. E. Milan (2008), Comment on "Jupiter: A fundamentally different magnetospheric interaction with the solar wind" by D. J. McComas and F. Bagenal, *Geophys. Res. Lett.*, *35*, L10101, doi:10.1029/2007GL032645.

Delamere, P. A., and F. Bagenal (2010), Solar wind interaction with Jupiter's magnetosphere, *J. Geophys. Res.*, *115*, A10210, doi:10.1029/2010JA015347.

Gurnett, D. A., W. S. Kurth, A. Roux, S. J. Bolton, and C. F. Kennel (1996), Evidence for a magnetosphere at Ganymede from plasma-wave observations by the Galileo spacecraft, *Nature, 384,* 535 - 537.

Hill, T. W., A. J. Dessler, and C. K Goertz (1983), Magnetospheric Models, in *Physics of the Jovian Magnetosphere*, edited by A. J. Dessler, p. 395, Cambridge Univ. Press, New York.

Joy, S. P., M. G. Kivelson, R. J. Walker, K. K. Khurana, C. T. Russell, and T. Ogino (2002), Probabilistic models of the Jovian magnetopause and bow shock locations, *J. Geophys. Res., 107,* 1309, doi: 10.1029/2001JA009146.

Khurana, K. K., and M. G. Kivelson (1989), On Jovian plasma sheet structure, *J. Geophys. Res.*, *94*, 11791-11803.

Khurana, K. K., and M. G. Kivelson (1993), Inference of the angular velocity of plasma in the Jovian magnetosphere from the sweepback of magnetic field, *J. Geophys. Res.*, *98*, 67.

Khurana, K. K. and H. K. Schwarzl (2005), Global structure of Jupiter's magnetospheric current sheet, *J. Geophys. Res.*, *110*, doi:10.1029/2004JA010757.

Khurana, K. K., M. G. Kivelson, D. J. Stevenson, G. Schubert, C. T. Russell, R. J. Walker, and C. Polanskey (1998), Induced magnetic fields as evidence for subsurface oceans in Europa and Callisto, *Nature, 395,* 777-780, doi: 10.1038/27394.

Khurana, K. K., M. G. Kivelson, V. M. Vasyliūnas, N. Krupp, J. Woch, A. Lagg, B. H. Mauk, and W. S. Kurth (2004), The configuration of Jupiter's magnetosphere, in *Jupiter: the Planet, Satellites, and Magnetosphere*, edited by F. Bagenal et al., Cambridge Univ. Press, New York.

Khurana, K. K., X. Jia, M. G. Kivelson, F. Nimmo, G. Schubert, and C. T. Russell (2011) Evidence of a global magma ocean in Io's interior, *Science*, *332*, 1186-1189, doi:10.1126/science.1201425.

Kivelson, M. G., and K. K. Khurana (2002), Properties of the magnetic field in the Jovian magnetotail, *J. Geophys. Res.*, *107*, 1196.

Kivelson, M. G. and D. J. Southwood (2005), Dynamical consequences of two modes of centrifugal instability in Jupiter's outer magnetosphere, *J. Geophys. Res.*, *110*, A12209, doi:10.1029/2005JA011176.s

Kivelson, M. G., K. K. Khurana, C. T. Russell, R. J. Walker, J. Warnecke, F. V. Coroniti, C. Polanskey, D. J. Southwood, and G. Schubert (1996), Discovery of Ganymede's magnetic field by the Galileo spacecraft, *Nature, 384,* 537 - 541.

Kivelson, M., K. Khurana, D. Stevenson, L. Bennett, S. Joy, C. Russell, R. Walker, C. Zimmer, and C. Polanskey (1999), Europa and Callisto: Induced or intrinsic fields in a periodically varying plasma environment, *J. Geophys. Res., 104{*A3), 4609-4625.

Kivelson, M., K. Khurana, C. Russell, M. Volwerk, R. Walker, and C. Zimmer (2000), Galileo magnetometer measurements: A stronger case for a subsurface ocean at Europa, *Science,* 252(5483), 1340-1343.

Krupp, N., A. Lagg, S. Livi, B. Wilken, J. Woch, E. C. Roelof, and D. J. Williams (2001), Global flows of energetic ions in Jupiter's equatorial plan: First-order approximation, *J. Geophys. Res.*, *106*, 26017-26032.

Kupo, I., Yu. Mekler, and A. Eviatar (1976), Detection of ionized sulphur in the Jovian magnetosphere, *Astrophys. Space Sci.*, *40*, 63.

Lepping, R. P., M. D. Desch, L. W. Klein, E. C. Sittler Jr., J. D. Sullivan, W. S. Kurth, and K. W. Behannon (1983), Structure and other properties of Jupiter's distant magnetotail, *J.*

Geophys. Res., *88*, 8801-8815.

McComas, D. J. and F. Bagenal (2007), Jupiter: A fundamentally different magnetospheric interaction with the solar wind, *Geophys. Res. Lett.*, *34*, L20106, doi:10.1029/2007GL031078.

Smith, E. J., L. Davis, Jr., D. E. Jones, P. J. Coleman, Jr., D. S. Colburn, P. Dyal, C. P Sonett, and A. M. A. Frandsen (1974), The planetary magnetic field and magnetosphere of Jupiter: Pioneer 10, *J. Geophys. Res.*, *79*, 25.

Thomas, N., F. Bagenal, T. W. Hill, and J. K. Wilson (2004), in *Jupiter: the Planet, Satellites, and Magnetosphere*, edited by F. Bagenal et al., Cambridge Univ. Press, New York.

Vasyliūnas, V. M. (1983), Plasma Distribution and Flow, in *Physics of the Jovian Magnetosphere*, edited by A. J. Dessler, p. 395, Cambridge Univ. Press, New York.

Zimmer, C., K. Khurana, and M. Kivelson (2000), Subsurface oceans on Europa and Callisto: Constraints from Galileo magnetometer observations, *Icarus, 147(2),* 329-347, doi:10.1006/icar.2000.6456.

CHAPTER 2

Properties and Periodicities of Reconnection Events in Jupiter's Magnetotail

2.1 Introduction

An important process in planetary magnetospheres is the release of mass and conversion of energy through magnetic reconnection. At the Earth, interaction with the solar wind introduces energy and momentum into the magnetosphere. The stored mass and energy can be released through large-scale dynamics, most often in the form of substorms, which are global instabilities of the magnetosphere that result in changes to the global magnetic field configuration. At Jupiter, an additional process contributes to the dynamics because the magnetosphere has an internal plasma source: the volcanically active moon Io, which releases about one ton of plasma per second. Ultimately the plasma must be removed from the system; one likely mechanism is magnetic reconnection and subsequent plasmoid release. In the Jovian magnetosphere, these dynamics are likely rotationally-driven rather than solar wind-driven as at the Earth, in part due to Jupiter's short 10-hour rotation period and the vast size of the magnetosphere.

In this chapter we present results from a survey of reconnection events identified in the Jovian magnetotail from the available magnetometer data. The goal of this survey is to characterize the spatial distribution, recurrence period, and other properties of these events. The results improve our understanding of Jupiter's magnetospheric dynamics by establishing where and how often reconnection occurs, and the local time distribution of reconnection events provides useful clues to the relative importance of the solar wind in driving reconnection. The

survey also contributes to our understanding of Jupiter's magnetospheric structure by identifying the location of a statistical separatrix separating inward and outward flow.

This chapter is organized as follows: first, we review the current understanding of magnetotail dynamics at both the Earth and in rapidly rotating magnetospheres such as at Jupiter. Next, we introduce the data used in this study and the quantitative selection methods used to identify events. Then, we show that the identified reconnection events occur at nearly all radial distances and local times for which data are available, and that they are observed in the magnetotail with roughly equal frequency in the pre- and post-midnight local time sectors. Finally, we discuss how our work relates to previous studies, what the results imply about a near-Jupiter neutral line, and whether or not the events exhibit any characteristic periodicity.

2.2 Dynamics in the terrestrial magnetosphere

In trying to understand observations from planetary magnetospheres, it is natural to draw comparisons with processes familiar from the Earth. Therefore, in this section we briefly introduce two dynamic processes that are important in the terrestrial magnetosphere: substorms and bursty bulk flows. This discussion is intended to provide context to help interpret the reconnection events observed at Jupiter that are discussed later in this chapter. In our introduction of terrestrial substorms we follow the discussion of *McPherron* [1992].

2.2.1 Substorms at Earth

The solar wind is the primary source of plasma and energy during substorms in the terrestrial magnetosphere. Substorms occur as a result of the magnetospheric interaction with the solar wind, and serve as a mechanism to release the energy and momentum that is transferred

into the magnetosphere through magnetic reconnection. A substorm occurs after brief (~one hour) sustained periods of southward interplanetary magnetic field (IMF), during which time the IMF can reconnect with the Earth's oppositely-oriented field (northward at the equator) at the dayside magnetopause. Field lines which are opened on the day side are pulled tailward by the solar wind, close again through reconnection in the tail, and then convect back to the day side in a process called the Dungey cycle [*Dungey*, 1961]. The Dungey cycle, illustrated in Figure 2.1, can occur as part of a substorm, in which mass and energy builds up in the magnetosphere and is explosively released, or as part of steady magnetospheric convection, in which the dayside reconnection rate is balanced by the tail reconnection rate.

In a substorm, dayside reconnection is followed by a series of characteristic auroral signatures [*Akasofu*, 1964], changes to the global magnetic field and plasma configuration, and energy release. During the growth phase of a substorm, magnetic flux reconnects on the dayside magnetopause faster than it can be replaced because the ionosphere has a finite conductivity, which slows the flow at the foot of the field lines. As a result, the return magnetospheric flow, limited by the ionospheric conductivity, is insufficient to replace the flux reconnecting on the dayside, and the dayside magnetopause is displaced Earthward. Magnetic flux is transported from the dayside magnetopause to the tail lobes. Increased pressure from the solar wind thins the plasma sheet. There are two competing phenomenological models, the near-Earth neutral-line model and the current disruption model, that describe how a substorm progresses following the plasma sheet thinning. Both models allow for global reconfiguration of the magnetosphere, the observed auroral signatures, and energy release and plasma loss through reconnection in the tail. However, recent results from the THEMIS mission [*Angelopoulos et al.*, 2008] suggest that the near-Earth neutral-line model most accurately fits the observations.

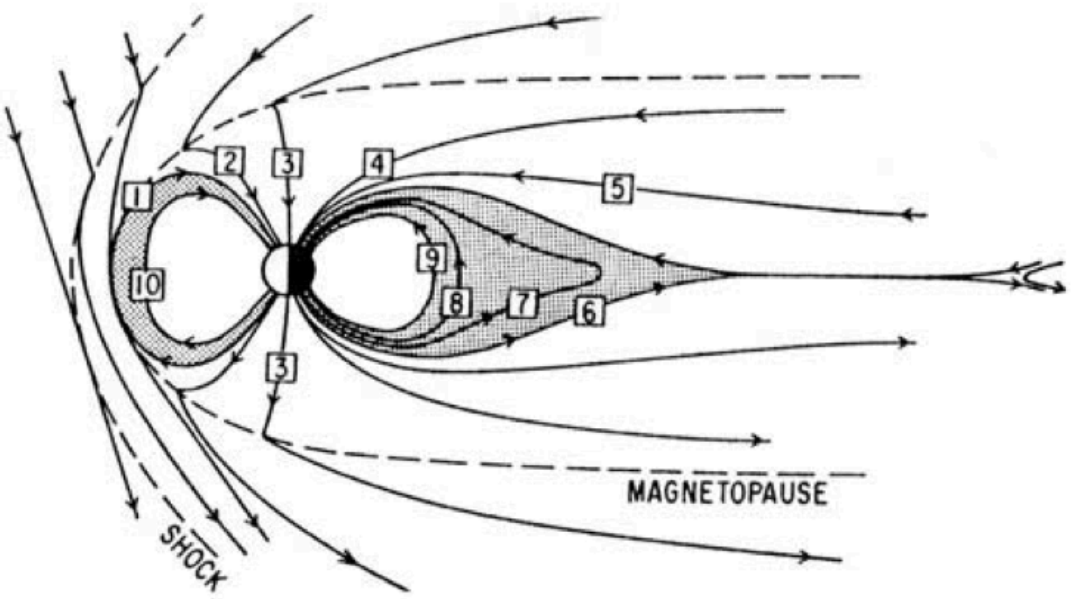

Figure 2.1: Schematic of the Dungey cycle [*Dungey*, 1961], shown in a meridional plane. In step 1 reconnection occurs on the day side between the earth's northward-oriented and the southward interplanetary magnetic field. The field lines which are opened on the day side are then pulled tailward by the solar wind (steps 2-4), close again through tail reconnection (6), and convect back to the day side (7, 8, 9). From *Axford* [1969].

In the near-Earth neutral-line model, the thinning of the plasma sheet enables reconnection during the substorm growth phase. As the plasma sheet thins, the vertical component of the magnetic field becomes smaller, until ions no longer behave adiabatically and reconnection occurs in the tail at a near-Earth neutral line. This reconnection forms a plasmoid, or a magnetic flux rope, as illustrated in Figure 2.2. The substorm expansion phase begins when reconnection proceeds on to open field lines. Magnetic pressure and tension pull the plasmoid down the tail, and a thin plasma sheet forms in its wake; inside of the x-line the flows are predominantly earthward. The x-line moves farther down the tail and the plasma sheet thickens. The recovery phase begins when the x-line has reached the location of the distant neutral line and auroral activity subsides.

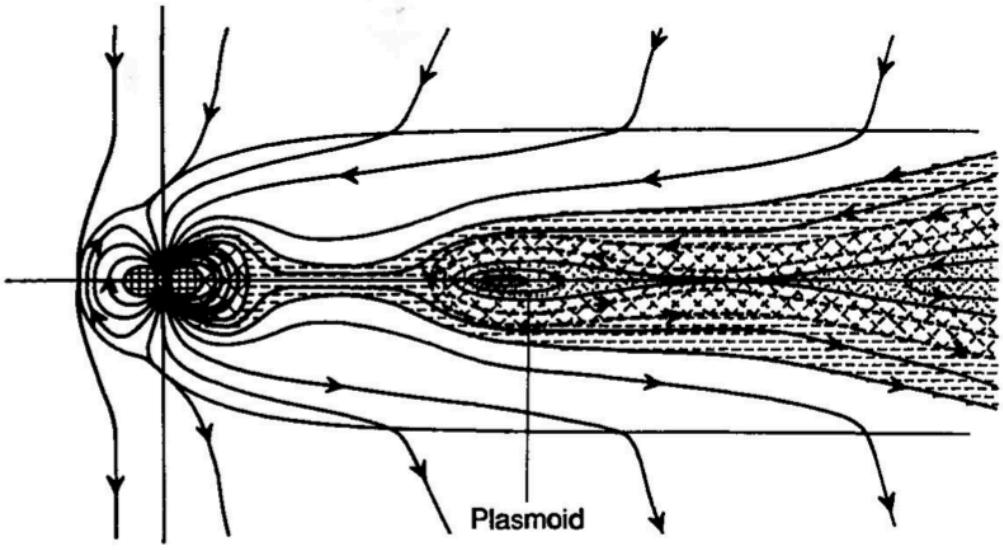

Figure 2.2: Illustration of the Earth's magnetosphere showing a plasmoid moving down the tail during the expansion phase of a substorm. From Figure 13.23 in *McPherron* [1995].

2.2.2 Bursty Bulk Flows

During a substorm, reconnection occurs across a substantial portion of the magnetotail, and the magnetosphere exhibits changes to the magnetic field and plasma that occur on large scales. However, more localized processes such as bursty bulk flows can also play an important part in the magnetosphere's mass, energy, and magnetic flux transport. In the Earth's inner central plasma sheet, observations have shown high-speed flows on time scales of ~1 minute that occur within longer intervals (~10 minutes) of enhanced velocity structures called bursty bulk flows, or BBFs [*Angelopoulos et al.*, 1992]. BBFs are typically associated with magnetic field dipolarizations [*Angelopoulos et al.*, 1992] and occur most frequently during geomagnetically active times, including substorms. Though the flow channel width is relatively narrow (~1-2 R_E, or ~10% of the tail width), BBFs are important mechanisms for mass, energy, and magnetic flux transport [*Angelopoulos et al.*, 1996]. Early estimates suggested that the typical rate of energy

transport for a BBF is ~10% of the power released during a substorm [*Angelopoulos et al.*, 1994], though more recent multi-point measurements from Cluster indicate that BBFs could account for as much as 20% of the typical substorm energy transport [*Cao et al.*, 2006].

2.3 Jupiter's Magnetospheric Dynamics: Observations and Questions

In the previous section we reviewed two of the dynamic processes in the Earth's magnetosphere, substorms and bursty bulk flows. We turn now to Jupiter, where dynamics are likely rotationally-driven rather than solar wind-driven as at the Earth, as we introduced in Chapter 1. A key process is the Vasyliūnas cycle, the internally-driven process in which mass-loaded flux tubes rotate to the night side, are stretched by centrifugal forces, pinch off, and form a plasmoid. Jupiter's short rotation period (~10 hours) and the vast size of the Jovian magnetosphere both contribute to the dynamical importance of rotational stresses. An additional factor distinguishing Jupiter's magnetosphere is that the primary source of plasma, the moon Io, is internal to the magnetosphere, rather than external, like the solar wind. In this section we review some of the discoveries revealed from Galileo particle and magnetometer measurements, and then discuss how the work in this thesis can improve our understanding of Jupiter's magnetospheric dynamics.

2.3.1 Observations from particle measurements

In situ particle and magnetic field measurements are available from the Galileo spacecraft, which orbited Jupiter from mid-1996 to 2003. Much of what we currently know about dynamics on a global scale is based on analysis of data from Galileo's energetic particle detector (EPD) instrument, which measured the temporal and spatial distribution of ions at energies from

20 keV to 55 MeV and electrons with energies between 15 keV and 11 meV [*Williams et al.*, 1992]. The EPD data provides particle anisotropies, which can in turn be used to infer flow, and have established a global flow pattern, primarily in the direction of corotation [*Krupp et al.*, 2001], and have revealed intermittent particle flow bursts in the magnetotail.

Woch et al. [2002] studied such inferred flow bursts at distances out to 150 R_J (1 R_J = 1 Jovian radius = 71,492 km) in the tail and identified a statistical separatrix separating inward and outward flow bursts. Outside of ~100 R_J in the post-midnight sector they observed primarily outward flow bursts. In the pre-midnight sector they drew two possible lines that could separate flow directions, recognizing that the limited data in the dusk sector did not establish its location in that region.

Particle anisotropies have also been studied by *Kronberg et al.* [2005, 2007, 2008] with good agreement between the inferred flows and magnetic field data. The authors identify 34 reconfiguration events which include disturbed intervals that are characterized by increases in the radial and corotational anisotropies occurring at the same time as increases to the north-south component of the magnetic field. Large, positive (negative) radial anisotropies occur at the same time as large negative (positive) B_θ signatures, both of which are consistent with outward (inward) flow and field dipolarization due to reconnection. The reconfiguration events can be as short as 3 hours or as long as 39 hours and they occur at radial distances from 63 to 142 R_J. With one exception, the reported reconfiguration events are located in the post-midnight sector. The disturbed intervals described in *Kronberg et al.* [2007] also display a ~2-3 day periodicity consistent with the periodic modulations in the plasma flux described by *Woch et al.* [1998].

Whereas particle data have been used to examine magnetospheric dynamics on a global scale, studies that make primary use of the magnetometer data have thus far focused on

individual events or orbits. Two of the most prominent reconnection events were reported by *Russell et al.* [1998]. The events occurred a few days apart in the G8 orbit, both in the post-midnight sector. These events are characterized by an increase in the magnitude of B_θ, the north-south component of the magnetic field, and in the total field magnitude. In one event the spacecraft was tailward of the x-line, and in the other the spacecraft was planetward of the x-line. In both events there were changes to the bendback angle that were large compared to the background fluctuations. The bendback angle represents how swept back (opposite the direction of planetary rotation) the field line is with respect to the radial direction. Changes to the bendback angle can be used to infer the direction of plasma flow, as will be discussed in later sections.

2.3.2 Motivating questions for this work

Dynamics at Jupiter are thought to be predominantly rotationally-driven. However, a major outstanding question is the degree to which dynamics are influenced by the solar wind. As we discussed in Chapter 1, most of the current models of Jovian magnetospheric dynamics agree that the solar wind plays a minor role, but disagree on its relative importance. Models range from a completely closed magnetosphere with nearly no solar wind influence (e.g., *McComas and Bagenal* [2007]) to significantly solar wind-driven, including a Dungey cycle and related x-line (e.g., *Cowley et al.* [2003]). Ultimately the models of Jovian magnetospheric dynamics must account for the reconnection and plasma flows that have been observed in magnetic field and particle data.

Previous studies of the magnetometer data have been restricted to individual orbits or events. Therefore, this work provides the first complete survey of reconnection events in the

Jovian magnetotail from the magnetometer data, which is a first step toward understanding whether the reconnection could be driven entirely by internal processes or is significantly influenced by the solar wind. We present a statistical analysis of the reconnection event distribution that can be compared with previous analyses of energetic particle distributions (such as the separatrix in *Woch et al.* [2002] and the distribution of events in *Kronberg et al.* [2005, 2007]). The results will help establish where and how often reconnection occurs in the Jovian magnetotail and provide a better understanding of what drives dynamics there. In particular, this work addresses the following questions:

- What is the spatial distribution of reconnection events in Jupiter's magnetotail?
- How frequently does reconnection occur?
- Where is the statistical separatrix separating inward and outward flow?
- What is the typical size and duration of Jupiter's reconnection events or plasmoids?
- Does reconnection at Jupiter occur with a statistically significant periodicity?

The answers will help us understand the relative importance of internal versus solar wind driving of dynamics at Jupiter. For example, a 2-3 day periodicity seen in flow bursts, reconfiguration events, and auroral polar dawn spots is thought to be related to the time scale of the internally driven dynamics [*Kronberg et al.*, 2007]. The presence of a similar periodicity in the reconnection events we identify could point to internal driving on the 2-3 day time scale, while the absence of a significant periodicity, or a periodicity that is present only during limited observation intervals, might suggest that reconnection is more heavily influenced by external factors like the solar wind. The local time distribution of reconnection events and the location of a statistical x-line can also provide clues to whether the dynamics are internally or solar wind

driven, as we expect that the x-line associated with solar wind-driven reconnection will be restricted to the dawn sector [*Cowley et al.*, 2003].

2.4 Identifying reconnection signatures in magnetometer data

In this section we describe the quantitative methods used in identifying reconnection events and the ways we used the magnetometer data to infer the flow direction. First we describe the data used in our analysis. Next we outline the event identification criteria, which include an increase in the magnitude of B_θ, the north-south component of the magnetic field. Changes of $|B_\theta|$ may be consistent with reconnection if they result in reconfiguration to a more dipolar field or a field reversal, so we examine changes to the elevation angle in our events. We then discuss how the bendback angle can serve as a proxy for flow and a useful tool in interpreting our events. Finally, we describe how the sign of B_θ can be used to infer the spacecraft's probable location with respect to an x-line and a statistical separatrix.

2.4.1 Data sources

For this analysis we included magnetometer data from Galileo orbits G1 (June 1996) through A34 (Jan. 2003), as well as magnetometer data from Pioneer 10, Voyager 1 and Voyager 2. These data are publicly available for download from the Planetary Data System at http://pds-ppi.igpp.ucla.edu/. We restricted ourselves to data with time resolution 60 seconds per vector or better, radial distances 30 R_J or greater, and nightside local times (from 18:00 to 06:00 hours). We also restricted ourselves to intervals when the spacecraft was within 15 degrees of the equatorial plane. As most of the data from the Galileo spacecraft were taken near the equator, this latter restriction was mostly relevant to data from the other spacecraft.

We excluded magnetosheath, bow shock, and solar wind data, as well as intervals 5 hours before or after a boundary crossing [Pioneer 10: *Intriligator and Wolfe*, 1976; Voyager 1 and Voyager 2: *Lepping et al.*, 1981; Ulysses: *Bame et al.*, 1992; Galileo: S. Joy, personal communication, 2009]. Periods when the spacecraft only briefly (fewer than 10 hours) crossed back into the magnetosphere from the magnetosheath were also excised. The boundary crossing restrictions ensured that we select only magnetospheric events and not processes occurring because of interaction with the magnetosheath or solar wind.

After selecting for data with the required time resolution, and from the required radial distances, local times, and latitudes, we were left with fewer than 200 hours of data from Voyager 1 and Pioneer 10.

Figure 2.3 shows the number of hours of data used in this study divided into bins of 15 R_J in radial distance by one hour in local time and plotted in the equatorial plane. This figure shows that the data are well distributed over all local times for radial distances inside of ~75 R_J. From ~75 R_J to ~120 R_J more data are available post-midnight than pre-midnight, and at the largest distances (R > 120 R_J) most of the data are within one hour of midnight. Beyond ~105 R_J the dusk sector coverage decreases, and several bins lack data entirely. In the analysis section we normalize the duration of events in each sector by the duration of available data, thereby obtaining an estimate of the event frequency in different regions of the magnetotail.

2.4.2 Quantitative event identification criteria

We identified reconnection events in the magnetometer data by requiring that the magnitude of $B_{\theta,}$ the north-south component of the magnetic field, increase over background levels. A positive increase in B_θ without corresponding changes to the magnitude of the other

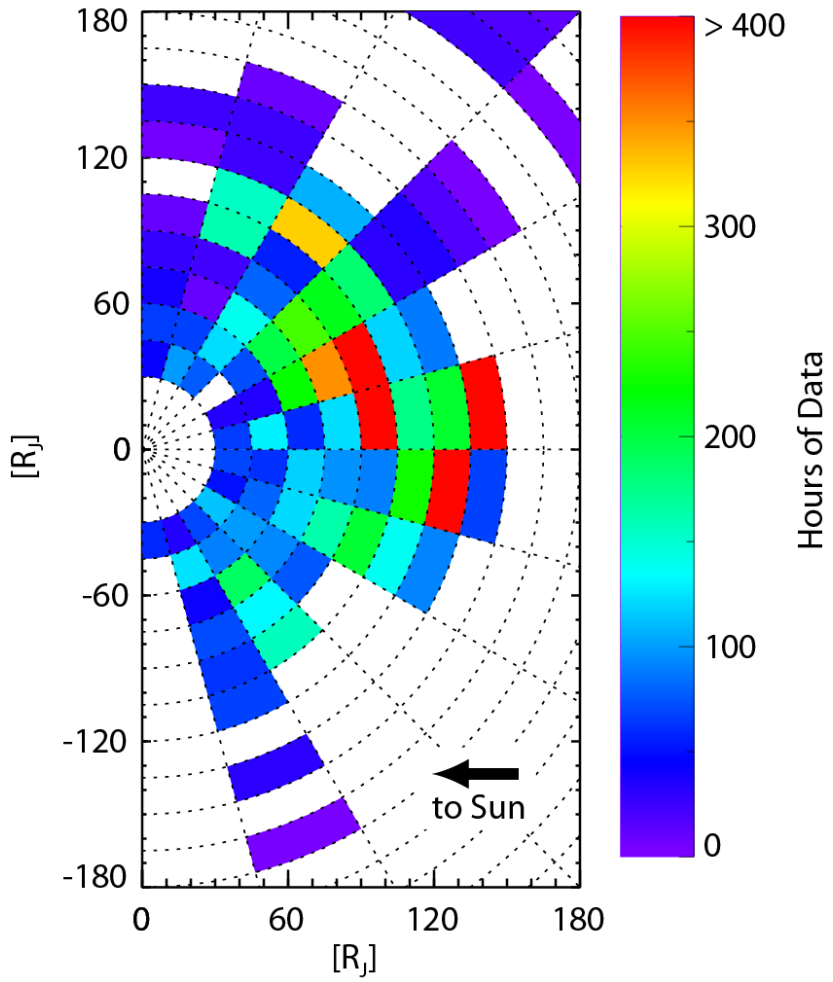

Figure 2.3: The number of hours of available magnetometer data plotted in bins of 15 R_J in radial distance by one hour in local time. This is an equatorial plane view, and the Sun is to the left. At small radial distances (< 75 R_J) the data are relatively evenly distributed in local time, but beyond ~75 R_J more data are available in the dawn sector than in the dusk sector. Beyond ~105 R_J the dusk sector coverage decreases, and several bins lack data entirely. White represents bins with no available data.

field components implies reconfiguration to a more dipolar field. Such a reconfiguration is shown in Figure 2.4. In the top panel we have drawn the initial field configuration, which is primarily radial except near the current sheet. In the second panel we have drawn reconnected field lines, noting the expected field orientation and flow directions. On either side of the

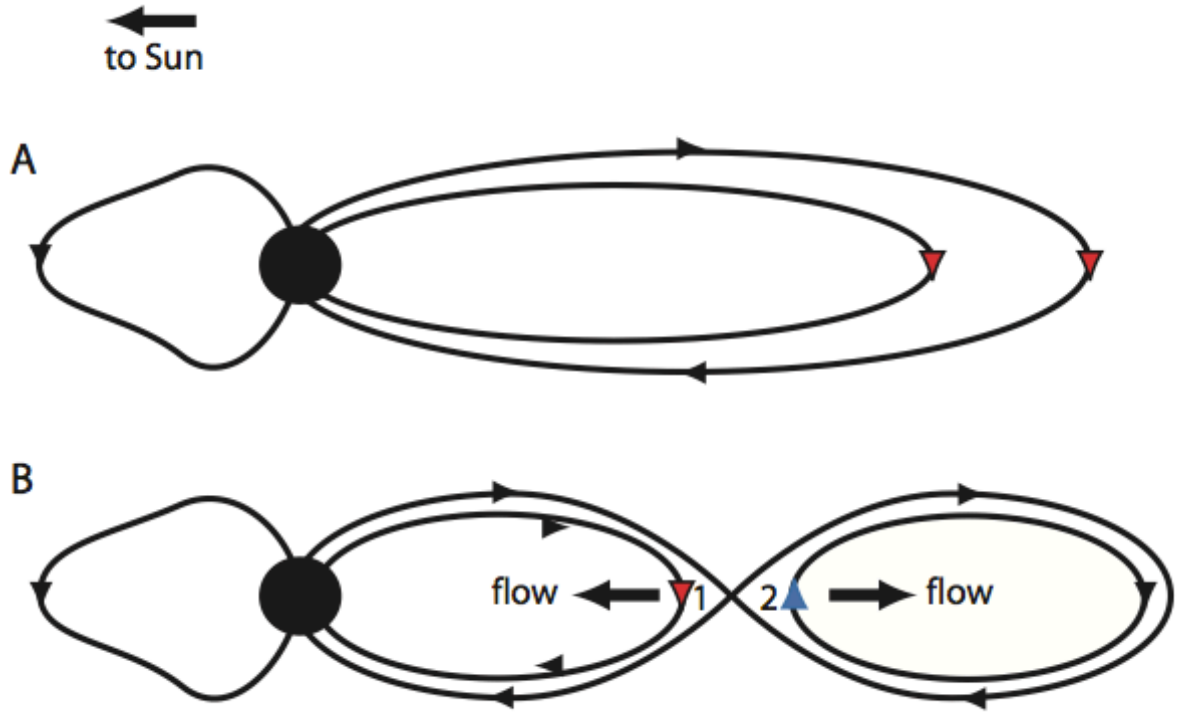

Figure 2.4: Reconnection in the Jovian magnetotail, illustrated here in a meridional view. The top panel shows the initial field configuration, which is primarily in the radial direction except near the current sheet. The second panel shows the reconfiguration to reconnected field lines, noting the expected field orientation and flow directions. On either side of the x-line the field is more dipolar than prior to reconnection. The effect corresponds to an increase of $|B_\theta|$. A positive B_θ is found when the spacecraft is either located planetward of the x-line (position 1) or far down the tail, while a negative B_θ is observed if the spacecraft is located tailward of the x-line (position 2).

reconnection point the field becomes more dipolar than prior to reconnection, and $|B_\theta|$ increases. A large, positive B_θ indicates that the spacecraft is located on the planetward side of the x-line (position 1 in the second panel). A reversal in B_θ indicates that the spacecraft is located on the tailward side of a reconnection x-line (position 2 in the second panel). On short time scales, such reconfigurations are consistent with reconnection.

We defined the reference background field by taking a 1-day running average of $|B_\theta|$. This provides a relatively smooth background that varies slowly in time but allows for large-scale radial and local time variations. As such, the background $|B_\theta|$ decreases with radial distance, is largest in the pre-midnight sector, and decreases with local time toward dawn.

With a working definition for the background $|B_\theta|$ established, the next step was to select a quantitative criterion for the B_θ increase over background levels. This proved to be a delicate task because there are many ways to define an increase over background levels. In the course of this study we tested a variety of criteria for identifying the signature of an increase over background levels, such as requiring: an absolute increase of a few nanotesla, an increase proportional to the background level, or an increase with a specified dependence on the radial distance. Each method selected several hundred events in the data. Although the number and duration of the events varied with the identification criteria, the strongest events were selected by all methods applied.

In this chapter we will describe the characteristics of events in which $|B_\theta|$ increases over background levels by at least a factor of 2, and typically by a factor of 3. The events selected by this method include the largest and most convincing events and exclude some of the possibly spurious events that were identified by other the selection methods we tested.

We began our event identification by searching for intervals in which $|B_\theta|$ was enhanced above the background level. Each event satisfied the following relation shown in equation 2.1:

$$\frac{|B_\theta|}{\langle |B_\theta| \rangle} \geq 2 , \tag{2.1}$$

where $\langle |B_\theta| \rangle$ is the reference background field (a 1-day running average of $|B_\theta|$). If the background $|B_\theta|$ was small (< 5 nT) we required a threefold increase over background levels. If the background B_θ was larger than 5 nT we required only a factor of two increase over the

background. Furthermore, we required $B_\theta > 3$ nT or $B_\theta < -2$ nT in order to ensure a robust event selection even when the background was small. (The background magnitude is frequently less than 1 nT at large radial distances in the post-midnight sector.) Although the selection criteria may have excluded some cases of magnetic activity, we believe that they are sufficiently rigorous that the events selected would be hard to account for other than as signatures of tail reconnection.

After identifying an initial $|B_\theta|$ enhancement, we required that $|B_\theta|$ remain enhanced for at least 60 seconds. We defined the event duration as the time before and after the initial enhancement where the field remained disturbed. For events in which the initial $|B_\theta|$ enhancement was during a period of positive B_θ, we defined the event as the time when $|B_\theta|$ remained larger than 1 nT or 1.25 times the background, whichever was larger (again, allowing for brief excursions below the threshold value). For events in which the initial $|B_\theta|$ enhancement was during a period of negative B_θ, we defined the event duration as the time when B_θ remained negative (allowing for brief – less than 2 minute – positive B_θ excursions). These criteria provided a preliminary list of events and specified their duration. To obtain our final event list, we considered two events that occurred within 30 minutes of each other to be part of the same new event. We then removed 47 events that lasted fewer than 10 minutes.

These quantitative identification conditions yielded 249 events, all characterized by an increase of $|B_\theta|$ over background levels. The events have an average duration of 59 minutes, with durations ranging from our lower cutoff of 10 minutes to just over 5 hours. Events occur at nearly all nightside local times (~19:00 to ~06:00 hours) and at radial distances between 33 to 155 R_J, the latter merely a reflection of the range of radial distances with good data coverage (as seen in Figure 2.3 there is little data beyond 150 R_J).

Examples of the identified events are given in Figures 2.5 through 2.7. For these three figures, the first panel shows the radial (B_R, in black) and azimuthal (B_φ, in blue) components of the magnetic field, in nT. The second panel shows the north-south component of the magnetic field (B_θ, in black) in nT. The background $|B_\theta|$, a 1-day running average of $|B_\theta|$ used in the event identification procedure, is shown in blue, and the event interval is outlined in red. The next two panels contain the field elevation and bendback angles, which will be defined later in Sections 2.4.3 and 2.4.4, respectively. The final panel shows the field magnitude, again in nT.

In the event of Figure 2.5, the spacecraft was located at a radial distance of ~87R_J and at nearly 02:00 local time. This event, on Galileo's G2 orbit, occurred on 20 September 1996, starting at approximately 13:00 UT and lasting for 3 hours. The background $|B_\theta|$ was ~1 nT as shown by the blue trace in the second panel. During this event B_θ reached -11.6 nT, more than 10 times the background level. This event is interesting because we observe both positive and negative B_θ during the period of enhanced $|B_\theta|$. The event occurs during the 20 September 1996 12:30-22:30 UT reconfiguration event from *Kronberg et al.* [2005].

The second example, shown in Figure 2.6, comes from Galileo orbit C23, when the spacecraft was located at ~42 R_J in radial distance and just past 19:00 local time. This event occurred on 18 September 1999 at approximately 20:00 UT and lasted for 20 minutes. The background $|B_\theta|$ was ~5 nT, much larger than the background value from the 20 September 1996 event, when the spacecraft was in the post-midnight sector.

A third example is given in Figure 2.7. This event occurred on 21 September 1996 at approximately 08:00 UT, under circumstances similar to those of the 20 September 1996 event: both occurred during orbit G2, near 02:00 local time, and just before 90 R_J. In both events B_θ changes sign, but the reversal occurs in opposite directions. In the 20 September 1996 event, B_θ

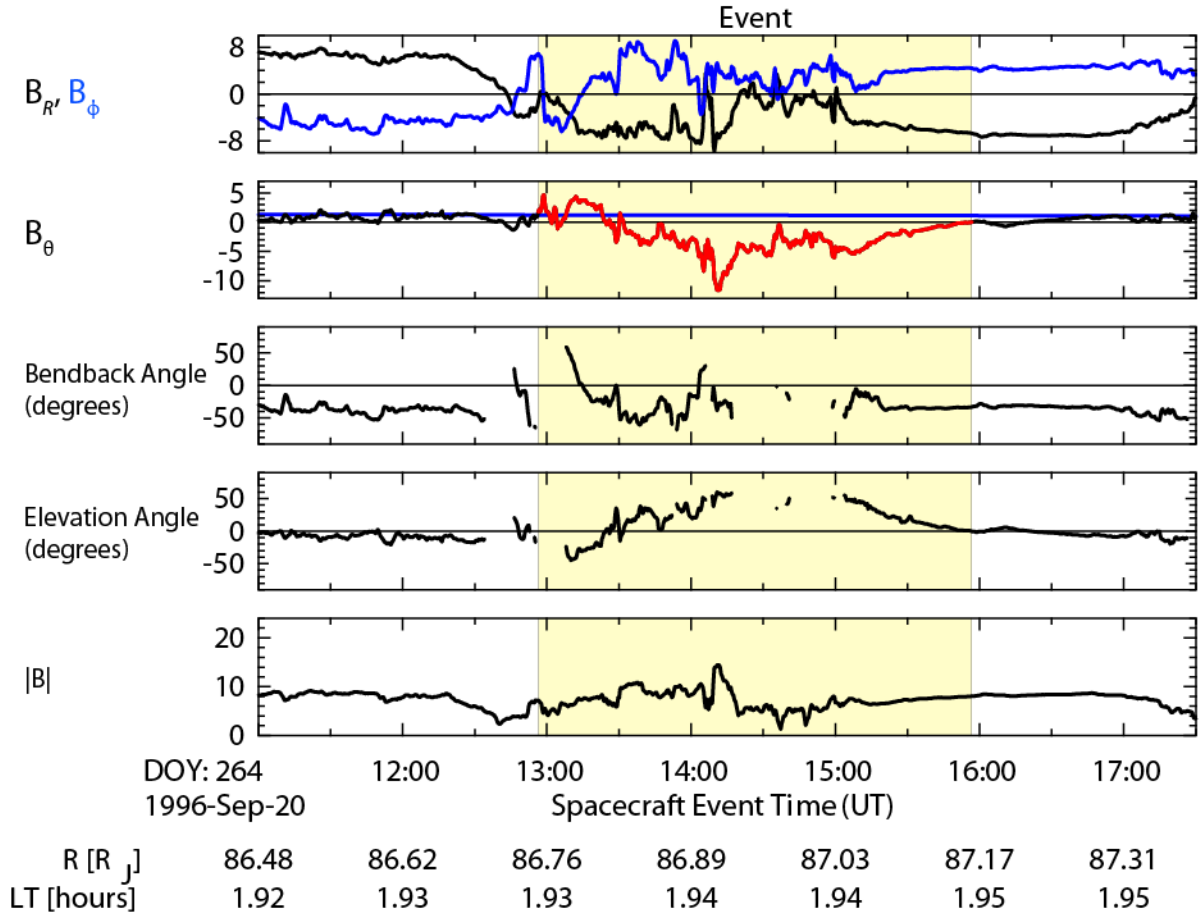

Figure 2.5: Magnetometer data from an example event on 20 September 1996, during Galileo orbit G2. The first panel shows the radial (black) and azimuthal (blue) components of the magnetic field. The second panel shows B_θ, the north-south component of the magnetic field, plotted in black with the event interval overplotted in red. The background $|B_\theta|$, which was used in the event identification procedure, is plotted in blue and is ~1 nT. The bendback angle is shown in the third panel and the elevation angle is shown in the fourth panel. We do not plot either angle when $|B_R| < 3$ nT. The elevation angle and bendback angle are defined in Sections 2.4.3 and 2.4.4, respectively. The spacecraft was at ~2:00 LT and ~87 R_J when it observed this event. B_θ changes sign during this event, which we interpret to be the signature of an x-line moving in over the spacecraft. The bendback changes in the third panel appear to be consistent with our interpretation (see Section 2.4.4 for discussion). The lowest panel shows the field magnitude.

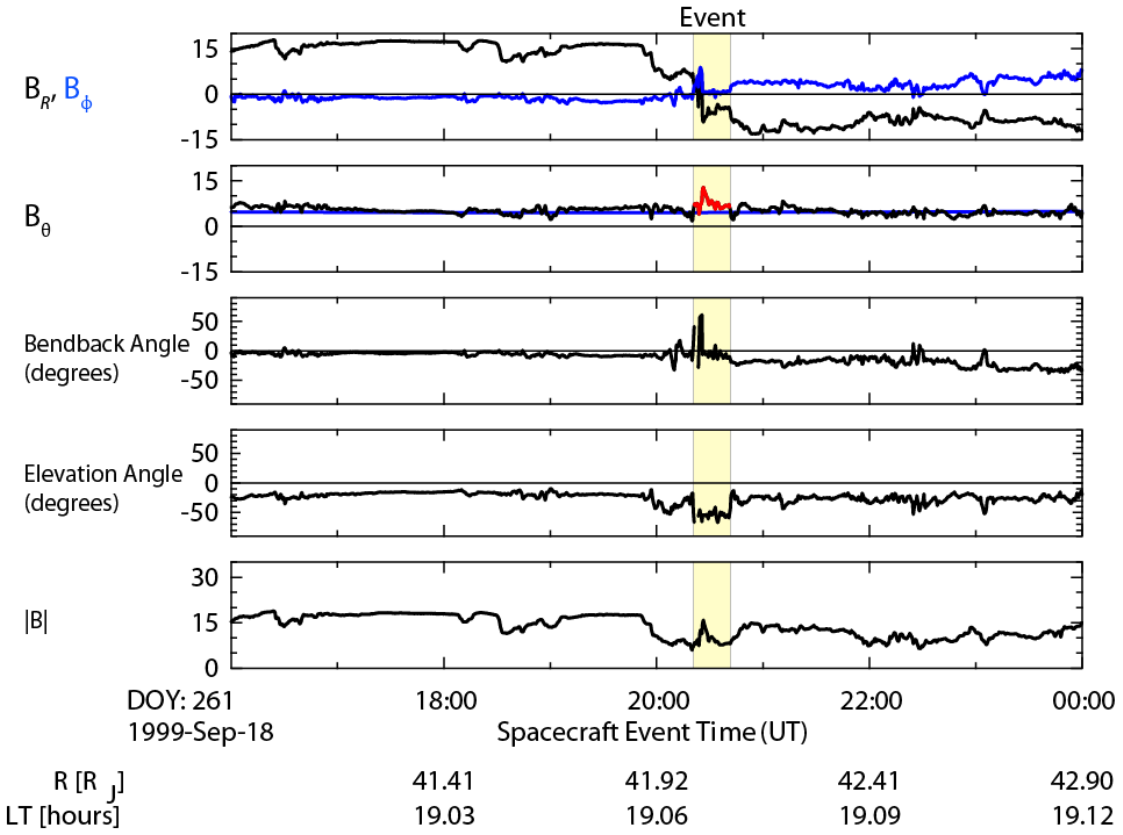

Figure 2.6: As in Figure 2.5, magnetometer data from an example event on 18 September 1999, during Galileo orbit C23. In this event the spacecraft was at ~19:00 LT and ~42 R_J. The background $|B_\theta|$ in the second panel has a magnitude of ~5 nT, much higher than the background for the event of Figure 2.5, which was observed in the dawn sector. Again, the event interval is outlined in red in the second panel. Because B_θ is positive during the event we interpret the spacecraft location to be planetward of an x-line. Again, the bendback changes, shown in the third panel, appear to be consistent with our interpretation of the spacecraft's location relative to an x-line.

changes sign from positive to negative, and in this event B_θ changes sign from negative to positive. Therefore we interpret the reversal as the signature of an x-line associated with a plasmoid moving out over the spacecraft and down the tail.

The two events from the G2 orbit occurred during an interval of disturbed magnetic field with corresponding auroral observations studied by *Prangé et al.* [2001]. The 20 September 1996

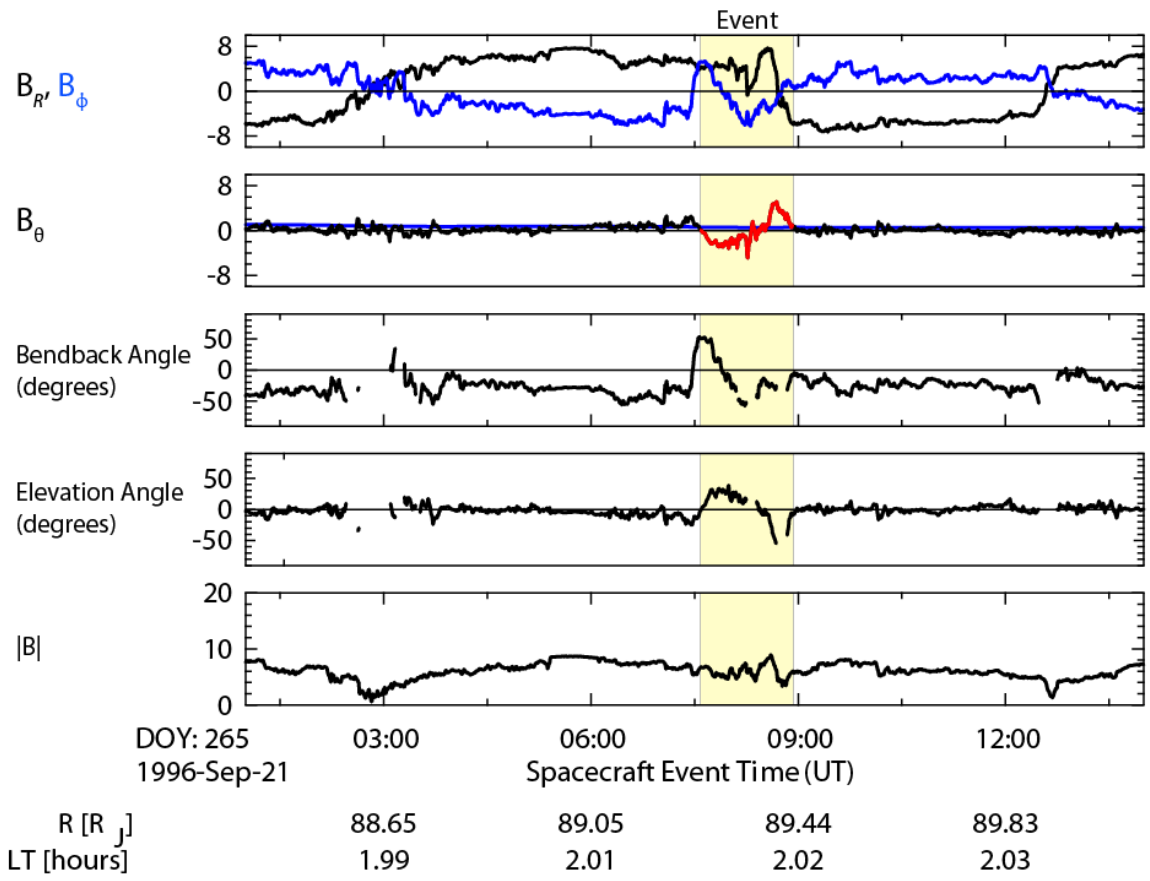

Figure 2.7: As in Figure 2.5, magnetometer data from an example event on 21 September 1996, during Galileo orbit G2. The event interval is outlined in red in the second panel. The bendback angle is shown in the third panel. As in the event of Figure 2.5, B_θ changes sign during this event, which we interpret to be the plasmoid and x-line moving out over the spacecraft. The bendback changes in the third panel appear to be consistent with our interpretation.

event was also included in the list of reconfiguration events published by *Kronberg et al.* [2005]. Though these events have been previously mentioned in the literature, we present them here in further detail because they are among the largest of our events, which facilitates illustrating both the $|B_\theta|$ increase that we require in selecting our events and the associated bendback and elevation angle changes.

Changes of $|B_\theta|$ may be consistent with reconnection if they result in reconfiguration to a more dipolar field or a field reversal. Therefore we also examined the elevation angle, or the

angle that the field makes with respect to the equatorial plane, to confirm that the $|B_\theta|$ increase in the events corresponds to a field reversal or a more dipolar field configuration.

2.4.3 Elevation angle changes in our events

An increase of $|B_\theta|$ is insufficient by itself to demonstrate that the field reconfiguration is consistent with nearby reconnection; we must also consider how the other field components change to ensure that the field has become more dipolar. A good quantity to consider is the elevation angle, which is the angle that the field makes with respect to the radial in the R-θ plane. At the equator the elevation angle is the angle that the field makes with respect to the horizontal. In this discussion we define the elevation angle as

$$\theta_{elevation} = \tan^{-1}\left(\frac{-B_\theta}{|B_R|}\right). \tag{2.2}$$

We use $-B_\theta$ in the numerator so that a northward field has a positive elevation angle, and $|B_R|$ rather than B_R in the denominator so that the angle changes smoothly as the spacecraft goes through the current sheet. When B_R is small the elevation angle changes rapidly with small fluctuations in B_R and such changes may not be meaningful. This is clear from our definition of $\theta_{elevation}$. We therefore evaluate $\theta_{elevation}$ only for $|B_R| > 3$ nT.

Using this definition of $\theta_{elevation}$, a field line with an elevation angle of -90º is purely southward, 0º is radial, and 90º is northward. At the equator, a large, negative elevation angle indicates a dipolar field configuration; a large, positive elevation angle indicates a nearly northward field on the tailward side of an x-line. Both signatures are consistent with reconnection. The equatorial B_θ is typically southward ($B_\theta > 0$) and in the post-midnight sector B_θ

is small compared to B_R, so the quiet-time, lobe field elevation angle in this region is approximately -10º.

In Figures 2.5-2.7, $|\theta_{elevation}|$ increases during the event, indicating that the field has become more dipolar compared to the background, or, if B_θ is negative, that the field has reversed and is strongly northward. For the G2 (dawn sector) events of Figures 2.5 and 2.7, the background elevation angle is roughly +/- 10º. The median $|\theta_{elevation}|$ during these events is ~20º, roughly twice the magnitude of the background angle, and for both events $|\theta_{elevation}|$ gets as large as ~55º. For the C23 (dusk sector) event of Figure 2.6, the background elevation angle is roughly -30º, and is larger than the background in the other two events because the background B_θ is larger. The median $|\theta_{elevation}|$ during the Sept. 18, 1999 event is ~54º, and $|\theta_{elevation}|$ gets as large as 66º.

Similar increases of the elevation angle are characteristic of most of our events. Figure 2.8 shows the median $|\theta_{elevation}|$ in each event (black trace) and the background $|\theta_{elevation}|$ (red trace). Here we define the background as the median of $|\theta_{elevation}|$ over the previous 10 hours, excluding intervals with other events. For this figure we have excluded events where we were unable to calculate the elevation angle (because $|B_R| < 3$ nT) for at least half the event duration. The median $|\theta_{elevation}|$ in the events is typically at least twice the background $|\theta_{elevation}|$. The elevation angles in Figure 2.8 are plotted versus event number, which increases with time, from March 1979 to December 2004. Later events (large event numbers) have larger background- and event- elevation angles; these events generally come from pre-midnight local times, where B_θ is larger than in the post-midnight sector. That we observe increases to the elevation angle along with the $|B_\theta|$ increase in our events indicates that the field reconfiguration is consistent with magnetic reconnection.

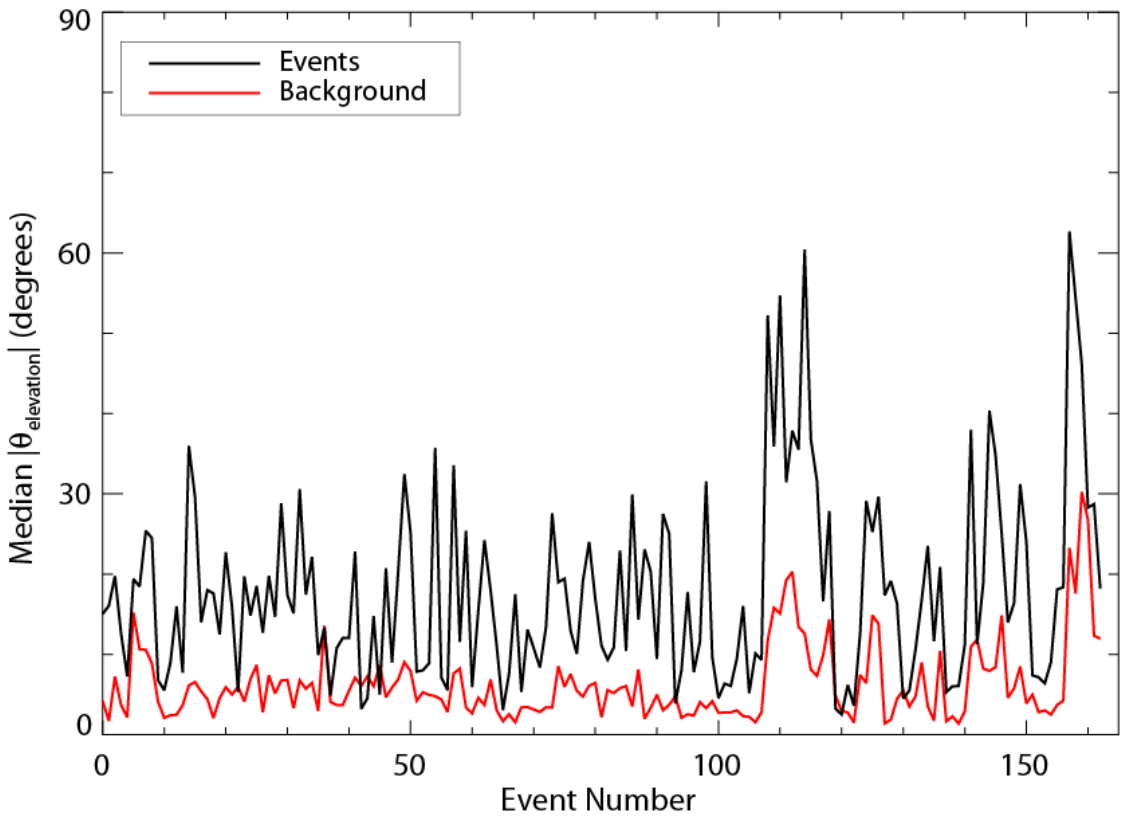

Figure 2.8: Median $|\theta_{elevation}|$ for events (black) and the background (red), plotted versus the event number, which increases with time. The median event $|\theta_{elevation}|$ is typically larger than the background $|\theta_{elevation}|$ by a factor of two or more. The event and background $|\theta_{elevation}|$ are largest for the later events because they occurred in the pre-midnight local time sector. In this figure we only include events in which we calculate the elevation angle ($|B_R| \geq 3$ nT) for at least half the event duration.

2.4.4 Bendback angle and sign of B_0 as proxies to flow

It is of interest to compare our events and their properties and distribution to those of intermittent flow bursts inferred from particle anisotropies in previous studies [*Kronberg et al.*, 2005, 2007]. Though the magnetometer does not directly measure flow, we expect there to be a high correlation between inward and outward radial flows and properties of the bendback angle

and the sign of B_θ. In this section we will outline how we interpret these quantities as evidence for flow, allowing us to compare our results with *Kronberg et al.* [2005, 2007] and others.

Measured changes of the bendback angle of the magnetic field provide a good proxy to measurements of flow bursts. The bendback angle, α, is defined by

$$\alpha = \tan^{-1}\left(\frac{B_\varphi}{B_R}\right) \tag{2.3}$$

Its value indicates the azimuthal sweep back of the field lines with respect to the radial direction. By this definition, because the field is typically swept back and B_R and B_φ are of opposite sign, the bendback angle is usually negative. A positive bendback angle would indicate that the field is swept forward.

Angular momentum conservation arguments link changes of the bendback angle to changes of radial flow. In the middle and outer Jovian magnetosphere (beyond 20 R_J) the field lines typically lag corotation at the equator because, in a steady state, plasma is slowly but continuously being transported radially outward; current systems linking the equator with the ionosphere act to maintain isorotation [*Hill*, 1979]. On time scales short compared with the communication time with the ionosphere the coupling with the ionosphere is ineffective [*Vasyliūnas*, 1994]. The outflowing plasma decreases its angular velocity in order to conserve angular momentum. The long time scale for communication with the ionosphere implies that it requires at least of order several hours for currents linking equatorial regions to the ionosphere to reaccelerate the outflowing plasma to the local rotation speed. As a result, the field lines, which are frozen into the flow, increase the angle at which they drape back. Evidently, inward flowing bursts will experience acceleration of the angular velocity and the bendback angle will decrease.

On the basis of the above argument, we use changes of the bendback angle to infer changes of the radial plasma flow by assuming that in events lasting less than 5 hours the flow

will conserve angular momentum and that the field is frozen into the flow. We then expect that $|B_\varphi|$ will increase and α will decrease (become more negative) in association with bursts of radial outflow and that $|B_\varphi|$ will decrease, and α will increase (become less negative) in association with bursts of radial inflow.

There are some challenges to quantitatively assessing changes to the bendback angle so that we can infer flow. As with the elevation angle, we can confidently calculate α only for $|B_R| >$ 3 nT. However, this poses difficulties in determining the bendback angle during the identified events because many of them are observed when the spacecraft is in or near the center of the current sheet and $|B_R|$ is small. Second, though we would like to compare the change in bendback to the sign of B_θ, we cannot reasonably expect complete, instantaneous agreement between the inferred flow and the magnetic signature. For example, in studies of bursty bulk flow events at Earth, the flow direction and the north-south direction of the magnetic field agree frequently but not invariably [*Angelopoulos et al.*, 1994].

The second way to infer probable flow from the magnetometer data is to use the sign of B_θ to identify the spacecraft's location with respect to the magnetic x-line. Although the correspondence between flow direction and the sign of B_θ is not invariable, it is most likely that inward of an x-line, flow is planetward and the associated perturbation in B_θ is positive and that outward of an x-line, flow is antiplanetward and the associated perturbation of B_θ is negative. This association is illustrated in Figure 2.4, which shows the configuration of reconnected field lines in the tail. A positive increase over background levels in B_θ suggests that the spacecraft is planetward of the x-line (position A), where we expect inward flow. The event shown from orbit C23 in Figure 2.6 is an example of this type of event, where the enhanced B_θ is positive and we expect inward flow. Similarly, we interpret a negative B_θ signature to mean that the spacecraft is

tailward of the x-line (position B), and therefore expect outward flow. When B_θ changes sign during an event, as occurred in the events of Figures 2.5 and 2.7, we interpret that change to be the x-line and/or plasmoid crossing over the spacecraft.

We use primarily the sign of B_θ to infer the direction of flow in this study because our estimates of the bendback angle are not continuous and are very sensitive to small fluctuations. This approach is not without ambiguity. For example, although we expect to see a positive B_θ associated with a dipolar field planetward of the x-line, the tailward edge of a plasmoid could also produce a positive B_θ signature. However, the reversed signature of a Jovian plasmoid is likely to be found far antisunward of the most distant Galileo orbits, so we believe that few such events are likely. Furthermore, x-lines need not remain stationary, and x-line motion could invalidate the relationship between the sign of B_θ and the flow direction that we have assumed. However, analysis of the reconfiguration events from *Kronberg et al.* [2005] has confirmed that the sign of B_θ is a good indicator of the flow direction [*Kronberg et al.*, 2008]. In all of their events that do not exhibit a bipolar B_θ, the flow direction obtained from the ion bursts matched the flow direction inferred from the sign of B_θ (i.e., tailward flow was accompanied by a negative B_θ magnetic signature, and planetward flow was accompanied by positive B_θ).

To further validate this assumption, we have analyzed the relation between the B_θ signature in our own events and radial anisotropies from the same periods. These radial anisotropies were measured by the Galileo EPD and can be used to estimate flow velocities [*Krupp et al.*, 2001]. In Figure 2.9 we have plotted B_θ versus radial anisotropy during our events, excluding years 1997 and 1998 (156 of 249 events) because high-resolution anisotropy data were not readily available. Because the time resolution of the anisotropy data is 12 minutes and the time resolution of the magnetometer data is at least 60 seconds, we have used the median B_θ

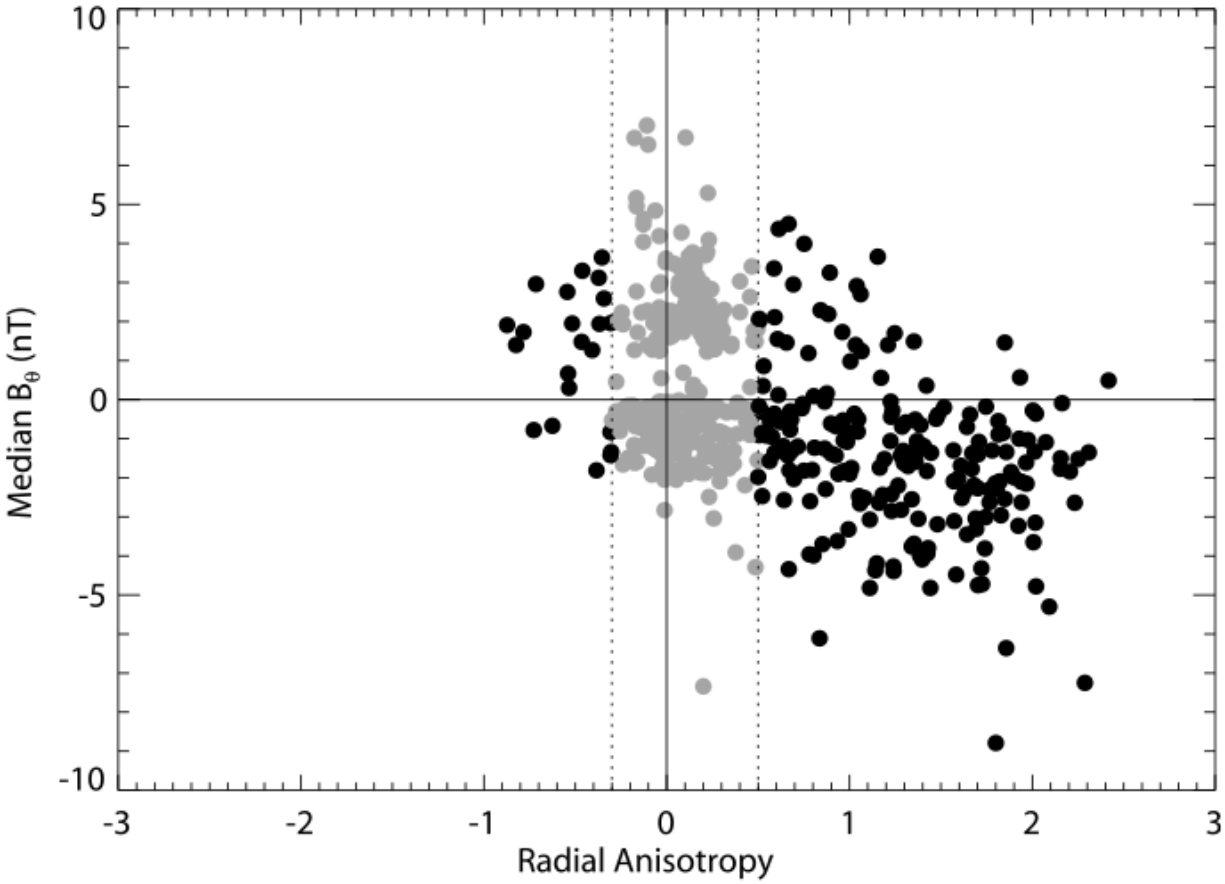

Figure 2.9: Scatter plot of median B_θ (nT) versus radial anisotropy from 93 of our events. We have excluded events from years 1997 and 1998 (156 of 249 events) because high resolution anisotropy data were unavailable. B_θ is the median value from the interval within 5 minutes of each anisotropy data point, because the time resolution of the magnetic field data (up to 24 seconds) is higher than that of flow anisotropy (12 minutes). Anisotropies between -0.3 and 0.5 do not represent a significant departure from corotation [E. Kronberg, personal communication, 2010], and these are drawn in gray. There is a clear trend between the median B_θ and the radial anisotropy, such that large positive (negative) radial anisotropy is typically accompanied by negative (positive) median B_θ. Radial anisotropies were kindly provided by N. Krupp.

from the interval within 5 minutes of each anisotropy data point. At times with large positive radial anisotropy (greater than 0.5), the median B_θ is most likely to be negative; at times with large negative radial anisotropy (less than -0.3), the median B_θ is most likely to be positive. We

ignore anisotropies between -0.3 and 0.5 because the deviation from corotation can be regarded as insignificant [E. Kronberg, personal communication, 2010]. We find that the sign of B_θ is statistically correlated with the flow direction in our events, a result consistent with the findings of *Kronberg et al.* [2008].

That the anisotropy direction and the sign of B_θ show good but imperfect agreement is in part related to the simplifying assumptions we have made in our analysis, such as using the median B_θ. We have included events with a bipolar B_θ signature, where the sign of B_θ is a more ambiguous proxy for the flow direction than in events where B_θ is purely positive/negative. While a negative B_θ implies a position tailward of the x-line, a positive B_θ could be seen on the planetward side of an outward moving x-line, or, in exceptional cases it could be the tailward edge of a plasmoid moving outward. However, on average there is support for the assumption that the magnetometer data can be used as a proxy for flows.

2.5 Results

Using the identification criteria described in Section 2.4.2, we obtained a list of 249 events. These events are characterized by an increase in $|B_\theta|$ over background levels and an accompanying increase in the elevation angle, indicating a field reconfiguration that is consistent with magnetic reconnection. The events are distributed over nearly all radial distances and local times that we surveyed (outward 30 R_J, and from 18:00-06:00 LT). Events were observed in radial distance from 33 to 155 R_J, and in local time from ~19:00 to ~06:00 hours. We did not identify any events from 18:00 to 19:00 LT but data coverage in this region is extremely limited (see Figure 2.3). They have an average duration of 59 minutes, ranging in duration from 10 minutes (imposed as a lower cutoff) to just over 5 hours. Three of the events come from Voyager

1 data (March 1979), five come from Voyager 2 (July 1979), and the remaining events come from Galileo (June 1996 to November 2002). There are no events in the Pioneer 10 data, but this is not significant because only 150 hours of data remained after selecting for the appropriate location (radial distance, local time, latitude) and high time resolution, as outlined in Section 2.4.1. A complete list of the event start and end times, locations (radial distance and local time), and B_θ signatures are provided as supplemental online material accompanying *Vogt et al*. [2010].

This section begins by describing the event spatial distribution, frequency, and occurrence rate, and how these properties change with radial distance and local time. We then discuss the distribution of inward and outward flow events, as inferred from the sign of B_θ. Finally, we examine changes to the bendback angle in our events.

2.5.1 Event distribution and frequency

The 249 reconnection events we identified are well-distributed in radial distance and occurred at nearly all nightside local times. An equatorial plane view of the event locations is given in Figure 2.10. The spatial distribution of events is also summarized in Table 2.1. Events that were also identified by *Kronberg et al.* [2005] are represented by empty triangles while new events from this study are represented with solid circles. The color coding indicates the inferred position planetward or tailward of an x-line as determined by the sign of B_θ; events in which B_θ is negative (positive) for more than 85 percent of the event duration are considered to be tailward (planetward) of an x-line. A blue symbol in Figure 2.10 indicates a tailward event; a red symbol indicates a planetward event. Events that exhibit a bipolar B_θ signature (B_θ is neither positive nor negative for more than 85 percent of the total event duration) are shown in green. Event locations

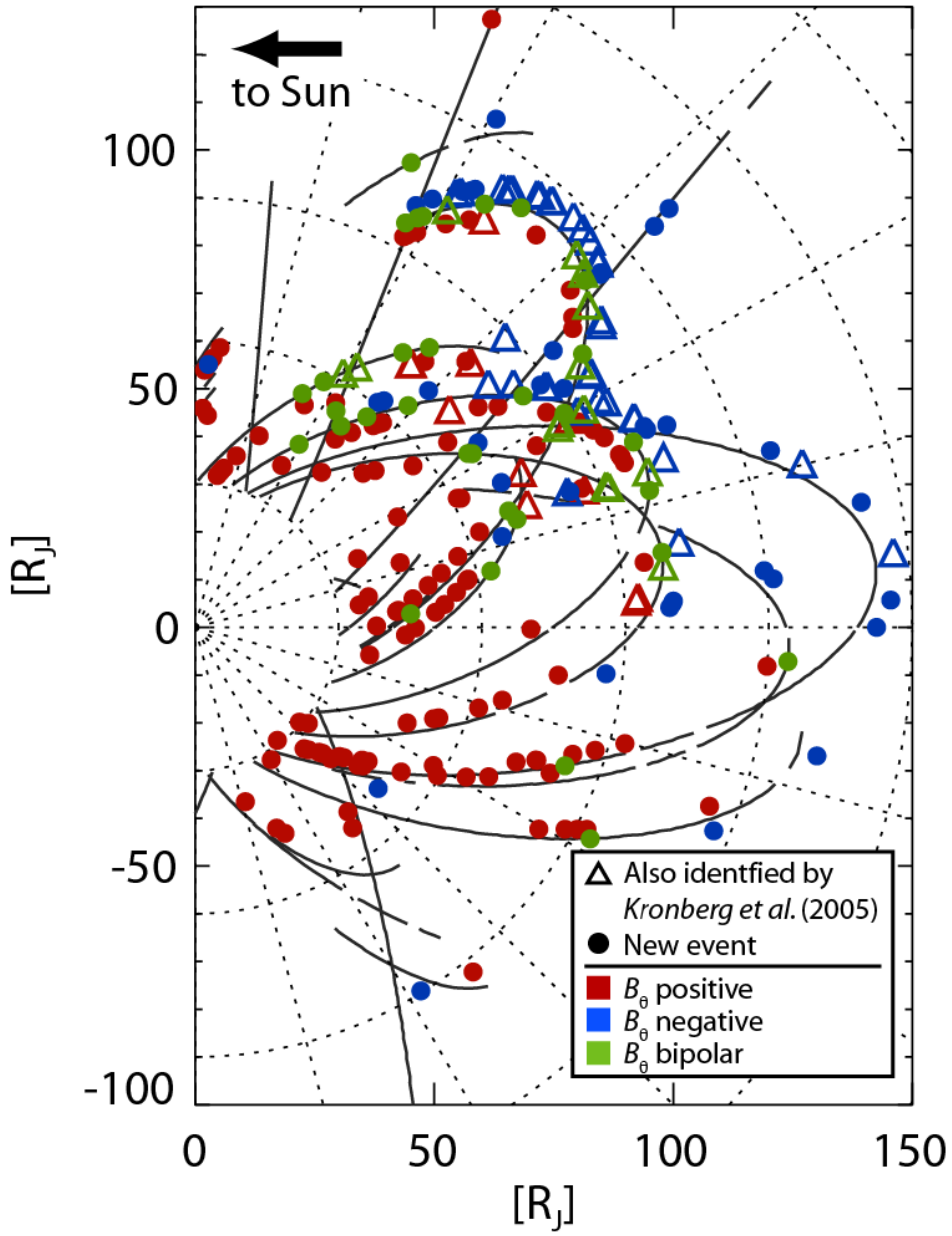

Figure 2.10: Spatial distribution of observed reconnection events, shown in the equatorial plane. Empty triangles denote events also identified by *Kronberg et al.* [2005]; solid circles denote new events. The color coding indicates the inferred location with respect to an x-line, as determined by the dominant sign of B_θ within each event: red symbols represent events in which B_θ is primarily positive (inferred planetward flow), blue symbols represent events in which B_θ is primarily negative (inferred tailward flow), and green symbols represent events with a bipolar B_θ signatures (B_θ is neither primarily negative nor primarily positive). The locations of the events have been shifted radially by -2 R_J for B_θ mostly positive events (red) and by +2 R_J for B_θ mostly negative events (blue) to prevent overlap. Events are found at nearly all radial distances and local times where data are available (black solid lines). The Sun is to the left.

have been shifted radially by -2 R_J for B_θ positive events (red) and by +2 R_J for B_θ negative events (blue) for visibility; bipolar B_θ events (green) remain at their original distances.

It is clear from inspection of Figure 2.10 that more events are observed in the post-midnight local time sector than in the pre-midnight sector. From a total of 249 events, only 57 events occurred pre-midnight. However, we must also consider the distribution of available data and the duration and frequency of the events in order to fully understand the distribution of these dynamic processes. The amount of available data varies with R and LT, so it is useful to consider the event occurrence rate rather than just the number and duration of events. For example, though fewer events were observed pre-midnight than post-midnight, more data are available in the post-midnight region at large radial distances (see Figure 2.3) so one might naturally expect to find more events in this region. We therefore examine the event occurrence rate, or the sum of the event durations for all events within a bin divided by the duration of data within a bin, throughout different regions of the magnetotail.

Table 2.1 Summary of event duration and spatial distribution

	All Events	**B_θ positive events**	**B_θ negative events**	**B_θ bipolar events**
Number of events (*percent of all events*)	249	130 (*52.2*)	74 (*29.7*)	45 (*18.1*)
Average duration (minutes)		47	75	66
LT range (hours)	19:04 – 05:52	19:04 – 05:52	20:07 – 05:49	22:07 – 04:21
Median LT (hours)	01:52	00:50	02:18	02:21
Number of events post-midnight (*percent of total*)	192 (*77.1*)	81 (*62.3*)	69 (*93.2*)	42 (*93.3*)
R range (R_J)	33.25-145.6	33.25-145.6	47.03-142.86	44.09-124.2
Median R (R_J)	84	61.6	100.22	89.26

Figure 2.11 shows the event occurrence rate, in bins of 15 R_J in radial distance by one hour in local time. Bins in which data are available but no events were identified are colored gray. Bins with two or fewer events or with less than 10 hours of data are colored black to prevent the small numbers from producing misleading statistics. At small radial distances there is no significant asymmetry in event frequency on either side of midnight. In the post-midnight sector, events occur most frequently from 02:00 to 04:00 LT, particularly between 90 and 120 R_J. In the pre-midnight sector, where data coverage is limited beyond ~90 R_J, events occur most frequently between 21:00 and 22:00 LT and from 45 to 75 R_J.

We can sum the event occurrence rate over all radial distances to obtain a distribution of event occurrence rate versus local time, as is plotted in Figure 2.12. From this perspective, the event frequency appears relatively symmetric across the different local time sectors, though there is a curious decrease just prior to midnight. Events in the pre-midnight sector appear to be concentrated in a small local time range (20:30-22:30 LT) whereas in the post-midnight sector the events are more spread out in local time (01:30–04:30 LT). Again, there is a peak in the occurrence rate between 02:00 and 04:00 LT. The color coding within each bin indicates the relative amount of time for negative (blue), positive (red), and bipolar B_θ (green) events.

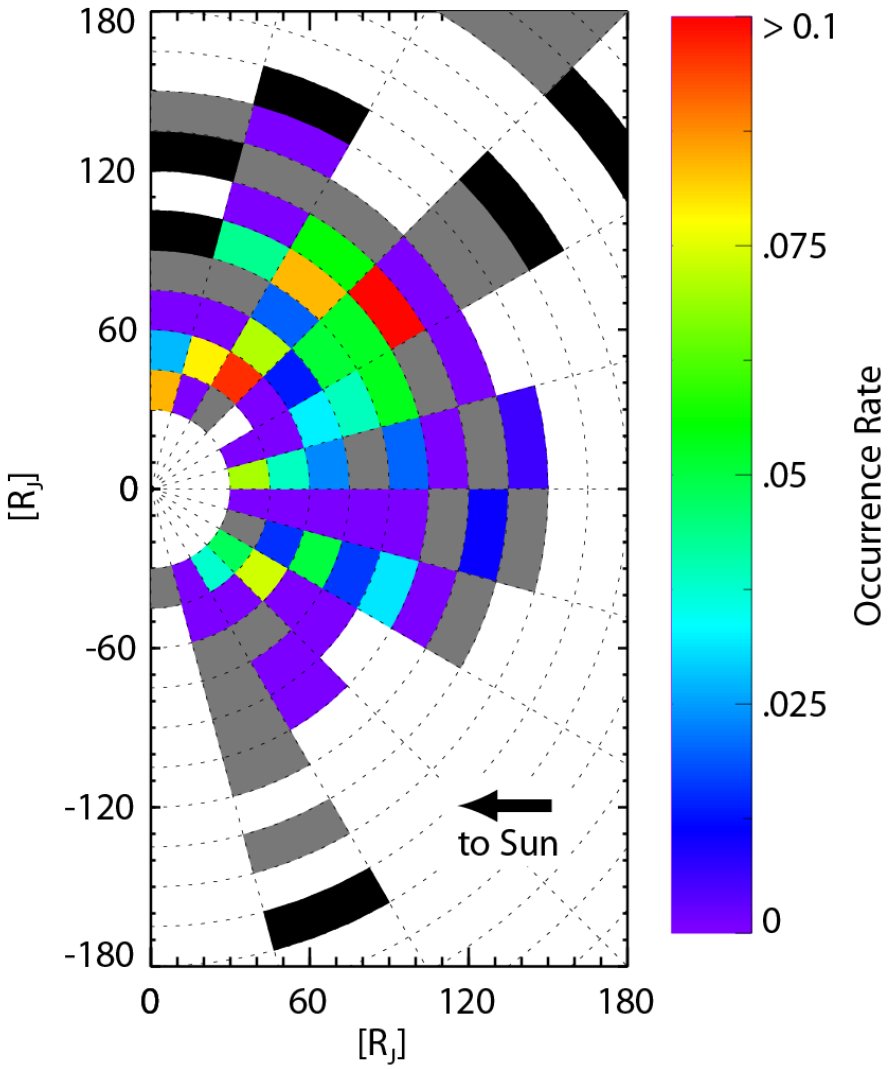

Figure 2.11: Event occurrence rate for bins of 15 R_J in radial distance by one hour in local time. The occurrence rate, or frequency, is the duration of all events in each bin divided by the duration of all data in each bin. Gray is used for bins in which we have not identified events but there are available data. White is used for bins with no available data. Black is used for bins with 1-2 events or with fewer than 10 hours of data. This is an equatorial plane view, and the Sun is to the left.

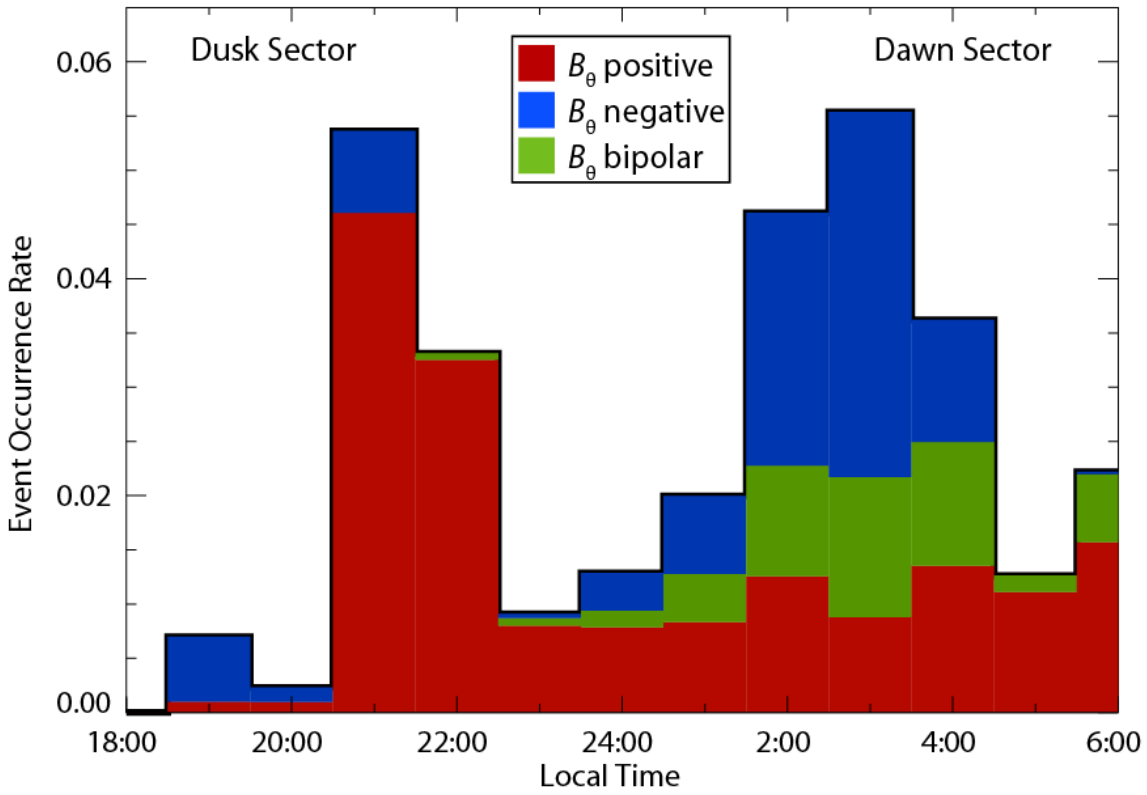

Figure 2.12: Event frequency as a function of local time. The colors represent the relative amount of time for tailward (blue), planetward (red), and bipolar B_θ (green) events in each bin. There is no significant asymmetry in event frequency about midnight, though the decrease at midnight is puzzling. Negative B_θ events are more prevalent on the dawn side, though this is may be due to the fact that there are more data available at large radial distances post-midnight than pre-midnight.

2.5.2 Evidence of inward and outward flow

Thus far in our analysis we have noted whether events are dominated by a positive, negative, or bipolar B_θ without remarking on the inferred flow pattern. As introduced in section 2.4.4, a positive (negative) B_θ is likely to correspond to inward (outward) flow as anticipated when the spacecraft is planetward (tailward) of a neutral line. There are events in which B_θ changes sign (the bipolar B_θ signature events) and the reversal can be interpreted as arising from the movement of a plasmoid or the x-line over the spacecraft. We return to the event distribution

illustrated in Figure 2.10 to examine the relative spatial distribution of B_θ positive (red), B_θ negative (blue), and bipolar B_θ (green) events and discuss possible locations of an x-line. Again, the spatial distribution of events is summarized in Table 2.1, which is also organized according to the B_θ signature in each event.

All but a handful of the events that exhibit a negative B_θ signature (shown in blue) are observed in the post-midnight sector and beyond 60 R_J. B_θ positive events are generally observed inside of ~100 R_J and are more evenly distributed in local time. The median radial distance is 61.6 R_J for B_θ positive events, 100.22 R_J for B_θ negative events, and 89.26 R_J for bipolar B_θ events.

For the pre-midnight local time sector, events that exhibit a positive B_θ signature (shown in red) dominate inside of ~60 R_J, and events that exhibit a negative B_θ signature dominate outside of ~90 R_J. Between ~60 and ~90 R_J the observed B_θ signature is both positive and negative, with many bipolar B_θ events. This is a likely region for the location of an x-line in the post-midnight sector. From the sign of B_θ we infer planetward flow inside of ~60 R_J, tailward flow outside of ~90 R_J, and a neutral line between ~60 and ~90 R_J. Figures 2.5 and 2.7 present cases that are representative of the events in this region. In those events, which were observed just inside of 90 R_J, the B_θ signature suggests that the x-line passed over the spacecraft.

It is difficult to describe the distribution of inferred inward and outward flow events in the pre-midnight sector because the data there are limited in radial distance. In general, the positive B_θ events dominate out to at least ~90 R_J (compared to ~60 R_J post-midnight). Positive, negative, and bipolar B_θ events (corresponding to the 60-90 R_J region in the post-midnight sector) are seen beyond ~90 R_J and inside of 120 R_J (the outward radial limit of data pre-midnight). The data do not extend sufficiently far in R to determine the location of an x-line

beyond which negative B_θ dominate. We can, however, conclude that an x-line would have to be beyond ~90 R_J and would likely be outside of ~120 R_J.

Figure 2.13 shows the spatial distribution of the dominant B_θ signature in each event and the location of an inferred x-line separating inward and outward flow. Bins of 1 hour (azimuthally) in local time by 15 R_J (radially) are colored according to the dominant direction of flow among the events in each bin. At all local times and inside of 75 R_J the bins are red, meaning positive B_θ events, or inferred inward flows, dominate. In the post midnight-sector one finds red, green (bipolar B_θ), and blue (negative B_θ, inferred outward flow) bins between 75 and 105 R_J, and exclusively blue bins outside of 105 R_J. We interpret this to mean that the most likely location of an x-line is close to 90 R_J in this local time sector. Within one hour of midnight the transition between red/green and blue bins (and likely location of an x-line) moves radially outward, starting at 90 R_J and ending near 105 R_J. At earlier local times we do not observe the transition to exclusively negative B_θ events (blue bins), suggesting that the location of the x-line continues to move radially outward, beyond the range of available data in this sector. This is also supported by the observation that the red bins, indicating positive B_θ events, are also located farther out (up to 105 R_J) pre-midnight than post-midnight.

The other quantity we use to infer flow direction is the change to the bendback angle, also described in section 2.4.4. We interpret a significant positive change of the bendback angle as an indication of inward flow, and we interpret a significant negative change of the bendback angle as an indication of outward flow. Data from the 20 September 1996 event shown in Figure 2.5 provides a good illustration of the bendback changes we observe in many events, and their qualitative agreement with the flows inferred from the sign of B_θ. During the quiet time before

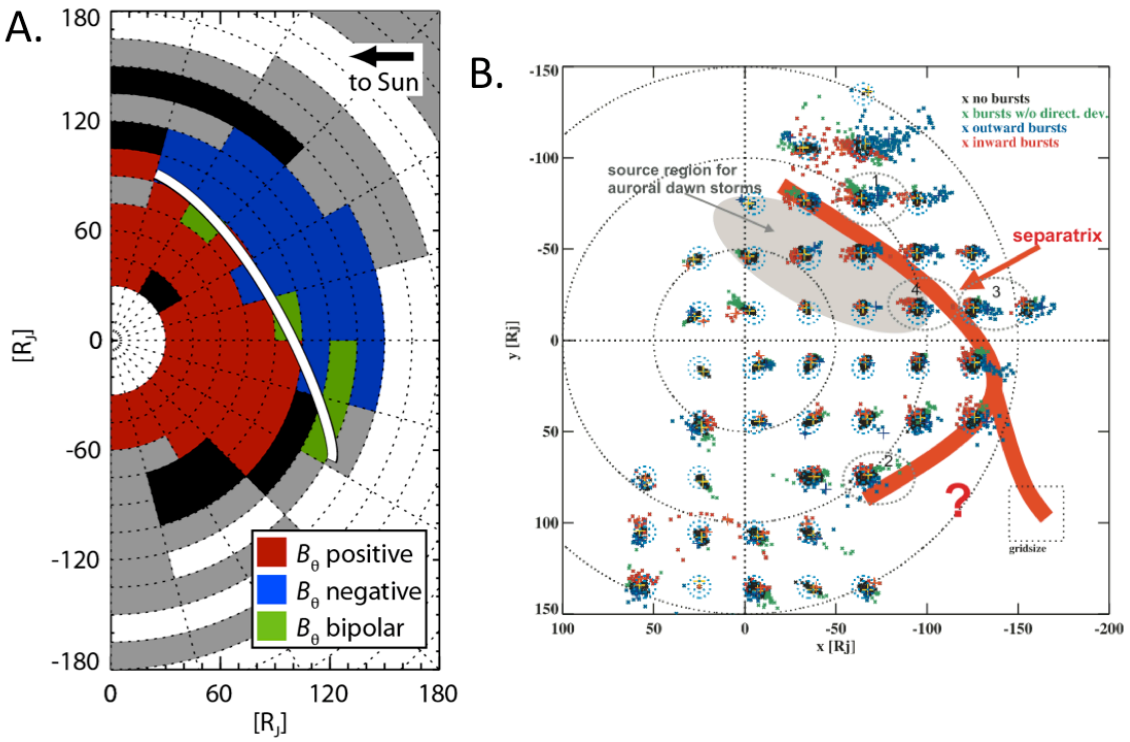

Figure 2.13: Comparison of the inferred flow direction and statistical separatrix identified using the magnetometer and energetic particle data. A: Distribution of the dominant B_θ signature (positive, negative, or bipolar B_θ). Bins are colored according to which type of event is most prevalent in the region of each bin plus one hour in local time on either side. Red bins are those in which positive B_θ positive events are most common; blue bins are those in which negative B_θ events are most common. Bins where the numbers of negative and positive B_θ events are the same are colored green; these bins also represent regions where the bipolar B_θ events are most common. A possible separatrix is drawn as a white line in the region where data are available. The total number of events is 249, distributed over nearly 80 possible bins. As in previous figures, white bins represent areas with no available data and gray bins are areas with data but no identified events. Black bins are areas where we have identified only one event, or where we have identified two events that do not have the same B_θ signature. This is an equatorial plane view, and the Sun is to the left. B: Location of flow bursts and a statistical separatrix identified by *Woch et al.* [2002], in good qualtitative agreement with our results.

and immediately after the event, the field is swept back at a steady angle of approximately -40º with respect to corotation. However, during the event the bendback angle experiences large, fast changes, and even changes sign (the field becomes swept forward). The flow directions inferred from these changes agree with the flow directions as inferred from the sign of B_θ; initially, when

B_θ is positive, the field is swept forward, a positive increase over the background. Then, the bendback angle becomes more negative, indicating outward flow, and B_θ changes sign, suggesting that the x-line has moved out over the spacecraft. Similarly, during the 18 September 1999 event illustrated in Figure 2.6, the bendback angle becomes more positive, even changing sign so that the field is swept forward. The bendback angle change coincides with the large, positive B_θ, and both signatures can be interpreted as evidence of inward flow.

As previously noted, we do not calculate the bendback angle when $|B_R| < 3$ because in that situation small changes in B_R produce large changes in the bendback angle. This means that bendback information is wholly or partially unavailable for many events, as the events tend to be observed when the spacecraft is in or near the current sheet and B_R is small. In roughly 30 percent (70 out of 249) of events the bendback angle information is insufficient to determine whether any inferred flow matches our expectations.

Despite the challenges to using the bendback angle as a proxy to flow, we do find qualitatively that large, fast changes of the bendback angle occur in most of the events for which we can measure the bendback. In just over 60 percent (106 of 179) of events with nearly full bendback information we see large bendback changes that qualitatively suggest inward or outward flow consistent with the B_θ signature.

2.6 Analysis

In this section we will discuss how our results compare to previous studies of particle anisotropies and flow bursts. Of particular interest is how the local time distribution of our events differs from that of the *Kronberg et al.* [2005] reconfiguration events and the comparison of our separatrix, inferred by the B_θ signature in our events, with one defined by the direction of particle

bursts [*Woch et al.*, 2002]. Next we use the velocity and event duration to calculate for each event the width of the flow channel (in the azimuthal direction). Finally, we will examine our events for evidence of a 2-3 day periodicity.

2.6.1 Comparison with particle data

Many of our reconnection events occur during the disturbed intervals identified by analysis of particle anisotropies in *Kronberg et al.* [2005]. That work identifies 34 periods with reconfiguration events, having an average duration of 14 hours. In comparing our events to the specific cases illustrated there and following studies [*Kronberg et al.*, 2007, 2008] we find that our events occur in conjunction with increases in the particle anisotropies, though our strict selection criteria miss some intervals of increased anisotropy. In only four of the 34 reconfiguration event intervals from *Kronberg et al.* [2005] do our selection criteria fail to identify any reconnection events. The remaining 30 reconfiguration event intervals encompass 61 of our 249 events.

A direct comparison between our events and the specific cases studied in *Kronberg et al.* [2005, 2007, 2008] ensures that our events coincide in time with theirs and show good agreement between the increases of $|B_\theta|$ and the particle anisotropies. In Figure 2.14 we have plotted the magnetic field data and first-order radial and azimuthal ion anisotropies from 12:00 on 21 September through 5 October 1996. The anisotropies were kindly provided by E. Kronberg and were measured by the Galileo EPD. This 15-day period is described in *Kronberg et al.* [2007] and includes both disturbed and quiet times. Times where we have identified events are highlighted in red in panel 3, which shows B_θ. Most of our events in this interval occur at the same time as large radial anisotropies and large flows; these are the same intervals identified as

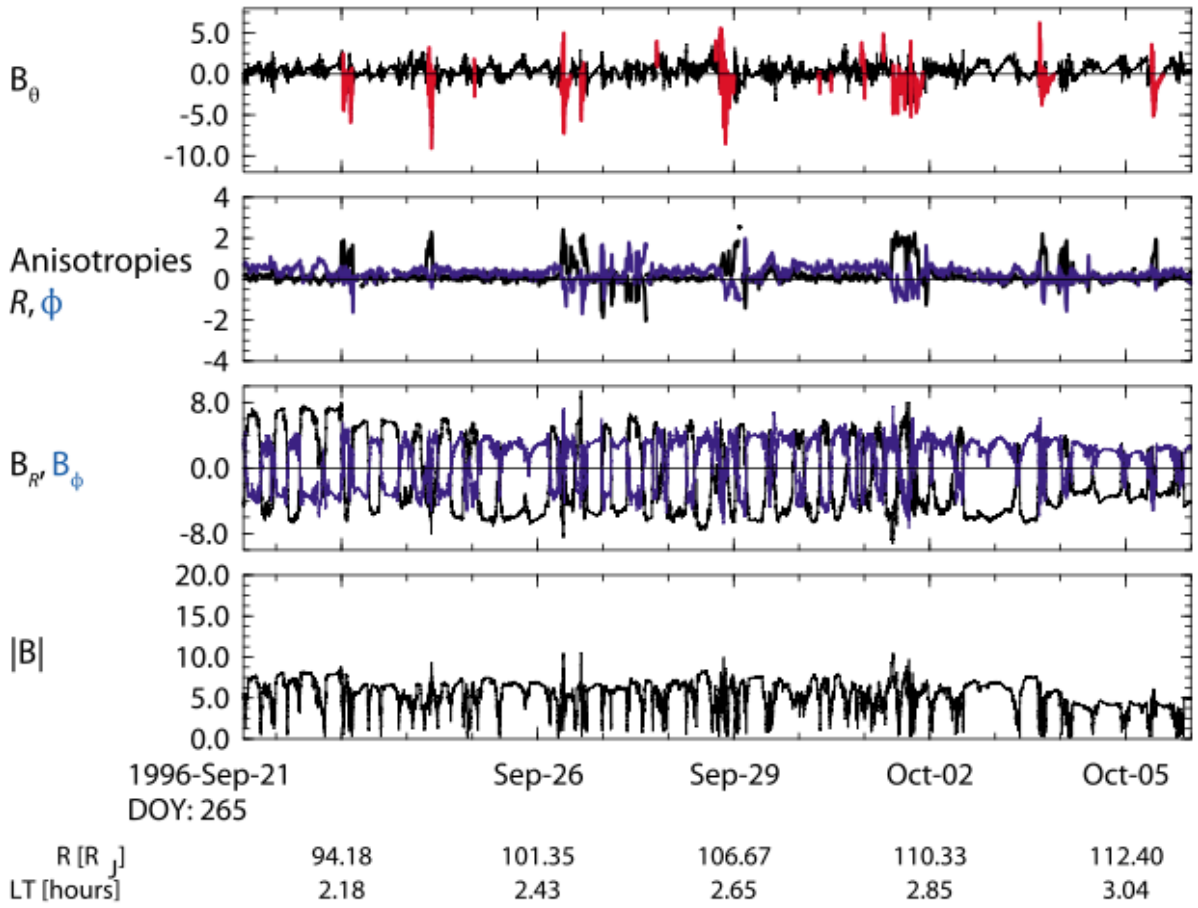

Figure 2.14: Particle anisotropies (60-120 keV), magnetic field components, and magnetic field magnitude for one of the intervals presented in *Kronberg et al.* [2007]. These data come from orbit G2. B_θ (nT) is plotted in panel 1 and is highlighted in red during the intervals that we have identified as events. First-order radial (black) and azimuthal (red) ion anisotropies (kindly provided by E. Kronberg) are plotted in panel 2. Panel 3 shows the radial and azimuthal components of the magnetic field (nT). The field magnitude is plotted in the last panel.

"disturbed", or the reconfiguration events, in *Kronberg et al.* [2007]. In similar comparisons with other cases we find that most of our events occur in conjunction with increases in the particle anisotropies, though our strict selection criteria miss some intervals of increased anisotropy.

Our results not only show good agreement with the Kronberg reconfiguration events but also expand on that work with the identification of additional events, particularly in the pre-midnight sector. We identified 57 reconnection events at pre-midnight local times. Only one of the *Kronberg et al.* [2005] reconfiguration events occurred pre-midnight, and that event was at a local time of 23:00, on day 237 of 1998. Interestingly, this pre-midnight reconfiguration event is one of the four *Kronberg et al.* events that does not match the reconnection events that we have identified in this study. The event did not meet our selection criteria because B_θ was never less than -2 nT or greater than 3 nT.

One possible explanation of why more events were found in the magnetometer data than in the particle anisotropy data is that the magnetic field is measured at much higher time resolution than is particle anisotropy. In this study we have restricted ourselves to magnetometer data at a time resolution of 60 seconds per vector or better; the time resolution in the particle data is 3 to 11 minutes. This can also explain why our identification methods sometimes select more than one event in each reconfiguration event interval of *Kronberg et al.* [2005]. Most of the magnetometer data we have used in this study have a time resolution of 24 seconds per vector, and this allows us to resolve finer features and find more individual events than were found in the particle anisotropy study.

Woch et al. [2002] studied flow bursts observed with the EPD instrument and determined the location of a statistical separatrix separating inward and outward flow bursts (see their Figure 3a). This separatrix is located at ~80-120 R_J in the post-midnight sector, and moves radially out as with local time from dawn to midnight. Outside of this line the flow bursts were primarily outward. Our results qualitatively agree with their findings post-midnight. As discussed in Section 2.5.2, the distribution of our reconnection events with positive and negative B_θ signatures

suggests a possible x-line location near 90 R_J on the dawn side (see Figure 2.13). The radial distance of our separatrix also appears to change with local time, and it is closer to the planet at dawn than at midnight.

In the pre-midnight region *Woch et al.* [2002] draw two possible separatrices, starting from ~125 R_J at midnight. One line continues to move radially outward, beyond 150 R_J, as it moves in local time from midnight to dusk. The other potential separatrix moves radially inward with local time for local times earlier than ~23:00, returning to ~100 R_J at ~20:00 LT. Like the magnetic field data, the EPD data cover a limited range of radial distances in the dusk sector, making it impossible to firmly establish the location of a separatrix in this region. Our results would favor the separatrix that continues to move outward in the dusk sector, since in this sector inside of 105 R_J almost all bins correspond to positive B_θ signatures and the negative and bipolar B_θ signatures extend from that distance to beyond 120 R_J.

2.6.2 Flow channel width

The flow channel width of bursty bulk flows at the Earth is known to be ~1-2 R_E, [*Angelopoulos et al.*, 1996] or less than 10 percent of the width of the Earth's magnetotail (~25-30 R_E). In this section we calculate the flow channel widths for our reconnection events at Jupiter and draw comparisons to BBFs at the Earth.

The flow channel width is taken as the event duration (in seconds) multiplied by the average of the azimuthal velocity magnitude, $|V_\varphi|$, during the event (in R_J per second). Because the velocity data have a time resolution of ~2 hours and the mean duration of our events is 59 minutes, velocity data are not available for all of our events. As a result, we are able to calculate the flow channel width for only 102 of 249 events.

For most events the flow channel width is less than 20 R_J. The mean flow channel width is 14.4 R_J and the mean is 18.3 R_J. The mean duration of the 102 events for which we calculated the flow channel width is 92 minutes (~5500 seconds), and the mean $|V_\varphi|$ during those events is 236 km/s (~.003 R_J per second). The largest flow channel width, 106.6 R_J, comes from an event on 10 October 1996 which lasted for 143.6 minutes and had a mean $|V_\varphi|$ of 884.7 km/s.

How does this compare to BBFs at the Earth? The Jovian magnetopause standoff distance has two probable locations, 60 and 90 R_J, depending on the solar wind dynamic pressure [*Joy et al*., 2002]. Assuming a magnetotail width of 3 times that distance, or ~180-270 R_J, we find that the mean flow channel width (~18 R_J), is ~6.67-10 percent of the magnetotail width. This is comparable to the relative width of BBF flow channels at Earth, where, assuming a ~2 R_E flow channel width and a ~30 R_E magnetotail width, the flow channel is ~6.67 percent of the magnetotail width.

Our calculation is only a rough estimate for the flow channel width. The flow channel width depends strongly on the event duration, which is defined by the event selection criteria outlined in Section 2.4.2. Our definition for the event start and end points is subjective and may over- or underestimate the interval of the disturbed field configuration. Additionally, the spacecraft may only be observing the event for a fraction of its total duration, so the flow channel width we calculate here is likely a lower bound for the actual value.

Finally, we would like to estimate the amount of flux transported during our events and draw further comparisons to terrestrial BBFs. Unfortunately the low time resolution of the velocity data (~2 hours) is insufficient for this calculation.

2.6.3 Event periodicities

Dynamics in the Jovian magnetosphere have been observed to occur with a 2-3 day periodicity; this periodicity has been documented in flow bursts [*Krupp et al.*, 1998; *Woch et al.*, 1998], reconfiguration events [*Kronberg et al.*, 2007], and auroral polar dawn spots [*Radioti et al.*, 2008]. The periodicity is thought to be related to the time scale of the internally driven mass-loading and release process at Jupiter [*Kronberg et al.*, 2007].

Many of the studies that noted the 2-3 day periodicity have considered only isolated intervals or a subset of spacecraft orbits. The *Kronberg et al.* [2007] reconfiguration events displaying this periodicity came from ~15 day intervals in Galileo orbits G2 (September – October 1996) and E16 (August – September 1998). At these times Galileo was at local times ranging from ~23:50 to ~3:10 LT. The periodic auroral polar dawn spots [*Radioti et al.*, 2008] were observed between 20 February and 10 March 2007, and also map to the post-midnight sector, but at later local times, 04:00-09:00 LT, than the periodic reconfiguration events. The 2-3 day periodicity has also been seen at pre-midnight local times; for example, *Woch et al.* [1998] found quasi-periodic behavior in energetic ion fluxes from orbits C9 (~18:00-23:00 LT) and C10 (~21:30-00:30 LT). Additionally, *Kronberg et al.* [2009] report that quasi-periodic variations of the ion spectral index γ are commonly observed, though not always with the 2-3 day period. They cite periodic behavior on 12 Galileo orbits, finding periods that range from 1.5 to 7 days are commonly observed, though a 2.5-4 day period is typical.

Visual inspection of our reconnection events during selected intervals or orbits, such as the 15-day interval shown in Figure 2.14, suggests that the 2-3 day periodicity is present for at least part of orbits G2, G8, C9, and E16. It is more difficult to visually estimate the event periodicity on a longer time scale, so we have calculated the Rayleigh power spectrum. The

Rayleigh power spectrum can be used to determine whether a statistically significant periodic signal is present among the occurrence times of discrete events. It has been used to study periodicities in quantities such as proton flare occurrences [*Bai and Cliver*, 1990]. In this section we will briefly introduce the Rayleigh power spectrum and explain how we have used it to investigate event periodicities; a more complete discussion of the Rayleigh power spectrum, its usage, and its limitations, can be found in *Mardia* [1972] and *Lewis* [1994].

The Rayleigh power z as a function of period T is given by the following equation:

$$z(T) = \frac{1}{n}\left[\left(\sum_{i=1}^{n}\cos\left(\frac{2\pi t_i}{T}\right)\right)^2 + \left(\sum_{i=1}^{n}\sin\left(\frac{2\pi t_i}{T}\right)\right)^2\right] \tag{2.4}$$

where n is the number of discrete events and t_i is the time of the i^{th} event. The Rayleigh power can be calculated for a range of user-specified periods T, and its significance depends in part on the number of independent Fourier frequencies within that range of periods. For a set of n events observed during a time interval τ, the independent Fourier spacing $\Delta\upsilon = 1/\tau$. The number of independent Fourier frequencies N is the number of independent Fourier spacings $\Delta\upsilon$ within the range of user-specified frequencies (corresponding to the range of user-specified periods T). The significance of a periodic signal with power z is given in the literature by the following expression:

$$1 - [1 - \exp(-z)]^N, \tag{2.5}$$

which represents the probability that the power of a randomly distributed data set will exceed z by chance. Thus by this definition a small significance value ($\ll 1$) indicates that a periodic signal is statistically meaningful. If one chooses to oversample, or calculate the Rayleigh power for frequencies at a higher resolution than $\Delta\upsilon$, equation 2.5 must be modified to include the effects of oversampling. For an oversampling factor A, equation 2.5 becomes:

$$1 - [1 - A \exp(-z)]^N \tag{2.6}$$

[*Lewis*, 1994]. In our calculations we will use an oversampling factor of 5.

We have calculated the Rayleigh power for selected events from Galileo orbit G2, which includes the 15-day interval of *Kronberg et al.* [2007]. The selected events are the largest as measured by the integrated $|B_\theta|$ power, $\sum(|B_\theta| \cdot \Delta t)$. In selecting the "largest" events we required that the integrated $|B_\theta|$ power surpass a threshold value; roughly one third of all 249 events meet this criterion. We have restricted our analysis to the largest events from the interval because many of the smaller events occur within a few hours of larger events and, as previously noted, in some instances we have identified more than one event for each of the *Kronberg et al.* [2005] reconfiguration event intervals. Therefore in this part of our analysis we include only the largest events because they are typically separated in time by ~days and are likely to be independent. Figure 2.15 shows the time spacing of the large events, which occurred from 11 September to 22 October 1996. Visual inspection supports an event periodicity of 2-3 days, though the mean separation between events is 2.2 days and the median separation is 1.9 days. Dashed vertical lines have been drawn every 2 days to guide the eye.

The Rayleigh power spectrum for these events is plotted in Figure 2.16. Sample significance levels are noted by the dashed horizontal lines. Since we would like to know whether there is a statistically significant periodic signal close to 2-3 days, we have chosen to examine the power for periods between 1 and 4 days. The largest peak in the Rayleigh power comes just before a period of 2 days, and there are two smaller peaks between 2 and 3 days. However, none of these peaks is statistically significant. For this interval, 11 September to 22 October 1996, τ = 41 days and $\Delta\upsilon = 2.823 \times 10^{-7}$ Hz. The range of frequencies corresponding to periods of 1 to 4 days is 1.157×10^{-5} Hz to 2.893×10^{-6} Hz, meaning that the number of

independent Fourier frequencies $N = (1.157 \times 10^{-5} - 2.893 \times 10^{-6})/2.823 \times 10^{-7} \sim 30$. The largest Rayleigh power is ~5.95 (at $T = 1.8$ days) and has a significance of $1 - [1 - 5 \exp(-5.95)]^{30}$, ~ 0.32 (recall that a significance value « 1 indicates that the periodic signal is unlikely to be due to chance). The Rayleigh power peak for periods of 2-3 days is 4.9 (at $T = 2.2$ days), and has a significance of 0.67. Such high significance levels suggest that none of the Rayleigh power peaks is statistically meaningful. Rejection of the null hypothesis generally requires a significance of 0.05 or better, that is, a probability of 5 percent or less that an occurrence is due to chance.

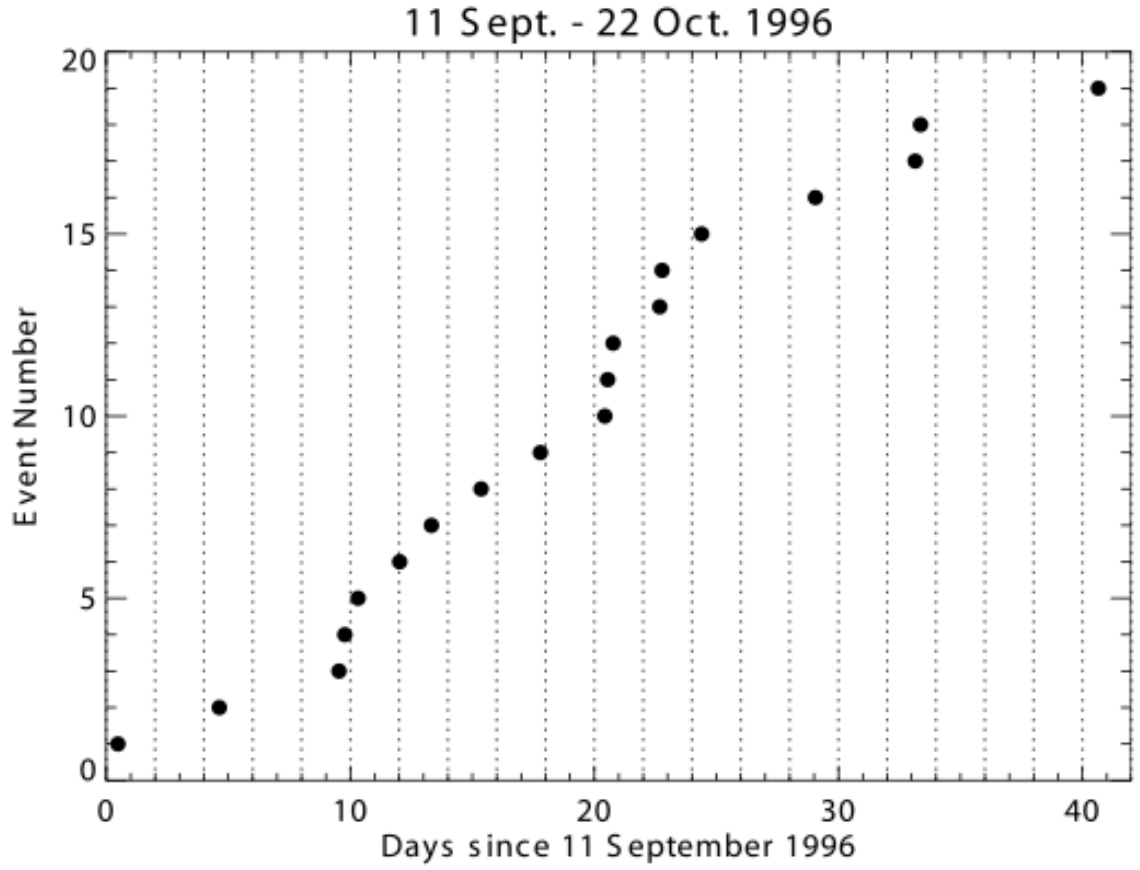

Figure 2.15: Time spacing of large events which occurred from 11 September to 22 October 1996, during Galileo's G2 orbit. The 2-3 day periodicity is visually apparent, and the mean separation between events in 2.2 days. Dashed vertical lines are drawn every 2 days to guide the eye.

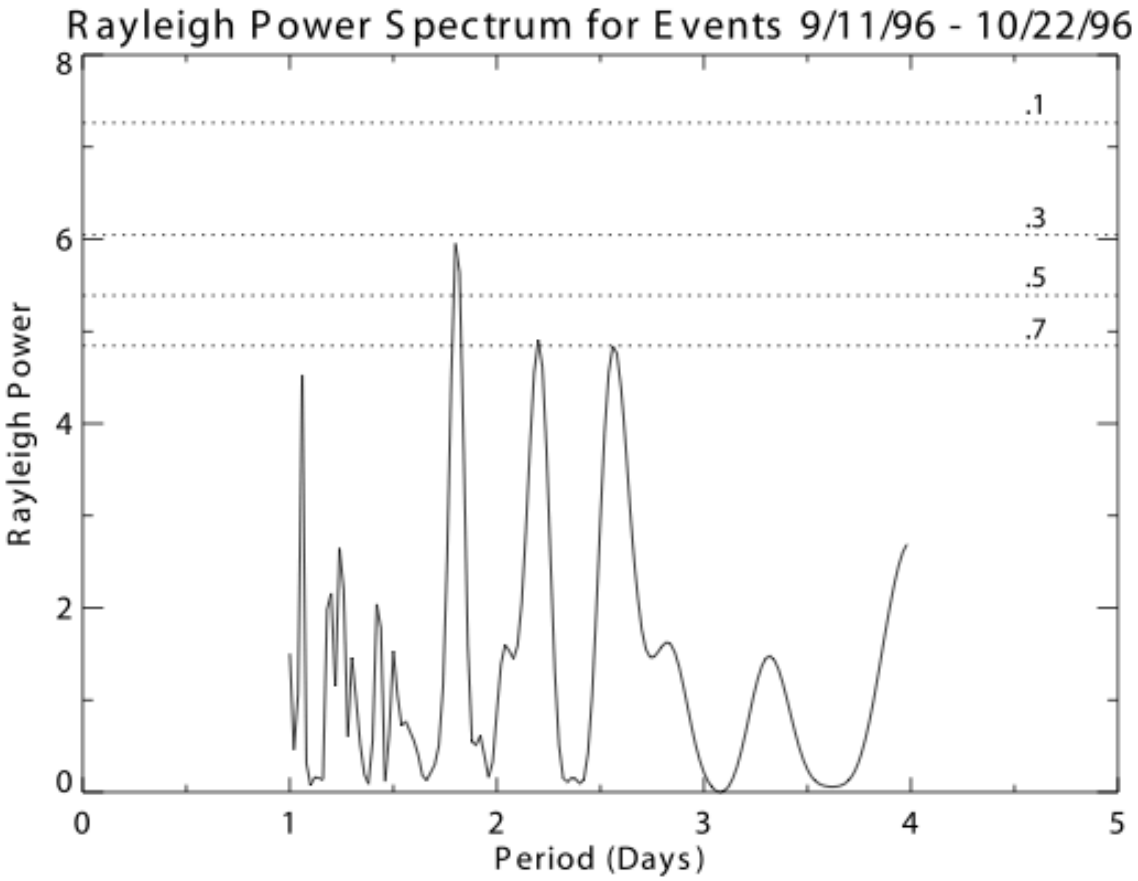

Figure 2.16: Rayleigh power spectrum for large events from Galileo orbit G2. The largest power comes at a period of 1.8 days, with two smaller peaks between 2-3 days, but none of the peaks is statistically significant. Select significance levels, or the probability that the power reaches a certain level by chance alone, are noted by the horizontal dashed lines.

We have expanded our analysis to other orbits (not shown) but still do not observe a statistically significant periodic signal between 1 and 4 days, though in some cases a 2-3 day periodicity is apparent visually, as noted above. We have also computed the Rayleigh power spectrum for all large events in Galileo orbits G1 through I24 to examine possible periodicities on a long time scale (just over 3 years). Results from the analysis are plotted in Figure 2.17. Again we considered only events with an integrated $|B_\theta|$ power beyond a threshold value, which left 69 events in the interval from 11 September 1996 to 30 October 1999. This list represents all

of the large events with the exception of one from 24 December 2000 (Galileo orbit G28), as well as two from March 1979 (Voyager 1), which were excluded because of the long gaps between these and the remaining events.

The peak power for the Rayleigh power spectrum from Figure 2.17 is 10.55 at a period of 1.8 days; with an oversampling factor of 5 there are 856 independent Fourier frequencies in this interval, so the significance of the peak power is 0.105 and the peak cannot be considered to be statistically meaningful.

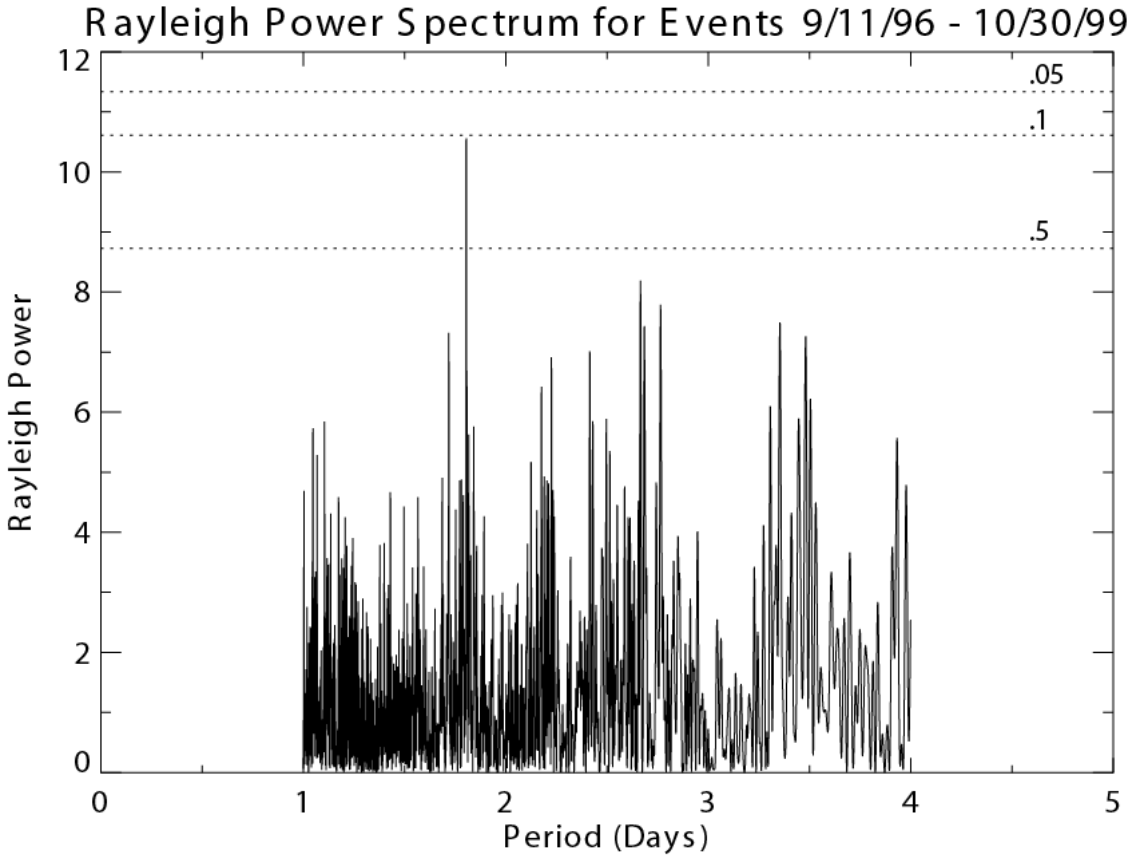

Figure 2.17: As in Figure 2.16, the Rayleigh power spectrum for large events in Galileo orbits G1 through I24. Events occurred from 11 September 1996 to 30 October 1999. There is a peak in the power at a 1.8 day period, but it is not statistically significant.

2.7 Discussion

In previous sections we presented the spatial distribution of the events and their occurrence rate, and determined the location of a separatrix. We also concluded that our events do not occur with any statistically significant periodicity. In this section we will briefly comment on how these results fit with or change the current understanding of Jovian magnetospheric dynamics.

What do our events and their properties tell us about the processes that drive global dynamics at Jupiter? Our results are consistent with both internally-driven and solar wind-driven reconnection, and we do not find strong evidence that one process is favored over another.

At Jupiter we expect that the x-line associated with solar wind-driven reconnection to be restricted to the dawn sector [*Cowley et al.*, 2003]. This x-line is analogous to the terrestrial near-Earth neutral line, and as in the terrestrial case, we would expect a distant reconnection line to exist farther down the tail. The available spacecraft observations are limited in their radial extent, so we do not expect to find direct evidence of the distant x-line. However, our events do support the presence of a near-Jupiter x-line that favors the dawn local time sector, where we observe planetward reconnection events inside of an x-line at ~90 R_J and tailward events outside. Events in the dusk sector are primarily planetward, and can be interpreted equally well as coming from the distant x-line or from centrifugally driven reconnection.

Our observations, particularly the event occurrence rate variation with local time, are well explained by the model of *Kivelson and Southwood* [2005]. In this model reconnection occurs when flux tubes rotate through the dusk sector, stretch due to centrifugal acceleration down the tail, and break. Our events occur with similar frequency in both the pre- and post-midnight

sectors. The occurrence rate drops just prior to midnight local time, and increases with local time until it peaks at 02:30-03:30 LT. These observations can be interpreted according to the qualitative model of *Kivelson and Southwood* [2005] as follows: flux tubes rotate through the dusk sector and are centrifugally accelerated outward down the tail. The plasma sheet thins and flux tubes break and are depleted of plasma, accounting for the high event occurrence rates observed at 20:30-22:30 LT. The empty flux tubes continue to rotate through the night side and via interchange motion they are carried inward, while full flux tubes are carried outward. Reconnection does not occur during this time; this would be consistent with the sharp decrease in event occurrence rate just after 22:30 LT. As the flux tubes continue to rotate through midnight, they refill and the stretching and pinching off process begins again after the full flux tubes have moved outward, though by this time they will have rotated several hours in local time. Thus we expect the event occurrence rate to increase, as it does beginning at 01:30 LT.

Finally, what can we say about the 2-3 day periodicity? It has been identified in flow bursts, auroral polar dawn spots, the *Kronberg et al*. [2005] reconfiguration events, and can be found visually in some of our reconnection events. But using the Rayleigh power spectrum analysis we do not find any statistically significant periodicity in our events, including for periods between 2 and 3 days. Furthermore, in this and other studies the 2-3 day periodicity appears to be present only in specific orbits or intervals. Given the absence of a persistent, statistically significant periodic signal, it seems unlikely that the 2-3 day time scale is characteristic of internal processes driving reconnection in the Jovian magnetotail. This is consistent with the report by *Kronberg et al.* [2009] that the ion spectral index displays periodic behavior with periods ranging from 1.5 to 7 days._We suggest that the reconnection events during intervals displaying the 2-3 day periodicity could be at least partly influenced by external

factors such as magnetospheric interaction with the solar wind. This suggestion is consistent with results from MHD simulations of Jupiter's magnetosphere, which have shown plasmoid release at ~30-100 hour periods that change with solar wind conditions [*Fukazawa et al.*, 2005, 2010]. The possibility that the solar wind can influence or impose a periodicity for plasmoid release would be an interesting topic for further study.

2.8 Future work

In this study we have established the frequency of reconnection events as a function of local time. However, our work has not accounted for local time asymmetries of background conditions such as the plasma sheet thickness. Jupiter's plasma sheet is thickest near dusk and thinnest near dawn [*Kivelson and Khurana*, 2002]. This means that $|B_\theta|$ is largest in the pre-midnight sector, where the plasma sheet is so thick that the Galileo spacecraft (located at the equator) rarely left the plasma sheet (as evidenced by the lack of the distinctive 5-hour periodicity in B_R). However, in the post-midnight sector, the spacecraft spent most of its time in the lobe field, entering the plasma sheet only briefly (~1 hour) once every 5 hours.

With the exception of traveling compression regions (TCRs), reconnection signatures are more easily observed when the spacecraft is in or near the plasma sheet rather than in the tail lobe. Therefore, in calculating the event frequency, it may not be sufficient to simply normalize by the amount of data available in each bin, but to also normalize by the fraction of time spent in or near the plasma sheet. For example, assuming the spacecraft's magnetic latitude varies sinusoidally, the spacecraft will spend roughly twice as much time inside the plasma sheet near dusk (half thickness ~6 R_J) compared dawn (half thickness ~2-3 R_J). This additional normalization could reduce the relative probability of events in the pre- and post-midnight

sectors, which would affect our interpretation of how the events fit with the description of *Kivelson and* Southwood [2005] and other models of global dynamics. However, there are other factors to consider, such as the fact that the spacecraft will still be able to observe TCRs even if it is not always located inside of the plasma sheet on the dawn side. Additionally, the data collected in the post-midnight sector are generally closer to the expected location of the statistical x-line than in the data pre-midnight sector, and taking this into account could increase the probability of events in the pre-midnight sector relative to the post-midnight sector. Further analysis is called for, though we expect that these considerations will affect our present calculations by at most a factor of ~2, and would not dramatically affect our conclusions.

2.9 Summary and conclusions

In this chapter we described the properties of reconnection events in the Jovian magnetotail identified in magnetometer data. These events are characterized by an increase in $|B_\theta|$, the north-south component of the magnetic field, over background levels and by an increase of the elevation angle magnitude compared to the quiet-time background. Such increases in $|B_\theta|$ and the elevation angle magnitude indicate a field reconfiguration consistent with magnetic reconnection. We also used the bendback angle and the sign of B_θ as proxies to flow.

We identified 249 reconnection events in the available magnetometer data, and found that the events are well-distributed in radial distance and occurred at nearly all nightside local times. Though most events were observed in the post-midnight local time sector, there was also more data available in that region. Therefore we also calculated the event frequency normalizing by the amount of data in hourly local time bins; the results showed that reconnection frequency is

comparable in the pre- and post-midnight local time sectors, with a curious minimum at midnight.

A direct comparison between our work and studies that used particle anisotropies to study dynamics in the tail shows good agreement between our events and intervals of large radial anisotropies. New events have been identified in the pre-midnight sector, supplementing the distribution of the reconfiguration events studied by *Kronberg et al.* [2005]. We also have compared the distribution of the radial flows, as inferred from the sign of B_θ, to the distribution of particle flow bursts by *Woch et al.* [2002]. In the post-midnight local time sector the x-line is likely located near 90 R_J, in qualitative agreement with the statistical separatrix from *Woch et al*. [2002]. In most of the pre-midnight sector the radial distribution of data is insufficient to determine the distance of an x-line, but we can conclude that the x-line is likely to lie near or beyond ~120 R_J.

Finally, we have discussed the periodicity of our events and the absence of the 2-3 day periodicity seen in flow bursts, reconfiguration events, and auroral polar dawn spots. For certain specific intervals, such as orbits E16 and G2, including the *Kronberg et al.* [2007] interval, we observe the 2-3 day periodicity visually in our events. However, the Rayleigh power spectrum does not show any statistically significant periodicities in our events, either for these individual orbits or on a longer time scale. Therefore we conclude that reconnection does not generally occur with any periodicity that is representative of the internal processes driving dynamics in the Jovian magnetotail.

Bibliography

Angelopoulos, V., W. Baumjohann, C. F. Kennel, F. V. Coroniti, M. G. Kivelson, R. Pellat, R. J. Walker, H. Lühr, and G. Paschmann (1992), Bursty Bulk Flows in the Inner Central Plasma Sheet, *J. Geophys. Res.*, *97*, 4027-4039.

Angelopoulos, V., C. F. Kennel, F. V. Coroniti, R. Pellat, M. G. Kivelson, R. J. Walker, C. T. Russell, W. Baumjohann, W. C. Feldman, and J. T. Gosling (1994), Statistical characteristics of bursty bulk flow events, *J. Geophys. Res.*, *99*, 21257.

Angelopoulos, V., F. V. Coroniti, C. F. Kennel, M. G. Kivelson, R. J. Walker, C. T. Russell, R. L. McPherron, E. Sanchez, C.-I. Meng, W. Baumjohann, G. D. Reeves, R. D Belian, N. Sato, E. Friis-Christensen, P. R. Sutcliffe, K. Yumoto, and T. Harris (1996), Multipoint analysis of a bursty bulk flow event on April 11, 1985, *J. Geophys. Res.*, *101*, 4967-4989.

Angelopoulous, V., J. P. McFadden, D. Larson, C. W. Carlson, S. B. Mende, H. Frey, T. Phan, D. G. Sibeck, K.-H. Glassmeier, U. Auster, E. Donovan, I. R. Mann, I. J. Rae, C. T. Russell, A. Runov, X.-Z. Zhou, and L. Kepko (2008), Tail Reconnection Triggering Substorm Onset, *Science*, *321*, pp. 391-935.

Axford, W. I. (1969), Magnetospheric convection, *Rev. Geophys.*, *7*, 421-459.

Bame, S. J., B. L. Barraclough, W. C. Feldman, G. R. Gisler, J. T. Gosling, D. J. McComas, J. L. Phillips, M. F. Thomsen, B. E. Goldstein, and M. Neugebauer (1992), Jupiter's magnetosphere: Plasma description from the Ulysses flyby, *Science*, *257*, *5076*, 1539-1543.

Cao, J. B., Y. D. Ma, G. Parks, H. Reme, I. Dandouras, R. Nakamura, T. L. Zhang, Q. Zong, E. Lucek, C. M. Carr, Z. X. Liu, and G. C. Zhou (2006), Joint observations by Cluster satellites

of bursty bulk flows in the magnetotail, *J. Geophys. Res.*, *111*, A04206, doi:10.1029/2005JA011322.

Cowley, S. W. H., E. J. Bunce, T. S. Stallard, and S. Miller (2003), Jupiter's polar ionospheric flows: Theoretical interpretation, *Geophys. Res. Lett.*, *30*(5), 1220.

Delamere, P. A., and F. Bagenal (2010), Solar wind interaction with Jupiter's magnetosphere, *J. Geophys. Res.*, *115*, A10210, doi:10.1029/2010JA015347.

Dungey, J. W. (1961), Interplanetary magnetic field and the auroral zones, *Phys. Rev. Lett.*, *6*, 47-48.

Fukazawa, K., T. Ogino, and R. J. Walker (2005), Dynamics of the Jovian magnetosphere for northward interplanetary magnetic field (IMF), *Geophys. Res. Lett.*, *32*, doi:10.1029/2004GL021392.

Fukazawa, K., T. Ogino, and R. J. Walker (2010), A simulation study of dynamics in the distant Jovian magnetotail, *J. Geophys. Res.*, *115*, A09219, doi:10.1029/2009JA015228.

Intriligator, D. S. and J.H. Wolfe (1976), Results of the Plasma Analyzer Experiment on Pioneers 10 and 11, *Jupiter*, edited by T. Gehrels, pp. 848-869, Univ. of Arizona Press, Tucson, Arizona.

Joy, S. P., M. G. Kivelson, R. J. Walker, K. K. Khurana, C. T. Russell, and T. Ogino (2002), Probabilistic models of the Jovian magnetopause and bow shock locations, *J. Geophys. Res.*, *107*, 1309.

Khurana, K. K., M. G. Kivelson, V. M. Vasyliūnas, N. Krupp, J. Woch, A. Lagg, B. H. Mauk, and W. S. Kurth (2004), The configuration of Jupiter's magnetosphere, in *Jupiter: the Planet,*

Satellites, and Magnetosphere, edited by F. Bagenal et al., Cambridge Univ. Press, New York.

Kivelson, M. G., and K. K. Khurana (2002), Properties of the magnetic field in the Jovian magnetotail, *J. Geophys. Res.*, *107*, 1196.

Kivelson, M. G. and D. J. Southwood (2005), Dynamical consequences of two modes of centrifugal instability in Jupiter's outer magnetosphere, *J. Geophys. Res.*, *110*, A12209, doi:10.1029/2005JA011176.

Kronberg, E. A., J. Woch, N. Krupp, A. Lagg, K. K. Khurana, and K.-H. Glassmeier (2005), Mass release at Jupiter: Substorm-like processes in the Jovian magnetotail, *J. Geophys. Res.*, *110*, A03211, doi:10.1029/2004JA010777.

Kronberg, E. A., K.-H. Glassmeier, J. Woch, N. Krupp, A. Lagg, and M.K. Dougherty (2007), A possible intrinsic mechanism for the quasi-periodic dynamics of the Jovian magnetosphere, *J. Geophys. Res.*, *112*, A05203.

Kronberg, E., J. Woch, N. Krupp, and A. Lagg (2008), Mass release process in the Jovian magnetosphere: Statistics on particle burst parameters, *J. Geophys. Res.*, doi:10.1029/2008JA013332.

Kronberg, E. A., J. Woch, N. Krupp, and A. Lagg (2009), A summary of observational records on periodicities above the rotational period in the Jovian magnetosphere, *Ann. Geophys.*, *27*, 2565-2573.

Krupp, N., J. Woch, A. Lagg, B. Wilken, S. Livi, and D. J. Williams (1998), Energetic particle bursts in the predawn Jovian magnetotail, *Geophys. Res. Lett.*, *25*, 1249-1252.

Krupp, N., A. Lagg, S. Livi, B. Wilken, J. Woch, E. Roelof, and D. Williams (2001), Global flows of energetic ions in Jupiter's equatorial plane: First-order approximation, *J. Geophys. Res.*, *106*(A11), 26017-26032.

Lepping, R. P., M. J. Silverstein, and N. F. Ness (1981), Magnetic Field Measurements at Jupiter by Voyagers 1 and 2: Daily Plots of 48 Second Averages, NASA Technical Memorandum 83864, National Aeronautics and Space Administration.

McPherron, R. L. (1995), Magnetospheric Dynamics, in *Introduction to Space Physics*, edited by M. G. Kivelson and C. T. Russell, Cambridge Univ. Press, New York.

McComas, D. J. and F. Bagenal (2007), Jupiter: A fundamentally different magnetospheric interaction with the solar wind, *Geophys. Res. Lett.*, *34*, L20106, doi:10.1029/2007GL031078.

Prangé, R., G. Chagnon, M. G. Kivelson, T. A. Livengood, and W. Kurth (2001), Temporal monitoring of Jupiter's auroral activity with IUE during the Galileo mission. Implications for magnetospheric processes, *Plan. Space Sci.*, *49*, 405-415.

Radioti, A., D. Grodent, J.-C. Gérard, B. Bonfond, and J. T. Clarke (2008), Auroral polar dawn spots: Signatures of internally driven reconnection processes at Jupiter's magnetotail, *Geophys. Res. Lett.*, *35*, L03104, doi:10.1029/2007GL032460.

Russell, C. T., K. K. Khurana, D. E. Huddleston, and M. G. Kivelson (1998), Localized Reconnection in the Near Jovian Magnetotail, *Science*, *280*, 1061-1064.

Vasyliūnas, V. M. (1983), Plasma Distribution and Flow, in *Physics of the Jovian Magnetosphere*, edited by A. J. Dessler, p. 395, Cambridge Univ. Press, New York.

Vasyliūnas, V. M. (1994), Role of the plasma acceleration time in the dynamics of the Jovian magnetosphere, *Geophys. Res. Lett.*, *21*, 401-404.

Vogt, M. F., M. G. Kivelson, K. K. Khurana, S. P. Joy, and R. J. Walker (2010), Reconnection and flows in the Jovian magnetotail as inferred from magnetometer observations, *J. Geophys. Res.*, doi: 10.1029/2009JA015098.

Williams, D. J., R. W. McEntire, S. Jaskulek, and B. Wilken (1992), The Galileo energetic particles detector, *Space Sci. Rev.*, *60*, 385-412.

Woch, J., N. Krupp, A. Lagg, B. Wilken, S. Livi, and D. J. Williams (1998), Quasi-periodic modulations of the Jovian magnetotail, *Geophys. Res. Lett.*, *25*, 1253.

Woch, J., N. Krupp, and A. Lagg (2002), Particle bursts in the Jovian magnetosphere: Evidence for a near-Jupiter neutral line, *Geophys. Res. Lett.*, *29*, 1138.

CHAPTER 3

Relating Jupiter's Auroral Features to Magnetospheric Sources

3.1 Introduction

For more than a decade, ground and space-based telescope observations have produced dazzling images of Jupiter's auroral emissions in ultraviolet, infrared, and visible wavelengths. These images have shown that Jupiter's aurora displays some unique features, such as satellite footprints, that are not present in Earth's aurora. Additionally, there are some features, such as Jupiter's main oval, that may seem similar to their terrestrial counterparts, but are linked to different magnetospheric processes than those that drive Earth's aurora. The main auroral oval emissions at Jupiter are thought to be associated with the breakdown of plasma corotation in the middle magnetosphere (e.g., *Kennel and Coroniti* [1975]; *Hill* [1979, 2001]; *Cowley and Bunce* [2001]), rather than the open/closed boundary as at the Earth. As a result, the boundary between open and closed flux in Jupiter's ionosphere is not well defined, though the region of open flux is generally thought to be small. Furthermore, the magnetospheric mapping of Jupiter's polar emissions is highly uncertain because global Jovian field models are known to be inaccurate beyond ~30 R_J.

In this chapter we present results of a new mapping approach to relate Jupiter's auroral features to source regions in the middle and outer magnetosphere. The approach is based on a flux equivalence calculation in which we require that the magnetic flux in some specified region at the equator equals the magnetic flux in the area to which it maps in the ionosphere. Equating the fluxes in this way allows us to link a given position in the magnetosphere to a position in the

ionosphere, and therefore learn about Jupiter's magnetospheric structure by identifying the source regions of polar auroral features. The flux calculation also enables mapping of the dayside magnetopause, thereby establishing possible locations of a portion of the open/closed flux boundary in Jupiter's polar cap; those results will have important consequences for our understanding of global dynamics and the open or closed nature of the Jovian magnetosphere.

This chapter is organized as follows: first we provide an overview of auroral observations at Jupiter. Next we review the current global field models and their limitations, then discuss some of the motivating questions for this work. Then, we describe the flux equivalence calculation used in our mapping, and present results and comparisons to auroral observations. Finally, we discuss the results in the context of current models of magnetospheric dynamics and suggest other applications for the mapping results, and conclude with a summary.

3.2 Overview of auroral observations

Auroral emissions at Jupiter have been observed at radio, infrared, visible, ultraviolet, and x-ray wavelengths. The observations have a long history dating back to the 1950s, when the radio emissions were first detected, and have been collected by a variety of instruments, ranging from spacecraft flybys to ground-based and space telescopes. In this section we review the present understanding of Jupiter's auroral emissions, starting with the atmospheric processes that produce the auroral emissions, then the instruments used to collect the data discussed later in this chapter, and finally describe the auroral features in detail. We largely restrict our discussion to the infrared and ultraviolet emissions because many observations are available at these wavelengths and they provide the best proxy to magnetospheric processes [e.g., *Prangé et al.*, 2001]. For a more complete history of auroral emissions at Jupiter, including radio and x-ray

wavelengths, we refer the reader to review chapters by *Bhardwaj and Gladstone* [2000] and *Clarke et al.* [2004], on which the discussion in the following two sections is based.

3.2.1 Why are there auroral emissions at Jupiter?

The ultraviolet auroral emissions at Jupiter are produced by the excitation of atmospheric H_2 and H by precipitating electrons. The UV emissions are most prominent in the H Lyman α line and H_2 Lyman and Werner bands. The Lyman α emission is produced by dissociative excitation of H_2 as follows:

$$e + H_2 \rightarrow H(2p, 2s) + H + e$$

$$H(2p, 2s) \rightarrow H + hv$$

while the H_2 Lyman and Werner emission is produced by electron excitation:

$$e + H_2 \rightarrow H_2(B, C) + e$$

$$H_2(B, C) \rightarrow H_2 + hv$$

[*Bhardwaj and Gladstone*, 2000].

The infrared emissions are thermal H_3^+ emissions that are produced by ionization of H_2 as follows:

$$e + H_2 \rightarrow H_2^+ + e_{primary} + e_{secondary}$$

$$H_2^+ + H_2 \rightarrow H + H_3^+$$

The fact that the infrared emissions are thermal emissions, rather than directly excited, means that the UV emissions are a better indicator of magnetospheric processes than the infrared emissions. Both the UV and the infrared H_3^+ emissions brighten in response to an increase in precipitating electron flux, though the infrared emissions can also indicate heating from nearby

active precipitation regions or ionospheric currents. Additionally, the UV emissions decrease nearly immediately after a decrease in the precipitating electron flux, while the H_3^+ emissions remain bright for time scales of ~10 minutes.

3.2.2 Instrumentation: ground-based and space telescopes

Jupiter's aurorae were first observed in 1979 during the Voyager 1 flyby by the satellite's Ultraviolet Spectrometer (UVS) instrument [*Broadfoot et al.*, 1979]. Shortly thereafter, the International Ultraviolet Explorer (IUE) satellite in Earth orbit [*Clarke et al.*, 1980] began collecting data, providing a way to study temporal variations in the auroral emissions. IUE observations of Jupiter's aurora spanned more than 15 years (1979-1996), with resolution of 1.078 arcsec/pixel [*Prangé et al.*, 2001].

High-resolution auroral imaging became possible through use of the Hubble Space Telescope, which launched in 1990. HST collected its first Jovian auroral observations in 1992 with the Faint Object Camera (FOC) [*Caldwell et al.*, 1992]. Most of the UV images we discuss in this chapter were taken with a more recent instrument, the Space Telescope Imaging Spectrograph (STIS), which has a typical spatial resolution of 0.024 arcsec/pixel [*Clarke et al.*, 2002].

Ground-based telescopes also provide valuable data of Jupiter's infrared auroral emissions. The Io footprint was first observed in the infrared by the ProtoCAM instrument at NASA's Infrared Telescope Facility (IRTF) on Mauna Kea, Hawaii [*Connerney et al.*, 1993]. Most of the observations we discuss in this chapter were taken with the more recent NSFCam (National Science Foundation Camera) instrument at the IRTF. Its resolution is 0.148 arcsec/pixel [*Satoh and Connerney*, 1999], lower than the HST STIS images.

3.2.3 Three main types of auroral emissions

Jupiter's auroral emissions can be classified into three main types: the satellite footprints, a main oval (main emissions), and the polar emissions [*Clarke et al.,* 1998]. All three components can be seen in Figure 3.1, which shows a polar projection of the UV auroral emissions in the northern hemisphere. Some of the auroral features, like the satellite footprints, have a clear and relatively well-understood link to magnetospheric source regions. Others, like the mysterious polar emissions, are more complicated and cannot be mapped reliably. In this section we review the primary features of Jupiter's auroral emissions, focusing on the current understanding of how these features relate to magnetospheric processes.

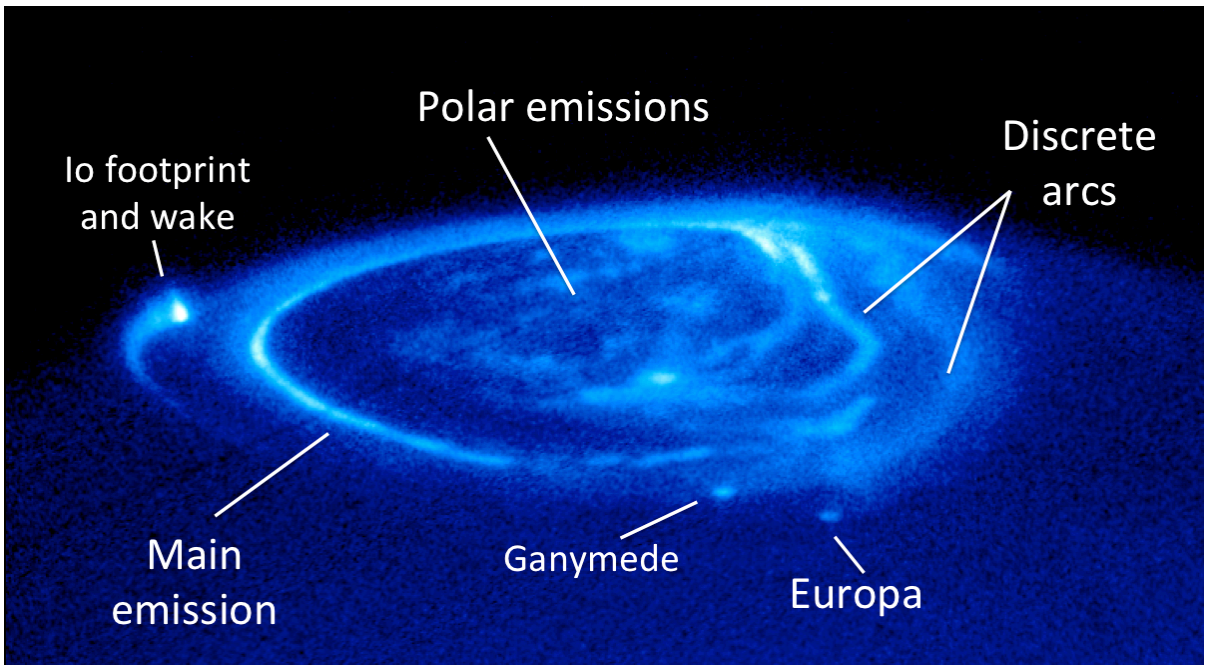

Figure 3.1: Jupiter's aurora as seen in the UV by the Hubble Space Telescope. Major auroral features such as the satellite footprints, main oval, and polar emissions, are labeled.

3.2.3.1 Satellite footprints

The most equatorward component of the Jovian auroral emissions are the satellite footprints, which are also the features that can be most reliably linked to their magnetospheric source regions. Auroral emissions have been observed at the ionospheric footprints of Io, Europa, and Ganymede [*Connerney et al.*, 1993; *Clarke et al*., 2002], and were recently discovered at the footprint of Callisto [*Clarke et al.*, 2011]. The footprints are key to our ability to map between the ionosphere and the magnetosphere because the satellites' orbital locations are known and a footprint's ionospheric location can, therefore, be linked reliably to a radial position in the magnetosphere. The longitudinal position can also be inferred, although with some small uncertainty (~1-2 hours of local time) as a consequence of the signal propagation time between the satellite and Jupiter's ionosphere. Thus satellite footprints are useful for constraining global field models and provide a check for field model accuracy at the orbital distances of Io (5.9 R_J), Europa (9.4 R_J), and Ganymede (15 R_J). More discussion of the field models is given in Section 3.3.

3.2.3.2 Main oval emissions

Poleward of the satellite footprints are the main auroral emissions, which are confined to a relatively constant, narrow (1º-3º latitudinal width) band that is fixed with respect to System-III longitude [*Grodent et al.,* 2003a]. In the northern hemisphere, the main emissions are not actually shaped like an oval, but display a kidney bean shape due to a "kink" that is also fixed in longitude; this shape can be seen in Figure 3.1. The main emissions in the southern hemisphere are more oval-shaped. A recent study [*Grodent et al.*, 2008b] revealed several morphological variations in the main oval as a function of local time: the dawn side portion forms a narrow arc,

the post-noon portion consists of auroral patches, and the dusk portion appears to broaden and break from the main oval. Additionally, there is a discontinuity, believed to map to the pre-noon local time sector, where the brightness is less than ~10% of the main oval brightness [*Radioti et al.*, 2008a]. Therefore, it was suggested that the term "main oval" should be replaced by the term "main emission".

It has long been recognized that the Jovian main auroral emissions do not map to the open/closed field line boundary as they do at the Earth. Instead, the main emissions are thought to be associated with the region where plasma corotation breaks down in the middle magnetosphere (e.g., *Kennel and Coroniti* [1975]; *Hill* [1979, 2001]; *Cowley and Bunce* [2001]). The major source of plasma in Jupiter's magnetosphere is the volcanically active moon Io, which releases ~0.5-1 ton of plasma per second into the Io torus. As this plasma diffuses radially outward through flux tube interchange, its angular velocity decreases in order to conserve angular momentum. As the plasma's angular velocity decreases, field lines in the equatorial magnetosphere are swept back azimuthally because the field is frozen into the flow. A current system develops fed by a field-aligned current coming out of the ionosphere on L-shells at and beyond ~20, an outward radial "corotation enforcement current" in the equator, and a returning field-aligned current into the ionosphere at larger L [*Hill,* 2001; *Cowley and Bunce,* 2001]. This current system is illustrated in Figure 3.2. In the equatorial plane, the radial (corotation-enforcement) current provides a $\vec{j}\times\vec{B}$ force in the direction of corotation, acting to drive the azimuthal velocity of the plasma back towards corotation. The main oval emissions are produced by downward-moving electrons accelerated as required in order to carry the upward (out of the ionosphere) field-aligned current [*Cowley and Bunce*, 2001].

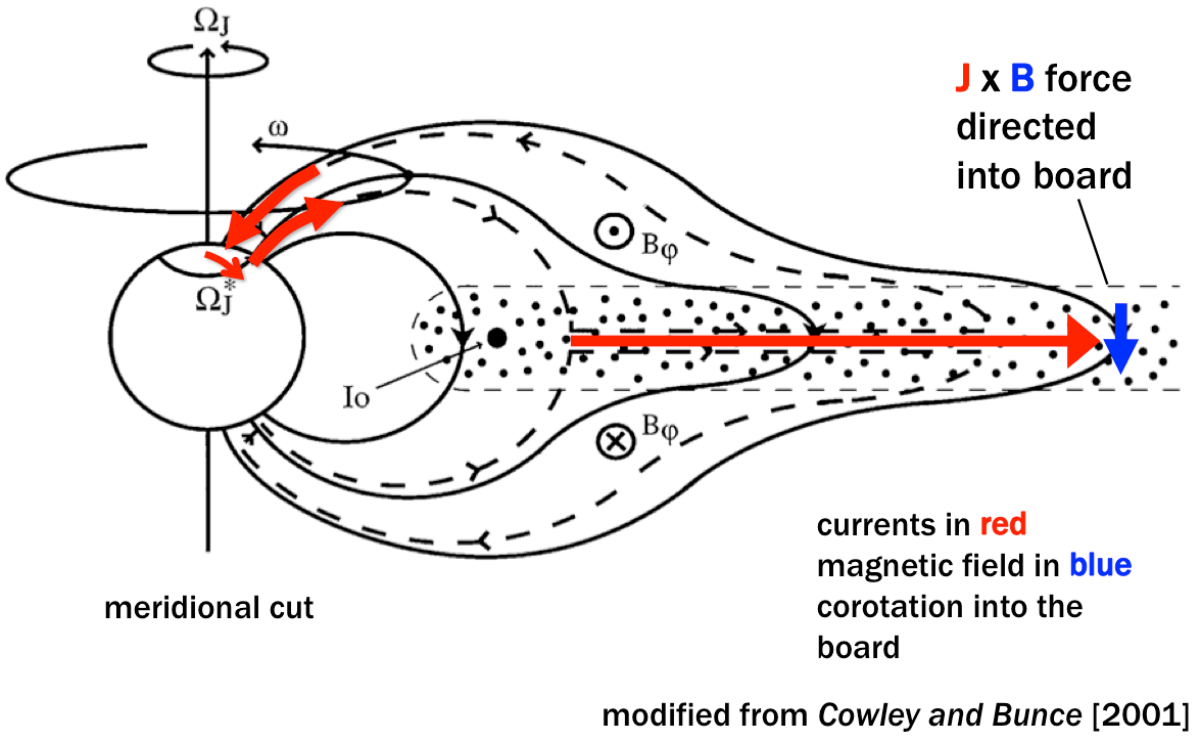

Figure 3.2: Schematic showing the current system that provides a $\vec{j}\times\vec{B}$ force that drives plasma in the azimuthal direction back toward corotation. Jupiter's main auroral emissions are thought to be produced by downward-moving electrons carried by the upward (out of the ionosphere) field-aligned current. Modified from *Cowley and Bunce* [2001].

Several theoretical studies have supported the view that corotation breakdown drives the main emissions at Jupiter, and have tried to estimate the distance to which the main oval maps in the equatorial magnetosphere. *Cowley and Bunce* [2001] used simple data-based models of the plasma velocity and north-south magnetic field component to calculate the magnitude of outward field-aligned currents in the middle magnetosphere. Inside of ~20 R_J they represented the equatorial B_Z as an axisymmetric dipole with a contribution from a current sheet model [*Connerney et al.,* 1981], and outside of ~20 R_J they represented B_Z as a function of radial distance based on a fit to Voyager 1 data [*Khurana and Kivelson*, 1993]. They found that the field-aligned currents associated with the breakdown of corotation peaked at radial distances of

~30-50 R_J in the magnetosphere, and that these currents map to a magnetic colatitude of ~16º, roughly consistent with the observed location of the main emissions. However, they also concluded that a field-aligned potential drop would be required to accelerate the electrons to high enough energies to drive the aurora. *Hill* [2001] performed a similar calculation under slightly different assumptions regarding the plasma rotational velocity [*Hill*, 1979]; he similarly concluded that the upward (out of the ionosphere) field-aligned current would be largest at L = 30, and that the main oval emissions could therefore be expected to map to ~30 R_J.

The main oval emission displays several interesting features that can be related to magnetospheric source regions. One is a "discontinuity", or region of decreased brightness (less than ~10% of the typical main oval brightness) that appears to map to the pre-noon local time region. In this region of the magnetosphere, the field-aligned current has been shown to reverse direction and flow downward into the ionosphere [*Radioti et al.*, 2008a; *Khurana*, 2001; *Bunce and Cowley*, 2001]. The brightness of the main oval decreases in this region because downward current does not require acceleration of magnetospheric electrons [*Bunce and Cowley*, 2001]. Other features include the quasi-parallel arcs in the diffuse emission located equatorward of the main oval on the dusk side (see Figure 3.1), which have been attributed to electron scattering by whistler mode waves [*Radioti et al.*, 2009]. The main oval emissions may also be accompanied by a fainter and variable secondary arc poleward of the main oval [*Pallier and Prangé*, 2001; *Vasavada et al.*, 1999], though the poleward arcs are not yet fully understood.

3.2.3.3 Polar aurora

The third major feature of the Jovian aurora is the highly variable and mysterious polar auroral emission, which is categorized into three regions, the active, dark, and swirl regions,

based on average brightness and dynamic behavior. The mapping of these polar emissions is exceptionally uncertain, partly because field models become increasingly undependable for high latitude field lines and partly because the shapes and locations of the three regions vary with time and as Jupiter rotates, as seen in Figure 3.3.

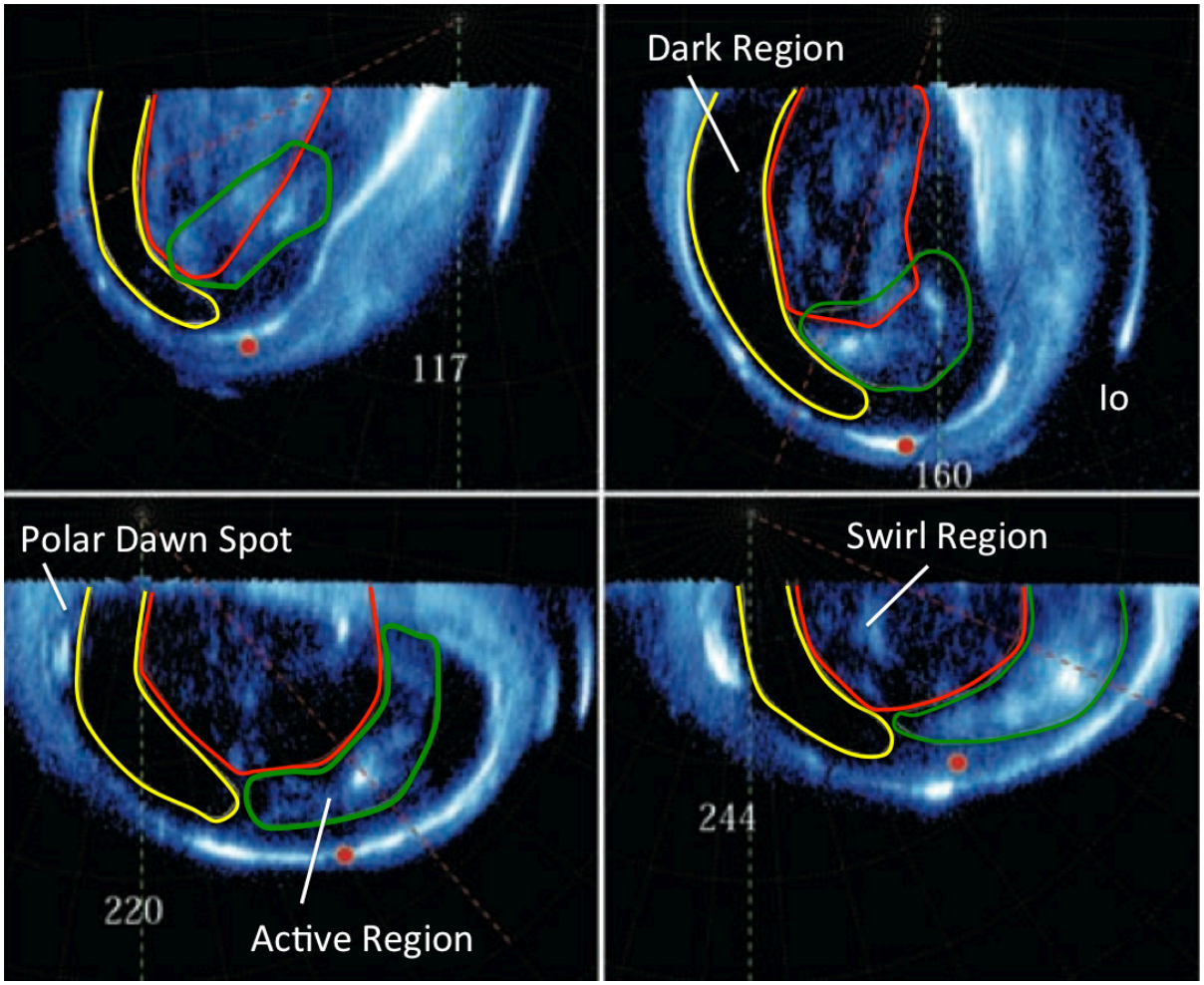

Figure 3.3: Polar projections of UV auroral emissions in Jupiter's northern hemisphere as imaged by the Hubble Space Telescope, shown for four different viewing orientations. The three polar auroral regions (active region in green, dark region in yellow, swirl region in red) have been labeled and their locations for this particular time are delineated by the colored contours. The Sun's direction differs in each panel but is generally toward the bottom of the page. Modified from Figure 5 in *Grodent et al.* [2003b].

The active region is very dynamic and is characterized by the presence of flares, bright spsots, and arc-like features. It maps roughly to the noon local time sector and is located just poleward of the main oval. The active region flares have a brightness of a few hundred kR [*Grodent et al.*, 2003b] (by comparison, the main oval brightness is typically 50-500 kR [*Grodent et al.*, 2003a]) and a characteristic time scale of ~minutes. Because of their location near noon local time, the spots, arcs, and flares in the active region are thought to be signatures of interaction with the solar wind or the polar cusp region [*e.g.*, *Pallier and Prangé*, 2001]. *Waite et al.* [2001] used the MHD model of *Ogino et al.* [1998] to map an observed polar flare to near the cushion region, ~40-60 R_J in the morning sector, and postulated that the flare could be produced by a magnetospheric disturbance due to a sharp increase in the solar wind dynamic pressure. Alternately, *Grodent et al.* [2003b] interpreted the polar flares as the signature of "explosive" magnetopause reconnection on the day side, based on their ~minutes-long characteristic time scale. They also suggest that the arc-like structures could be the signature of a Dungey cycle dayside x-line, following the arguments of *Cowley et al.* [2003].

The dark region is located just poleward of the main oval, occupying a crescent shape region in the dawn to pre-noon local time sector. As its name suggests, the dark region is an area that appears dark in the UV, displaying only a slight amount of emission (0-10 kR) above the background level [*Grodent et al.*, 2003b]. By comparison, the main oval brightness is typically 50-500 kR [*Grodent et al.*, 2003a]. It is fixed in local time but its size contracts and expands as Jupiter rotates [*Grodent et al.*, 2003b]. The jovicentric location of the dark region roughly matches the area where *Pallier and Prangé* [2001] observed faint inner ovals, or arcs; the most poleward arcs are roughly aligned with the poleward edge of the dark region. *Pallier and Prangé*

[2001] suggested that these arcs map to closed field lines in the outer magnetosphere (out to ~70 R_J based on the VIP4 model).

Other interpretations of the dark region turn to models of global magnetospheric dynamics to explain the observations. For example, *Grodent et al.* [2003b] associated the UV dark region with the *Stallard et al*. [2003] rotating Dark Polar Region (r-DPR), an area of subcorotating ionospheric flows, as measured by the Doppler shifts of infrared emission spectra. The dawn side r-DPR, and thus the dark region, is thought to be linked to the Vasyliunas-cycle [*Vasyliūnas*, 1983] return flow of depleted flux tubes [*Cowley et al.*, 2003]. In the Vasyliunas-cycle [*Vasyliūnas*, 1983], mass-loaded flux tubes are stretched as they rotated into the night side; they eventually pinch off, and reconnection occurs in the midnight-predawn local time sector, releasing a plasmoid that can escape down the tail, while empty flux tubes rotate back around to the day side. Similarly, *Southwood and Kivelson* [2001] argued that the main oval emissions map to the plasma disk, which would mean that the dark region, just poleward of the main oval, maps to the cushion region. The cushion region is an area of southward-oriented and strongly fluctuating field in the outer magnetosphere in the post-dawn to noon local time sector where the field becomes more dipole-like than in the inner magnetosphere. It has been associated with empty flux tubes that were emptied by Vasyliūnas-type reconnection as they rotated through the night side [*Kivelson and Southwood*, 2005].

The swirl region is an area of patchy, ephemeral emissions that exhibit turbulent, swirling motions. The swirl region is located poleward of the active and dark regions, and is roughly the center of the polar auroral emissions. It is generally interpreted as mapping to open field lines [*Pallier and Prangé*, 2001; *Cowley et al.*, 2003; *Stallard et al.*, 2003]. *Grodent et al.* [2003b] found that the UV swirl region is nearly colocated with a feature seen in the infrared emission

called the fixed Dark Polar region (f-DPR), where ionospheric flows are nearly stagnant in a reference frame fixed to the magnetic poles as they rotate with the planet [*Stallard et al.*, 2003]. A comparison between the f-DPR and swirl regions is given in Figure 3.4. The stagnant flows in the f-DPR (swirl region) then suggest that the area maps to open field lines associated with Dungey cycle return flows [*Cowley et al.,* 2003], which are expected to flow across the ionosphere slowly because the Jovian magnetotail is ~hundreds or thousands of R_J in length.

An additional feature of the polar auroral emissions is the presence of transient spots located at the equatorward edge of the dark region. Because of their location, emitted power, and periodic recurrence, these polar dawn spots have been associated with the internally driven reconnection process and especially with the inward-moving flow initiated during reconnection [*Grodent et al.*, 2004; *Radioti et al.*, 2008, 2010]. Nightside spots, mapping roughly to the pre-midnight local time sector, have also been observed, and are also thought to indicate inward flow due to tail reconnection [*Grodent et al.*, 2004; *Radioti et al.*, 2011]. The polar dawn spots appear to occur with a 2-3 day periodicity similar to the reported recurrence interval of reconfiguration events seen in the particle data [*Kronberg et al.*, 2005]. They persist for time scales of ~minutes to ~1 hour, similar to the ~tens of minutes time scale for the observed reconnection events seen in the magnetometer data [*Vogt et al.*, 2010].

If these spots are really the signature of flow associated with reconnection, we would expect them to map inside of ~90-100 R_J, the distance to the statistical x-line [*Woch et al.*, 2002; *Vogt et al.*, 2010]. Though the available field models are not accurate beyond ~30 R_J, an improved mapping method would provide a way to test the interpretation by identifying the source region of the polar dawn spots and relating their radial mapping to the location of a statistical x-line.

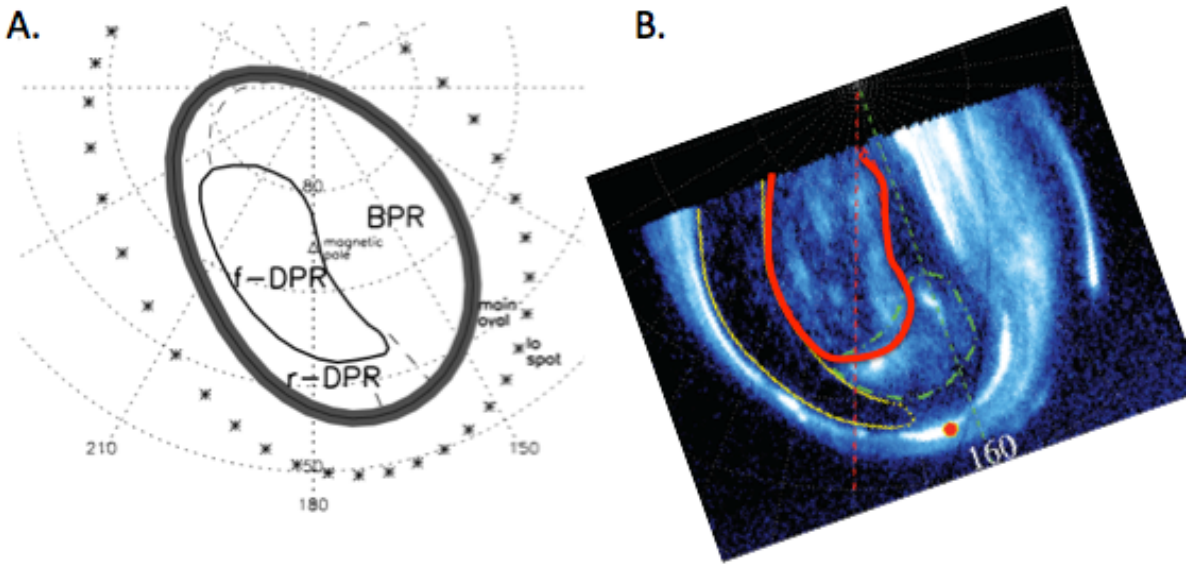

Figure 3.4: Comparison of the IR and UV polar aurora observations. A: The f-DPR region identified from IR auroral observations. B: The UV auroral swirl region outlined in red, rotated to match the orientation of panel A.

3.3 Limitations of current magnetic field models

The satellite footprints have played a key role in the development of Jovian internal magnetic field models because the footprints can be used to check field model accuracy out to 15 R_J, the orbit of Ganymede. Beyond these distances there are no satellite footprints to constrain the field models, and azimuthal currents stretch field lines and compromise the mapping. Therefore the models are relatively accurate inside of 30 R_J but cannot be used to reliably map auroral features to the middle and outer magnetosphere.

There are three major internal field models that have been constructed using the satellite footprints as a check for accuracy. The first is the VIP4 field model [*Connerney et al.*, 1998], which was developed to match the Voyager 1 and Pioneer 11 magnetic field observations and to ensure that the model field lines traced from 5.9 R_J matched the Io footprint in the ionosphere.

The VIP4 model generally does a good job of fitting the Io footprint, though in the northern hemisphere the model deviates from the observations in the "kink" sector that gives the Io footprint its characteristic kidney bean shape. This is seen in Figure 3.5, which shows the observed locations of Ganymede's footprint (circles) and the positions where the traced model field lines of VIP4 and two other models reach the ionosphere (triangles) for comparison. The footprint data for the northern hemisphere come from Table 1 in *Grodent et al.* [2008b], and for the southern hemisphere the data come the same set of HST FUV images acquired with the STIS and ACS instruments. The points are separated by 10º in longitude in the equator. To guide the eye, the symbols are plotted in a repeating sequence of six colors: red, yellow, green, blue, purple, and black. For the observations (circles), the color used in the plot indicates the longitude of the satellite at the equator. For the model results (triangles), the color indicates the initial equatorial longitude used in tracing the model field lines from the equator to the ionosphere. The observations should be compared to the closest mapped triangle of the same color.

The Grodent anomaly model [*Grodent et al.*, 2008b] improved the agreement between the model and footprint observations in the northern hemisphere through the addition of a magnetic anomaly. Inclusion of the magnetic anomaly improved the match to the Io footprint, especially in the "kink" sector, and also improved the match to the Callisto and Ganymede footprints. The model is a version of the VIP4 plus current sheet model with modified Schmidt coefficients, with the magnetic anomaly represented as an additional dipole located close to the planetary surface. In the northern hemisphere, the Grodent anomaly model improves the agreement between the model and observations by ~several degrees compared to VIP4, as seen in Figure 3.5. In both hemispheres the error is mostly in the direction along the curve rather than

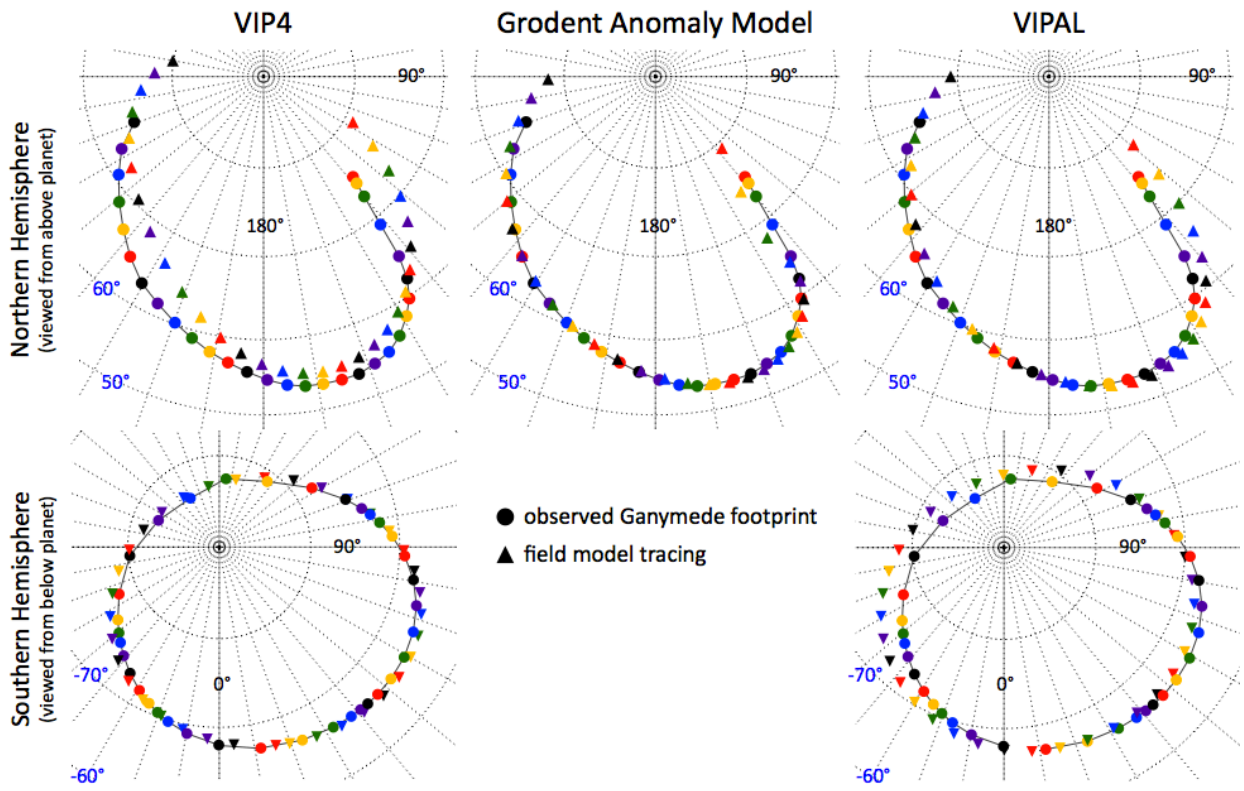

Figure 3.5 The location of the observed Ganymede footprint (circles) and the ionospheric footprint of model field lines traced from 15 R_J at the equator (triangles). To guide the eye the symbols are plotted in a repeating sequence of six colors: red, yellow, green, blue, purple, and black, rather than a continuous color bar. The observations (circles) should be compared to the closest mapped triangle of the same color, indicating that the equatorial longitude of Ganymede for a given observed footprint (circle) is the same as the initial equatorial longitude used in the field model tracing (triangle). The points are separated by 10 degrees in longitude at the equator. For most points, the mapped ionospheric footprint comes close to matching the observed footprint.

in the latitudinal direction, and is likely due to inaccuracies in the field models and not to to the propagation time delay of the Alfvén waves [*Bonfond et al.*, 2009].

Mostly recently, the VIPAL internal field model [*Hess et al.*, 2011] provided an update to the VIP4 model that included the effects of the magnetic anomaly in the kink sector and the longitudinal constraint of the Io footprint. As a result, the VIPAL model fits the observed Io,

Callisto, and Ganymede footprints with a higher accuracy than VIP4. VIPAL does not match the satellite footprint locations as well as the Grodent anomaly model does in the northern hemisphere (see Figure 3.5), but it does predict a surface magnetic field strength that better agrees with the observed radio emissions.

Even with recent improvements such as the inclusion of a magnetic anomaly, the available internal field models are still accurate only within distances of ~30 R_J in the equatorial plane because of the strong azimuthal currents that stretch field lines in the more distant magnetosphere. These currents have been incorporated into some global field models, though those models have limitations such as neglecting the effects of magnetopause currents [*Khurana*, 1997] or ignoring the 10º dipole tilt and dawn-dusk asymmetry of the equatorial magnetic field [*Alexeev and Belenkaya*, 2005]. Additionally, most models have been based on data from a limited number of spacecraft flybys. Clearly another approach is needed to obtain a mapping model valid in the middle and outer magnetosphere and with sufficient accuracy to constrain the shape and size of the polar cap or to identify the source of specific auroral features, such as the polar dawn spots.

3.4 Motivating questions

The purpose of the work described in this chapter is to answer questions regarding the link between auroral features and magnetospheric processes. We present mapping results from a flux equivalence calculation, described in section 3.5.2, with several advantages compared to tracing field lines from a model. Our method allows us to relate auroral features to their magnetospheric sources at a large range of radial distances and local times, a result that was

previously inaccessible due to the lack of field models accurate beyond ~30 R_J. In particular, we will address the following questions:

- Where, and how big, is Jupiter's polar cap?
- Where do the polar auroral features (active, dark, and swirl regions) map to in radial distance and local time in the equatorial plane?
- Do the polar dawn spots and nightside spots map to distances inside of the statistical x-line?
- Do the main oval emissions map to similar equatorial radial distances at all longitudes?
- What are the magnetospheric sources of the multiple auroral arcs? Where do they map, and what processes produce them?

The answers contribute new information about Jupiter's global magnetospheric dynamics. For example, a major hindrance to understanding the relative importance of the solar wind in dynamics at Jupiter is the fact that the polar aurora do not display clear evidence of a persistent polar cap. This ambiguity has led to considerable disagreement regarding the amount of open flux in Jupiter's magnetosphere. If Jupiter's magnetosphere is closed, as suggested by *McComas and Bagenal* [2007], then one expects Jupiter's polar cap to be small (~10º across). They propose that magnetic flux that is opened via dayside reconnection with the solar wind is closed by reconnection on the magnetopause, near the polar cusps, rather than by reconnection in the tail. However, if cusp reconnection is unable to close all of the flux opened on the day side, as *Cowley et al.* [2008] argue, and the magnetosphere is open, then Jupiter's polar cap would correspond to a more significant fraction of the area inside the main auroral oval. There are a number of additional questions that arise from this interpretation. For example, if the swirl region

is indeed associated with open field lines, why is the region is not aurorally dark in the UV? Why isn't there a persistent feature that can be identified as the polar cap? Are *Delamere and Bagenal* [2010] correct in their suggestion that the high variability in the size, shape, and brightness of the swirl region indicates that it is not on open field lines, and that there is little steady open flux?

Another way that an improved mapping model will contribute to our understanding of magnetospheric dynamics is by identifying the source regions of polar dawn and nightside spots. As discussed in Section 3.2.3.3, these spots are thought to be the ionospheric signature of inward flow associated with tail reconnection. Since the available field models are not accurate beyond ~30 R_J, an improved mapping method is needed to test the interpretation and relate the radial mapping to the location of a statistical x-line (~90-100 R_J) [*Woch et al.*, 2002; *Vogt et al.*, 2010].

3.5 Methods

Our objective is to map auroral features to their magnetospheric sources. One approach to such a mapping is to trace equatorial magnetic field lines from the magnetosphere to the ionosphere, as is frequently done in studies of the terrestrial magnetosphere. However, that method requires an accurate global Jovian magnetic field model, and field models are highly uncertain at radial distances beyond ~30 R_J. The error arises, in part, because an azimuthal current flows through the equatorial plasma and stretches field lines at all local times. Though the available global field models are accurate only in the inner to middle magnetosphere, spacecraft observations of the magnetotail are available out to ~150 R_J, and we wished to consider auroral features that may map to the outer magnetosphere. We, therefore, took a different approach in our mapping. We started our mapping at the orbit of Ganymede, where the link to the auroral ionosphere can be determined from emissions identifiably linked to the moon.

Thereafter, rather than following field lines along a field model, we mapped equatorial regions beyond Ganymede's orbit to the ionosphere by requiring that the magnetic flux threading a specified region at the equator must equal the magnetic flux in the area to which it maps in the ionosphere. Details of the procedure we used for the mapping follow.

3.5.1 Establishing the radial and local time dependence of the equatorial B_N

Measurements of the Jovian magnetic field are available at radial distances out to ~150 R_J and at nearly all local times. Previous studies [*Khurana and Kivelson*, 1993; *Kivelson and Khurana*, 2002] have quantitatively described how B_z falls with radial distance (z is aligned with the spin axis and on average is normal to the current sheet), but little has been done to model changes with local time. Such changes are especially relevant for nightside modeling of B_N, the component of the magnetic field normal to the current sheet, which is known to be larger in the dusk hemisphere than in the dawn hemisphere.

An important step in our mapping procedure is the calculation of the magnetic flux through the magnetic equator, which is a non-planar surface in which the field magnitude reaches its minimum value along every flux tube. Calculation of the equatorial magnetic flux requires an accurate estimate of the average equatorial value of B_N, accounting for changes with radial distance and local time. We developed a two-dimensional model of the equatorial B_N by fitting field measurements to a functional form that represents the dependence of the field on radial distance and local time. The data come from all spacecraft that have provided multi-day measurements of the Jovian magnetic field: Pioneer 10, Pioneer 11, Voyager 1, Voyager 2, Ulysses, and Galileo. We restricted ourselves to data within 15 degrees latitude of the jovigraphic equator, beyond 20 R_J, and with a time resolution of 24 seconds or better. To

calculate B_N, we took 15-minute running averages of B_R, B_θ, and B_Φ, interpolated the data to a time resolution of 8 seconds or better, and then, for each pass through the equatorial current sheet, we calculated the field magnitude from the three field components. Smoothing and interpolating the data in this fashion allowed us to more precisely identify B_N, defined as the minimum in the field magnitude during a current sheet crossing (within a few minutes of a B_R and B_Φ reversal).

In Figure 3.6 we have plotted the averaged B_N values so determined (left panel) and the two-dimensional fit to those measured values (right) in the equatorial plane. The figure indicates how B_N varies with radial distance and local time. This figure also shows the two most probable magnetopause locations (thick solid black lines) corresponding to a compressed and expanded magnetopause [*Joy et al.*, 2002]. The dayside magnetopause standoff distance is ~60 R_J for the compressed magnetosphere and ~90 R_J for the expanded magnetosphere. In Figure 3.7 we have plotted the B_N data (circles) and model (solid and dashed lines) as a function of radial distance for four different local time bins. The solid lines are taken for the median local time in each bin, with the dashed lines indicating how the model changes across each local time bin (i.e., for the 0200-0400 bin, the dashed lines are 0200 and 0400, and the solid line is 0300). Both Figures 3.6 and 3.7 show that the measured B_N falls roughly exponentially with radial distance, and is strongest in the noon to dusk local time sector (bottom left panel in Figure 3.7, 1400-1600 LT). The observations plotted here represent a range of solar wind and magnetospheric conditions, which could explain some of the variation in B_N at a given position in the equatorial plane. For example, one expects the field strength to increase in response to magnetospheric compression from the solar wind. Analogously, internally driven dynamics may influence the magnetospheric configuration [*Woch et al.*, 1998; *Kronberg et al.*, 2007].

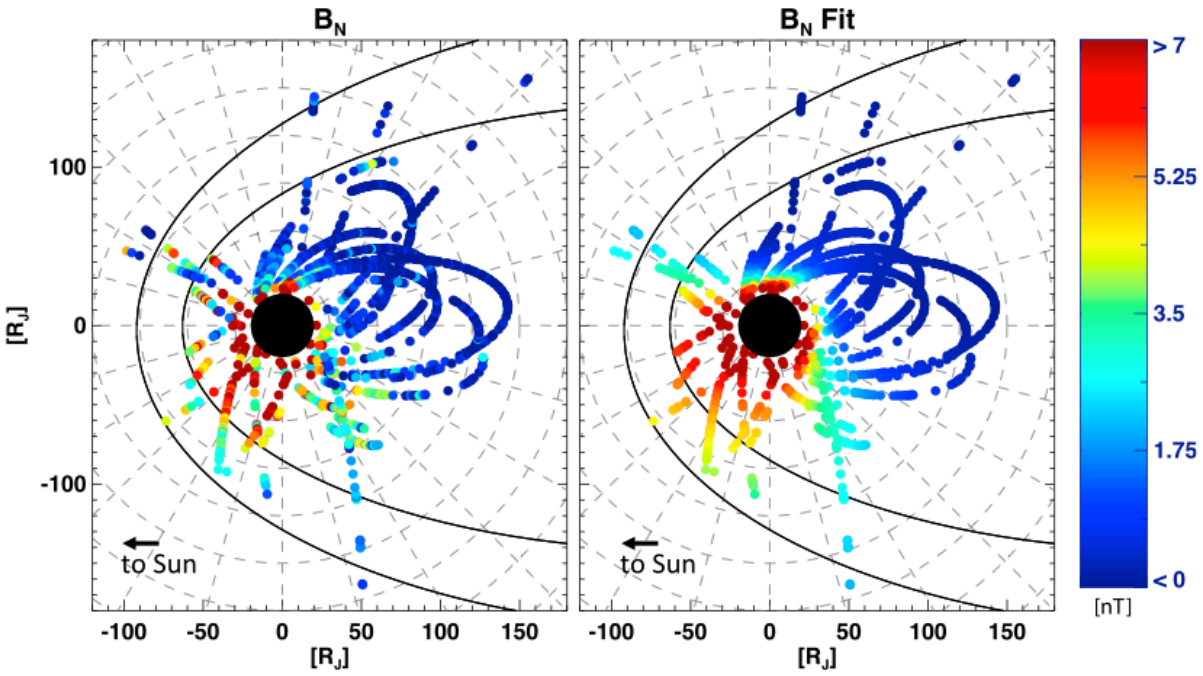

Figure 3.6: Values for B_N (left) from spacecraft measurements and equivalent values from a model fit (right) plotted vs. radial and local time in the equatorial plane. Probable magnetopause locations (one compressed, one expanded) are drawn in black [*Joy et al.*, 2002]. In both the data and the model, the field in the current sheet is strongest in the noon to dusk local time sector and weakest in the early morning.

The fit was done using a routine that computes a non-linear least squares fit to the data with a gradient-expansion algorithm. We assumed a functional form

$$B_N(R,\varphi) = A\,R^{(B+C\cos(\varphi-D))} + \left[E + F\cos(\varphi - G) + H\cos\left(2\times(\varphi - I)\right) + J\cos\left(3\times(\varphi - K)\right)\right]\times e^{-R/150} \quad (3.1)$$

where B_N is in units of nT; R is the radial distance in R_J; φ is the local time, measured from midnight, in radians; and A, B, C, D, E, F, G, H, I, J, and K are constants that are determined by the fitting routine. Their values are provided in Table 3.1. This functional form was chosen to account for field changes with radial distance and local time, and to ensure that B_N approaches

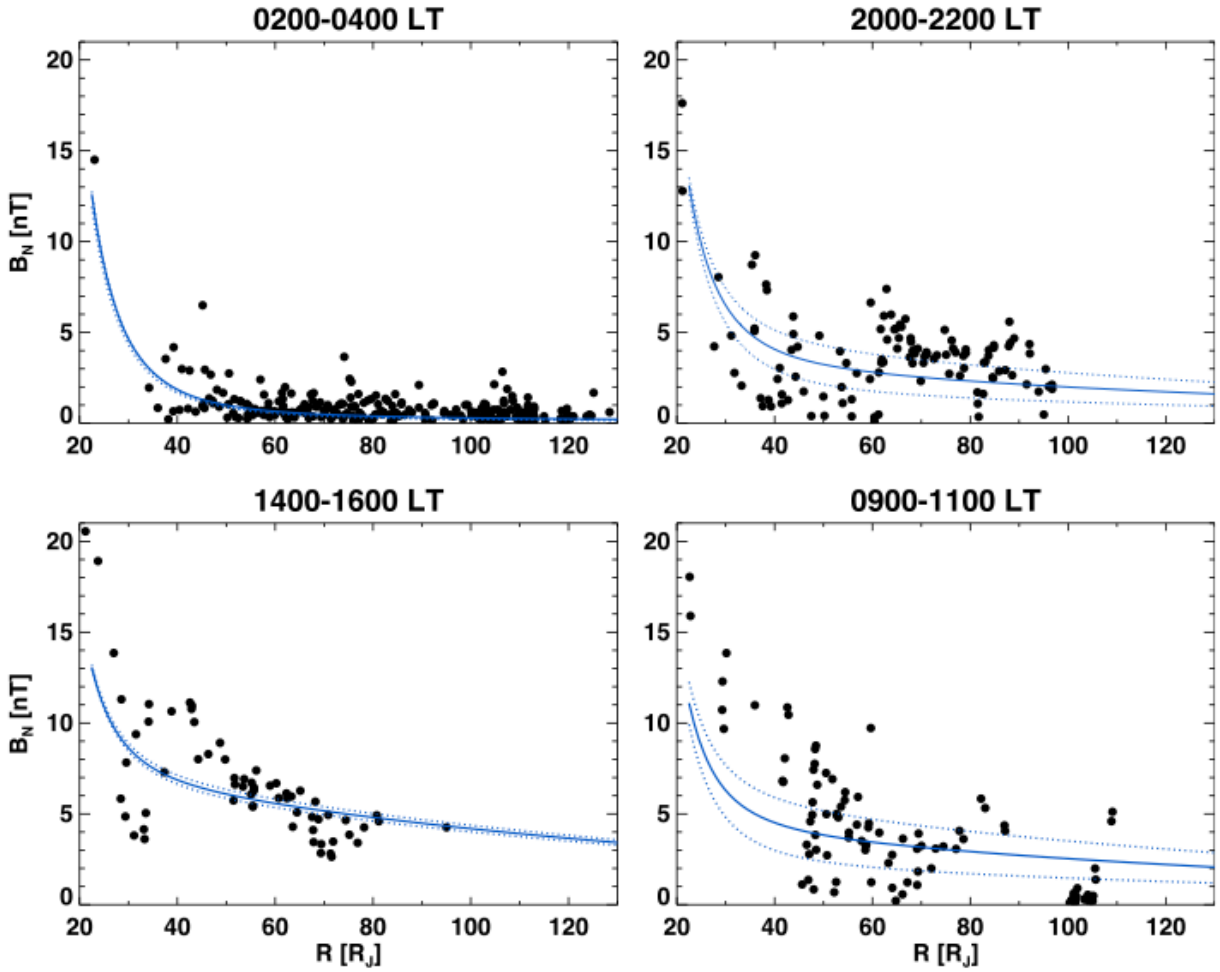

Figure 3.7: B_N data (dots) and model (solid and dashed lines) values as a function of radial distance for four local time bins. The solid lines indicating the model B_N are taken for the median local time in each bin, with the dashed lines indicating how the model changes across each local time bin (i.e., for the 0200-0400 bin, the dashed lines are 0200 and 0400, and the solid line is 0300).

zero as R approaches infinity. The fit does a good job of reproducing the local time and radial dependences seen in the data; both the observed and model field are strongest near ~15:00 LT (bottom left panel in Figure 3.7), and weakest in the post-midnight sector (top left panel in Figure 3).

Table 3.1 B_N fit parameters									
A	*B*	*C*	*D*	*E*	*F*	*G*	*H*	*I*	*J*
1.030e6	-3.756	-0.120	3.562	3.797	-4.612	0.825	0.606	0.473	0.913

3.5.2 Mapping using the flux equivalence calculation

As remarked above, rather than tracing field lines using a global field model, we have mapped from the equator to the ionosphere by means of a flux equivalence analysis. A flux equivalence analysis has been used previously to estimate currents, flows, and magnetic mapping of Jupiter's ionosphere [*Cowley and Bunce*, 2001], although they used a simplified axisymmetric magnetic field model to estimate the magnetic flux. A key contribution of our work is that we calculate the magnetic flux using a two-dimensional data-based B_N fit that accounts for local time asymmetries. This will allow us to reliably map the source(s) of dawn-dusk asymmetries in the auroral emissions. In this section we describe the calculation used to map from the equator to the ionosphere.

To begin, we identified the ionospheric footprint of an equatorial circle at 15 R_J, the orbit of Ganymede and a distance where field models are reasonably accurate, by following model magnetic field lines from the equator to the ionosphere. This step is represented in Figure 3.8 by the solid green field lines, which connect the 15 R_J equatorial curve (black circle) to the 15 R_J ionospheric reference contour (black). In the northern hemisphere, we trace field lines from the field model of *Grodent et al.* [2008b], described above in section 3.3. This field model uses a version of the VIP4 plus current sheet model [*Connerney et al.*, 1998] with modified Schmidt coefficients and the addition of a magnetic anomaly in the form of an additional dipole located

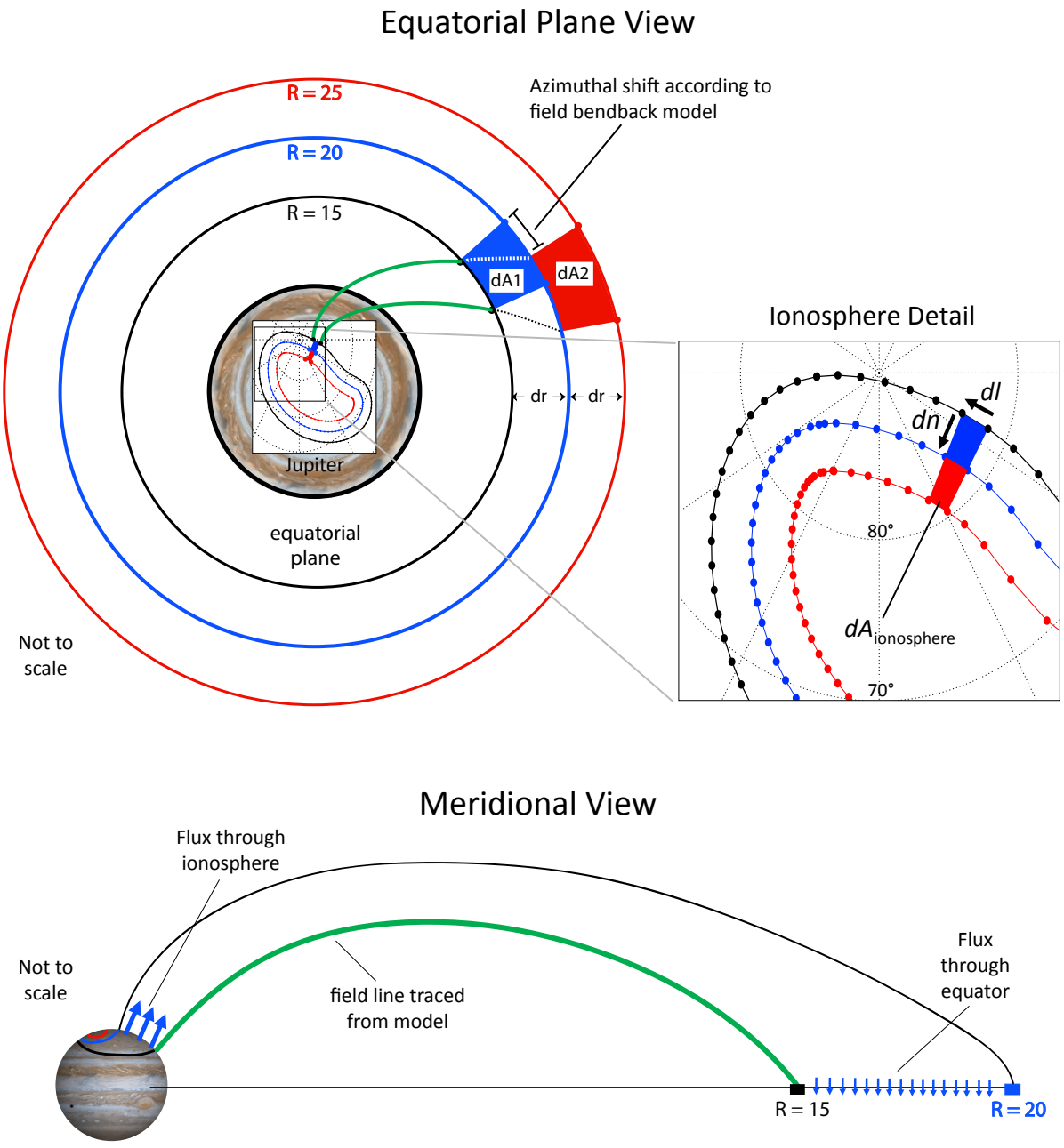

Figure 3.8: Illustration (not to scale) of the method used to map equatorial magnetic flux to the ionosphere by equating flux in the two regions. We begin by tracing along a field model from 15 R_J in the equator, where the accuracy of the field model can be tested against observations of Ganymede's auroral footprint; this step is illustrated by the green lines. Next we calculate the flux through the equator in the magnetosphere through a specified area pixel, labeled dA_I here. We then determine how far to move the ionospheric boundary poleward, by solving for dn according to equation 3.6. This gives us the mapping of a pixel linked to the 20 R_J equatorial circle (in blue); further iterations of the calculation (illustrated in red) provide the mapping of successively distant equatorial circles.

close to the surface to improve the agreement between the model and the satellite footprints in the northern hemisphere. Since the model is underconstrained, *Grodent et al.* [2008b] presented two possible solutions for the location and orientation of the perturbation dipole; we have used the one poleward of the Io footpath. For mapping to the southern hemisphere, we used the VIP4 plus current sheet model [*Connerney et al.*, 1998] with the original (unmodified) Schmidt coefficients, rather than the modified VIP4 model with magnetic anomaly, which had been constructed without regard to how the northern magnetic anomaly might affect the field in the southern hemisphere.

We have a high level of confidence in the accuracy of our 15 R_J reference contour because it matches observations of Ganymede's auroral footprint, as seen in Figure 3.5, which compares the observed footprint locations to the predictions from model field lines. For the Grodent anomaly model, the point obtained by tracing the field model falls close to the observed footprint at most longitudes. The largest errors in the northern hemisphere are at the extreme ends of the curve defined by the footprint path, and for all points but one the model (triangles) falls at larger SIII left-handed longitudes than the observed footprint locations (circles). In both hemispheres the error is mostly in the direction along the curve rather than in the latitudinal direction. However, as demonstrated by *Bonfond et al.* [2009], in the case of the Io footprint most of this longitudinal shift cannot be attributed to the propagation time delay of the Alfvén waves. They suggested that the shift was due to inaccuracies of the magnetic field models. Such inaccuracies of the internal field models essentially affect our local time mapping with an estimated average local time error of ~0.7 hours, and a maximum of ~1.6 hours, though we can be confident in the validity with which radial distance and ionospheric latitude are linked.

The next step was to calculate the equatorial magnetic flux for pixels of radial increment 5 R_J and an initial longitudinal width of 5-15 degrees. The pixels' azimuthal width was allowed to vary in order to ensure that the ionospheric pixels were relatively evenly-spaced. The schematic illustration of Figure 3.8 explains the approach used (not to scale). In the figure, a typical pixel in the equator, labeled dA_1, is drawn in blue. The flux through the equator is given by

$$d\Phi_{equator} = B_{N,equator}(R, \varphi) \cdot dA_{equator}, \tag{3.2}$$

where the normal component of the magnetic field at the equator, $B_{N,equator,}$ is a function of radial distance R and local time φ given by the fit of equation 3.1. We approximate the equatorial flux by

$$d\Phi_{equator} = B_{N,equator}(R, \varphi)\, R\, dr\, d\varphi. \tag{3.3}$$

In the mapping from 15 to 20 R_J, no shifts in local time were used. At larger radial distances, the equatorial pixels were shifted azimuthally in the equator according to a simple field bendback model. We developed this field bendback model using a simple functional form to fit measured B_R and B_ϕ values, again using the non-linear least squares fitting procedure. The data used in the fit are the same as those shown in Figure 8 of *Khurana and Schwarzl* [2005]. Our field bendback model is shown in Figure 3.9, where we have plotted the field line projections onto the equatorial plane. This field bendback model varies with both radial distance and local time and, as a result, the equatorial area pixels do not have a fixed longitudinal width. The bendback model reproduces the data well, and includes a strongly bent back field in the post-midnight sector and a bent forward field in the dusk local time sector. We have illustrated the effects of including the field bendback in Figure 3.9, where the dashed black and white lines between 15 and 20 R_J represent the field bendback in the equatorial plane and dictate how two pixels at the same local

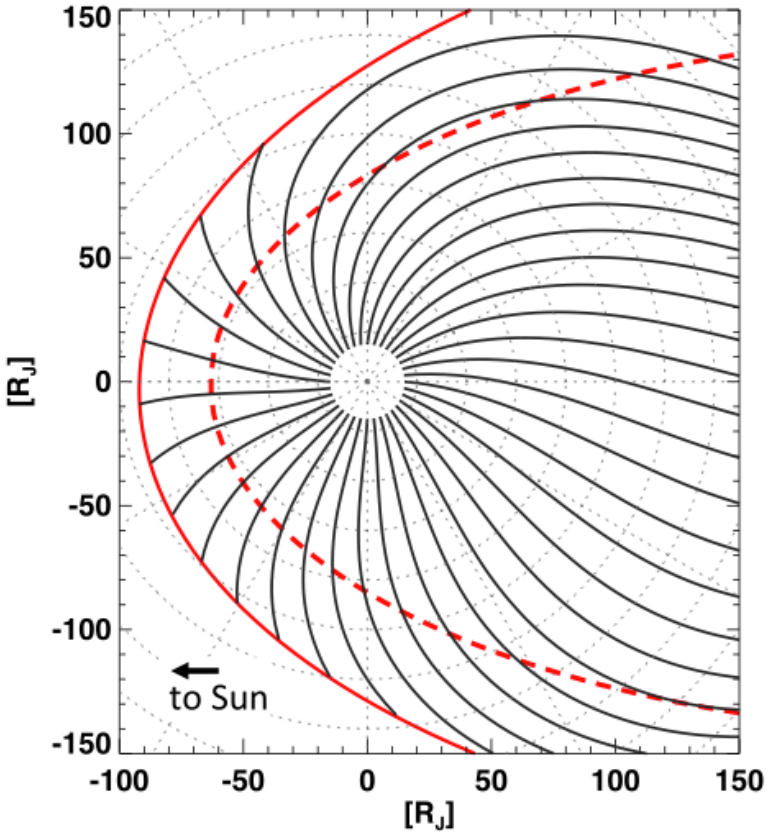

Figure 3.9: Field bendback model, projected into the equatorial plane, based on a fit to the data presented by *Khurana and Schwarzl* [2005]. Field lines are the most bent back near dawn, and are bent forward near dusk. Two probable magnetopause locations are drawn in red [*Joy et al.,* 2002].

time in the equator can be found misaligned in the ionosphere. Because the bendback changes with longitude, the azimuthal widths of area elements dA_2 and dA_1 may differ.

After evaluating the equatorial magnetic flux through a typical pixel, we matched the ionospheric flux by moving along a normal to the ionospheric reference curve. Equating the equatorial magnetic flux with the ionospheric flux determines how far poleward we should place the auroral boundary of each ionospheric pixel to obtain the ionospheric mapping of the 20 R_J circle at the equator. This poleward distance, which we call *dn* (see insert in Figure 3.8, top

panel), is determined by the flux equivalence calculation as follows: the ionospheric magnetic flux is given by

$$d\Phi_{ionosphere} = B_{R,ionosphere}(R = 0.95\ R_J,\ \theta,\ \varphi) \cdot dA_{ionosphere}, \tag{3.4}$$

where θ and φ are the colatitude and azimuthal angle in spherical coordinates, respectively. We estimate the radial component of the ionospheric field, $B_{R,\text{ionosphere}}$, using the same internal field models (different for north and south) used for mapping the 15 R_J circle to the ionosphere. The ionospheric area element, $dA_{ionosphere}$, is computed as the product of *dl*, the length in the direction along the ionospheric contour, and *dn*, the length in the poleward direction to be determined (see inset in the top panel of Figure 3.8). Following *Grodent et al.* [2008], we used a sphere of radius 0.95 R_J to approximate Jupiter's oblate surface (~0.935-0.9585 R_J) over the range of latitudes (90º to ~53º) of interest in the northern hemisphere. For consistency we also use a sphere of radius 0.95 R_J when calculating the flux through the southern hemisphere. This approximation introduces a negligible (less than one percent) error in the calculated flux at the surface, though for certain specific applications mapping to a different reference surface may be required.

We can approximate equation 3.4 as

$$d\Phi_{ionosphere} = B_{R,ionosphere}(R = 0.95\ R_J,\ \theta,\ \varphi) \cdot dn\ dl. \tag{3.5}$$

Finally, we set $d\Phi_{equator} = \mathrm{d}\Phi_{\text{ionosphere}}$, and solve for *dn*:

$$dn = \frac{B_{N,equator}(R_{equator},\varphi_{equator})\ R\ dr\ d\varphi}{B_{R,ionosphere}(R = 0.95,\theta,\varphi)\ dl}. \tag{3.6}$$

It is this final calculation that gives us the location of a portion of the ionospheric contour corresponding to the 20 R_J circle at the equator (blue curves in Figure 3.8).

Iteration of the calculation provides the ionospheric mapping of successively distant circles (illustrated in Figure 3.8 by the red curves representing the mapped 25 R_J equatorial circle). We continue the flux equivalence calculation out to a radial distance of 150 R_J, the limit

of the magnetic field data coverage in the magnetotail and the valid region of our B_N fit. However, the Jovian magnetotail is estimated to extend for thousands of R_J [*Lepping et al.*, 1983], so we have mapped only a small fraction of the magnetotail. We expect that this omission will have only a minor effect on the results because the equatorial flux will be relatively small at distances beyond 150 R_J, and give quantitative arguments to that effect in section 3.7.2.

Inspection of equation 3.6 shows that *dn* is proportional to $B_{N,\text{equator}}$, which is itself a function of radial distance and local time. The variation of $B_{N,\text{equator}}$ with local time shown in Figure 3.6 makes it evident that the ionospheric contours mapping to a constant radial distance in the equator will have the largest separation in the ionosphere in the post-noon to dusk local time sector, where $B_{N,equator}$ attains its maximum value.

3.6 Results

We have mapped the equatorial magnetospheric flux at radial distances between 20 and 150 R_J into the ionosphere. The results depend on how the ionospheric region of interest is oriented with respect to the Sun, or local noon, because the flux equivalence calculation involves B_N, which is a function of local time. The effect of the orientation is familiar from images of the aurora at different CMLs (Central Meridian Longitudes), i.e., the Jovian longitude facing the direction of the Earth. Therefore in Figures 3.10-3.12 (northern hemisphere) and 3.13-3.15 (southern hemisphere) we present mapping results for four different viewing orientations, with local noon at 0º, 90º, 180º, and 270º SIII left-handed longitude. In these figures we have plotted the contours corresponding to constant radial distances, every 10 R_J from 20 R_J to 150 R_J. The outermost black dashed line is the 15 R_J reference contour, matching Ganymede's auroral footprint, obtained by tracing a field model as outlined in section 3.5.2.

In Figures 3.10, 3.11, 3.13, and 3.14 we use color to represent the equatorial radial distance to which different portions of the auroral contours map, ranging from 20 (black) to 150 (red) R_J. In Figures 3.12 and 3.15 we use color to represent the equatorial local time to which different portions of the auroral contours map. The field lines to the left generally map to the morning and pre-dawn sector, while field lines to the right generally map to the dusk sector. The contours of constant radial distance (10 R_J equatorial separation) have the largest separation on the right (~dusk) side because of the local time asymmetry in the equatorial B_N, which is strongest in the afternoon sector (see Figure 3.6). As a result, the area of open flux is shifted toward the predawn to dawn side (left/upper left).

We terminate the contours where the field lines map to the *Joy et al.* [2002] magnetopause (~60 R_J at noon and ~85 R_J at dawn/dusk for the compressed case, and ~90 R_J at noon and ~130 R_J at dawn/dusk for the expanded case). The white or empty area interior to the colored contours maps beyond 150 R_J on the night side and beyond the magnetopause on the day side; we interpret these areas as open flux, and will justify this interpretation in section 3.7.2. The magnetopause lies closer to the planet for the compressed case than for the expanded case, and, therefore, the area of open flux is larger for the compressed magnetopause (Figures 3.11, 3.14) than for the expanded magnetopause (Figures 3.10, 3.13).

When comparing the areas of open flux between the compressed and the expanded cases, it is important to note that we use the same flux equivalence calculation method and model B_N field strength in both cases. The assumption that B_N is not affected by displacement of the magnetopause is undoubtedly an oversimplification, as one would expect that the field strength would increase in response to a magnetospheric compression from the solar wind. For example, *Hanlon et al.* [2004] found that an interplanetary shock observed by Cassini during its approach

to Jupiter produced a ~3 nT increase in the magnitude of B_Z (from an average magnitude of ~2 to 5 nT) as recorded by Galileo, inside the Jovian magnetosphere at ~60-80 R_J and ~20:00 LT. However, our model B_N is itself an average of values relevant to all possible magnetopause locations, so it is not possible to correct consistently for changes of the size of the magnetosphere. As discussed in Section 3.5.2, and as is evident from equation 3.6, the separation of the ionospheric contours, *dn*, is proportional to B_N. This means that if we underestimate $B_{N,}$ for the compressed case, then we also underestimate *dn*, and overestimate the area of open field lines; equivalently, we probably underestimate the area of open flux for the expanded case. As a consequence, the configurations we considered here can be seen as the extreme cases.

Changes in the viewing orientation influence the mapping results, as can be clearly seen in the difference between subsolar longitude 0º and subsolar longitude 180º in the northern hemisphere. For both orientations the ionospheric contours of constant radial distance are farthest apart near noon local time, where the equatorial field strength is the strongest, and are closest together at nightside local times, where the equatorial field strength is weakest. However, for subsolar longitude 0º the spacing between contours on the day side is at least twice as large as for subsolar longitude 180º. Similarly, the nightside contours are much closer together for subsolar longitude 0º than for subsolar longitude 180º. This occurs because the ionospheric B_R is not uniform, as can be seen in Figure 3.16. For subsolar longitude 180º the ionospheric field in the region mapping near noon is at least 15 Gauss, while for subsolar longitude 0º the ionospheric field in the region mapping near noon is ~7 Gauss. Because *dn* is inversely proportional to B_R, the weak ionospheric field for subsolar longitude 0º means that the ionospheric contours near the day side will be farther apart for subsolar longitude 0º than for subsolar longitude 180º.

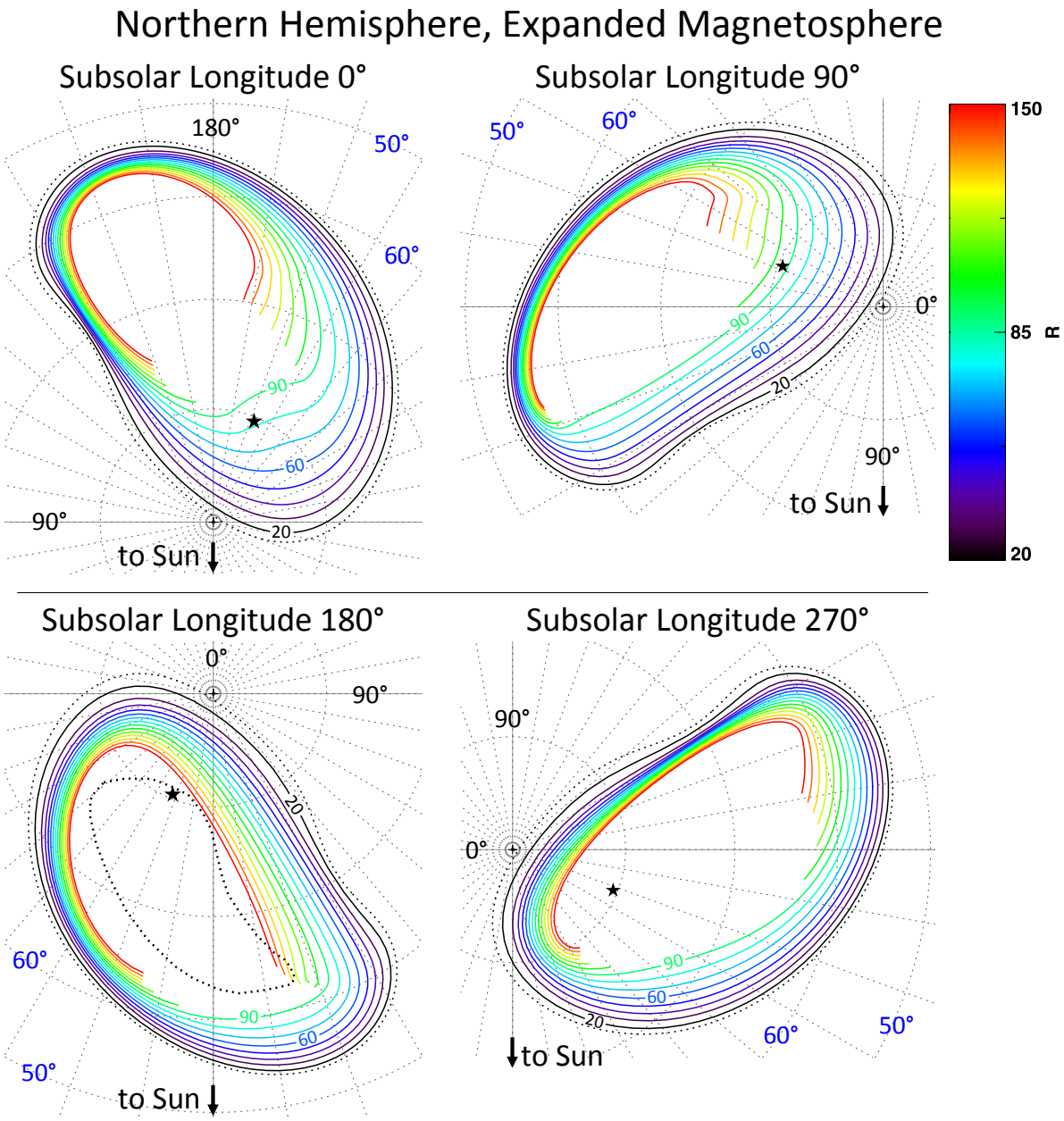

Figure 3.10: Northern polar view of the flux mapping results for the expanded magnetosphere (dayside magnetopause standoff distance ~90 R_J), for four different viewing orientations. Local noon is indicated by arrows and is in the same direction for all four panels, dawn is to the left, and dusk is to the right. Contours are colored to indicate the equatorial radial distances to which they map, ranging from 20 R_J (solid black) to 150 R_J (red) in 10 R_J increments. The outer dashed black line is the 15 R_J reference contour, which matches the Ganymede footprint. In all four panels the contours are closer together on the left/upper left side, which maps roughly to the post-midnight to dawn local time sector, than on the right side, which maps roughly to the noon to dusk sector. This is expected because the equatorial B_N, and thus the magnetic flux through the equator, is strongest in the post-noon to dusk local time sector. Black stars indicate the location of the magnetic pole, at 9.6º latitude and 212º SIII longitude. All four panels are plotted on the same scale.

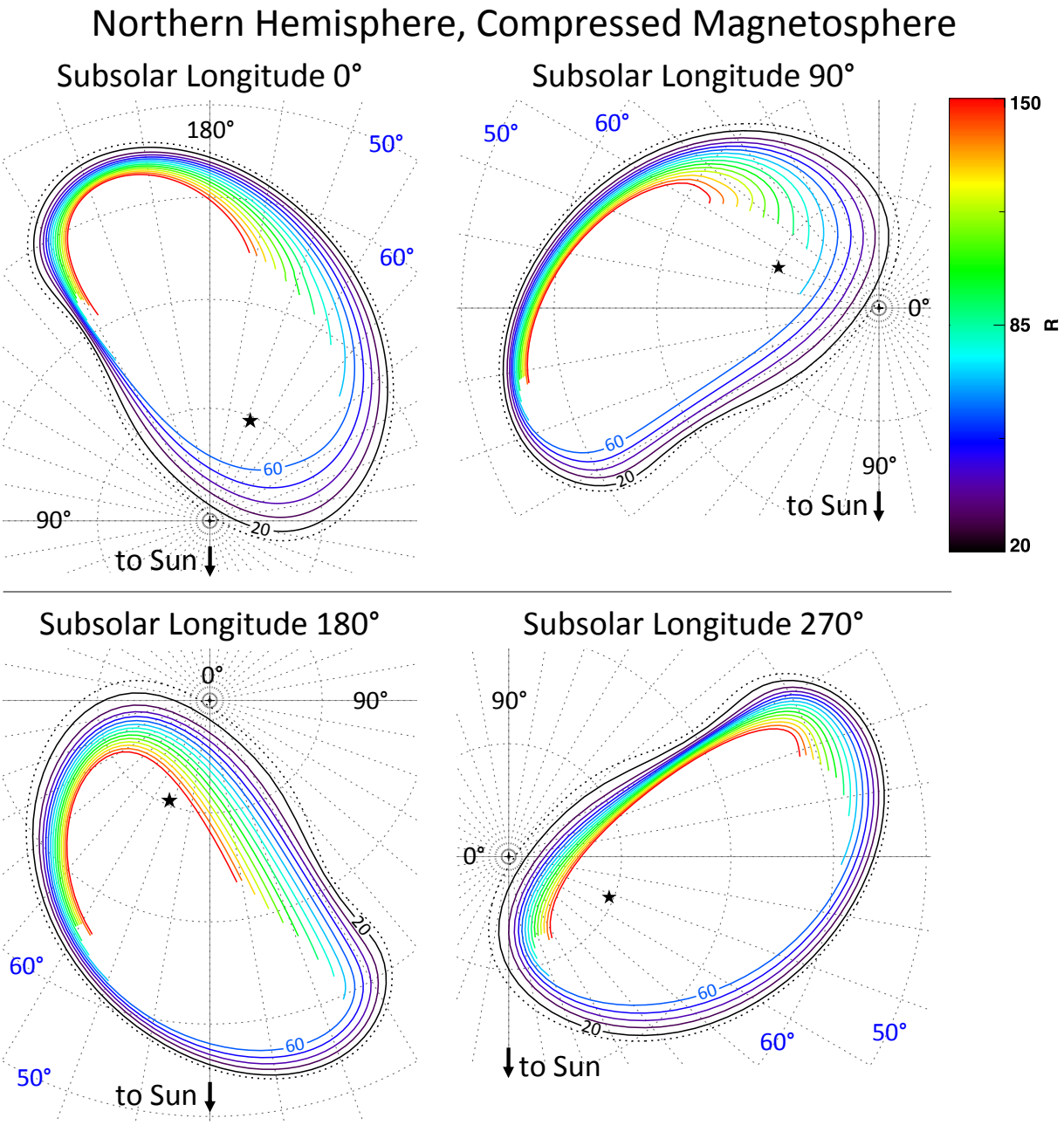

Figure 3.11: As in Figure 3.10, but for a compressed magnetosphere (dayside magnetopause standoff distance ~60 R_J). The area of open flux, or the white area interior to the colored contours, is larger for the compressed magnetopause case than for the expanded magnetopause.

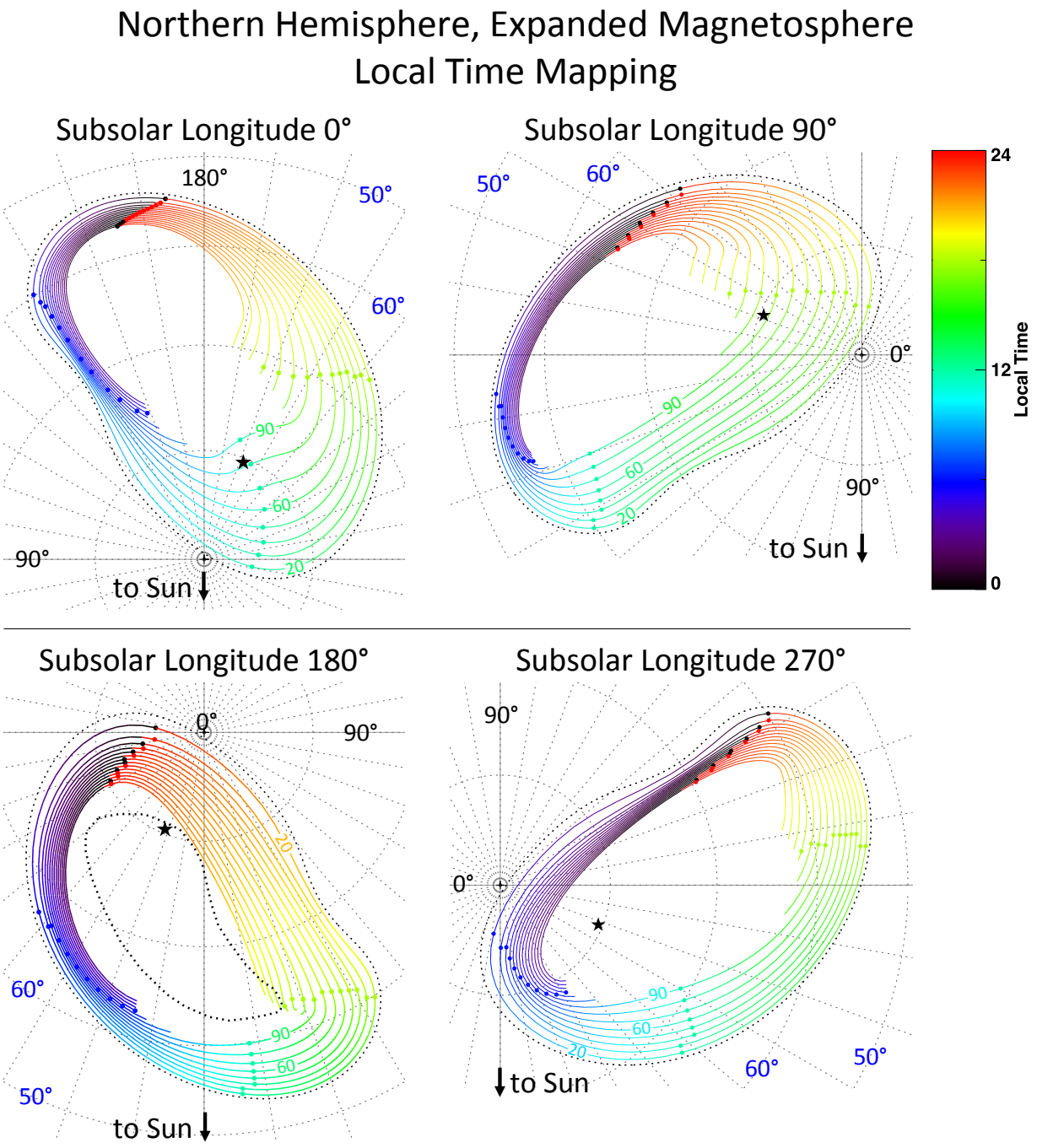

Figure 3.12: As in Figure 3.10, but the colors now indicate the equatorial local time mapping along the contour. The region on the left/upper left side where the contours are closest together maps to the post-midnight to dawn local time sector (black to blue), where the equatorial B_N is weakest. Small colored circles indicate the point closest to local midnight (red or black circles), dawn (dark blue), noon (blue-green), and dusk (light green/yellow).

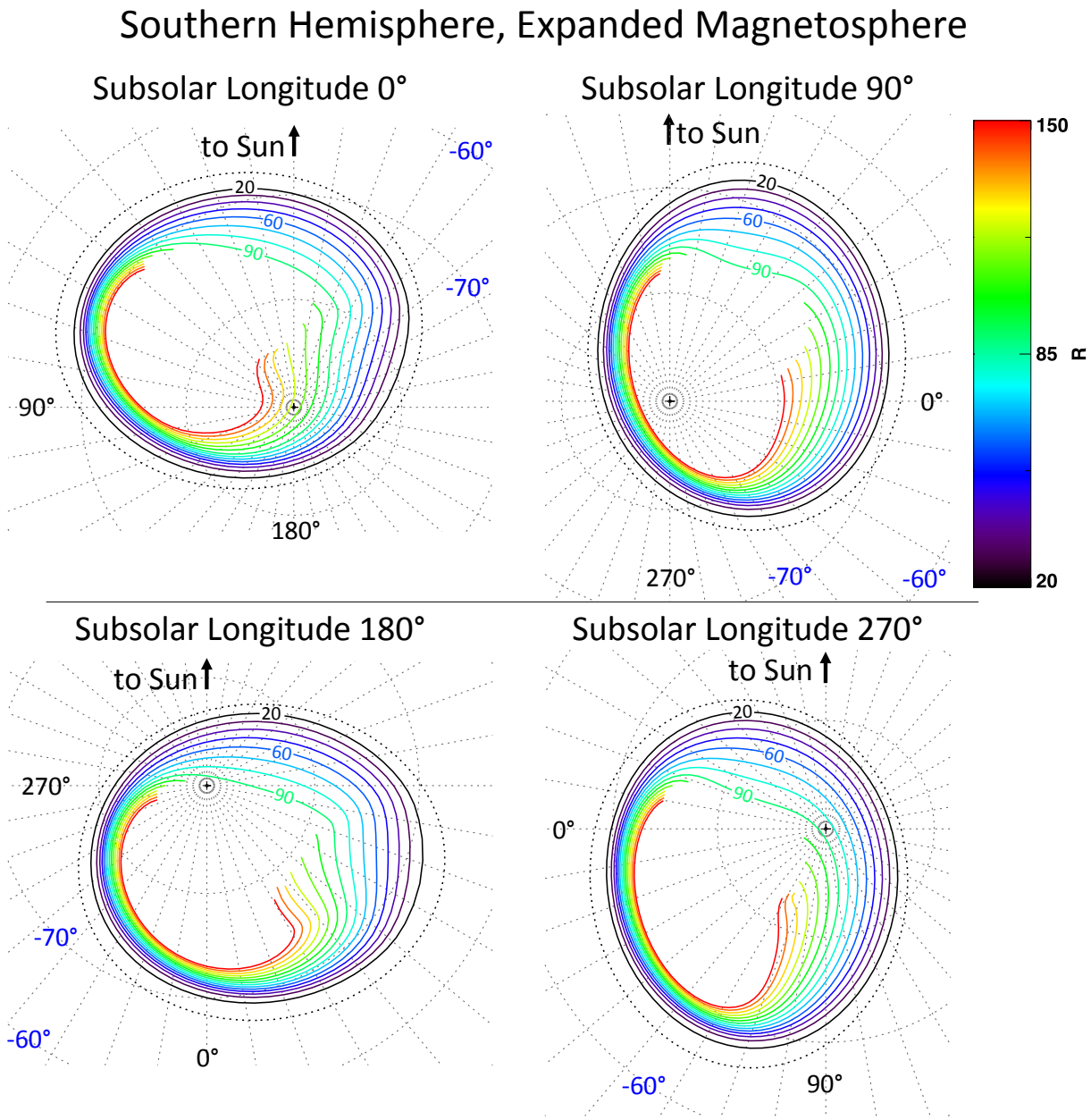

Figure 3.13: As in Figure 3.10, but for the southern hemisphere, as seen by an observer looking up at the planet. The Sun's direction is now toward the top of the page, dawn is to the left, and dusk is to the right.

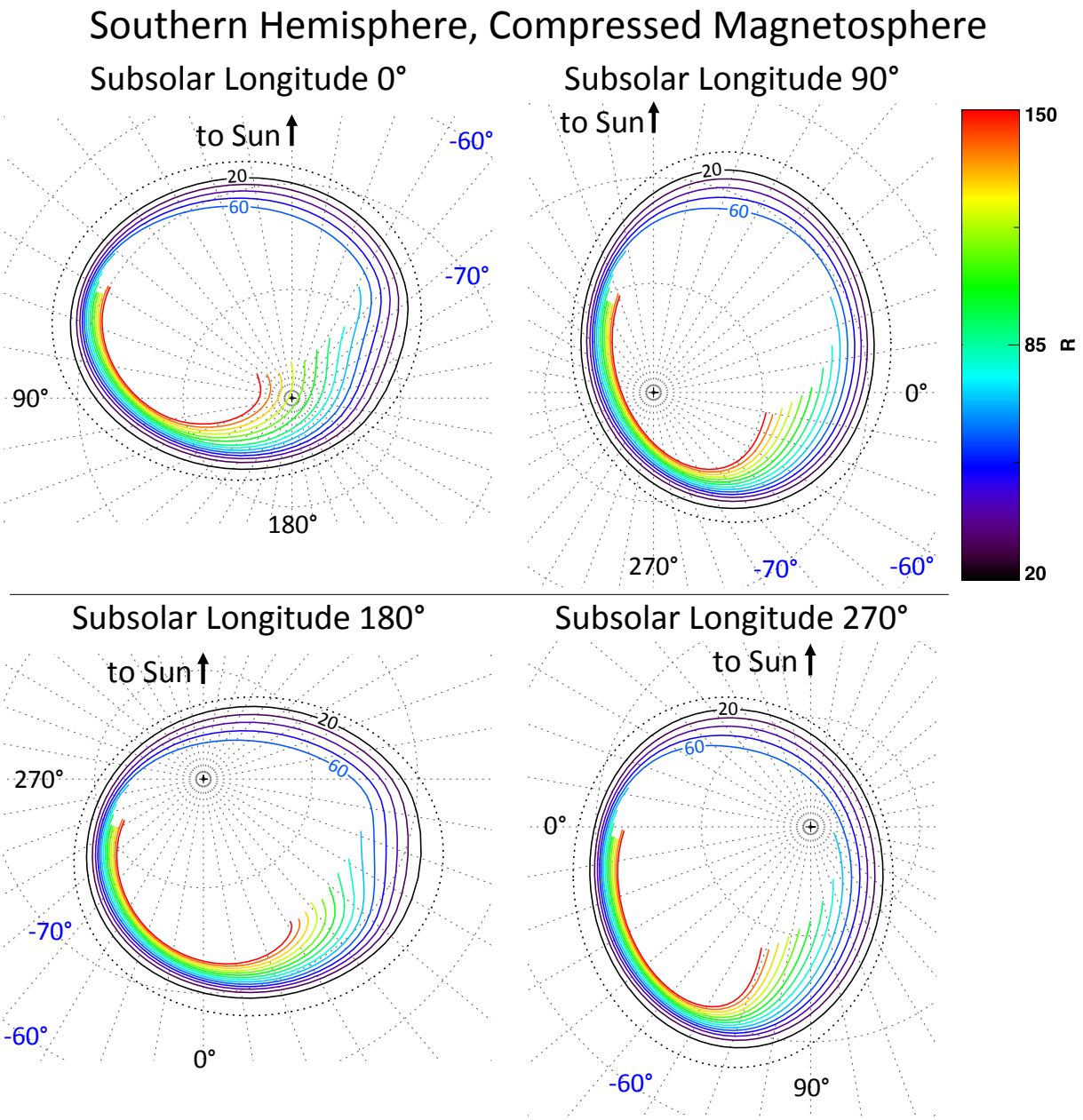

Figure 3.14: As in Figure 11, but for the southern hemisphere.

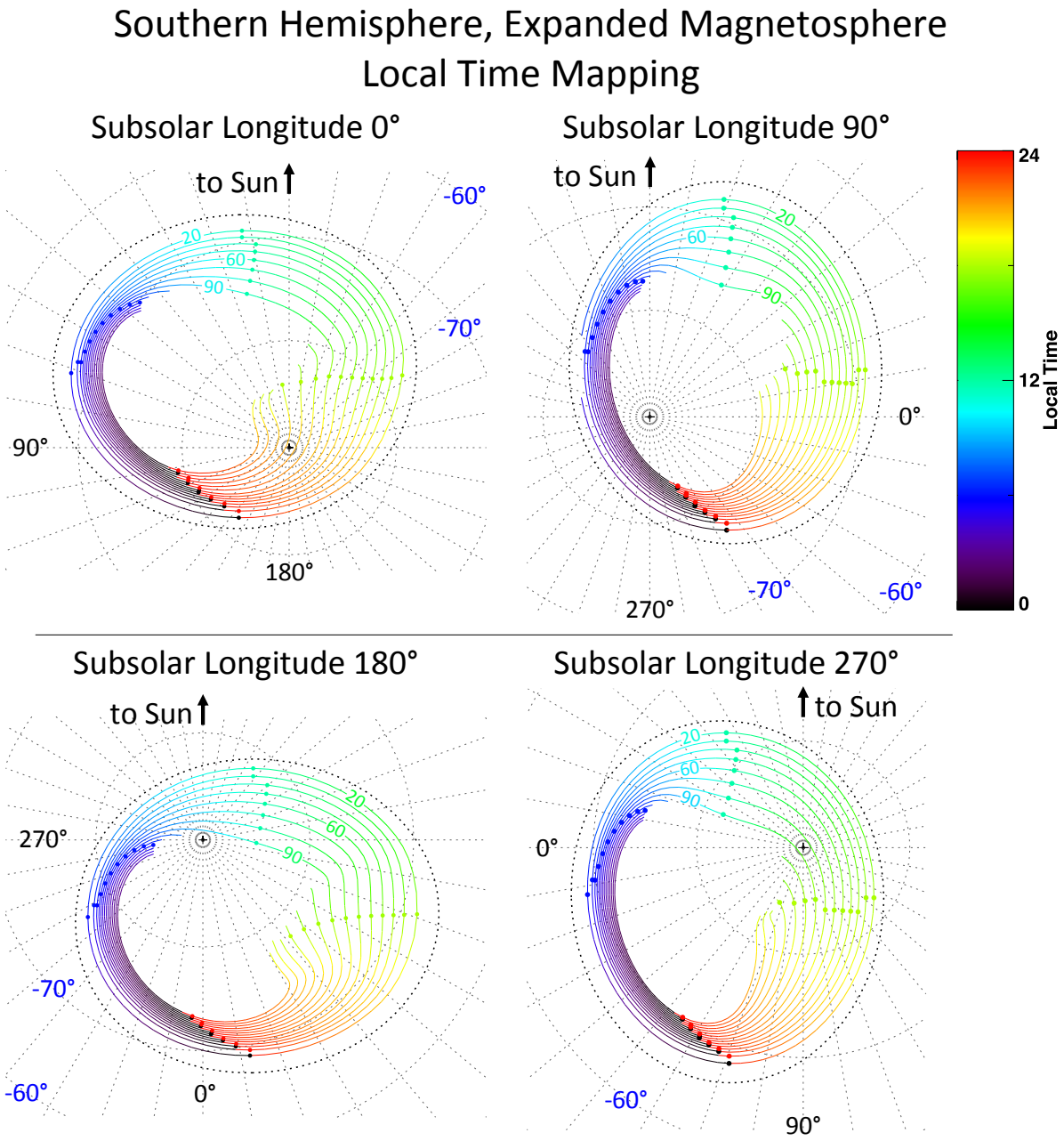

Figure 3.15: As in Figure 3.12, but for the southern hemisphere.

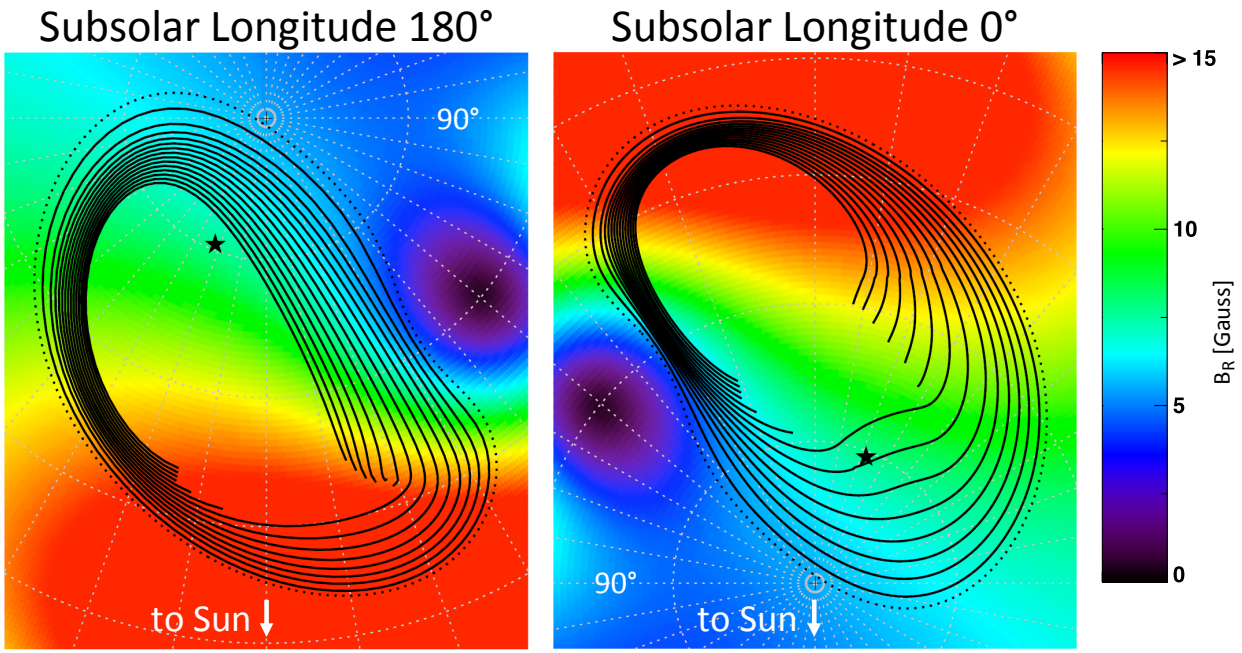

Figure 3.16: Ionospheric B_R strength in the northern hemisphere, with mapping contours overplotted in black. The magnetic field is given by the Grodent anomaly model described in Section 3.3. The direction of the Sun is indicated by the white arrows. For subsolar longitude 180º, the ionospheric field is strongest in the region that maps near local noon, where the equatorial field strength is also strongest. Half a Jovian rotation later, at subsolar longitude 0º, the ionospheric field is weakest in the region that maps near local noon. As a result, the ionospheric contours mapping near noon are farther apart for subsolar longitude 0º than for subsolar longitude 180º.

3.7 Analysis

With models of the link between different magnetospheric regions and their magnetic footprints in the ionosphere established, it is of interest to compare the results to UV and IR auroral observations. The comparison can be used to describe the size and location of Jupiter's polar cap.

3.7.1 Comparison to auroral observations

Auroral emissions in the UV provide a direct signature of magnetospheric particle precipitation [*Prangé et al.*, 2001], and the UV observations typically have a much higher spatial resolution than in the IR, as discussed in section 3.2.2. Therefore, in this section we focus our discussion on UV auroral emissions and only briefly discuss a comparison with the ionospheric flow patterns and resulting open/closed flux boundary inferred from IR auroral observations.

As discussed in Section 3.2.3.3, the UV polar auroral emissions can be categorized by their brightness, morphology, and temporal variability into three regions: the active, dark, and swirl regions. The shapes, sizes, and locations of the three polar regions vary with solar wind conditions and as the planet rotates; the mapping also varies (see Figures 3.10-15). Therefore, in this section we will compare the mapped contours to UV auroral observations at two different CMLs, or the Jovian longitude in the direction toward the Earth. We will restrict the discussion to auroral observations in the northern hemisphere, for which more observations are available than for the southern hemisphere as a consequence of the viewing geometry [*Grodent et al.*, 2003b].

In Figures 3.17 and 3.18 we present in panels A through C our mapping results for two different viewing orientations – CMLs 160º and 220º SIII left-handed longitude, respectively – and in panel D, the corresponding UV auroral observations [modified from Figure 5 in *Grodent et al.*, 2003b]. Panel A in these figures shows mapping results for an expanded magnetopause, and the contours colored to indicate the equatorial radial distance to which they map; panel B shows the same mapping results but the colors indicate the equatorial local time mapping. Panel C follows the same format as panel A but presents mapping results for a compressed magnetopause. The Sun direction is indicated by black arrows.

To facilitate comparison with the UV and IR auroral observations, we have added contours relating the auroral observations to our mapping results. *Grodent et al.* [2003b] drew contours delineating the active (green), dark (yellow), and swirl (red) regions in the polar aurora, as shown in panel D of Figures 3.17 and 3.18. (These regions are also discussed in Section 3.2.3.3.) In panels A-C we have overplotted the contours of Grodent et al. as thick curves at the same jovicentric coordinates to outline the three polar auroral regions (substituting black for yellow to outline the dark region). The inner dashed black contour in panels A-C in Figure 3.17 is the jovicentric location of the fixed dark polar region (f-DPR) from the IR auroral observations of *Stallard et al.* [2003]. Because of the stagnant flow within this region, it is believed to contain open field lines. The f-DPR location was derived from observations taken at CMLs of ~160º to ~180º and should only be compared to mappings representing similar CMLs [T. Stallard, personal communication, 2010]. Therefore, we have not included it in Figure 3.18 (CML 220º).

Figure 3.17 shows mapping results and auroral observations for CML 160º. In this orientation the Sun direction is oriented to the bottom of the page and slightly to the right, as indicated by a black arrow. The auroral active region maps to field lines just outside the dayside magnetopause, plausibly open field lines in the polar cusp. The swirl region maps to tail field lines at distances larger than 150 R_J, plausibly open field lines; the *Stallard et al.* [2003] f-DPR lies within that region. The dark region maps to both open and closed field lines near dawn local time, and the degree to which it is on open field lines changes greatly between the compressed and uncompressed expanded cases. We will comment on this further in Section 3.8. In panel E, the composite of auroral observations and mapping results show that the main oval radial mapping changes with local time/longitude. The main oval maps to ~15-30 R_J near dawn, ~30-50 R_J near noon, and 50-60 R_J at ~15:00 LT.

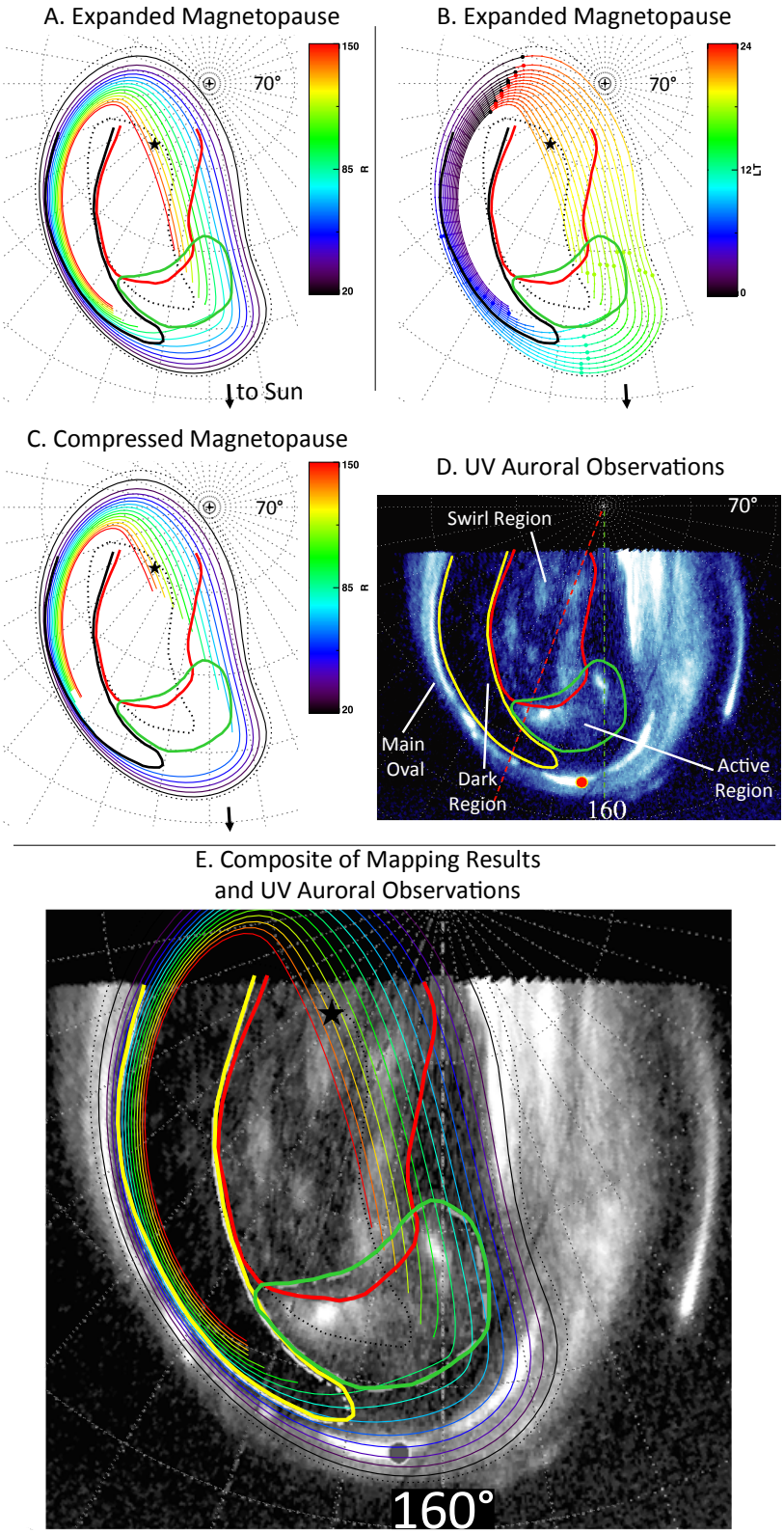

Figure 3.17: Mapping results compared to auroral observations. A: Mapping results for the expanded magnetopause locations of *Joy et al.* [2002]. The color of each contour indicates the radial distance, ranging from 20 R_J (black) to 150 R_J (red). The interior dashed black line

indicates the location of the *Stallard et al.* [2003] dark polar region. B: As for A, but for the compressed magnetosphere. C: Contours for the expanded magnetopause color coded by the local time of the equatorial field line crossing. D. UV auroral observations modified from Figure 5 in *Grodent et al.* [2003b]. E: A composite of the UV observations from panel D and the mapping results of panel A. The figures are presented with 160º SIII longitude directly to the bottom of the page, and the direction of the Sun toward the bottom of the page and slightly to the left as indicated by arrows. The latitude and longitude grid separation is 10º. The boundaries of the three polar auroral regions are drawn in at the same jovicentric coordinates in all panels. The active region maps to just beyond the dayside magnetopause boundary, the swirl region maps to field lines outside of 150 R_J, and the dark region maps to both open and closed field lines. The main oval maps to ~15-30 R_J near dawn, ~30-50 R_J near noon, and 50-60 R_J at ~15:00 LT.

Figure 3.18 shows mapping results and auroral observations for CML 220º. In this orientation the Sun is toward the lower right, and one can see that the auroral emissions have rotated with the planet. Now the dusk local time sector maps roughly to the upper right, while dawn local time maps roughly to the lower left (see panel B). As in Figure 3.17, the boundaries of the auroral polar regions have been marked by the thick green (active region), black (dark region), and red (swirl region) lines.

By comparing the UV observations for the two CMLs we can see that the shapes and relative sizes of the polar regions shift as the planet rotates from CML 160º to CML 220º. For example, the active region (outlined in green) has become elongated in longitude and shifted equatorward. Our mapping contours have also shifted in Figure 3.18 compared to the their position and configuration shown in Figure 3.17. As a result, we find that the polar auroral regions map to generally the same magnetospheric region(s) for CML 220º as they did for CML 160º. The active region still maps to field lines just beyond the (compressed) dayside magnetopause boundary, though it maps to a wider range of local times – from slightly post-dawn through dusk – than in Figure 3.17. The swirl region again maps to field lines on distances beyond 150 R_J. The dark region now maps almost entirely to field lines outside the dayside

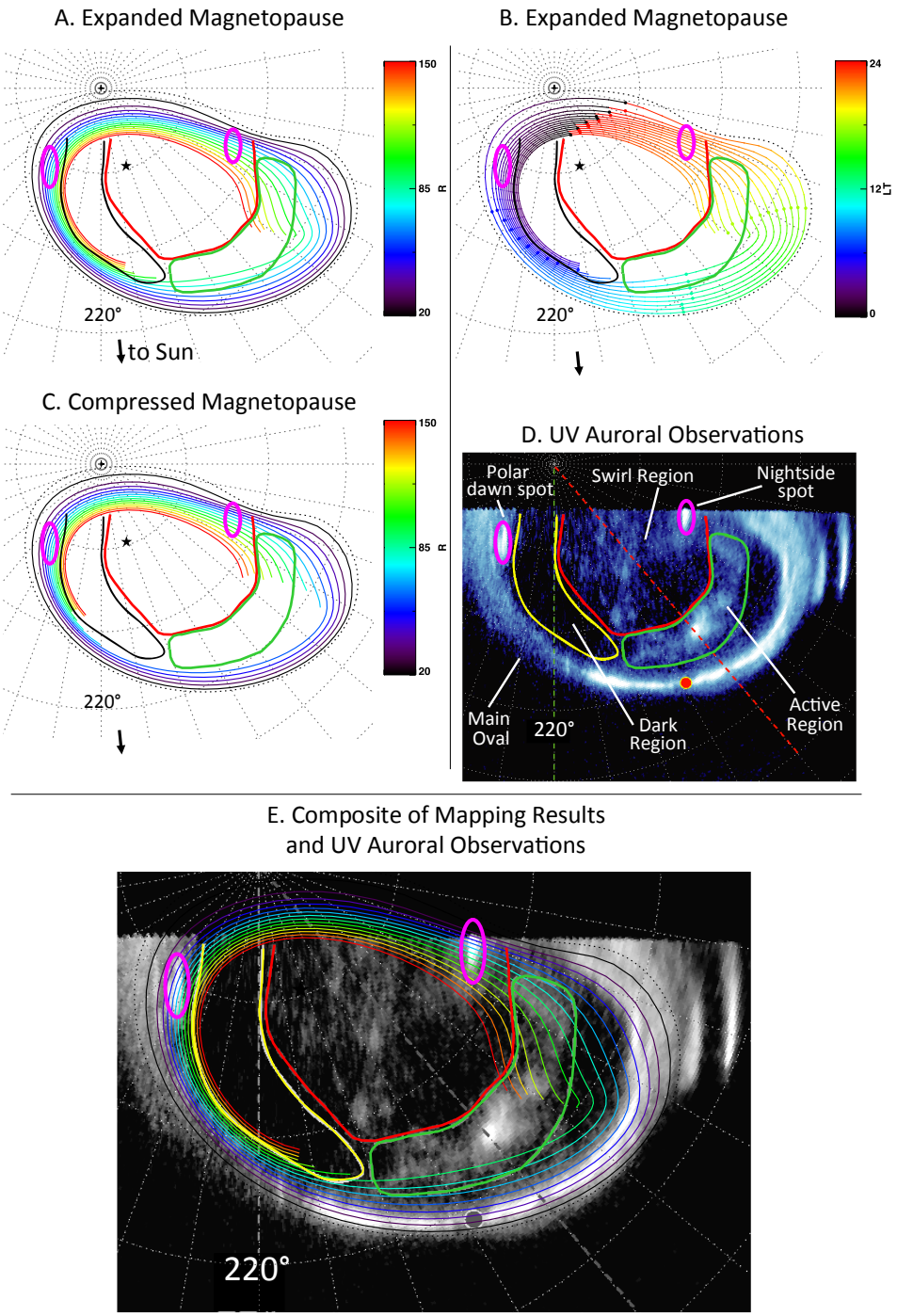

Figure 3.18: As in Figure 3.17, but for CML 220º. The active region continues to map just beyond the dayside magnetopause, and the swirl region maps to tail field lines outside of 150 R_J. The dark region now maps almost entirely to field lines beyond 150 R_J in the pre-dawn local time sector. The main oval maps to ~20-30 R_J near dawn, ~30-50 R_J pre-noon, and 50-60 R_J post-noon. Also shown are a polar dawn spot and a nightside spot, which map to distances inside of a statistical x-line, consistent with the interpretation that these spots are the auroral signature of inward flow released during tail reconnection.

magnetopause or beyond 150 R_J for both the compressed and expanded cases, whereas for CML 160º a portion of the dark region mapped to field lines within the dayside magnetopause or inside of 150 R_J. Whereas the dark region mapped to post-midnight to pre-noon local times for CML 160º, it now maps roughly to the midnight to dawn local time sector. The main oval mapping again varies with local time, from ~20-30 R_J near dawn, to ~30-50 R_J pre-noon, and ~50-60 R_J post-noon.

The auroral observations for CML 220º include two spots, one in the dawn sector and one nightside spot, that are thought to be the signature of magnetic reconnection in the tail [*Grodent et al.*, 2004]. The spot locations from panels C and D are indicated in the other three panels of Figure 3.18 by magenta ovals. However, because the spots are so close to the limb their locations in the polar projection are subject to error because of stretching due to limb fitting. Taking this error into account, we find that the polar dawn spot maps to ~50-80 R_J and ~0200-0400 LT, and the nightside spot maps to ~50-90 R_J and ~2100-2400 LT. That both spots map to equatorial regions planetward of the statistical x-line supports the association with inward moving flow released during tail reconnection, as has been shown in *Radioti et al.* [2010] for the polar dawn spots and recently in *Radioti et al.* [2011] for the nightside spots.

On the basis of the above comparison with auroral observations we interpret the polar auroral active region as forming Jupiter's polar cusp, and the swirl region as Jupiter's polar cap. It is also clear that there are several ways in which to explain the absence of emissions in the dark region. Where the dark region maps to open field lines the relative lack of auroral emissions can be explained by an exceptionally low plasma density. On closed field lines coupled to the dark region, one potential explanation for the relative lack of auroral emissions is the presence of downward (into the ionosphere) closure currents, analogous to the terrestrial black aurora that are

also associated with downward field-aligned currents on closed field lines [e.g., *Marklund*, 2009]. Our interpretation is in line with the previous discussion of *Cowley et al.* [2003], who suggested that aurorally dark regions at Jupiter might be associated with either open field lines or downward (into the ionosphere) currents on depleted flux tubes as part of the Vasyliunas-cycle return flow. In Figure 3.19 we present a schematic illustration of the relationship between polar auroral features and their magnetospheric sources. The figure shows both closed (dark blue) and open (light blue) field lines emerging from the dark region, on either side of the open/closed flux boundary (dashed pink line). An open field line is also shown emerging from the swirl region, which we have interpreted as the polar cap. The active region is labeled as the polar cusp.

Our flux equivalence calculation assumes an equatorial field value B_N averaged over all solar wind and magnetospheric conditions, even though we have analyzed our results for boundaries at locations consistent with high and low solar wind dynamic pressure. Our results, therefore, are not fully consistent with any specific solar wind condition. Nonetheless, in this section we have drawn comparisons to the polar auroral observations taken at a specific moment in time, under a specific set of solar wind conditions, and we cannot expect our model to represent the actual boundaries for those conditions. We expect that the shapes and locations of the three polar regions will change in time. This error is not expected to greatly affect our interpretation of the active and swirl regions, though we are less confident in our dark region mapping and interpretation because for one CML the dark region maps partially inside 150 R_J, but for the other CML it maps almost entirely beyond 150 R_J.

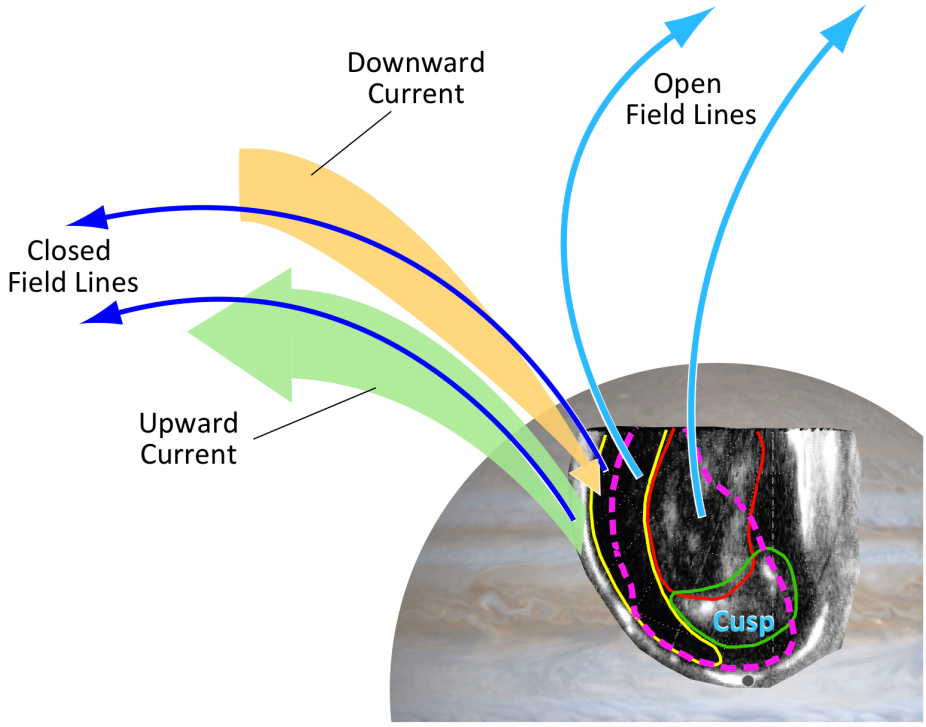

Figure 3.19: Schematic (not to scale) illustrating the mapping of Jupiter's polar auroral regions, which are outlined with colored contours as in Figure 3.17, to their magnetospheric sources. The open/closed flux boundary is shown as a dashed pink line. We interpret the active region as the Jovian polar cusp, the swirl region is interpreted as the open field lines of the polar cap, and the dark region maps to both open and closed field lines. Poleward of the open/closed flux boundary, open field lines (light blue) exit the ionosphere from both the dark and swirl regions and are pulled back toward the night side. A second field line, equatorward of the open/closed flux boundary, is shown emerging from the dark region. The light green arrow shows the upward (out of the ionosphere) field-aligned current associated with the main oval emissions, which are also on closed field lines. The orange arrow shows the closure or downward (into the ionosphere) field-aligned current, which could explain the relative lack of auroral emissions on closed field lines in the dark region.

3.7.2 Size and location of Jupiter's polar cap

In the previous section, we identified the polar auroral swirl region as the Jovian polar cap because it maps to lobe field lines beyond 150 R_J that we believe to be open, in part because this region is characterized by extremely low density plasma, < 10^{-5}/cm^3 [*Gurnett et al.* 1980]. In this section we will assume that most of the region beyond 150 R_J in the tail and outside the

dayside magnetopause are open and discuss in more detail the size and shape of the polar cap, to which the open flux maps in both the northern and southern hemispheres. We will also compare the flux through the polar cap to the estimated lobe flux based on spacecraft measurements in the magnetotail.

Results of the flux equivalence calculation show that the region of open flux is skewed toward the dawn side. In both hemispheres the extent of the open region is roughly 40 degrees in longitude and 20 degrees in latitude, though the shape and size change with viewing angle (see panels A-D in Figures 3.10-15) and with the assumed magnetopause standoff distance (compare the compressed magnetopause mappings in Figures 3.17 and 3.18 to those for the expanded magnetopause).

The flux equivalence calculation was performed only out to R=150 R_J, the limit of data availability and the valid region of the B_N fit; however, the Jovian magnetotail is known to extend far beyond this distance. Estimates of the Jovian tail length range from ~900 R_J, based on Cassini data [*Krupp et al.*, 2004] to ~9000 R_J based on Voyager 2 data [*Lepping et al.*, 1983]. More recently, New Horizons found that Jupiter's magnetotail possesses a coherent structure until at least ~1600 R_J [*McNutt et al.*, 2007]; the spacecraft's trajectory took it into the magnetosheath beyond this distance. By assuming that field lines that cross the equator beyond 150 R_J are open, we have undoubtedly overestimated the region of open flux in the ionosphere.

We can correct for this overestimate and account for the magnetic flux that closes through the tail by assuming a radial dependence for B_N and integrating the function from 150 to 9000 R_J. *Kivelson and Khurana* [2002] found that B_z, which on average is normal to the current sheet and can be considered equivalent to B_N, is given by:

$$B_z(R) = 4.32 \times 10^4 \; R^{-2.44} \tag{7}$$

where B_z is in nT and R is in Jovian radii. The magnetic flux closing through the equator in the magnetotail is therefore given by

$$\Phi_{equator} = \int_{R=150}^{R=9000} B_z(R)\, R\, d\varphi\, dR = \int_{R=150}^{R=9000} 4.32\times10^4\, R^{-1.44}\, d\varphi\, dR. \quad (8)$$

where we have carried out the integration to the greatest proposed tail length in order not to underestimate the amount of closed flux in the tail. Inclusion of the additional flux from 150 to 9000 R_J shrinks the size of the polar cap by only ~a few degrees of latitude, as we show by the red shaded region in Figure 3.20. The shape and boundaries of the red shaded region should not be taken literally; they are provided merely as illustrative examples such that the area of the red shaded region matches the ionospheric flux to the additional closed equatorial flux between 150 and 9000 R_J. We then identify the light and dark green shaded regions in Figure 3.20 as the polar cap. Its area is equivalent to that of a circle around the pole with an ~11º latitudinal width – only slightly smaller than the ~15º latitudinal width of the polar cap at the Earth.

If the polar cap is accurately identified, the open flux linked to that region in the ionosphere should equal the tail lobe flux. We calculate that the open flux through the region we have identified as the polar cap in the northern ionosphere is ~1.41 × 10^5 nT R_J^2 (~720 GWb); this number assumes that the area of open flux is associated with a compressed magnetopause and excludes the area that maps to radial distances from 150 to 9000 R_J (the red shaded region in Figure 3.20). We calculated the open flux by summing $B_R\, dA$ over the open region (light and dark green shaded regions in Figure 3.20), in bins of one degree of longitude by one degree of latitude. As discussed in section 3.6 above, the area of open flux is larger for the compressed magnetopause (green shaded regions in Figure 3.20) than for the expanded magnetopause (only the light green shaded region), so our estimate is on the high end of the range of expected values. A similar calculation for the southern hemisphere finds that the amount of open flux through the

southern hemisphere is ~1.49 × 10^5 nT R_J^2 (~762 GWb). The calculated values closely match the amount of open lobe flux in the magnetotail: magnetometer data show that B_R ~ 7 nT at R = 80 R_J, where the magnetotail width varies from 115 R_J (compressed) to 165 R_J (expanded) [*Joy et al.*, 2002]. Assuming a compressed magnetosphere with a width of 115 R_J, the lobe flux, $\int B \cdot dA$, is 7 nT × π × (115 R_J)^2 × ½ = 1.45 × 10^5 nT R_J^2 (~741 GWb), very close to the amount of open flux through both the northern and southern ionosphere.

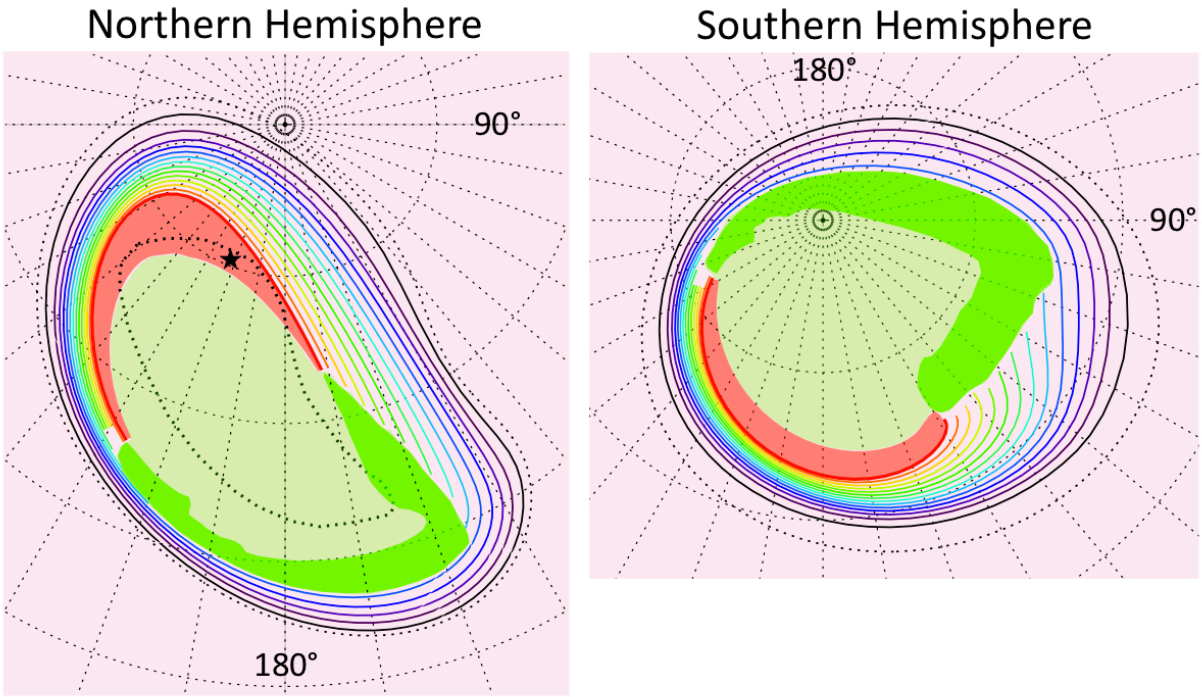

Figure 3.20: Summary of mapping results between the aurora and its magnetospheric sources for subsolar longitude 180º. The area mapping to closed field lines is shaded pink, and the region of closed flux accounted for by integrating B_z from 150 to 9000 R_J is shaded in red. The green shaded areas indicate the area mapping to beyond 150 R_J or beyond the magnetopause, which we have interpreted as open flux. The dark green area maps to the region between the two preferred magnetopause locations (~60-90 R_J at noon) and may be on open or closed field lines depending on which magnetopause location one assumes. Color scheme and presentation adapted from *Bagenal* [2007], Figure 10.

3.8 Discussion

In section 3.6 we presented the flux equivalence calculation results, and in section 3.7 we compared the mapping to the auroral observations. We found that the polar auroral swirl region can be interpreted as the Jovian polar cap, and the polar auroral active region can be interpreted as linked to the Jovian polar cusp. In this section we address the previous assumption that most of the empty area interior to our contours maps to open flux. We also address the main oval mapping as a function of local time and the mapping of the cushion region. The section concludes by reviewing some applications of our mapping results.

3.8.1 What can we learn about global dynamics by mapping auroral features?

Auroral observations can provide clues to the extent of the solar wind interaction with Jupiter's dayside magnetopause. For example, polar flares in the active region could be the signature of magnetic reconnection on a magnetopause Dungey cycle x-line [*Grodent et al.*, 2003b] or the signature of a magnetospheric disturbance due to a sharp increase in the solar wind dynamic pressure [*Waite et al.*, 2001]. However, we have mapped the active region to an area beyond the dayside magnetopause, so it appears that only the most equatorward polar flares could map to the magnetopause.

In our analysis, we interpreted empty areas (those mapping beyond the magnetopause or beyond 150 R_J on the night side, roughly in the same location as the UV swirl region and the IR f-DPR) as being on open field lines. As quantified in section 3.7.2, this is an oversimplification because the magnetotail extends beyond 150 R_J; however, the amount of flux from 150 to 9000 R_J is relatively small so we feel justified in approximating the open/closed flux boundary by the 150 R_J contour on the night side, and by the magnetopause boundary on the day side. The empty

areas may still not map to open field lines, however, if one assumes that Jupiter's magnetosphere is closed, following the arguments of *McComas and Bagenal* [2007]. They suggest that magnetic flux opened via dayside reconnection with the solar wind is closed on the magnetopause, near the polar cusps. As a result, Jupiter's polar cap would be expected to be small – only ~10º across, rather than the ~40º longitude by ~20º latitude we have suggested (see Figure 17) – and we feel that it is unlikely that the polar cap would be so small. *Cowley et al.* [2008] point out that it is difficult for cusp reconnection to close all of the flux opened on the day side. We do not find evidence to support the claim of *Delamere and Bagenal* [2010], who similarly propose that Jupiter's magnetosphere is closed, that the f-DPR maps to the cushion region and region of viscous interaction between the solar wind and the magnetospheric flanks. Additionally, we have shown the flux through the empty area in both the northern and southern hemispheres very closely matches the open magnetic flux contained in the magnetotail lobes, further suggesting that this empty area in the ionosphere maps to open field lines. If we are correct, the question then becomes what processes produce the swirl region auroral emissions.

3.8.2 Main oval mapping with local time

The main oval emissions are associated with corotation enforcement currents and are not expected to map to a constant radial distance [*Grodent et al.,* 2003a]. Indeed, our analysis shows that the main oval mapping varies with local time. Near dawn, the main emissions map to ~20-30 R_J, while near dusk they map farther out, ~50-60 R_J. These results suggest that either the radial location of the corotation enforcement currents varies with local time, or the plasma outflow rate differs among local time sectors, or both. In a recent study of nine years of HST data, *Grodent et al.* [2008a] found that the main oval location has shifted over time by as much as 3º in latitude.

They proposed that the latitudinal shift could be explained by variations in the current sheet density or thickness and not just by a response to changing solar wind conditions. Similarly, we suggest that the main oval variation with local time seen here could be explained by a local time dependence on these current sheet properties or the plasma outflow rate.

3.8.3 Cushion region mapping

Thus far we have concentrated on mapping auroral features to their magnetospheric sources, though it is also of interest to consider how certain magnetospheric features, such as the cushion region, map into the ionosphere. The cushion region is located in the post-dawn to noon local time sector, at ~40-60 R_J when the magnetopause is compressed and ~70-90 R_J when the magnetopause is expanded. It has been suggested through theoretical arguments that the cushion region may be associated with the polar auroral dark region [*Kivelson and Southwood*, 2005]. However, our results show that the cushion region does not map to the auroral dark region but instead to the area just poleward of the main oval and just equatorward of the active region. Figure 3.21 shows a polar mapping for subsolar longitude with the cushion region mapping shaded in gray. For this mapping we have assumed a compressed magnetosphere, such that the cushion region is located at a radial distance of 40-60 R_J, and have amended the B_N model to more accurately match the measured cushion region field values. The B_N model represents a fit to data from all solar wind conditions, including magnetospheric expansions when the cushion region is located farther out, at 70-90 R_J. Therefore, we amended our B_N model by approximating the field in the cushion region as 8 nT, typical of the larger field values in the 40-60 R_J region (see Figure 3.6). The yellow shaded region indicates the area of additional closed flux calculated by using this more realistic cushion region field value, with the assumption that the cushion

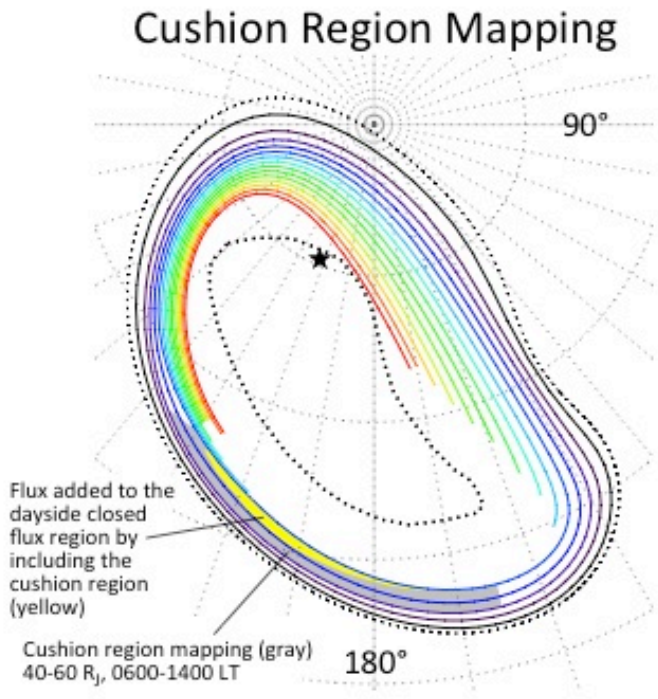

Figure 3.21: Cushion region mapping for subsolar longitude 180º, highlighted in gray. This figure assumes a compressed magnetosphere, such that the cushion region is located at 40-60 R_J and 0600-1400 LT. The yellow shaded region indicates the area of additional closed flux calculated by using a more realistic cushion region field value in the magnetosphere rather than an averaged value (see text).

region extends from 40 to 60 R_J at local times 0600-1400. The figure shows that the cushion region does not map to a large enough area to account for the polar dark region. We have accounted for possible underestimates in the field model and find that the correction does not significant affect our results.

3.8.4 Applications: Identifying the source regions of polar flares and spots

Our mapping model can be applied to matters of interest in Jovian dynamics by comparing the mapping of magnetospheric reconfiguration events [*Kronberg et al.*, 2005] and an associated x-line [*Woch et al.*, 2002; *Vogt et al.*, 2010] to observed auroral polar dawn spots

[*Radioti et al.*, 2008b]. For example, the auroral observations shown in Figure 3.18 include two spots, one in the dawn sector and one nightside spot, that are thought to be the signature of magnetic reconnection in the tail [*Grodent et al.*, 2004]. The spots are located very close to the limb, making their polar projection highly subject to error because of stretching due to limb fitting. However, even taking this error into account, both spots appear to map to equatorial regions well inside of the statistical x-line [*Woch et al.*, 2002; *Vogt et al.*, 2010]: the polar dawn spot maps to ~50-80 R_J and ~0200-0400 LT, and the nightside spot maps to ~50-90 R_J and ~2100-2400 LT. That both spots map to distances inside of the statistical x-line supports the spots' association with inward moving flow released during tail reconnection [*Radioti et al.*, 2010].

In a recent study, *Radioti et al.* [2011] used our mapping model to identify the source region of UV and IR auroral spots that were observed at nearly the same time as a reconnection signature in the Galileo magnetometer data [*Vogt et al.* 2010]. Again, all spots mapped to distances inside of the statistical x-line, and the nightside UV spot mapped close to the position of Galileo at ~56 R_J and ~21.6 LT. Additionally, the emitted power derived from the flow bubble in the magnetic field measurements closely matches the emitted power of the nightside spot seen with HST. It is interesting to note that in both the observations shown in Figure 3.18 and the Radioti et al. study, the nightside reconnection spots were accompanied by polar dawn spots. Could this mean that reconnection at Jupiter typically occurs simultaneously at multiple points across the tail? Without multi-point spacecraft measurements, and with only small statistics from which to draw inferences from the auroral data (spots at any local time appear infrequently in the auroral images), it is impossible to say. Further observations of these auroral features are needed

to help answer this question and provide further insight into Jupiter's global magnetospheric dynamics.

Another recent use of our model was to determine the source region of quasi-periodic polar flares that have been observed inside the main oval [*Bonfond et al.*, 2011]. These pulsating emissions were observed in the southern hemisphere during two HST observation orbits and display a typical 2-3 minute recurrence period. *Bonfond et al.* [2011] used the flux equivalence mapping model to map the polar location of the flares to source regions in the magnetosphere. They found that, for both sets of observations, the flares map to the dayside magnetopause, in one case near 11:00 LT, and in the other case near ~16:00 LT. Figure 3.22 shows an example of the flares and their mapped location in the equatorial plane. Based on the mapped location near the dayside magnetopause and the 2-3 minute recurrence period, *Bonfond et al.* [2011] suggested that the periodic flares could be the signature of flux transfer events due to pulsed reconnection with the solar wind. FTEs at Jupiter have been observed to have a ~1-4 minute recurrence time [*Walker and Russell*, 1985], similar to the periodicity of the auroral flares.

In order to facilitate use of our model, we have created a website that allows a user to magnetically map a point in Jupiter's ionosphere to the magnetosphere, and vice versa. This online mapping tool is available online at http://www.igpp.ucla.edu/people/mvogt/mapping/

3.9 Future Work

In the previous section we outlined some potential uses for our mapping model in future studies of auroral observations. An additional task that is more directly related to our model and could be done in the future is to use other available internal field models (VIP4, VIPAL) to estimate B_R in the flux equivalence calculation, and compare with the results presented here. In

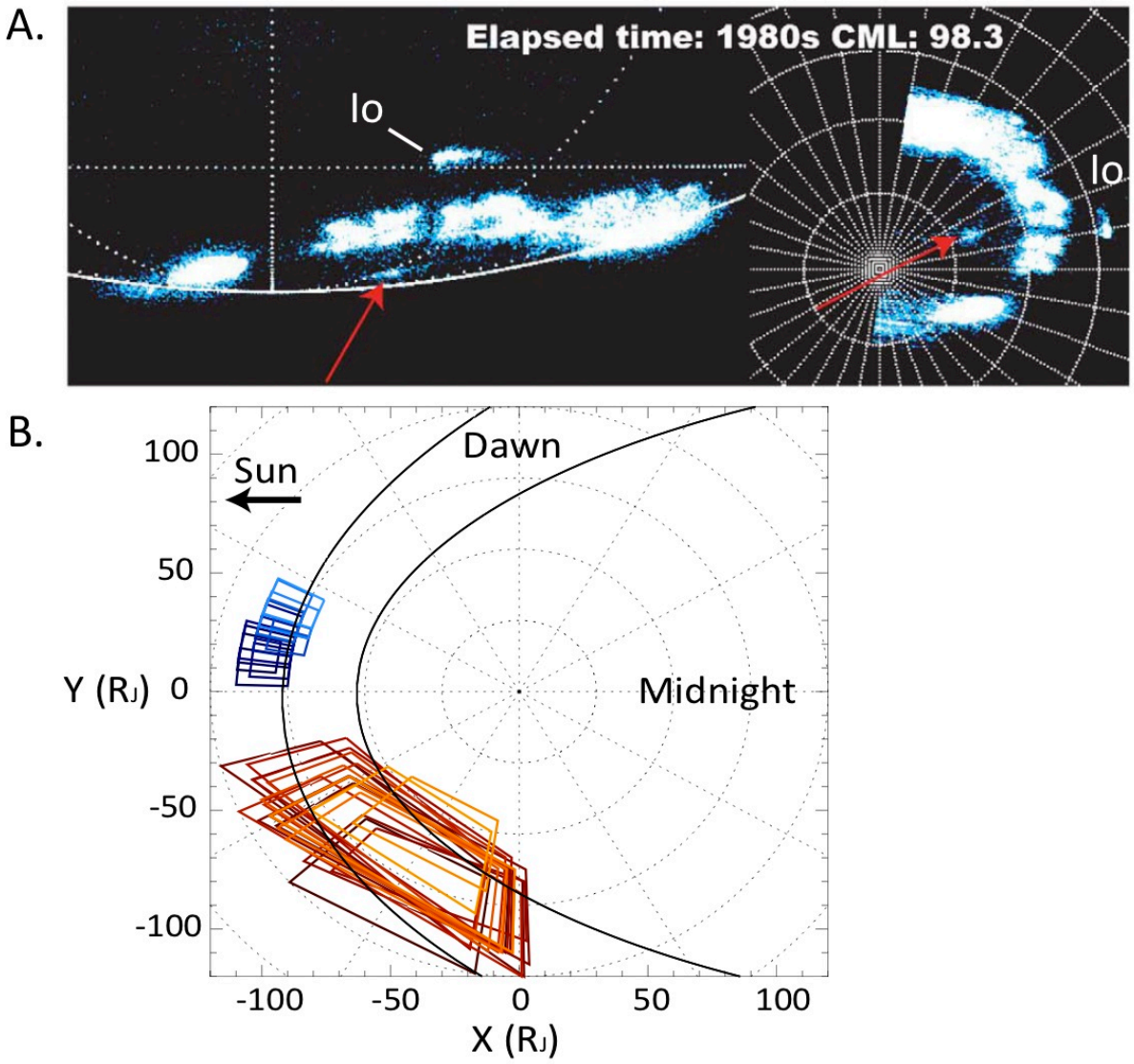

Figure 3.22 (a) HST observations of a flare in Jupiter's southern UV aurora. The right hand side of the image is a polar projection. These flares display a 2-3 minute recurrence period. (b) The mapped location of the flares in the equatorial plane. The thick black lines show the two preferred locations of Jupiter's magnetosphere [*Joy et al.*, 2002], and the two sets of boxes represent two different dates of observations. The size of the boxes reflects the positioning uncertainty of the flares because they are located close to the limb. Figures from *Bonfond et al.* [2011].

particular, it is of interest to examine any differences in the resulting polar cap size and location or the amount of open flux. Those differences will help us understand quantitatively how errors

in the internal field models affect our mapping results. Additionally, since each internal field model has its own advantages and limitations, one model may be preferred over the others for certain applications or mappings.

Finally, we note that even with a novel approach such as the flux equivalence calculation we have performed here, we are still limited by the accuracy of the available internal field models. In our flux calculation, we assumed an initial ionospheric contour mapping to 15 R_J based on the available internal field models. The field model used faithfully maps Ganymede's ionospheric footprint to an equatorial distance of 15 R_J, but even at this distance the local time mapping is subject to an error of up to ~1.6 hours. Therefore another potential extension of the work presented here is to compare our results to a mapping obtained by simply following a field model from the equator to the ionosphere. Such a comparison would help us understand the limitations of the current Jovian field models and could facilitate the development of an improved model.

3.10 Summary

The work in this chapter provides a reliable mapping between Jovian polar auroral features and their magnetospheric sources and establishes the size and location of Jupiter's polar cap and polar cusp. We have used a flux equivalence calculation based on the requirement that the magnetic flux through an area in the ionosphere equals the flux through the equatorial region to which it maps. This approach is preferred to tracing model field lines because the available magnetic field models are inaccurate at distances beyond ~30 R_J.

Calculating the magnetic flux through the equator required a model for B_N, the component of the magnetic field normal to the current sheet. We developed a model, based on a

fit to the available spacecraft data that accounts for changes with radial distance and local time. The local time dependence was of particular importance for accurately mapping local time asymmetries in the auroral emissions.

We mapped equatorial field lines from 15 R_J, where auroral data have provided improved field models that can accurately reproduce the location of Ganymede's auroral footprint, out to 150 R_J in the tail, the farthest limit of available spacecraft observations. However, this distance represents only a small fraction of the Jovian magnetotail, which is known to extend as far as ~9000 R_J. The additional equatorial flux between 150 and 9000 R_J was found to shrink the size of the polar cap by only ~a few degrees of latitude and does not greatly affect our conclusions relating to the need for an extended region of open flux in the polar cap.

Our mapping reproduces several key auroral features. The region of open flux is shifted toward dawn because the equatorial B_N (normal to the current sheet) is strongest in the afternoon local time sector. We find that the main oval mapping varies with local time, moving outward from ~15-30 R_J near dawn to ~50-60 R_J post-noon. The polar auroral active region maps to just outside the dayside magnetopause, a region that we identify as the Jovian polar cusp. The polar auroral swirl region maps to open tail field lines and is interpreted as the Jovian polar cap. These interpretations are consistent with some earlier predictions based on auroral observations (see section 3.2.3). The dark region mapping remains ambiguous, as it appears to be partly on open field lines and partly on closed field lines, and the mapping varies over a Jovian rotation period.

Factors such as solar wind conditions are expected to affect the mapping results, but without an upstream solar wind monitor it is difficult to determine quantitatively how changing solar wind conditions influence B_N and modify the flux equivalence calculation. Therefore, in this paper we presented a calculation using B_N values averaged over all solar wind conditions,

and our results are not fully representative of any particular solar wind condition. Despite the inconsistency of using averaged B_N with specific magnetopause locations, we carried out magnetic flux mapping for two preferred magnetopause locations and for four different phases of a Jovian rotation period (similar to considering different viewing geometries or CMLs) to obtain contours that can be compared with auroral observations. Our contours change shape and orientation in ways that are distinctly similar to changes observed in the UV aurora, which gives us considerable confidence in the validity of the mapping we have done. We, therefore, believe that our conclusions regarding the source regions of auroral activity described by *Grodent et al.* [2003] and by *Pallier and Prangé* [2001] are realistic.

In addition to mapping the source of the polar auroral features, we argued that a significant fraction of the area inside the main oval emissions must map to open field lines. We have interpreted the empty area, or the area mapping beyond the magnetopause or beyond roughly 150 R_J down the tail, as being on open field lines. Further justifying our interpretation is the fact that the flux through this empty area in both hemispheres very closely matches the open magnetic flux contained in the magnetotail lobes. We conclude that the size of Jupiter's polar cap is equivalent to a symmetric circle about the pole with an ~11º latitudinal width (though the Jovian polar cap itself is asymmetric). Alternate interpretations include the model of *McComas and Bagenal* (2007), who suggest that Jupiter's magnetosphere is closed and that the "empty" area in the ionosphere maps to closed field lines formed by a second reconnection with the solar wind at high latitudes (i.e. near the cusp), or of *Delamere and Bagenal* [2010], who also suggest that Jupiter's magnetosphere is closed but that the empty area maps instead to the cushion region and region of viscous interaction between the solar wind and the magnetospheric flanks. We feel

that this is unlikely, particularly in view of the evidence that the flux through the empty area in the ionosphere is effectively the same as the flux through the lobes of the magnetotail.

Finally, we have made our mapping results freely available online at http://www.igpp.ucla.edu/people/mvogt/mapping/. This website allows users to magnetically map a point in Jupiter's ionosphere to the magnetosphere, and vice versa.

Bibliography

Alexeev, I. I. and E. S. Belenkaya (2005), Modeling of the Jovian Magnetosphere, *Ann. Geophys.*, *23*, 809-826.

Bagenal, F. (2007), The magnetosphere of Jupiter: Coupling the equator to the poles, *J. Atmos. Sol. Terr. Phys.*, *69*, 387–402, doi:10.1016/j.jastp.2006.08.012.

Baron, R. L., T. Owen, J. E. P. Connerney, T. Satoh, and J. Harrington (1996), Solar wind control of Jupiter's H_3^+ auroras, *Icarus*, *120*, 437-442.

Bhardwaj, A., and G. R. Gladstone (2000), Auroral Emissions of the Giant Planets, *Rev. of Geophys.*, *38*, *3*, 295-353.

Bonfond, B., D. Grodent, J.-C. Gérard, A. Radioti, V. Dols, P. Delamere, and J. Clarke (2009), The Io UV footprint: Location, inter-spot distances and tail vertical extent, *J. Geophys. Res.*, 114, A07224, doi:10.1029/2009JA014312.

Broadfoot, A.L., M. J. Belton, P. Z.Takacs, B. R. Sandel, D. E. Shemansky, J. B. Holberg, J. M. Ajello, S. K. Atreya, T. M. Donahue, H. W. Moos, J. L. Bertaux, J. E. Blamont, D. F. Strobel, J. C. McConnell, A. Dalgarno, R. Goody, and M. B. McElroy (1979), Extreme ultraviolet observations from Voyager 1 encounter with Jupiter, *Science*, *204*, 979-982.

Caldwell, J., B. Turgeon, and X.-M. Hua (1992), Hubble Space Telescope Imaging of the North Polar Aurora on Jupiter, *Science*, *257*, 1512-1515.

Clarke, J. T., H. W. Moos, S. K. Atreya, and A. L. Lane (1980), Observations from earth orbit and variability of the polar aurora on Jupiter, *Astrophys. J.*, *241*, L179–L182, 1980.

Clarke, J. T., G. Ballester, J. Trauger, J. Ajello, W. Pryor, K. Tobiska, J. E. P. Connerney, G. R.

Gladstone, J. H. Waite Jr., L. B. Jaffel, and J.-C. Gérard (1998), Hubble Space Telescope imaging of Jupiter's UV aurora during the Galileo orbiter mission, *J. Geophys. Res.*, *103*, 20,217-20,236.

Clarke, J. T., J. Ajello, G. Ballester, L. B. Jaffel, J. Connerney, J.-C. Gérard, G. R. Gladstone, D. Grodent, W. Pryor, J. Trauger, and J. H. Waite Jr. (2002), Ultraviolet emissions from the magnetic footprints of Io, Ganymede and Europa on Jupiter, *Nature*, *415*, 997.

Clarke, J. T., J. Nichols, J.-C. Gérard, D. Grodent, K. C. Hansen, W. Kurth, G. R. Gladstone, J. Duval, S. Wannawichian, E. Bunce, S. W. H. Cowley, F. Crary, M. Dougherty, L. Lamy, D. Mitchell, W. Pryor, K. Retherford, T. Stallard, B. Zieger, P. Zarka, and B. Cecconi (2009), Response of Jupiter's and Saturn's auroral activity to the solar wind, *J. Geophys. Res.*, 114, A05210, doi:10.1029/2008JA013694.

Clarke, J. T., S. Wannawichian, N. Hernandez, B. Bonfond, J.-C. Gerard, and D. Grodent (2011), Detection of auroral emissions from Callisto's magnetic footprint at Jupiter, *EPSC Abstracts*, *6*, EPSC-DPS2011-1468.

Connerney, J., M. Acuña, and N. Ness (1981), Modeling the Jovian Current Sheet and Inner Magnetosphere, *J. Geophys. Res.*, *86*(A10), 8370-8384.

Connerney, J. E. P., R. Baron, T. Satoh, and T. Owen (1993), Images of excited H_3^+ at the foot of the Io flux tube in Jupiter's atmosphere, *Science*, *262*, 1035-1038.

Connerney, J. E. P., and M. H. Acuña (1998), New models of Jupiter's magnetic field constrained by the Io flux tube footprint, *J. Geophys. Res.*, *103*, 11929-11939.

Cowley, S. W. H., and E. J. Bunce (2001), Origin of the main auroral oval in Jupiter's coupled magnetosphere-ionosphere system, *Plan. Space Sci.*, *49*, 1067-1088.

Cowley, S. W. H., E. J. Bunce, T. S. Stallard, and S. Miller (2003), Jupiter's polar ionospheric flows: Theoretical interpretation, *Geophys. Res. Lett.*, *30*(5), 1220.

Cowley, S. W. H., S. V. Badman, S. M. Imber, and S. E. Milan (2008), Comment on "Jupiter: A fundamentally different magnetospheric interaction with the solar wind" by D. J. McComas and F. Bagenal, *Geophys. Res. Lett.*, 35, L10101, doi:10.1029/2007GL032645.

Delamere, P. A., and F. Bagenal (2010), Solar wind interaction with Jupiter's magnetosphere, *J. Geophys. Res.*, *115*, A10201, doi:10.1029/2010JA015347.

Grodent, D., J. T. Clarke, J. Kim, J. H. Waite, and S. W. H. Cowley (2003a), Jupiter's main auroral oval observed with HST-STIS, *J. Geophys. Res.*, 108, 1389, doi:10.1029/2003JA009921.

Grodent, D., J. T. Clarke, J. H. Waite Jr., S. W. H. Cowley, J.-C. Gérard, and J. Kim (2003b), Jupiter's polar auroral emissions, *J. Geophys. Res.*, *108*, doi:10.1029/2003JA010017.

Grodent, D., J.-C. Gérard, J. T. Clarke, G. R. Gladstone, and J. H. Waite (2004), A possible auroral signature of a magnetotail reconnection process on Jupiter, *J. Geophys. Res.*, 109, A05201, doi:10.1029/2003JA010341.

Grodent, D., J.-C. Gérard, A. Radioti, B. Bonfond, and A. Saglam (2008a), Jupiter's changing auroral location, *J. Geophys. Res.*, 113, A01206, doi:10.1029/2007JA012601.

Grodent, D., B. Bonfond, J.-C. Gérard, A. Radioti, J. Gustin, J. T. Clarke, J. Nichols, and J. E. P. Connerney (2008b), Auroral evidence of a localized magnetic anomaly in Jupiter's northern hemisphere, *J. Geophys. Res.*, *113*, doi:10.1029/2008JA013185.

Gurnett, D. A., W. S. Kurth, and F. L. Scarf (1980), The structure of the Jovian magnetotail from plasma wave observations, *Geophys. Res. Lett.*, 7(1), 53–56, doi:10.1029/GL007i001p00053.

Gurnett, D. A., W. S. Kurth, G. B. Hospodarsky, A. M. Persoon, P. Zarka, A. Lecacheux, S. J. Bolton, M. D. Desch, W. M. Farrell, M. L. Kaiser, H.-P. Ladreiter, H. O. Rucker, P. Galopeau, P. Louarn, D. T. Young, W. R. Pryor, and M. K. Dougherty (2002), Control of Jupiter's radio emission and aurorae by the solar wind, *Nature*, *415*, 985-987.

Hanlon, P. G., M. K. Dougherty, N. Krupp, K. C. Hansen, F. J. Crary, D. T. Young, and G. Tóth (2004), Dual spacecraft observations of a compression event within the Jovian magnetosphere: Signatures of externally triggered supercorotation?, *J. Geophys. Res.*, 109, A09S09, doi:10.1029/2003JA010116.

Hess, S. L. G., B. Bonfond, P. Zarka, and D. Grodent (2011), Model of the Jovian magnetic field topology constrained by the Io auroral emissions, *J. Geophys. Res.*, *116*, A05217, doi:10.1029/2010JA016262.

Hill, T. W. (1979), Inertial Limit on Corotation, *J. Geophys. Res.*, *84*(A11), 6554-6558.

Hill, T. W. (2001), The Jovian auroral oval, *J. Geophys. Res.*, *106*, 8101-8107.

Joy, S. P., M. G. Kivelson, R. J. Walker, K. K. Khurana, C. T. Russell, and T. Ogino (2002), Probabilistic models of the Jovian magnetopause and bow shock locations, *J. Geophys. Res.*, *107*, doi:10.1029/2001JA009146.

Khurana, K. K. (1997), Euler potential models of Jupiter's magnetospheric field, *J. Geophys. Res.*, *102*(A6), 11295-11306.

Khurana, K. K. (2001), Influence of solar wind of Jupiter's magnetosphere deduced from currents in the equatorial plane, *J. Geophys. Res.*, *106*, 25999.

Khurana, K. K., and M. G. Kivelson (1993), Inference of the angular velocity of plasma in the Jovian magnetosphere from the sweepback of magnetic field, *J. Geophys. Res.*, *98*, 67.

Khurana, K. K. and H. K. Schwarzl (2005), Global structure of Jupiter's magnetospheric current sheet, *J. Geophys. Res.*, *110*, doi:10.1029/2004JA010757.

Kivelson, M. G., and K. K. Khurana (2002), Properties of the magnetic field in the Jovian magnetotail, *J. Geophys. Res.*, *107*, 1196.

Kivelson, M. G. and D. J. Southwood (2005), Dynamical consequences of two modes of centrifugal instability in Jupiter's outer magnetosphere, *J. Geophys. Res.*, *110*, A12209, doi:10.1029/2005JA011176.

Kronberg, E. A., J. Woch, N. Krupp, A. Lagg, K. K. Khurana, and K.-H. Glassmeier (2005), Mass release at Jupiter: Substorm-like processes in the Jovian magnetotail, *J. Geophys. Res.*, *110*, A03211, doi:10.1029/2004JA010777.

Kronberg, E. A., K.-H. Glassmeier, J. Woch, N. Krupp, A. Lagg, and M.K. Dougherty (2007), A possible intrinsic mechanism for the quasi-periodic dynamics of the Jovian magnetosphere, *J. Geophys. Res.*, *112*, A05203.

Krupp, N., J. Woch, A. Lagg, S. Livi, D. G. Mitchell, S. M. Krimigis, M. K. Dougherty, P. G. Hanlon, T. P. Armstrong, and S. A. Espinosa (2004), Energetic particle observations in the

vicinity of Jupiter: Cassini MIMI/LEMMS results, *J. Geophys. Res.*, *109*, A09S10, doi:10.1029/2003JA010111.

Lepping, R. P., M. D. Desch, L. W. Klein, E. C. Sittler Jr., J. D. Sullivan, W. S. Kurth, and K. W. Behannon (1983), Structure and other properties of Jupiter's distant magnetotail, *J. Geophys. Res.*, *88*, 8801-8815.

Marklund, G., T. (2009), Electric fields and plasma processes in the auroral downward current region, below, within, and above the acceleration region, *Space Sci. Rev.*, *142*, 1-12.

McComas, D. J. and F. Bagenal (2007), Jupiter: A fundamentally different magnetospheric interaction with the solar wind, *Geophys. Res. Lett.*, *34*, L20106, doi:10.1029/2007GL031078.

McNutt, R. L. Jr., D. K. Haggerty, M. E. Hill, S. M. Krimigis, S. Livi, G. C. Ho, R. S. Gurnee, B. H. Mauk, D. G. Mitchell, E. C. Roelof, D. J. McComas, F. Bagenal, H. A. Elliott, L. E. Brown, M. Kusterer, J. Vandegriff, S. A. Stern, H. A. Weaver, J. R. Spencer, and J. M. Moore (2007), Energetic particles in the Jovian magnetotail, *Science*, *318*, 220-222.

Nichols, J. D., E. J. Bunce, J. T. Clarke, S. W. H. Cowley, J.-C. Gérard, D. Grodent, and W. R. Pryor (2007), Response of Jupiter's UV auroras to interplanetary conditions as observed by the Hubble Space Telescope during the Cassini flyby campaign, *J. Geophys. Res.*, 112, A02203, doi:10.1029/2006JA012005.

Ogino, T., R. Walker, and M. Kivelson (1998), A global magnetohydrodynamic simulation of the Jovian magnetosphere, *J. Geophys. Res.*, *103*(A1), 225-235.

Pallier, L. and R. Prangé (2001), More about the structure of the high latitude Jovian aurorae, *Planet. Space Sci.*, *49*, 1159-1173.

Prangé, R., G. Chagnon, M. G. Kivelson, T. A. Livengood, and W. Kurth (2001), Temporal monitoring of Jupiter's auroral activity with IUE during the Galileo mission. Implications for magnetospheric processes, *Plan. Space Sci.*, *49*, 405-415.

Radioti, A., J.-C. Gérard, D. Grodent, B. Bonfond, N. Krupp, and J. Woch (2008a), Discontinuity in Jupiter's main auroral oval, *J. Geophys. Res.*, *113*, A01215, doi:10.1029/2007JA012610.

Radioti, A., D. Grodent, J.-C. Gérard, B. Bonfond, and J. T. Clarke (2008b), Auroral polar dawn spots: Signatures of internally driven reconnection processes at Jupiter's magnetotail, *Geophys. Res. Lett.*, *35*, L03104, doi:10.1029/2007GL032460.

Radioti, A., A. T. Tomás, D. Grodent, J.-C. Gérard, J. Gustin, B. Bonfond, N. Krupp, J. Woch, and J. D. Menietti (2009), Equatorward diffuse auroral emissions at Jupiter: Simultaneous HST and Galileo observations, *Geophys. Res. Lett.*, 36, L07101, doi:10.1029/2009GL037857.

Radioti, A., D. Grodent, J.-C. Gérard, and B. Bonfond (2010), Auroral signatures of flow bursts released during magnetotail reconnection at Jupiter, *J. Geophys. Res.*, 115, A07214, doi:10.1029/2009JA014844.

Radioti, A., D. Grodent, J.-C. Gérard, M. F. Vogt, M. Lystrup, and B. Bonfond (2011), Nightside reconnection at Jupiter: Auroral and magnetic field observations from July 26, 1998, *J. Geophys. Res.*, *116*, A03221, doi:10.1029/2010JA016200.

Satoh, T. and J. E. P. Connerney (1999), Jupiter's H_3^+ emissions viewed in corrected jovimagnetic coordinates, *Icarus*, *141*, 236-252.

Southwood, D. J., and M. G. Kivelson (2001), A new perspective concerning the influence of the solar wind on the Jovian magnetosphere, *J. Geophys. Res.*, 106*(A4)*, 6123-6130.

Stallard, T. S., S. Miller, S. W. H. Cowley, and E. J. Bunce (2003), Jupiter's polar ionospheric flows: Measured intensity and velocity variations poleward of the main auroral oval, *Geophys. Res. Lett.*, *30*(5), 1221, doi:10.1029/2002GL016031.

Woch, J., N. Krupp, and A. Lagg (2002), Particle bursts in the Jovian magnetosphere: Evidence for a near-Jupiter neutral line, *Geophys. Res. Lett.*, *29*, 1138.

Vasavada, A. R., A. H. Bouchez, A. P. Ingersoll, B. Little, and C. D. Anger (1999), Jupiter's visible aurora and Io footprint, *J. Geophys. Res.*, 104*(E11)*, 27133-27142.

Vasyliūnas, V. M. (1983), Plasma Distribution and Flow, in *Physics of the Jovian Magnetosphere*, edited by A. J. Dessler, p. 395, Cambridge Univ. Press, New York.

Vogt, M. F., M. G. Kivelson, K. K. Khurana, S. P. Joy, and R. J. Walker (2010), Reconnection and flows in the Jovian magnetotail as inferred from magnetometer observations, *J. Geophys. Res.*, doi: 10.1029/2009JA015098.

Waite, J. H. Jr., G. R. Gladstone, W. S. Lewis, R. Goldstein, D. J. McComas, P. Riley, R. J. Walker, P. Robertson, S. Desai, J. T. Clarke, and D. T. Young (2001), An auroral flare at Jupiter, *Nature*, *410*, 787–789.

Zieger , B. and K. C. Hansen (2008), Statistical validation of a solar wind propagation model from 1 to 10 AU, *J. Geophys. Res.*, 113, A08107, doi:10.1029/2008JA013046.

CHAPTER 4

Simulating the Effect of Centrifugal Forces in Jupiter's Magnetosphere

4.1 Introduction

In the Earth's magnetosphere, gravitational and centrifugal forces are small compared to magnetic forces and can generally be ignored when considering particle motion. However, in Jupiter's magnetosphere, centrifugal forces are important due to the combination of three factors: a fast planetary rotation period (~10 hours), large scale sizes (average magnetopause standoff distance is ~75 R_J), and the fact that much of the plasma consists of heavy ions (oxygen and sulfur, ~20 proton mass) as opposed to protons. As a result, the corotational energy $\frac{m\rho^2\Omega^2}{2}$, where m is mass, ρ is cylindrical radial distance, and Ω is the rotation frequency, of an ion in the middle magnetosphere can be comparable to or larger than the plasma temperature. For example, the corotational energy of a 20 m_p (proton mass) particle at ρ = 50 R_J is ~41 keV, whereas estimates of the plasma temperature range from 10 to ~100 keV [*Kane et al.*, 1995]. Therefore, the centrifugal force can have a significant effect on magnetospheric plasma. Table 4.1 compares some relevant quantities, including scale sizes and ion corotational energies, to illustrate the relative importance of rotational stresses at the Earth and Jupiter.

The influence of centrifugal forces can be seen in many aspects of the structure and dynamics in the Jovian magnetosphere. For example, in the inner magnetosphere the centrifugal force confines plasma to the centrifugal equator, which is defined on each field line as the point farthest from the spin axis. The density off the equator falls according to an exponential scale height [*Hill and Michel*, 1976; *Bagenal et al.*, 1980; *Bagenal and Sullivan*, 1981]. Centrifugal

Table 4.1 Comparison of relevant quantities for the terrestrial and Jovian magnetospheres		
	Earth	**Jupiter**
Planetary radius	1 R_E = 6371 km	1 R_J = 71492 km
Rotation period = $\frac{2\pi}{\Omega}$	24 hours	~10 hours
Magnetopause standoff distance	10 R_E = 6.3×10^4 km	~60 to ~90 R_J depending on solar wind conditions = 4.2×10^6 to 6.4×10^6 km
Distance to the dusk terminator	~15 $R_=$ 9.6×10^4 km	~85 to ~130 R_J = 6.1×10^6 to 9.3×10^6 km
Proton corotational energy (middle magnetosphere) = $\frac{m\rho^2\Omega^2}{2}$	2.8×10^{-2} eV (at R = 5 R_E)	731 eV (at R = 30 R_J)
Proton corotational energy at R = 10 R_P (planetary radii)	0.11 eV	81 eV
Heavy ion corotational energy (m = 20 m_p), middle magnetosphere	5.6×10^{-1} eV (at R = 5 R_E)	14.63 keV (at R = 30 R_J)
Thermal pressure gradient	1.57e-4 kg s^{-2} m^{-2} [*Spence et al.*, 1989]	4.62e-8 kg s^{-2} m^{-2} [*Khurana et al.*, 2004]

stresses are thought to be the dominant factor in driving magnetospheric dynamics, as we discussed in Chapter 1. Finally, it has also been proposed that the effects of centrifugal forces and field line stretching could be responsible for the observed dawn-dusk asymmetry of the plasma sheet thickness; this idea is the topic of the present chapter.

Jupiter's plasma sheet is thinnest in the post-midnight to dawn local time sectors, thickens as it rotates through the morning sector through noon, and becomes thickest near dusk [*Kivelson and Khurana*, 2002; *Waldrop et al.*, 2005]. The plasma sheet heating and thickening near noon can be explained as a response to increased pressure from the solar wind, as the magnetopause distance decreases by ~30 percent from dawn to noon. However, one might then expect that the plasma sheet would thin as the magnetopause distance increases from noon to

dusk, but observations show that the opposite is true, and that the plasma sheet actually thickens in this local time sector. How, then, can we explain the observed dawn-dusk asymmetry? One idea, proposed by *Kivelson and Southwood* [2005], attributes the dusk side plasma sheet heating and thickening to the effects of centrifugal forces and rapid, non-adiabatic field line stretching which occurs between noon and dusk. They suggest that as a result of rotation, low energy particles gain parallel energy as they move radially outward, and the resulting anisotropy makes the plasma sheet unstable.

The focus of this chapter is a large-scale kinetic (LSK) simulation that was developed to test the key physical processes in the *Kivelson and Southwood* [2005] idea. In the simulation we follow a collection of rotating particles as they move in a time-varying, rotating magnetic field that reproduces the rapid stretching that occurs as field lines rotate from noon to dusk. We examine how the energy and pitch angle distributions change in response to the centrifugal force and non-adiabatic field line stretching. The results are intended to serve as a proof-of-principle for the physical processes that occur in Jupiter's magnetosphere, though they are applicable generally in cases where centrifugal energy is comparable or large compared to particle thermal energy, and where time or distance scales are such that the second adiabatic invariant is violated because bounce periods are long compared with the time scales for changes to the magnetic field.

We begin the chapter by presenting observations of Jupiter's plasma sheet in the dawn and dusk local time sectors, emphasizing differences in the plasma sheet thickness, and discuss some potential explanations for the local time asymmetries. Next we review particle bounce motion and adiabatic invariants in the rotating frame, explaining how the centrifugal force can increase particle energy and why a simulation is necessary to test the *Kivelson and Southwood* idea. In section 4.4 we describe our simulation and its assumptions and initial conditions, from

how we developed our time-dependent magnetic field model to how we loaded the initial particle distribution. Next, we describe how the energy, pitch angle, and spatial distributions evolved with time, comparing results for non-adiabatic, fast stretching to a baseline run where the flux tube expansion occurred adiabatically. Finally, we examine how the total thermal energy evolves with time and address whether the relative energy increase and resulting anisotropy is sufficient to produce instability in the plasma sheet and account for the thickening observed from noon to dusk. We conclude with a summary.

4.2 Plasma sheet thickness: observations and theoretical explanation

In this section we review the observations and theory that motivated this study. We begin by discussing the local time asymmetries in Jupiter's plasma sheet and then present two proposed explanations for the thickening at dusk. We end this section by presenting some of the motivating questions behind this work.

4.2.1 Observations of Jupiter's plasma sheet

The plasma in Jupiter's middle and outer magnetosphere is concentrated in a hinged plasma sheet that is located between the centrifugal and magnetic equators, then runs parallel to the solar wind beyond ~60 R_J. Jupiter's plasma sheet exhibits strong dawn-dusk asymmetries, being thickest near dusk and thinnest in the post-midnight to dawn local time sector [*Kivelson and Khurana*, 2002]. The typical half-thickness is ~2-3 R_J near dawn, and > 6 R_J near dusk [*Khurana and Schwarzl*, 2005], though high-latitude observations from Ulysses near dusk detected periodic plasma sheet signatures at more than ~25 R_J off of the jovigraphic equator [*Lanzerotti et al.*, 1993]. At a given radial distance the component of the magnetic field normal

to the current sheet, which indicates the current sheet thickness, can vary by as much as a factor of ~5 [*Vogt et al.*, 2011].

Figure 4.1 shows magnetic field and particle data collected during five typical plasma sheet crossings by the Galileo spacecraft during orbit E6. At this time, the spacecraft was orbiting in the jovigraphic equator just before 04:00 LT. The sign of B_R, the radial component of the magnetic field, reverses every ~5 hours as the current sheet moves over the spacecraft due to Jupiter's 10º dipole tilt. B_φ, the azimuthal component of the magnetic field, reverses sign with and maintains the opposite sign of B_R, indicating the field's swept-back orientation. The ion fluxes in the top panel also display a ~5 hour periodicity, peaking when the spacecraft is in the plasma sheet, or when B_R goes through zero. The Galileo spacecraft remained near the jovigraphic equator, reaching peak magnetic latitudes of +/- ~10º. Therefore, the square, flattened peaks in B_R indicate that the spacecraft easily enters the lobes and that the current sheet is relatively thin in this local time sector.

By comparison, magnetic field measurements from orbit G28 in the dusk local time sector show more rounded fluctuations in B_R, indicating a thicker current sheet. These measurements are shown in Figure 4.2, which presents the three components of the magnetic field from the dawn (black lines) and dusk (blue lines) local time sectors as a function of radial distance. From this plot we can see that the field configuration differs between dawn and dusk, though the field magnitude is roughly the same at both local times. The radial component of the magnetic field, seen in the first panel, is largest at dawn, indicating a more stretched field configuration than at dusk. (Note that the Pioneer 10 spacecraft on the dawn side was at ~9º SIII latitude, or magnetic latitude ~0º-20º, so the spacecraft does not fully cross the current sheet but does encounter the current sheet every ~10 hours, as evidenced by the minimum in the field

magnitude and reversals in B_R.) The second panel of Figure 4.2 shows B_θ, the north-south component of the magnetic field. This component of the field is much stronger, indicating a thicker current sheet and more dipolar field configuration, in the dusk local time sector than at dawn.

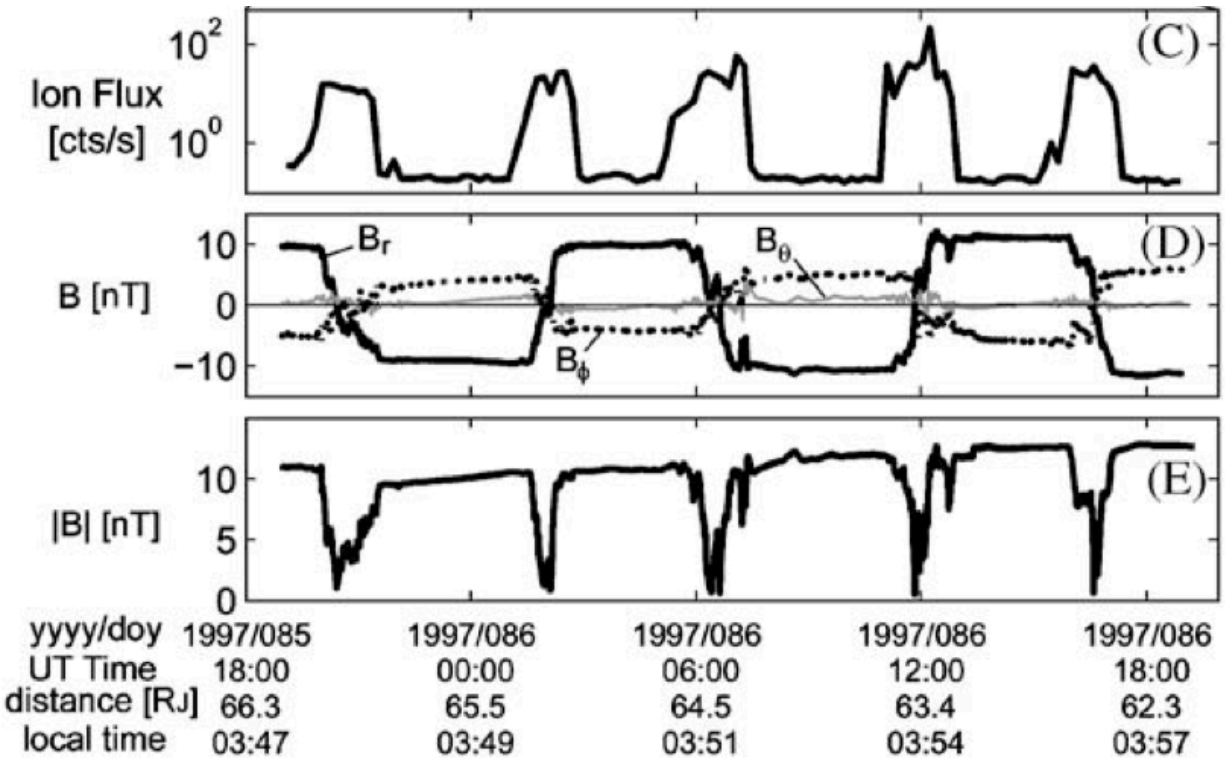

Figure 4.1: Magnetic field and particle measurements from several plasma sheet crossings observed by Galileo near the jovigraphic equator in the pre-dawn local time sector. In this local time sector the plasma sheet is thin and relatively well-ordered. The five hour periodicity in the magnetic field configuration occurs as the plasma sheet moves up and down over the spacecraft due to Jupiter's 10º dipole tilt. The ion fluxes peak every ~5 hours when the spacecraft is in the plasma sheet. Modified from *Waldrop et al.* [2005], Figure 1.

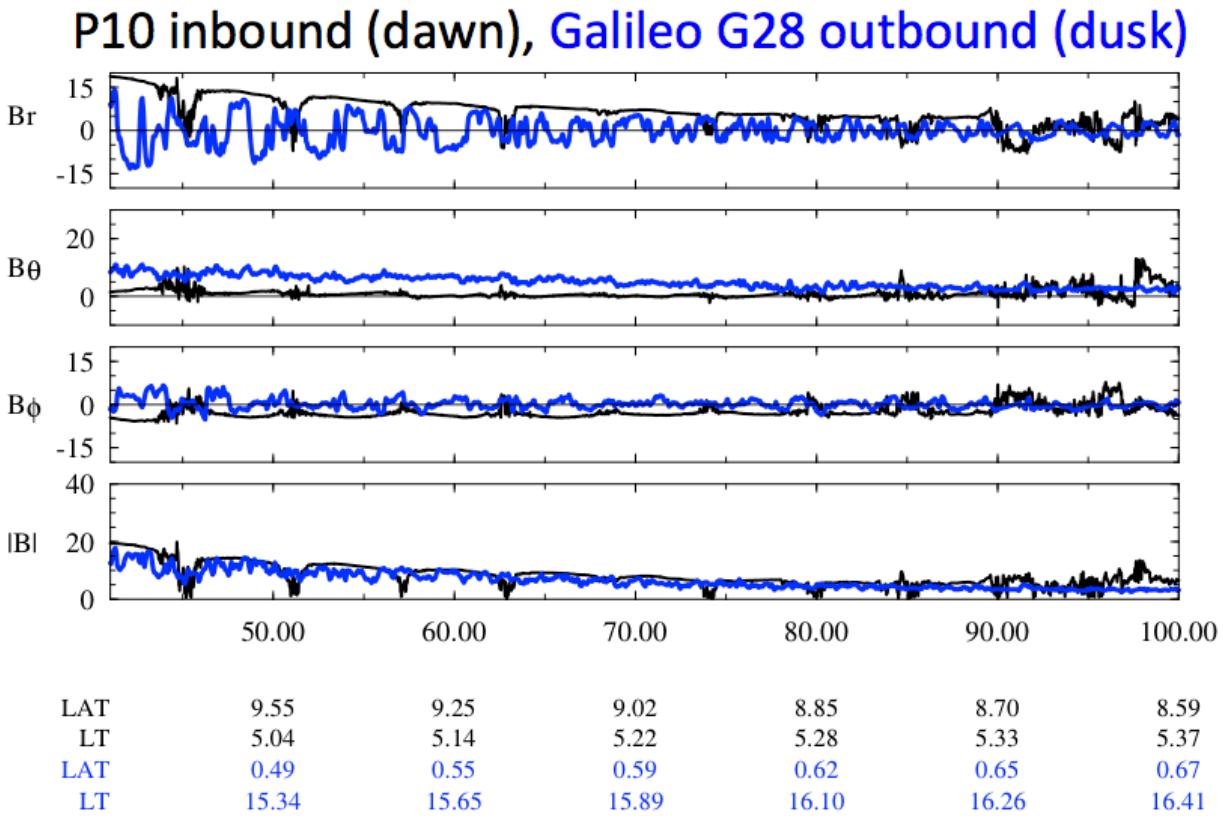

Figure 4.2: Magnetic field data from Pioneer 10 (black lines), in the dawn local time sector, and Galileo orbit G29 (blue lines), near dusk, plotted versus radial distance. The plasma sheet is much thicker for G29, as evidenced by the larger B_θ, and more rounded B_R fluctuations, than P10.

4.2.2 Why is the plasma sheet thickest near dusk?

Some of the local time changes in the plasma sheet thickness can be understood in terms of proximity to the magnetopause. We expect the plasma sheet to be thinnest on the night side, where field lines are unconstrained by the magnetopause and are highly stretched, in part due to centrifugal forces. Between the dawn flank and noon, the magnetopause distance decreases by roughly one third (~85 to ~60 R_J for the compressed case, or ~130 to ~90 R_J for the expanded case [*Joy et al.*, 2002]). The observed plasma sheet thickening that occurs between dawn and noon can be explained as a response to increased solar wind pressure as the magnetopause

distance decreases. However, this argument does not explain the observed dawn/dusk asymmetry, for one might then expect that the plasma sheet would thin from noon to dusk in response to the reduced solar wind pressure as the distance to the magnetopause increases again.

One potential explanation for the dawn/dusk asymmetry in plasma sheet thickness is that corotational flow on the dusk side is opposed by sunward return flow from tail reconnection at a distant neutral line. The difference in plasma sheet thickness could be accounted for if the distribution of open flux is also asymmetric across the magnetotail, as would be observed if convection in Jupiter's magnetotail were restricted to a single cell on the dawn side [*Khurana et al.* 2004; *Cowley et al.*, 2003]. This single-cell convection may be expected because corotation would oppose sunward return flow from tail reconnection in the dusk sector but would enhance the return flow in the dawn sector. As a result, the azimuthal flow would be slowest at dusk and faster at dawn, the north-south component of the magnetic field would be stronger at dusk, and the plasma sheet would thicken. Particle observations, from which flow velocities are derived, do show a slow azimuthal velocity near dusk and much faster flow near dawn [*Krupp et al.*, 2001]. However, in a steady state, flux transport [proportional to $\int v_\varphi B_\theta r dr$] across the dawn meridian must be the same as that across the dusk meridian, and with B_θ much larger near dusk than near dawn, the flow near dusk must be much slower. This means that one cannot tell whether the flow slows because B_θ is large for some reason other than the change of flow speed, such as a thickening of the plasma sheet, or whether B_θ becomes large because the flow has slowed.

Another explanation for the dawn/dusk asymmetry comes from *Kivelson and Southwood* [2005]. They suggest the dusk side plasma sheet heating and associated plasma sheet thickening result from the combined effect of centrifugal forces due to Jupiter's rapid rotation and the field line stretching which occurs as the magnetopause distance increases between noon and dusk.

Their argument stems from the fact that a bouncing, rotating particle will gain parallel energy from the centrifugal force as it moves outward to a larger radial distance. They therefore suggest that, as field lines rotate from noon to dusk and stretch so that all of the particles end up at larger values of ρ, the centrifugal force could produce a net increase in parallel energy. (Whether the field line stretching results in a net increase or decrease of particle energy depends on a variety of factors, and a complete discussion of how the centrifugal force affects particle energy requires a detailed explanation of particle bounce motion in the rotating frame. In section 4.3 below we review how the centrifugal force affects particle energy and bounce motion, and then, with that background understanding established, revisit the specifics of the *Kivelson and Southwood* argument.)

Assuming for now that the centrifugal force could produce a net increase in parallel energy, how would increasing the parallel energy make the plasma sheet thicken? *Kivelson and Southwood* [2005] emphasize that because the centrifugal force increases only the parallel energy, it creates a pressure anisotropy which produces a "centrifugal instability" in the plasma sheet. The force density felt by the plasma in the direction perpendicular to the magnetic field is given by

$$\vec{F}_{\perp} = -\nabla_{\perp}\left[p_{\perp} + \frac{B^2}{2\mu_0}\right] + \left(p_{//} - p_{\perp} - \frac{B^2}{\mu_0}\right)\frac{\vec{R}_C}{R_C^2} + \rho_m\left(\Omega^2\vec{r} - 2\Omega\times\vec{v}\right)_{\perp}, \qquad (4.1)$$

where ρ_m is mass density, p is pressure, R_c is the field line radius of curvature, and v is velocity in the rotating frame. Near the center of the outer plasma sheet, R_C is small, and the second term in equation 4.1 dominates, so that force balance requires $p_{//} - p_{\perp} - \frac{B^2}{\mu_0} \approx 0$. Increasing the parallel pressure such that $p_{//} > p_{\perp} + \frac{B^2}{\mu_0}$ results in the firehose instability, and the resulting instability

and stresses in the plasma sheet lead to ballooning. Increasing the thermal energy of the plasma would increase its scale height, so the plasma fills a larger portion of the flux tube and the plasma sheet thickens.

4.2.3 Motivating questions for this work

The purpose of the simulation described in this chapter is to test the idea of *Kivelson and Southwood* [2005] that the dusk side plasma sheet heating and thickening results from the combined effect of centrifugal forces due to Jupiter's rapid rotation and the field line stretching which occurs between noon and dusk. We will examine:

- How do centrifugal forces and field line stretching affect the plasma energy distribution and pitch angle distribution?
- If there is a net gain in energy, is it sufficient to explain the observed plasma sheet thickening from noon to dusk?
- What are the consequences of nonadiabatic behavior that arises because the time scale for field line stretching is short compared with particle bounce periods?
- How are our results influenced by the initial plasma energy, pitch angle, and spatial distribution?

Why must we use a simulation to answer these questions? We are interested in the effect of the centrifugal force and rapid flux tube expansion on particle energy. We can derive a simple expression for how adiabatic flux tube expansion affects particle energy, as we discuss in the following section. However, a key point in the *Kivelson and Southwood* argument is that the flux tube expansion occurs on short time scales that violate the second adiabatic invariant of most particles in the distribution, so that there is no energy constant that can be used to analytically

determine how particle energy changes in response to the field line stretching. Therefore we developed a simulation to study the effects of the centrifugal force and field line stretching on a large collection of particles with a range of initial energies, positions, and pitch angles.

4.3 Particle motion and adiabatic invariants in the rotating frame

The kinetic simulation that we use to establish the changes of total energy in an expanding, rotating flux tube includes the effects on a particle's energy and pitch angle of centrifugal force and rapid flux tube expansion that violates the second adiabatic invariant. Therefore in this section we begin by reviewing the adiabatic invariants and particle bounce motion in a rotating frame, following the discussion of *Northrop and Birmingham* [1982]. The discussion will show how, for a static magnetic field in the rotating frame, the centrifugal force changes particle energy over a bounce period. The centrifugal force also affects particle energy during adiabatic flux tube expansion, but as we will explain, its effects depend on factors such as the particle's initial energy and pitch angle. Finally, we discuss some predictions for how the particle energy will evolve under rapid flux tube expansion, and illustrate why we must run a simulation if we want to understand the non-adiabatic effects on a collection of particles.

In this and all other sections in this chapter we assume rigid rotation; for this section only we also assume that the magnetic field has no other time dependence other than the rigid rotation, and that $\vec{E} \cdot \vec{B} = 0$.

4.3.1 First adiabatic invariant

The first adiabatic invariant, μ, is the magnetic moment, and is given by

$$\mu = \frac{1/2\, m \left| v_\perp - v_D \right|^2}{B}, \tag{4.2}$$

where m is the particle mass, B is the magnetic field magnitude, $v_\perp$ is the perpendicular component of the velocity in the observer's frame of reference, and v_D is the drift velocity, or the velocity of the guiding center, and is perpendicular to the magnetic field [*Northrop,* 1963; *Roederer*, 1970]. Typically $v_D << v_\perp$, so we approximate equation 4.2 as

$$\mu = \frac{1/2\, m v_\perp^2}{B}. \tag{4.3}$$

This quantity is conserved under the assumption that the time scale for changes in the magnetic field is long compared with a gyroperiod, and that the gyroradius is small compared to the scale length for changes in the magnetic field (such as the radius of curvature).

For a nonrotating particle in the inertial frame, the drift velocity v_D includes gradient and curvature drift, which are typically small compared with $v_\perp$. For a rigidly rotating particle in the inertial frame the drift velocity would also include the rotational velocity, $\vec{\Omega} \times \vec{r}$, where $\vec{\Omega}$ is the angular frequency and $\vec{r}$ is the particle position with respect to the origin on the rotational axis. At Jupiter, the rapid rotation period (~10 hours) and large distance scales mean that the corotational energy of a proton at an equatorial distance of 40 R_J is ~1.3 keV; the bulk plasma is dominated by heavy sulfur and oxygen ions with an average mass per unit charge of ~20 m_p, which have a corotational energy of ~26 keV at 40 R_J. Therefore, at relatively low energies of a few keV it is convenient to work in the rotating frame, where equation 4.3 is still valid assuming the guiding center motion (due to gradient and curvature drift, which are discussed in section 4.3.3) is slow compared with the particle gyro velocity.

4.3.2 Second adiabatic invariant

The second adiabatic invariant, also called the longitudinal invariant, is the sum of the parallel momentum over a complete bounce period, or from one mirror point to the other and then back to the initial position [*Northrop*, 1963]. It is given by

$$J = \oint p_{//} ds \,, \tag{4.4}$$

where $p_{//}$ is the parallel momentum and s is the distance along the field, with both quantities in the guiding center frame. As with the first adiabatic invariant, J is conserved only under certain assumptions – in this case, that the magnetic field changes slowly compared to the bounce period. *Northrop and Birmingham* [1982] showed that J is conserved in the rotating frame for the general case of a rigidly-rotating magnetic field at an arbitrary angle to $\vec{\Omega}$ in the absence of a parallel electric field.

4.3.3 Particle drift and bounce motion in the rotating frame

In the inertial frame with a static, nonrotating magnetic field, particle motion is dictated according to the following equation of motion, known as the Lorentz force equation:

$$m\frac{d\vec{v}}{dt} = q\left(\vec{E} + \vec{v} \times \vec{B}\right), \tag{4.5}$$

where $\vec{v}$ is the particle velocity in the nonrotating frame. We follow *Northrop and Birmingham* [1982] and assume $\vec{E} \cdot \vec{B} = 0$ in our discussion. The absence of a parallel electric field means that the effect of the electric field is simply to introduce a guiding center drift velocity of $\left(\vec{E} \times \vec{B}\right) \Big/ B^2$. Energy will be conserved in the absence of any electric field because the remaining force $\vec{v} \times \vec{B}$

is perpendicular to the particle motion and therefore does no work. Conservation of μ and J dictate a particle's bounce motion and define the drift shell on which the particle bounces.

In the case of particles on a rotating flux tube, the equation of motion in the rotating frame can be derived from equation 4.5. The velocity $\vec{w}$ in the rotating frame is given by

$$\vec{w} = \vec{v} - \vec{\Omega} \times \vec{r} \,. \tag{4.6}$$

Transformation into the rotating frame changes the time derivative of a vector $\vec{a}$ according to

$$\left(\frac{d\vec{a}}{dt}\right)_r = \left[\left(\frac{d}{dt}\right)_i - \vec{\Omega}\times\right]\vec{a} \,, \tag{4.7}$$

[*Goldstein*, 1950], where the subscripts *r* and *i* indicate the rotating and inertial reference frames, respectively. The time derivative of equation 4.6 can then be transformed into the rotating frame as

$$\left(\frac{d\vec{v}}{dt}\right)_i = \left(\frac{d\vec{w}}{dt}\right)_r + 2\vec{\Omega}\times\vec{w} + \vec{\Omega}\times\left(\vec{\Omega}\times\vec{r}\right) \tag{4.8}$$

where the second term on the right hand side of the equation is the Coriolis force, and the third term is the centrifugal force. Equation 4.5 can then be written in the rotating frame as

$$m\frac{d\vec{w}}{dt} = q\left(\vec{E} + \left(\vec{w} + \vec{\Omega}\times\vec{r}\right)\times\vec{B}\right) - m\left(2\vec{\Omega}\times\vec{w} + \vec{\Omega}\times\left(\vec{\Omega}\times\vec{r}\right)\right), \tag{4.9}$$

where $\vec{E}$ is the electric field as observed from the nonrotating frame, and includes the corotation electric field. Equation 4.9 can then be further simplified because the electric field for a rigid rotator, or the corotation electric field, is given by

$$\vec{E}_{corotation} = \left(\vec{r}\times\vec{\Omega}\right)\times\vec{B} \tag{4.10}$$

[*Birmingham and Northrop*, 1979], which cancels the second term in $\left(\vec{w} + \vec{\Omega}\times\vec{r}\right)\times\vec{B}$. In the rotating frame, the Lorentz force equation is then given by

$$m\frac{d\vec{w}}{dt} = q\left(\vec{w}\times\vec{B}\right) - m\left(2\vec{\Omega}\times\vec{w} + \vec{\Omega}\times\left(\vec{\Omega}\times\vec{r}\right)\right), \tag{4.11}$$

assuming there is no electric field other than the corotation electric field.

The equation of motion in the rotating frame (4.10) has two additional terms compared with equation 4.5 in the inertial frame and absence of rotation. The first is the Coriolis force, $-2m\left(\vec{\Omega}\times\vec{w}\right)$; this term has no effect on the particle energy in the guiding center frame because it is perpendicular to the particle motion and therefore does no work, though it does introduce an azimuthal drift averaged over a gyroperiod. The second term, the centrifugal force, does affect the particle energy, and can also be written in terms of a centrifugal potential, $\nabla\frac{1}{2}\rho^2\vec{\Omega}^2$, where ρ is the cylindrical distance to the rotational axis. As *Northrop and Birmingham* [1982] note, it is easily shown by dotting equation 4.11 with $\vec{w}$ that $\left(\left|\vec{w}\right|^2-\rho^2\Omega^2\right)$ is a constant of the particle motion. Therefore, a particle bouncing on a magnetic field line will gain or lose kinetic energy as it moves in ρ during a bounce period.

How does the centrifugal force affect the particle bounce motion? The constant of particle motion $\left(\left|\vec{w}\right|^2-\rho^2\Omega^2\right)$ can also be written as

$$K\equiv\frac{m}{2}\left(w_{//}^2-\rho^2\Omega^2\right)+\mu B \tag{4.12}$$

where K is a constant of the particle motion, assuming the conditions required to conserve μ and J are met. (Note that constancy of K assumes the absence of an electric field in equation 4.11; if there is a non-zero electric field a constant of the particle may still be defined if $\nabla\times\vec{E}=0$ [*Northrop and Birmingham*, 1982].) Equation 4.12 shows that the centrifugal force affects particle energy in only the parallel and not the perpendicular component. (The perpendicular component produces a guiding center drift with velocity $\vec{v}_D\propto\vec{F}_\perp/qB$, but this drift does not affect

the particle gyro-energy.) In planetary magnetic fields, the centrifugal force concentrates particles near the centrifugal equator by restricting inward motion, causing the particles to mirror farther from the planet than they would in the absence of the centrifugal force.

From the above discussion we can understand the two cases of particle bounce motion shown in Figure 4.3. (Note that though in our illustration in Figure 4.3 we have used an axially-symmetric dipole field and a dipole-aligned spin axis, the previous discussion was equally applicable to a more general field configuration and rotation axis, following *Northrop and Birmingham* [1982].)

In the first case, particle A is in the inertial frame, with a nonrotating flux tube and no electric field. The trajectory shows that particle A begins at the equator with energy E_0 and pitch angle α = 30º, then moves along the field, conserving μ and energy, until the particle is reflected at its mirror point, where $v_{//} = 0$, and the particle turns around and moves along the field line, crossing the equator and continuing through to the other mirror point. The field magnitude at the two mirror points is

$$B_{mirror} = \frac{B_{equator}}{\sin^2 \alpha_{equator}}, \tag{4.13}$$

which can be derived from equation 4.3 and conservation of energy.

In the second case, particle B is bouncing in a rotating plasma, though the magnetic field is otherwise identical to the one for the upper diagram, and we again assume no electric field other than the corotation electric field, so that the equation of motion is given by equation 4.11. The particle's trajectory is shown and relevant quantities are calculated in the rotating frame. As with the nonrotating particle A, the rotating particle B begins at the equator with energy W_0 (as defined in the rotating frame) and α = 30º, and conserves μ during its bounce period. However, particle B's energy is not conserved: as it moves along the field to smaller ρ it moves against the

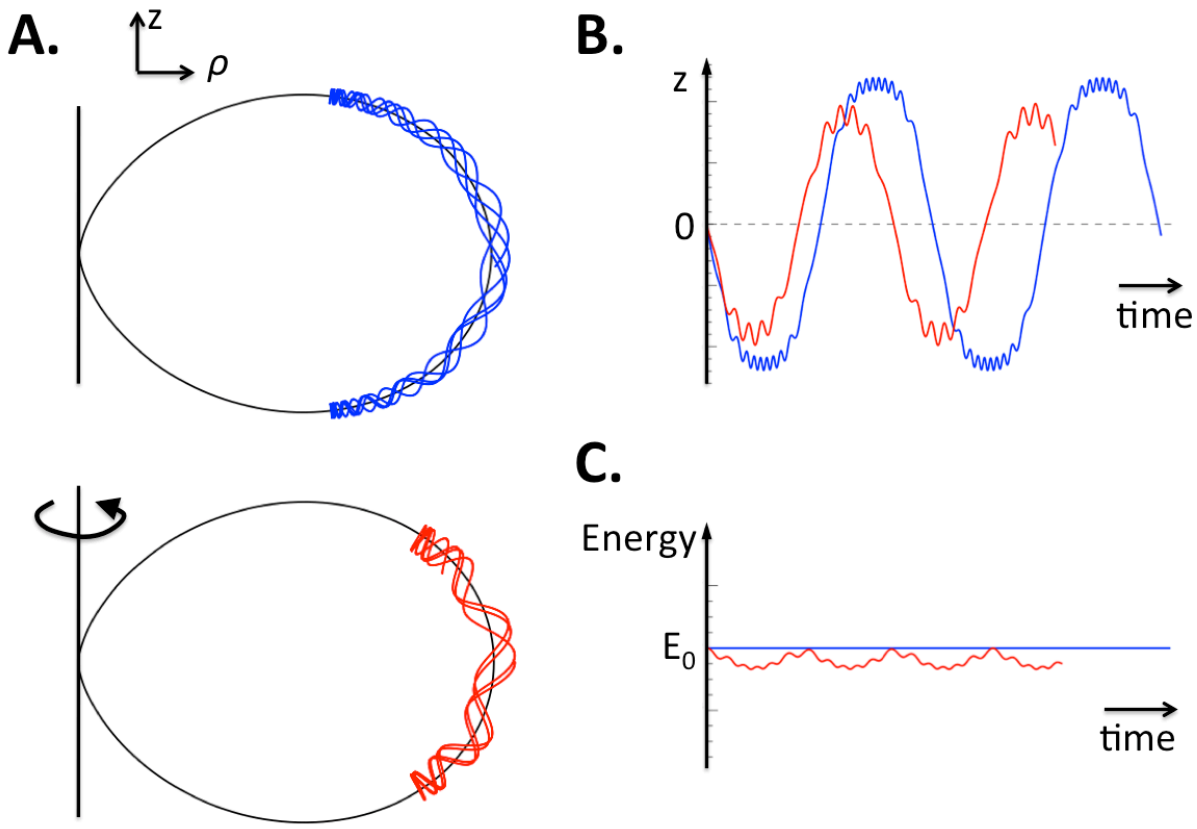

Figure 4.3: A: Particle bounce motion in a dipole magnetic field in the inertial frame (blue) and on a rotating flux tube in the rotating frame (red). The two particles have the same equatorial energy and pitch angle. In the inertial frame, the particle moves along the field line until it reaches its mirror point given by equation 4.13. On a rotating flux tube in the rotating frame, the centrifugal force restricts particle motion up the field, so that the particle mirrors farther from the planet. B: Particle location in the z direction versus time during its bounce motion. Notice that the particle on the rotating flux tube (red) has a shorter bounce period and travels a shorter distance in z than the particle in the inertial frame (blue). C: Particle energy as a function of time, on the same time scale as in panel B. In the inertial frame (blue), the particle energy remains constant, whereas the particle on a rotating flux tube loses energy to the centrifugal force as it travels along the field to smaller ρ.

centrifugal potential and loses parallel energy. Because the particle conserves μ but loses parallel energy, its total energy decreases. The mirror point can be calculated using equation 4.12 as follows:

$$\mu B_{mirror} - \frac{m\Omega^2}{2}\rho_{mirror}^2 = W_0 - \frac{m\Omega^2}{2}\rho_{equator}^2 , \tag{4.14a}$$

which can be rearranged as

$$B_{mirror} = \frac{W_0 - \frac{m\Omega^2}{2}\left(\rho_{equator}^2 - \rho_{mirror}^2\right)}{\mu} \tag{4.14b}$$

and because $\mu = \frac{W_0 \sin^2 \alpha_{equator}}{B_{equator}}$, we conclude:

$$B_{mirror} = \left[\frac{W_0 - \frac{m\Omega^2}{2}\left(\rho_{equator}^2 - \rho_{mirror}^2\right)}{W_0}\right]\frac{B_{equator}}{\sin^2 \alpha_{equator}} . \tag{4.14c}$$

The bracketed quantity in equation 4.14c is < 1, so particle B will mirror at a smaller *B* (and larger radial distance) than particle A. Upon reaching its mirror point, the rotating particle B will then turn around, gaining parallel energy as it returns to the equator, and then loses energy again as it continue to the other mirror point. Though particle B does not conserve energy, we know that the quantity $\left(|\vec{w}|^2 - \rho^2\Omega^2\right)$ is conserved, so each time particle returns to the equator it will have its initial energy W_0, and will have the same energy each time it reaches one of its mirror points. In summary, the centrifugal force affects particle bounce motion by: 1) changing the parallel energy within a bounce period so that particles reach their maximum energy at the point along the field line that is farthest from the planet, and 2) confining particles to positions closer to the (centrifugal) equator.

4.3.4 Adiabatic flux tube expansion for a static magnetic field under the effects of the centrifugal force

Adiabatic flux tube expansion, in which a field line's equatorial crossing point moves out to a larger radial distance, can be produced by an azimuthal electric field (in addition to a possible radially-oriented corotation electric field in the inertial frame). The electric field produces an $\vec{E} \times \vec{B}$ drift that carries the flux tube radially outward, and as a result, particles experience changes in the magnetic field. Adiabaticity requires that this outward drift occurs on time scales that are long compared to the particle gyro and bounce periods. In the presence of an electric field, a constant of motion similar to K from equation 4.12 can still be defined if the electric field is derivable from a scalar potential ϕ such that

$$\vec{E} = -\nabla\phi, \tag{4.15}$$

and $\nabla \times \vec{E} = 0$ so that at the magnetic field at a given position is constant in time [*Northrop and Birmingham*, 1982]. Under those assumptions, the constant of motion is modified (now using C to denote the energy constant to avoid confusion with equation 4.12) as follows:

$$C_i \equiv \frac{m}{2} v_{//}^2 + \mu B + q\phi \tag{4.16a}$$

or

$$C_r \equiv \frac{m}{2}\left(w_{//}^2 - \rho^2\Omega^2\right) + \mu B + q\phi \tag{4.16b}$$

where equation 4.16a is applicable to the inertial frame for a nonrotating flux tube and equation 4.16b is applicable to the rotating frame. *Northrop and Birmingham* [1982] considered only static magnetic fields such that $\nabla \times \vec{E} = 0$, and showed that μ and J are conserved for a rotating plasma in a static magnetic field. In this introductory discussion we consider only the case where

$\nabla \times \vec{E} = 0$ so that we can assume conservation of μ and J; however, in later sections we will work with magnetic field models that are not constant in time, so that μ and J are not necessarily conserved.

For the case of a nonrotating flux tube in the inertial frame, μ and J are conserved assuming the outward drift occurs slowly compared to particle bounce and gyro periods. Conservation of μ implies that adiabatic flux tube expansion will affect the particle's perpendicular energy. Expansion to a larger radial distance, where the magnetic field magnitude is weaker, requires that the perpendicular energy decrease to conserve μ; conservation of μ also means that the field magnitude at the mirror point will remain the same, which means that a particle with finite parallel energy will move to a larger distance along the field to reach its mirror point after expansion than it did on the original flux tube. From conservation of J we infer that a particle loses parallel energy when moving to a flux tube at larger ρ. This net kinetic energy loss implies drift to a larger ϕ to conserve the net energy in equation 4.16a.

For the case of a rotating plasma viewed in the rotating frame, whether a particle gains or loses energy during outward motion is more nuanced. The particle will gain parallel energy as it moves to a larger ρ along the centrifugal potential (assuming very high conductivity in the ionosphere such that the plasma remains in cororotation), but may lose some parallel energy to conserve J, and will lose perpendicular energy to conserve μ as it moves to a weaker magnetic field. Thus the net energy gain or loss depends on the gradients of B and the centrifugal energy $\frac{m}{2}\rho^2\Omega^2$, and on how the parallel energy changes to conserve J. The amount of energy gain or loss will also depend on a particle's initial energy and pitch angle, since the change of perpendicular energy is proportional to the initial perpendicular energy by conservation of μ. In this chapter we will be working with field models that at large distances fall off slowly with r, so

the increase in energy from the centrifugal force will be larger than the decrease in perpendicular energy due to the magnetic field decrease. However, the parallel energy will also decrease to conserve J, and the net result, as we show in section 4.5.1, is that a rotating particle will generally experience a decrease in energy as it moves out.

Because a rotating particle loses perpendicular energy and gains centrifugal potential as it moves to larger ρ during adiabatic expansion in a time stationary magnetic field, its pitch angle will become more field-aligned. However, the increase in ρ means that the strength of the centrifugal force also increases, so particles become further confined to the equator. Thus, for adiabatic flux tube expansion for a rotating flux tube and static magnetic field in the rotating frame: 1) particles may experience a net increase or decrease in energy, depending on a particle's initial pitch angle and the gradients of the magnetic field and centrifugal energy 2) the pitch angle distribution will become more field-aligned, and 3) particles become further confined to the centrifugal equator.

4.3.5 Non-adiabatic flux tube expansion: making the case for a kinetic simulation

Returning now to the *Kivelson and Southwood* [2005] theory of plasma sheet thickening, in which a key point is that the flux tube expansion, which occurs as flux tubes rotate from noon to dusk, happens on time scales that are short compared to particle bounce periods, so the second adiabatic invariant is violated. The large scale size of Jupiter's magnetosphere means that the typical bounce period of a 1keV, 20 m_p particle in the middle magnetosphere is ~4-7 hours (see Table 4.2); by comparison, the time scale for the field line stretching and rotation between noon and dusk is only 5 hours, assuming an azimuthal flow speed of half corotation. The bounce times

listed in Table 4.2 were calculated numerically for the field model described in section 4.4, and all bounce times are long compared with the time for rotation between noon and dusk (5 hours).

There is some disagreement in the literature regarding typical plasma temperatures, with estimates ranging from ~1-2 keV [*Goertz et al.*, 1979; *McNutt et al.*, 1981] to ~4-8 keV [*Frank and Paterson*, 2002, 2004], and even ~20-100 keV [*Kane et al.*, 1995, 1999]. *Krimigis et al.* [1981] showed that at Jupiter, ions follow a kappa distribution [*Vasyliūnas*, 1968], which is comprised of a Maxwellian with ~20-50 keV temperature linked to a high energy tail. The high temperature estimates from *Kane et al.* [1999] are based on an analysis which includes the contribution of the higher energy part of the distribution, which does not dominate the density but does dominate the energy density. The bulk plasma falls in the quasi-Maxwellian part of the distribution, so we will focus on energies ranging from tens of eV to ~12 keV. Even assuming energies of tens of keV, the second adiabatic invariant will be violated because bounce times are long compared to the 5 hour stretching time scale: most low energy particles (< 10 keV) will complete only a fraction of a bounce period as the field stretches, and even the higher energy particles, such as 50 keV, will only complete ~1-2 bounce periods in 5 hours and will not maintain adiabaticity. This will have important implications for how the energy and pitch angle distributions evolve.

How can the long bounce times influence the net change in particle energy? Consider two particles with the same equatorial energy on a rotating flux tube, with particle 1 located at its mirror point at a distance ρ_m, and particle 2 located at the equator at ρ_e. Half a bounce period later, particle 1 will have moved down the field to the equator, gaining energy $\frac{m}{2}\Omega^2(\rho_e^2 - \rho_m^2)$, though particle 2 will have moved up the field to its mirror point, losing energy $\frac{m}{2}\Omega^2(\rho_e^2 - \rho_m^2)$, so that there is no net change in the energy of the two particles. Similarly, if the field line

Table 4.2: Bounce times for particles of mass 20 m_p, on a stationary field line in the rotating frame [Ω ~ 1/(20 hours)], starting with 100 eV-50 keV energy at the equator.			
Equatorial Energy	**Equatorial pitch angle (degrees)**	**Field line equatorial crossing distance (R_J)**	**Bounce time (hours)**
100 eV	20	40	6.06
100 eV	40	40	5.89
100 eV	60	40	5.70
100 eV	80	40	5.59
1 keV	20	30	9.39
1 keV	40	30	7.13
1 keV	60	30	5.62
1 keV	80	30	4.92
1 keV	20	40	7.57
1 keV	40	40	6.03
1 keV	60	40	4.80
1 keV	80	40	4.20
1 keV	20	50	6.49
1 keV	40	50	5.41
1 keV	60	50	4.43
1 keV	80	50	3.92
10 keV	20	40	9.00
10 keV	40	40	4.59
10 keV	60	40	2.49
10 keV	80	40	1.82
50 keV	20	40	4.47
50 keV	40	40	2.69
50 keV	60	40	1.28
50 keV	80	40	0.85

stretches adiabatically, particle 1 will gain energy as it moves from its mirror point to the equator, where the field line is located at $\rho_e + \Delta\rho_e$, and particle 2 will lose energy as it moves along the field line to its new mirror point at $\rho_m + \Delta\rho_m$. Since the field stretches slowly compared to the bounce period, $\Delta\rho_m \sim \Delta\rho_e = \Delta\rho$, and the net change in energy of the two particles will be small, and only due to the adiabatic expansion of distance $\Delta\rho$. However, for rapid field line

stretching, the outward field line motion can be so large so that particle 2 may even mirror at a point $\rho > \rho_m$, so that both particles will gain centrifugal energy during the expansion. This is illustrated in Figure 4.4.

Violation of the second adiabatic invariant due to rapid flux tube expansion means that an energy constant, as in equation 4.16, can no longer be defined and the simple expressions from section 4.3.4 no longer apply. Additionally, if the magnetic field is not constant in time, as is the case for the field models we use in the simulation (see section 4.4), we may not be able to assume conservation of J and there is no energy constant equivalent to equation 4.16b. Therefore, we cannot analytically determine how the particle energy and pitch angle distributions evolve in response to the flux tube expansion, and must instead track particles by solving their equations of motion, as, for example, is done numerically in a large-scale kinetic simulation. In the next section we describe how we developed this simulation to study the effects of rapid flux tube expansion, and the assumptions and initial conditions that we used.

4.4 Methods: Developing and using a LSK model

4.4.1 Overview and purpose of the simulation

The goal of this simulation was to test the key physical processes in the idea that rotation and field line stretching can produce an increase in net energy and particle anisotropy. We have used a large-scale kinetic (LSK) model [*Ashour-Abdalla et al.*, 1992] to create a toy problem where we follow particles on one flux tube as a proof-of-principle to study how the energy and pitch angle distributions change as particles move in a system that is meant to mimic the

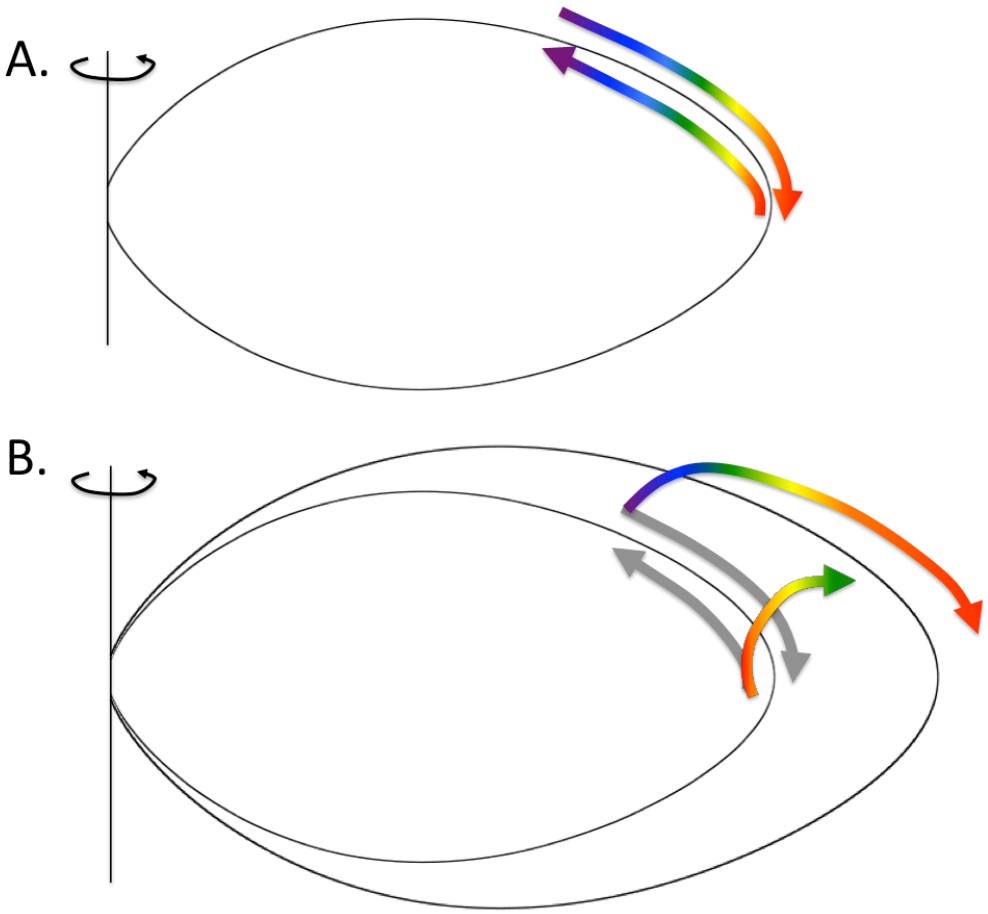

Figure 4.4: Illustration showing how particle energy changes during a fraction of a bounce period on (a) a rotating flux tube, and (b) a rotating and stretching flux tube; color indicates particle energy with purple being lowest and red being highest. For the static field in panel A, the individual particles change energy as they bounce up and down the flux tube but they gain as much energy in moving from mirror point to equator as they lose in moving from equator to mirror point. For the stretching field in panel B, both particles gain centrifugal energy during the expansion to larger ρ so there is a net increase in energy.

conditions in the Jovian noon-to-dusk magnetosphere. Jupiter's magnetopause flares between noon and dusk, so that flux tubes rotating through this local time sector expand and increase their equatorial crossing distance by as much as 50%. In our model we represent this rotation and expansion by modeling an axially-symmetric, rotating flux tube in the rotating frame that

stretches over the time it takes for a flux tube to rotate from noon to dusk in Jupiter's magnetosphere.

Our results will show how the combined effects of the centrifugal force and rapid field line stretching influence particle energy and pitch angle distributions over time. However, we must compare the end distributions not to the initial values but to how the distributions would have evolved if the field line expansion proceeded adiabatically, since we expect some changes due simply to the outward expansion. Therefore, we will run our simulation twice, once with a realistic, non-adiabatic (5 hour) stretching time scale, and once with a much slower (500 hour) time scale and will compare the properties of the final particle distributions. Note that, as we mentioned in section 4.3.5, in our simulation we use a time-varying magnetic field model and therefore cannot assume adiabaticity, even for the slow stretching time scale. However, we have tested the slow stretching case with a varying field and find that, for a 500 hour stretching time scale, J is conserved to at least 5 significant figures for test particles across our energy and pitch angle range of interest. (By comparison, for the 5 hour stretching time scale and these same test particles, J was conserved to zero or one significant figure, as expected.) Therefore we can consider the slow stretching case to be adiabatic, despite the fact that we cannot define an energy constant due to the time-varying magnetic field.

In the following subsections we explain how we developed our LSK model, beginning with an overview of how LSK models track particle motion. We then describe how the electric and magnetic field models were constructed to approximate the actual rotational stresses and field line stretching observed in the Jovian magnetosphere. Next we review some of the limitations of our model, and then address model accuracy, explaining some of the tests that we

performed to ensure our model was working correctly. Finally, we discuss how we chose the initial energy and pitch angle distributions to load the model field lines with simulated particles.

4.4.2 Solving the Lorentz force equation with LSK

An LSK approach rather than an MHD simulation is required for our purposes because the effects of centrifugal forces differ for particles of different energy and equatorial pitch angle. As we discussed in section 4.3.3, a rotating, bouncing particle will gain and lose energy during its bounce period. Whether a plasma, or a collection of particles, gains or loses energy in a specific time interval depends on the initial conditions specific to individual particles, such as energy, pitch angle, and starting position within its bounce motion. Therefore, we cannot use a fluid approximation and must instead consider the motion of individual particles. Additionally, the second adiabatic invariant J would not be conserved for most particles in the energy range of interest, even in a time-independent magnetic field, because bounce times are long (~hours) compared with the time for rotation from noon to dusk (~2.5 hours for rigid corotation at a 10 hour rotation period or longer for a more realistic rotation rate closer to half of rigid corotation).

In our LSK model we use a fourth-order Runge-Kutta method, a common approach to solve differential equations numerically. LSK models integrate particle orbits by solving the particle equation of motion, or the Lorentz force equation, which can be written in the inertial frame as

$$m\frac{d\vec{v}}{dt} = q\left(\vec{E} + \vec{v} \times \vec{B}\right), \tag{4.17}$$

where $\vec{E}$ and $\vec{B}$ are specified global electric and magnetic fields, respectively, that may be a function of time, and $\vec{v}$ is velocity in the inertial frame. The electric and magnetic field models that we use in this simulation are presented in section 4.4.3. Because we are interested in the

effects of both rotation and a time-varying magnetic field, the electric field in the inertial frame will have three contributions. The first is the rotational electric field, given by $-\vec{v}_{\varphi} \times \vec{B}$; however, as was discussed in section 4.2.3, in the rotating frame the rotational electric field is no longer present. The second is the induction electric field that arises from time variations in the magnetic field:

$$\nabla \times \vec{E}_{induction} = -\frac{\partial \vec{B}}{\partial t} . \tag{4.18}$$

The final component of the electric field would be the potential electric field, $\vec{E}_{potential} = -\nabla\phi$, though we will assume that there is only the inductive electric field. For the rotating frame, the Lorentz force equation (eq. 4.17), then becomes

$$m\frac{d\vec{w}}{dt} = q\left(\vec{E}_{induction} + \vec{w}\times\vec{B}\right) - m\left(2\vec{\Omega}\times\vec{w} + \vec{\Omega}\times\vec{\Omega}\times\vec{r}\right), \tag{4.19}$$

where $\vec{w}$ is the velocity in the rotating frame.

We will work in the rotating frame because it is very close to the guiding center frame, or the plasma rest frame, in the absence of the motion associated with field stretching. The induction electric field that we use to stretch the field produces a guiding center drift velocity

$$\vec{v}_D = \frac{\vec{E}_{induction}\times\vec{B}}{B^2} , \tag{4.20}$$

which must be accounted for when determining a particle's thermal energy, which is defined with respect to the (drifting) guiding center. Additionally, we drop the term in equation 4.19 associated with the Coriolis force, and retain only the component of the centrifugal force that is parallel to $\vec{B}$ so that the final equation of motion solved in the LSK simulation is

$$m\frac{d\vec{w}}{dt} = q\left(\vec{E} + \vec{w}\times\vec{B}\right) - m\left(\vec{\Omega}\times\vec{\Omega}\times\vec{r}\right)\cdot\hat{b}, \tag{4.21}$$

where $\hat{b}$ is a unit vector along the magnetic field. We justify dropping the Coriolis force term because the effect of the Coriolis force on an outward-moving plasma is to produce a drift opposite to the rotational flow direction, which would bend the field line. This effect is independent of particle energy. Magnetopause currents or magnetic tension would provide a restoring force that tends to straighten the field line and maintain rigid rotation; however, we have not included either the field bendback or those forces in our simulation so we also remove the Coriolis force for consistency and focus on the consequences of outward displacement of the plasma and flux tubes. Similarly, we neglect the component of the centrifugal force perpendicular to $\vec{B}$ because the effect is to produce an azimuthal drift, which will depend on ρ (though, like the Coriolis force, is independent of particle energy), and can still be ignored because we have assumed complete azimuthal symmetry. Finally, we assume the field lines are rigidly rotating with a rotation period of 20 hours, of half of Jupiter's rotation period, for consistency with the subcorotational flow velocities observed in the middle magnetosphere.

4.4.3 Electric and magnetic fields used in this simulation

We represent Jupiter's magnetic field by a simplified, axisymmetric, and time-varying model developed from the *Khurana* [1997] field. This field can be derived from two scalar stream functions, *f* and *g*, such that

$$\vec{B} = \nabla f \times \nabla g \tag{4.22}$$

which is possible because $\vec{B}$ is divergenceless. The Euler potentials *f* and *g* are constant along a field line. For simplicity, we assume an axially symmetric magnetic field, so that the centrifugal and jovigraphic equators are collocated, with no bendback or lag. The field is constructed according to the following stream functions:

$$f(\rho,\varphi,z,t) = M_J \frac{\rho^2}{\left(z^2+\rho^2\right)^{3/2}} - C_1(t)\rho\left[\tanh\left(\frac{r_{01}(t)}{r}\right)\right]^{A1} \operatorname{lncosh}\frac{z}{D_1}$$
$$-\frac{A(t)}{B(t)^2}e^{-\rho B(t)}\left(B(t)\rho+1\right)-\frac{C(t)}{D(t)^2}e^{-\rho D(t)}\left(D(t)\rho+1\right)$$
$$-\frac{E(t)}{F(t)^2}e^{-\rho F(t)}\left(F(t)\rho+1\right)+\frac{G(t)\rho^2}{2}$$

$$g(\rho,\varphi,z,t) = \varphi\,. \tag{4.23}$$

Here ρ, φ, and z define the cylindrical coordinate system; M_J is the dipole moment; r is the spherical radial distance; A_1 and D_1 are constants, and the remaining terms ($C_1(t)$, $A(t)$, $B(t)$, etc.) vary linearly with time. The first term in the stream function f contains the contributions of the dipole field, while the remaining, time-varying, terms contain the field stretching due to the current sheet.

From equation 4.22, the field can be written as

$$\vec{B} = \left\{-\frac{1}{\rho}\frac{\partial f}{\partial z}, \frac{\partial g}{\partial \rho}\frac{\partial f}{\partial z}, \frac{1}{\rho}\frac{\partial f}{\partial \rho}\right\} = \left\{-\frac{1}{\rho}\frac{\partial f}{\partial z}, 0, \frac{1}{\rho}\frac{\partial f}{\partial \rho}\right\} \tag{4.24}$$

such that the components of the magnetic field in cylindrical coordinates are

$$B_\rho(t) = \frac{3M_J\rho z}{r^5} - C_1(t)a_1 r_{01}(t)\frac{z}{r^3}\left(\tanh\left(\frac{r_{01}(t)}{r}\right)\right)^{A1-1}\left[\sec h\left(\frac{r_{01}(t)}{r}\right)\right]^2 \operatorname{lncosh}\left(\frac{z}{D_1}\right)+$$
$$\frac{C_1(t)}{D_1}\left(\tanh\left(\frac{r_{01}(t)}{r}\right)\right)^{A1}\tanh\left(\frac{z}{D_1}\right)$$
$$B_\varphi = 0 \tag{4.25}$$
$$B_Z = \frac{M_J(2z^2-\rho^2)}{r^5} + C_1(t)a_1 r_{01}(t)\frac{\rho}{r^3}\left(\tanh\left(\frac{r_{01}(t)}{r}\right)\right)^{A1-1}\left[\sec h\left(\frac{r_{01}(t)}{r}\right)\right]^2 \operatorname{lncosh}\left(\frac{z}{D_1}\right)$$
$$-\frac{C_1(t)}{\rho}\left(\tanh\left(\frac{r_{01}(t)}{r}\right)\right)^{A1}\operatorname{lncosh}\left(\frac{z}{D_1}\right)+A(t)e^{-\rho B(t)}+C(t)e^{-\rho D(t)}+E(t)e^{-\rho F(t)}+G(t)$$

The resulting field is shown in Figure 4.5.

The induction electric field must be consistent with the time variations in the magnetic field to satisfy equation 4.18. The magnetic field can be written as the curl of a vector potential $\vec{A}$, so that

$$\vec{B} = \nabla \times \vec{A} = \nabla f \times \nabla g = \nabla \times \left(f \nabla g \right) \tag{4.26}$$

and

$$\vec{A} = f \nabla g = \frac{f}{\rho} \hat{\varphi}. \tag{4.27}$$

Then by equation 4.18

$$\vec{E}_{induction} = -\frac{\partial \vec{A}}{\partial t} = -\frac{1}{\rho} \frac{\partial f}{\partial t} \hat{\phi}. \tag{4.28}$$

where f is the scalar Euler potential from equation 4.23.

The temporal variations in the magnetic field were constructed to mimic the effect of field line stretching, which occurs over several hours as the field lines rotate from noon to dusk. The model reproduces two main observed features of the field changes from noon to dusk. The first is that the equatorial crossing point of the flux tube moves radially outward by as much as ~35 R_J from noon to dusk as the magnetopause distance increases from ~60 R_J at noon to ~85 R_J at dusk in the compressed case, or from ~90 R_J at noon to ~125 R_J at dusk in the expanded case [*Joy et al.*, 2002]. The second feature is that the field is more dipolar (i.e., has a larger radius of curvature) at dusk than at noon. Figures 4.6 and 4.7 show how the model field lines evolve with time, assuming a 5 hour time scale for the rapid flux tube expansion.

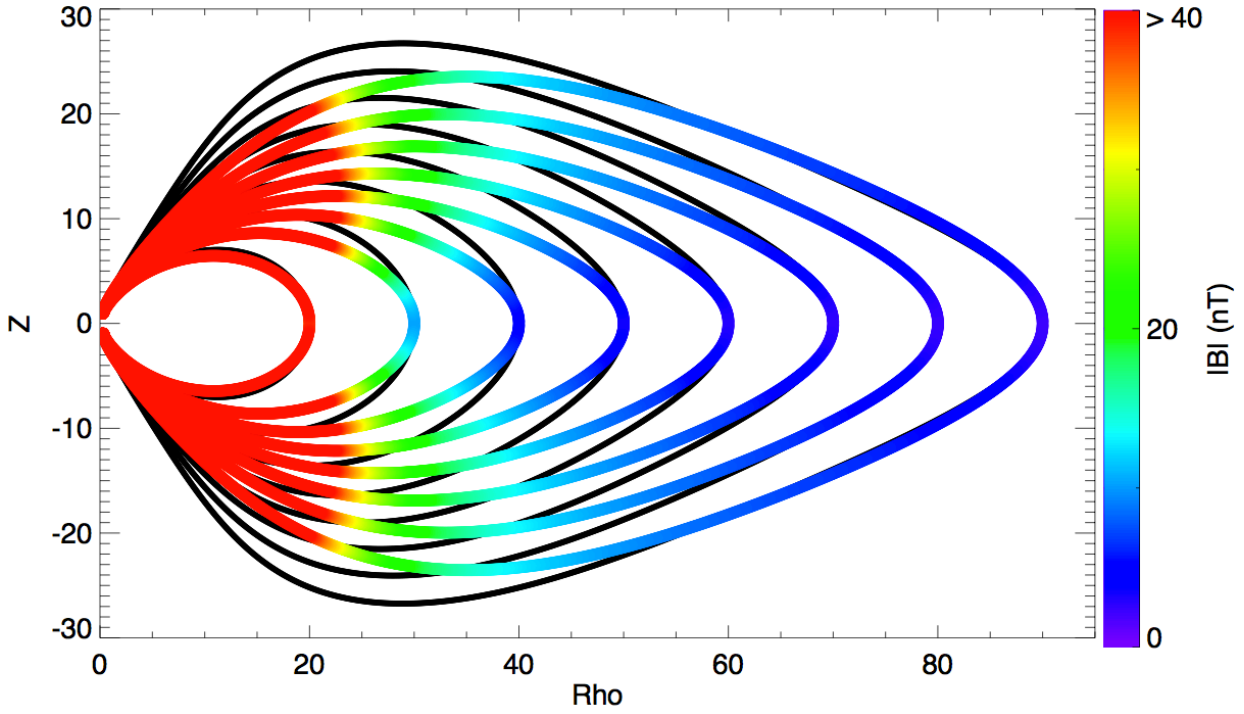

Figure 4.5: Model magnetic field configuration, shown in a meridional plane. The colored lines show the configuration at time T=0, with the color indicating the field magnitude, while the black lines show the field configuration 5 hours later at the same equatorial crossing points. See Figure 4.6 for an illustration of how the initial (color) field lines stretch over time for rapid expansion case.

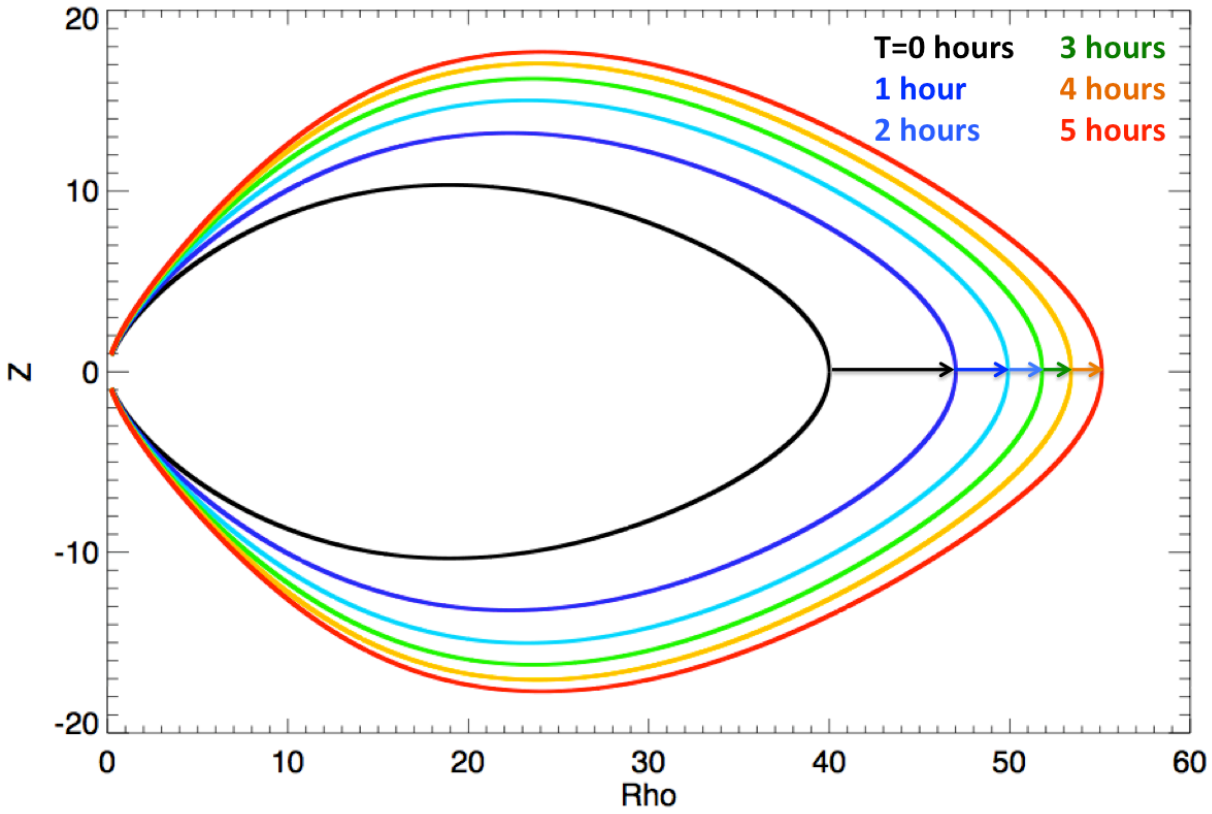

Figure 4.6: Time evolution of a model field line starting with an equatorial crossing distance of 40 R_J then stretching radially outward over 5 hours.

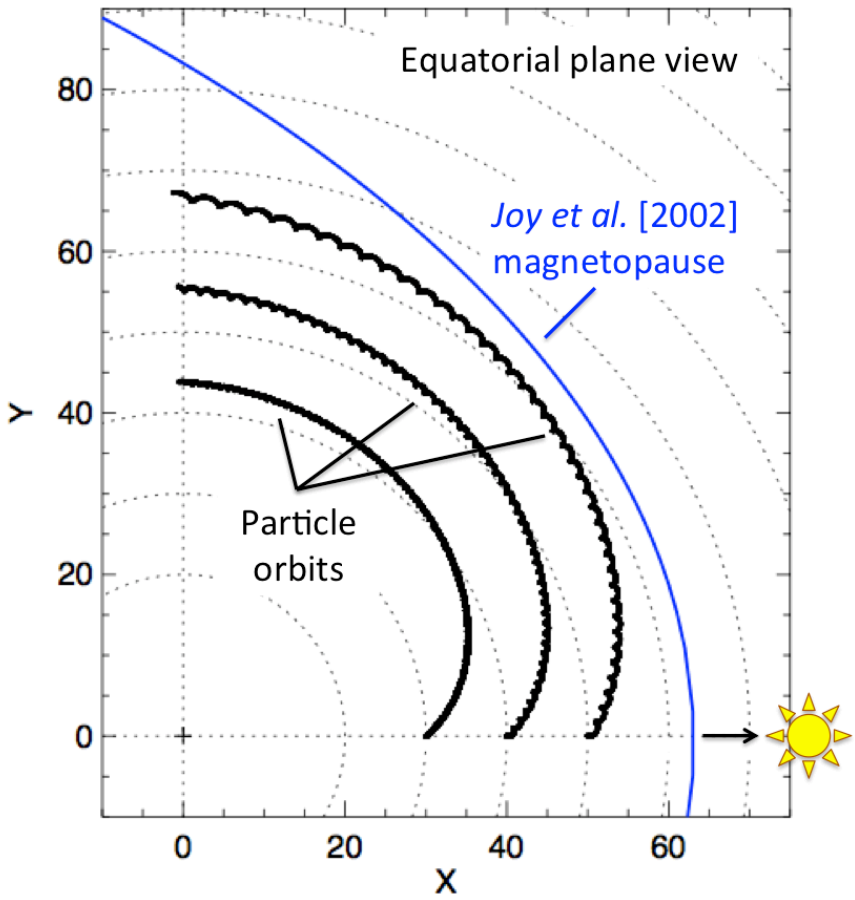

Figure 4.7: Evolution of a 90º pitch angle particle in the equatorial plane showing outward motion from noon to dusk.

4.4.4 Model limitations

Our work is intended as a proof-of-principle to compare the effects of rapid flux tube expansion to adiabatic expansion in a rotating system. Therefore, we have made several simplifying assumptions in constructing our simulation, ranging from the axially-symmetric magnetic field model to the fact that we simulate not an entire magnetosphere, but just one representative flux tube in the noon-to-dusk local time quadrant. In general, these simplifications have the result of easing our computing requirements and allowing us to isolate the processes, flux tube expansion and rapid rotation, that are relevant to our study. In addition, our model also

has some important limitations, and is not fully self-consistent. In loading the flux tube we did not require balance between the forces exerted by the plasma particles and magnetic pressure and curvature forces, and in later time steps we do not allow the plasma to influence the magnetic field geometry or affect the particle distributions. Among other implications, this means that the particle distributions will not scatter in pitch angle even if the distribution function is anisotropic. Since the time scale for pitch angle scattering is short (~one quarter of a bounce period or shorter [*Treumann and Baumjohann*, 2001]), we would expect some pitch angle scattering to occur even during the 5-hour time scale for rapid flux tube expansion. Therefore, any anisotropy that exists at the end of our simulation run is likely to be an overestimate, since in reality at least some of the distribution would have re-isotropized through pitch angle scattering.

4.4.5 Testing for accuracy

With the time-varying field model established, the next step in developing our LSK simulation was to test the output to ensure that the model was working correctly. The code used in this simulation was written specifically for this work, though it was modeled after existing LSK code [e.g., *Ashour-Abdalla et al.*, 1992], and accuracy is a particular concern with the development of new code. We have performed all operations with double-precision numbers, and required numerical precision to at least 5 significant figures.

Wherever possible, we have tested our results for both numerical and physical accuracy. For example, we confirmed that, in the absence of the centrifugal force, our Runge-Kutta method conserved, to at least 5 significant figures, energy and the first and second adiabatic invariants. These tests were performed using a few sample particles with various initial starting positions, energies, and pitch angles. We also confirmed that particle energy and bounce motion in both the

inertial and rotating frames proceeded according to our physical expectations (as outlined in section 4.3), again for particles with a range of initial conditions. Finally, we have thoroughly tested our method of field line expansion, ensuring that the outward drift velocity is consistent with the induction electric field and time variations in the magnetic field model (eqs. 4.18 and 4.20), and that the first adiabatic invariant is still conserved under the field line expansion. The second adiabatic invariant is not conserved when the field line expansion time scale is only 5 hours, but we found that increasing the expansion time scale so that it was long compared to particle bounce periods increased the precision with which J was conserved, as expected.

4.4.6 Loading the field lines

After checking our simulation code with a few dozen test particles, we became ready to fully load the field lines with particles representing the complete distributions in energy and pitch angle. We loaded particles on a flux tube with an initial 40 R_J equatorial crossing distance; we chose this distance because it is within both the compressed (~60 R_J) and uncompressed (~90 R_J) magnetopause at noon, but also far enough that the outward expansion would cover a significant distance.

Selecting an appropriate initial distribution function was a crucial step because as we discussed in section 4.3, whether flux tube expansion results in a net increase or decrease in energy depends on a variety of factors, including the initial energy, position, and pitch angle distributions of particles on the field line. Since our results would depend strongly on our choice of the initial distribution function, we wanted to begin with a distribution function that would remain constant in the presence of a time-independent magnetic field in the rotating frame. Therefore we would be able to attribute any changes to the pitch angle or energy distribution to

the effects of outward expansion. In the absence of rotation such a steady-state distribution could be constructed using an isotropic Maxwellian with a constant density along the flux tube. However, we know that the outward-directed centrifugal force opposes individual particle inward motion, causing particles to mirror at larger radial distances than they would if they were not rotating, therefore confining particles to near the centrifugal equator and altering the plasma density along the flux tube. Therefore, we must account for the effects of the centrifugal force when constructing a steady-state distribution functions for plasma on a rotating flux tube.

Huang and Birmingham [1992] derived a function for density along the flux tube by assuming a bi-Maxwellian equatorial distribution function and using the Vlasov equation,

$$\frac{\partial f}{\partial t} + \vec{v} \cdot \nabla_{\vec{x}} f + \vec{F} \cdot \nabla_{\vec{v}} f = 0, \tag{4.29}$$

where for a rotating system the force $\vec{F}$ includes both the Lorentz and centrifugal forces, as in equation 4.21, to determine how the distribution function evolves along the field line. Though they began with a bi-Maxwellian distribution at the equator, a similar approach can be used to calculate the distribution function along the field line, and therefore the density, given a Maxwellian distribution at the equator. The equatorial Maxwellian distribution function is given by

$$f(v) = Ae^{-\frac{mv^2}{2kT}}, \tag{4.30}$$

where k is the Boltzmann constant, T is temperature, and the constant $A = n_0 \left(\frac{m}{2\pi kT}\right)^{3/2}$, where n_0 is the equatorial density. Solving for the distribution function at an arbitrary point (ρ,z) on the field line leads to:

$$f(\rho, z, v) = Ae^{-\frac{mv^2}{2kT}} e^{\frac{m(\rho^2 - \rho_e^2)\Omega^2}{2kT}}, \tag{4.31}$$

where ρ_e is the field line's cylindrical radial distance at the equator. (Note that this expression is consistent with the result derived by *Huang and Birmingham* [1992] using a bi-Maxwellian, after setting $T_{\parallel} = T_{\perp}$.)

The density at a point (ρ,z) on the field line is found by integrating the distribution function in equation 4.31 over velocity space, which yields

$$n(\rho) = n_0 e^{\frac{m(\rho^2 - \rho_e^2)\Omega^2}{2kT}}. \tag{4.32}$$

This expression describes how the density varies along a flux tube under the effect of the centrifugal force. Note that the density fall off is proportional to Ω and inversely proportional to kT, so a faster rotation period or lower temperature means that the plasma is confined to the centrifugal equator, but hot plasma with a high temperature would be able to overcome the effects of the centrifugal force and fill the flux tube more uniformly. For a dipole field, $\rho_e^2 - \rho^2 \approx z$, so equation 4.32 becomes

$$n(\rho, z) \approx n_0 e^{-\frac{mz\Omega^2}{2kT}}, \tag{4.33}$$

which is the familiar exponential scale height relationship derived for a rotating system by several authors using different approaches [*Gledhill*, 1967; *Hill and Michel*, 1976; *Bagenal and Sullivan*, 1981; *Vasyliūnas*, 1983].

The initial energy and density distribution we used in this simulation is illustrated in Figure 4.8. Panels A and B shows the initial density distribution along the field line, following equation 4.32, with color indicating density in panel B. Particles were placed at points with a 0.1 R_J separation along the field line, from the equatorial crossing point at 40 R_J in to 20 R_J, which we chose as our inner cutoff, because the number of particles inside of this distance was negligible compared to the number of particles launched at the equator. (To account for this cutoff we also placed a reflecting boundary at 18 R_J, such that any particle whose bounce motion

took it inside of 18 R_J would be reflected back with the same energy and supplementary pitch angle, to ensure the density of particles in the steady-state solution would remain constant.) Particles were launched at random gyrophase, and for the energy and pitch angle distribution we used an isotropic Maxwellian with a temperature of 2 keV, following equation 4.31. This temperature is consistent with early observations of the plasma temperature in the middle magnetosphere [*Goertz et al.*, 1979; *McNutt et al.*, 1981], but lower than more recent estimates from Galileo, ranging from 4-9 keV [*Frank and Patterson*, 2002] to 40-80 keV [*Kane et al.*, 1999]. We address this discrepancy and its possible implications for our results in section 4.6. Particles were launched in 36 different energy bins, with equatorial energies ranging from 25 eV to 12 keV, meaning all of the particles had bounce periods long compared to the 5 hour stretching time; at points off the equator we shifted the energy bins by $\frac{m(\rho^2-\rho_{eq}^2)\Omega^2}{2}$, so that the energy distribution at every point along the field would be consistent with the equatorial energy distribution after accounting for the effects of the centrifugal force.

Finally, we tested our initial distribution by running our simulation with a constant magnetic field, but including the centrifugal force, to ensure our initial energy and density distributions were indeed stable in the absence of any field line expansion. Each of the energy, density, and pitch angle distributions showed very little variation over more than 40 hours – several bounce periods, as we show in Figure 4.9. Though there is some scatter, particularly in the pitch angle distribution, the evolution in Figure 4.9 can be compared to similar plots in Figures 4.11 and 4.12, which show much more dramatic changes in the pitch angle and energy distributions, respectively, under adiabatic flux tube expansion.

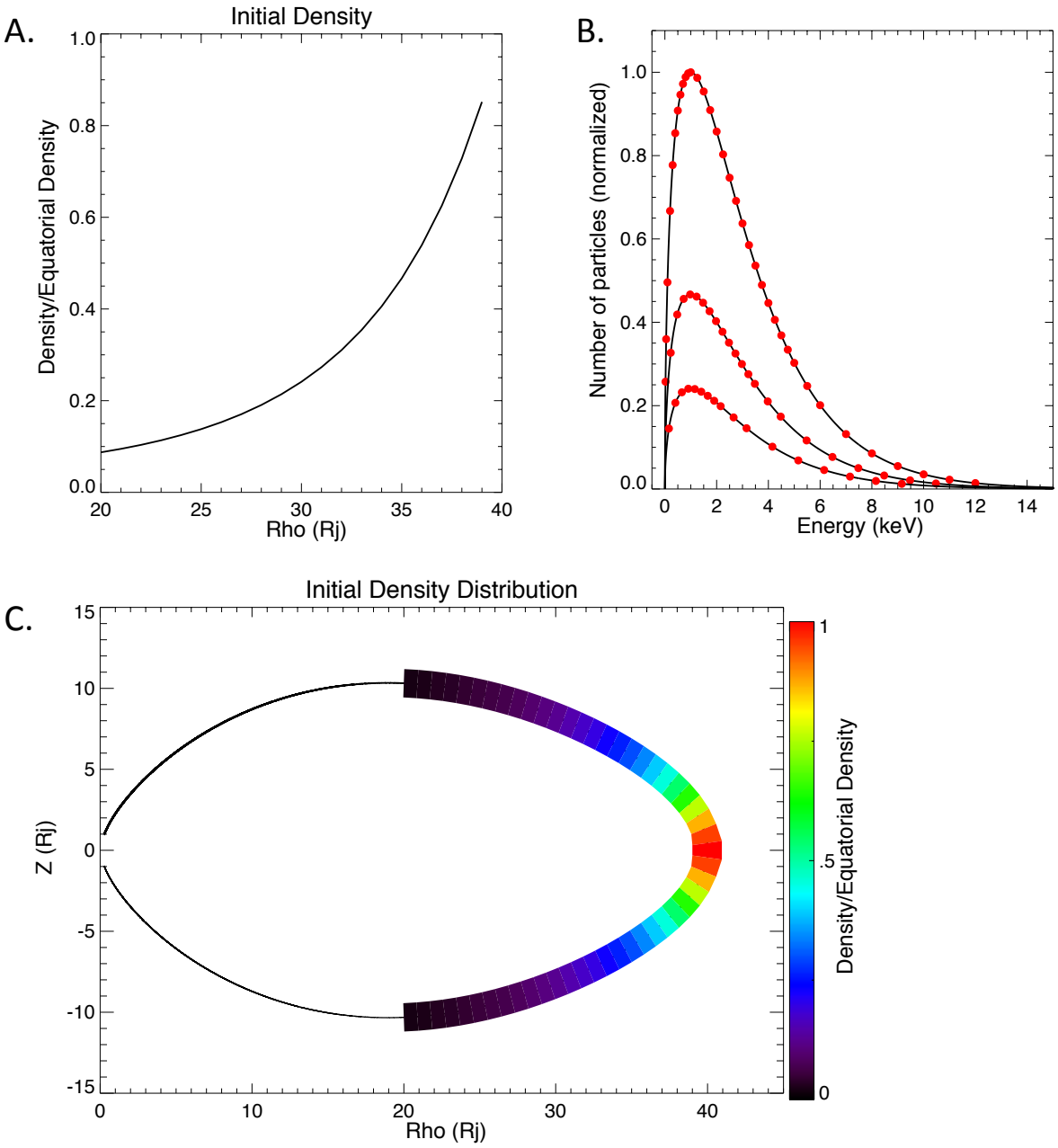

Figure 4.8: Initial density, position, and energy distribution of the particles launched in the simulation. Panels A and C show the density distribution along the field line that crosses the equator at 40 R_J. Panel B shows the initial Maxwellian distribution at three distances along the field line corresponding to ρ = 30, 35, and 40 R_J; the red dots indicate the energies at which we have launched particles. The three curves, which represent the number of particles at each energy, have different maximum peaks because the density decreases with distance along the field line.

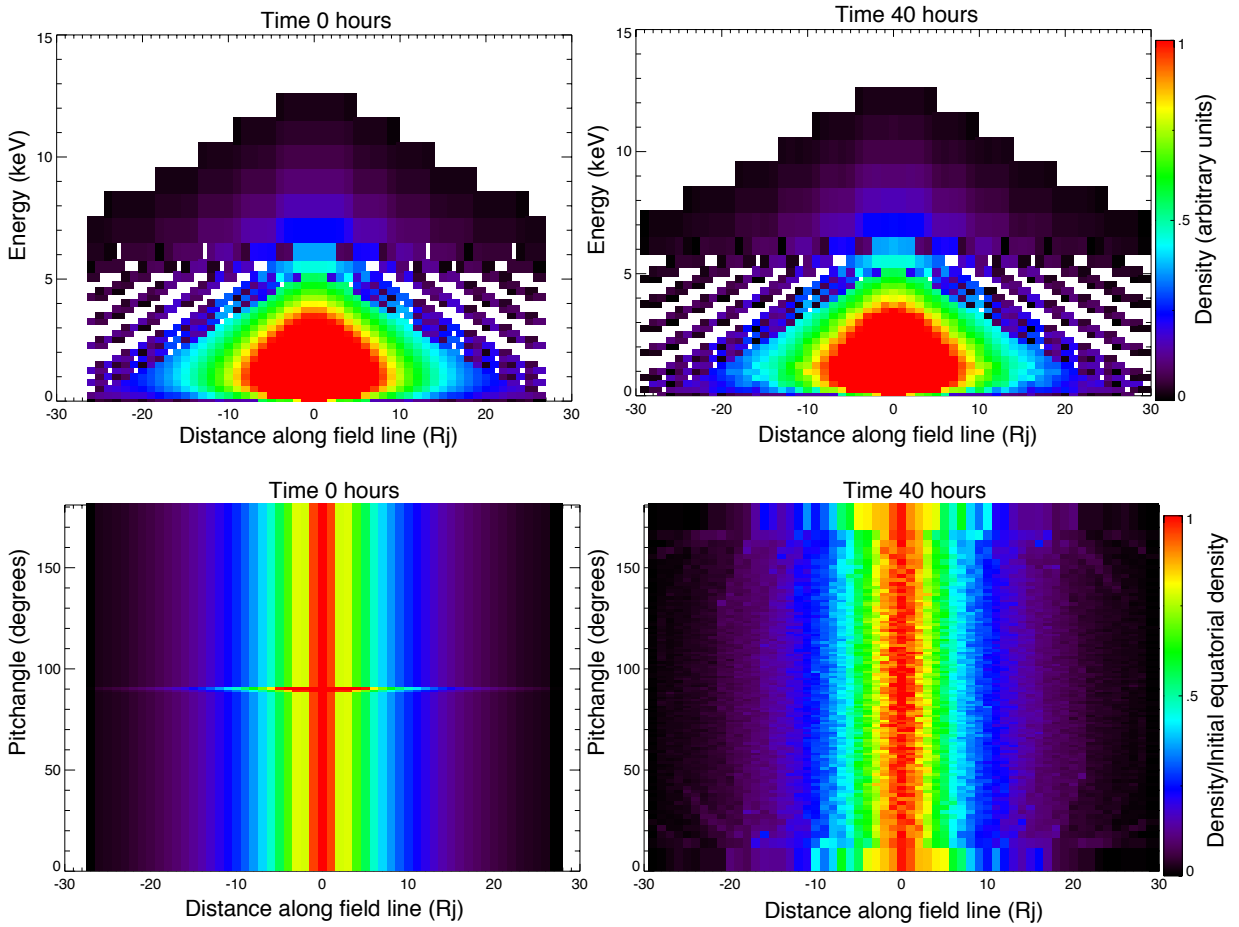

Figure 4.9: Energy and pitch angle distributions at time 0 and time 40 hours, run in a rotating system accounting for the centrifugal force but with a static (non-stretching) magnetic field. This comparison shows that the initial steady-state distribution, described in section 4.4.6, remains essentially constant over at least 40 hours.

4.5 Results

Using the LSK simulation and initial distribution outlined in section 4.4 above, we launched 955,864 particles and tracked their motion through our time-dependent magnetic field model in which the flux tube that initially crosses the equator at 40 R_J ends just beyond 55 R_J. These simulated particles have a mass of 20 m_p. We ran the simulation twice using the same initial conditions: once for a flux tube expansion time scale of 500 hours, which is sufficiently long compared with particle bounce periods to conserve the second adiabatic invariant, and once for an expansion time scale of 5 hours. For the second case, with rapid non-adiabatic stretching,

we chose a time scale of 5 hours because the time scale for the field line stretching and rotation between noon and dusk in Jupiter's magnetosphere is 5 hours, assuming an azimuthal flow speed of half corotation.

In the following subsections we describe how the energy, pitch angle, and spatial distributions evolved with time for each case. We also compare the results of the non-adiabatic, fast stretching case to the adiabatic stretching case, which serves as a baseline for the changes due simply to adiabatic outward expansion. The model we are testing attributes significant changes to the plasma energy density from non-adiabatic acceleration processes, so we must establish how the properties of the plasma will differ at the end of the outward expansion and rotation from noon to dusk if the rotation is slow enough for the expansion to be adiabatic or if the rotation is fast enough for the expansion to be non-adiabatic.

4.5.1 Pitch angle and energy evolution under adiabatic stretching

In section 4.3 we described qualitatively how particle pitch angle and energy distributions evolve in response to adiabatic field line expansion on a rotating flux tube in the rotating frame. We would like to quantify these changes to provide a baseline for comparison to our results for the non-adiabatic, rapid stretching case, since we expect outward expansion alone, regardless of the time scale, will result in changes to the energy and pitch angle distributions. In the absence of an induction electric field, one can define an energy constant that, along with conservation of μ and J, can be used to calculate changes to a particle's energy and pitch angle. However, in our model we have used time variations in the magnetic field to create an induction electric field used to stretch the flux tube, and therefore we must use our simulation to track the outward particle motion, rather than calculating the energy change directly.

Figures 4.10 through 4.13 show the time evolution of the position, density, pitch angle, and energy distributions of particles as the flux tube stretched outward, expanding from an initial equatorial crossing distance of 40 R_J out to just past 55 R_J. These distributions evolve qualitatively as expected from the discussion in section 4.3, that is, we expect that the pitch angle distribution will become more field-aligned, particles will become further confined to the centrifugal equator, and we expect to see a net decrease in energy because the perpendicular energy decreases to conserve μ. Though the centrifugal force acts to increase the parallel energy, the parallel energy may decrease because of conservation of J, and the net result is that the total energy decreases. As the flux tube moves outward its volume increases (the cross-sectional area increases like $1/B$ and the flux tube length increases as it expands) so the density decreases along the field line but maintains a maximum at and decreases little near the equator, as seen in Figure 4.10. In fact, the number of particles in a volume element at the equator increases with time, but the density there decreases because the flux tube volume increases. As the flux tube moves out, the initially isotropic pitch angle distribution, shown in Figure 4.11, becomes more field-aligned near the equator. As the flux tube expands and particles move to large distances off the equator, the pitch angle distribution in those regions peaks near 90º because particles that have reached that distance are at or near their mirror points. Finally, as seen in Figures 4.12-13, which illustrate how the energy distribution evolves in time, there is a net decrease in energy because conservation of μ requires that the plasma's perpendicular energy decrease as it moves out, and the increase in parallel energy from the change of centrifugal potential is not strong enough to compensate for the loss of perpendicular energy.

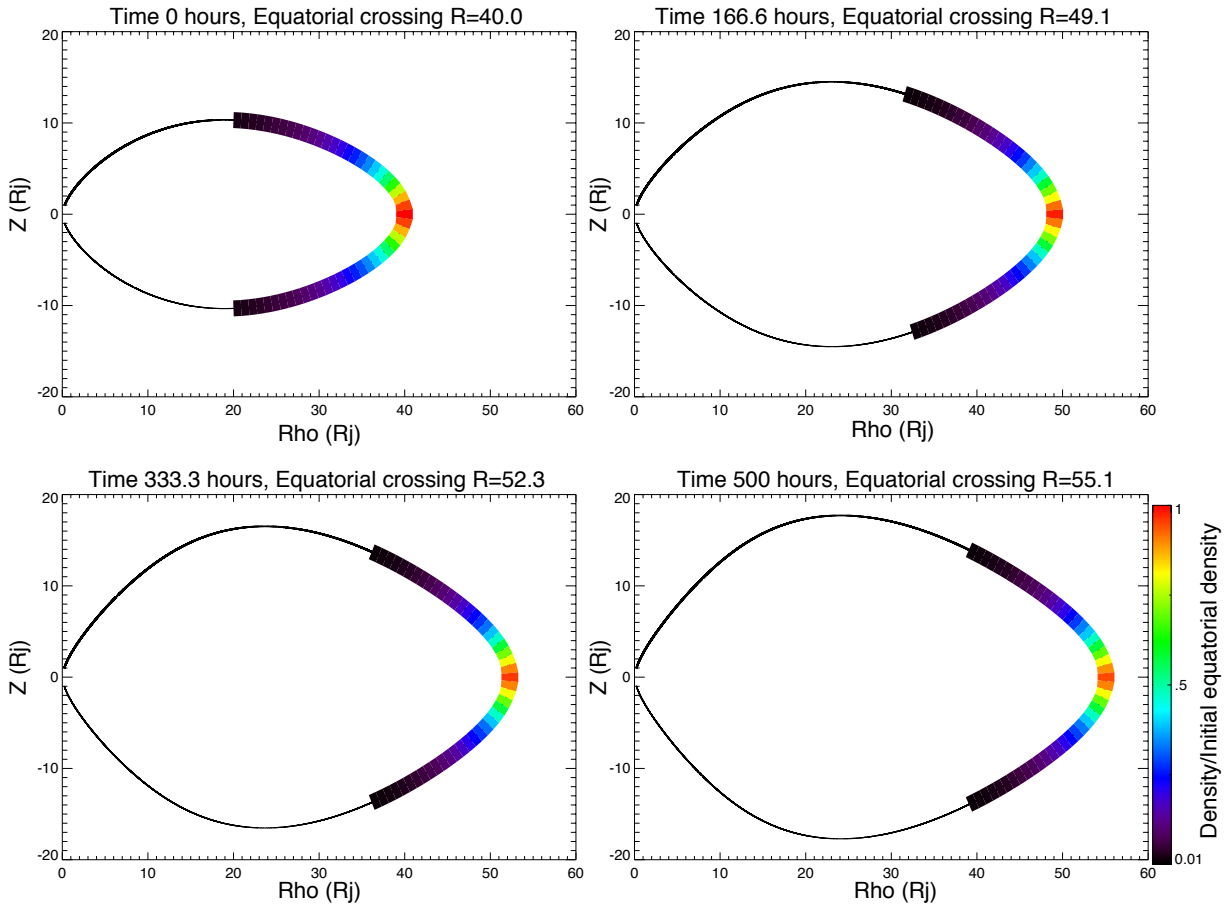

Figure 4.10: Time evolution of density along the field line for the adiabatic, or slow stretching case, in which the field line's equatorial crossing point moves outward from 40 R_J to ~55 R_J over 500 hours. Color indicates density, in bins of equal distance along the field line, relative to the initial density at the equator.

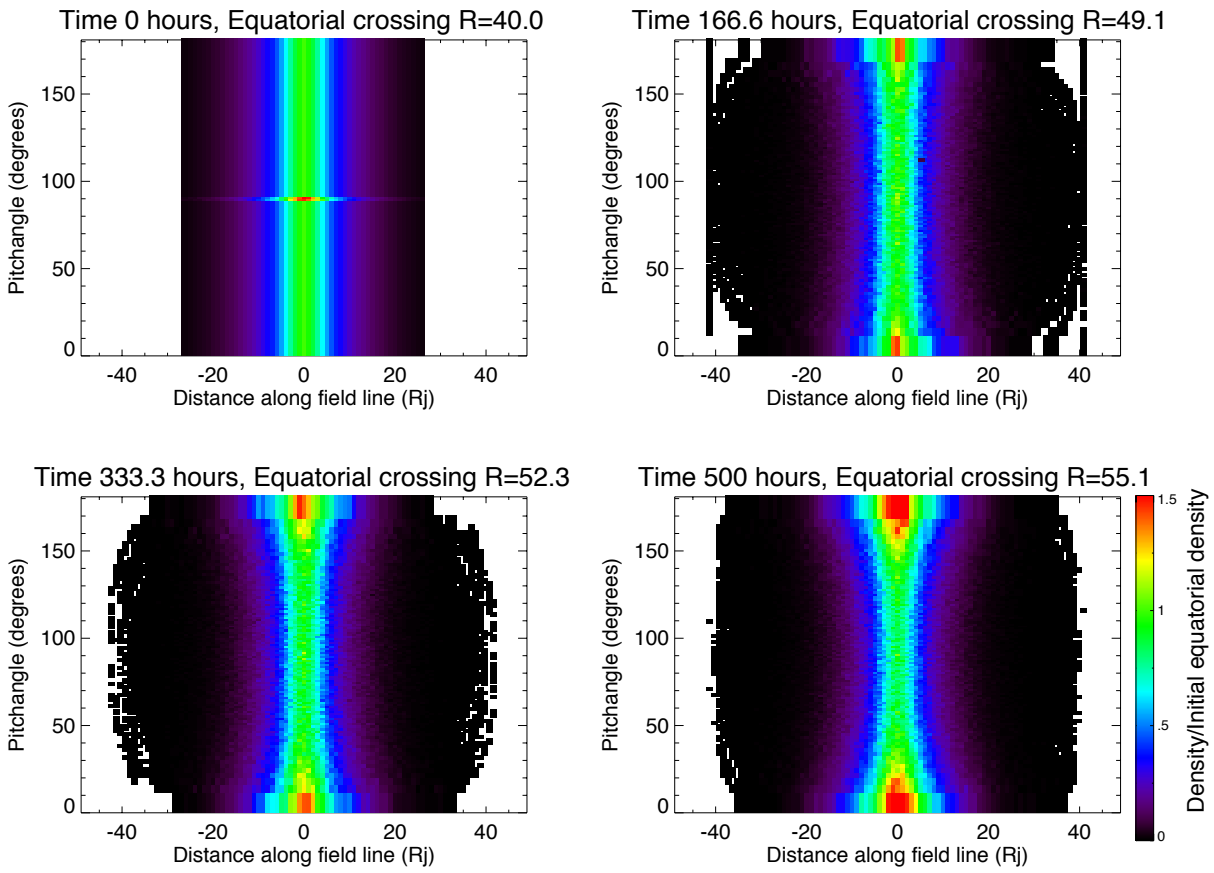

Figure 4.11: Pitch angle distribution for the adiabatic stretching case, shown here as a function of distance along the field line (defined as 0 at the equator, and positive northward). Color indicates density of particles inside pitch angle bins of size d(cos α). The initial distribution consists of vertical color bands (with the exception of a peak near 90 degrees due to binning), indicating the initial isotropic distribution. As the field line stretches outward, particles spread along the field, and the distribution becomes more field-aligned near the equator.

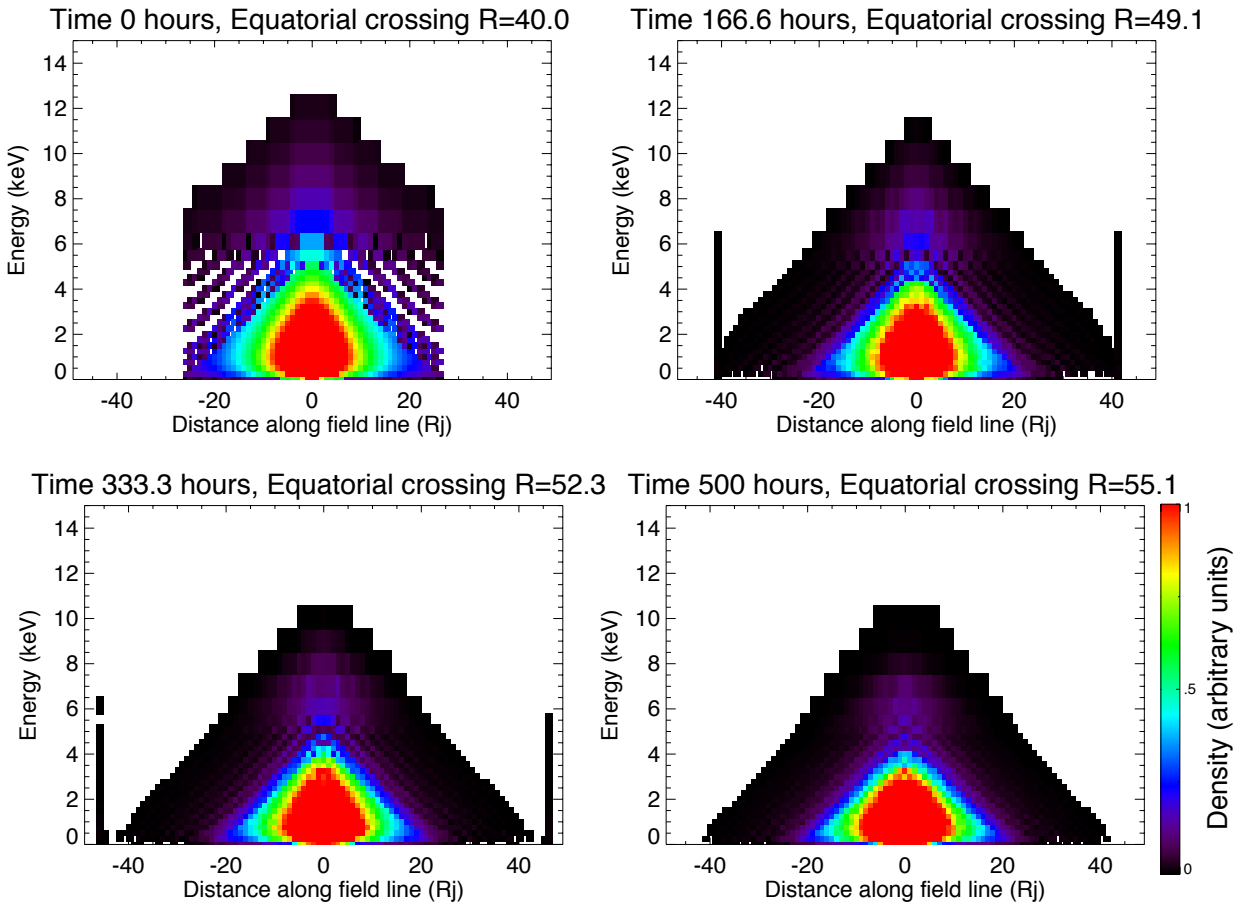

Figure 4.12: Time evolution of the plasma energy distribution as a function of distance along the field line, for the adiabatic stretching case. As the flux tube expands radially outward, the particles move farther along the flux tube and the energy decreases at all points along the field line. Gaps in the initial distribution are due to binning, and the anomalous peaks near the largest distances in some of the plots are due to the reflective boundary requiring particles remain at distances larger than $\rho = 18\ R_J$.

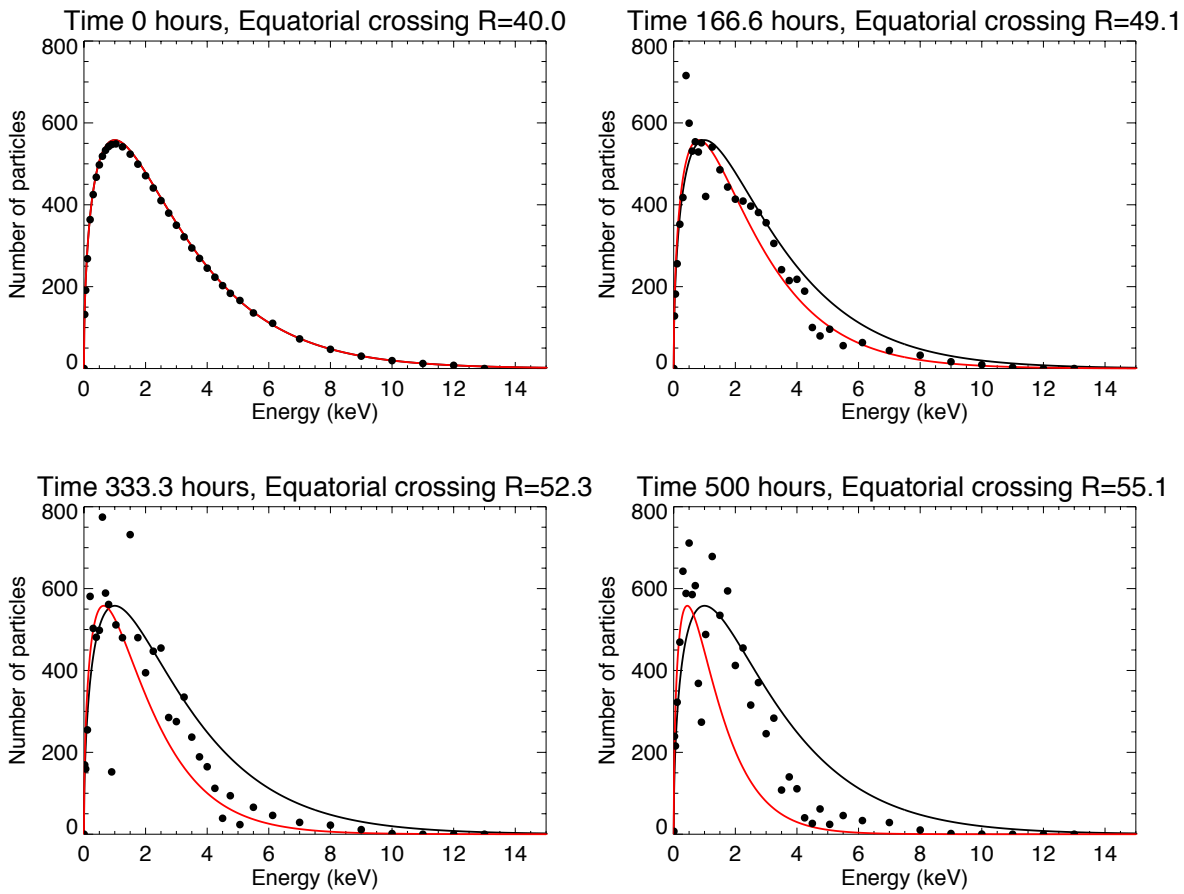

Figure 4.13: Energy distribution at the equator for four different time periods in the adiabatic run. The black curve indicates the starting Maxwellian distribution, with temperature 2 keV, and the red curve indicates how the Maxwellian distribution of 90º pitch angle equatorial particles would change to conserve μ as the flux tube expands and B decreases. There is a fair amount of scatter due to binning, but it appears that the energy distribution remains approximately a Maxwellian, but the temperature decreases with time, as evidenced by the peak shifting to the left and narrowing between ~0 and ~2 keV. However, the energy of the simulated particles (black dots) remains larger than for the 90º pitch angle equatorial particles (red line).

4.5.2 Pitch angle and energy evolution under rapid (non-adiabatic) stretching

Compared to the adiabatic stretching case, for which the particle distributions evolved smoothly, the results from the fast stretching case show much sharper changes, with more variability, which are noticeable very early in the simulation. For example, as early as one

minute into the simulation, the pitch angle distribution has become more field-aligned, specifically in the direction toward the equator, which is consistent with our expectations since the centrifugal force confines particles to the centrifugal equator. The flux tube's initial outward drift velocity is comparable to the thermal speed of a particle with energy of nearly 6 keV, meaning that the equatorial crossing point moves from 40 R_J to ~40.2 R_J in only 60 seconds. In that time, particles in our energy range of interest won't have moved far enough to significantly alter the density distribution (a 1 keV particle will move ~0.08 R_J in 60 seconds), but the outward motion is sufficient to provide enough additional parallel energy to shift the pitch angle distribution by ~2º. Figure 4.14 shows the pitch angle shifts after one minute; panel B shows the overall distribution shift, with bins of pitch angle versus distance along the field line colored according to the change of particle density within each bin. An enhancement is seen near 0º above the equator and near 180º below the equator, or in the direction toward the equator along the field line. Panel D shows the range in pitch angle changes for particles of all energies initially located below the equator, between 1 and 2 R_J along the field line (the range is due to differences in initial energy or position of each particle). Though each individual particle experiences a relatively small shift in pitch angle, the net effect is that the entire distribution in this region is shifted toward 180º (toward the equator), as seen in panels C and D.

As time progresses, the pitch angle distribution continues to shift to the equatorward pitch angles (near 0º above the equator and near 180º below), as seen in the first few panels of Figure 4.15. At the same time, particles are bouncing along the field, so the peak in the pitch angle distribution proceeds through Figure 4.15 in a clockwise manner. Particles that begin in the upper left quadrant of the figure, or located below the equator with anti-field-aligned (toward the equator) pitch angles, will shift to the right as they move along the field, through the equator,

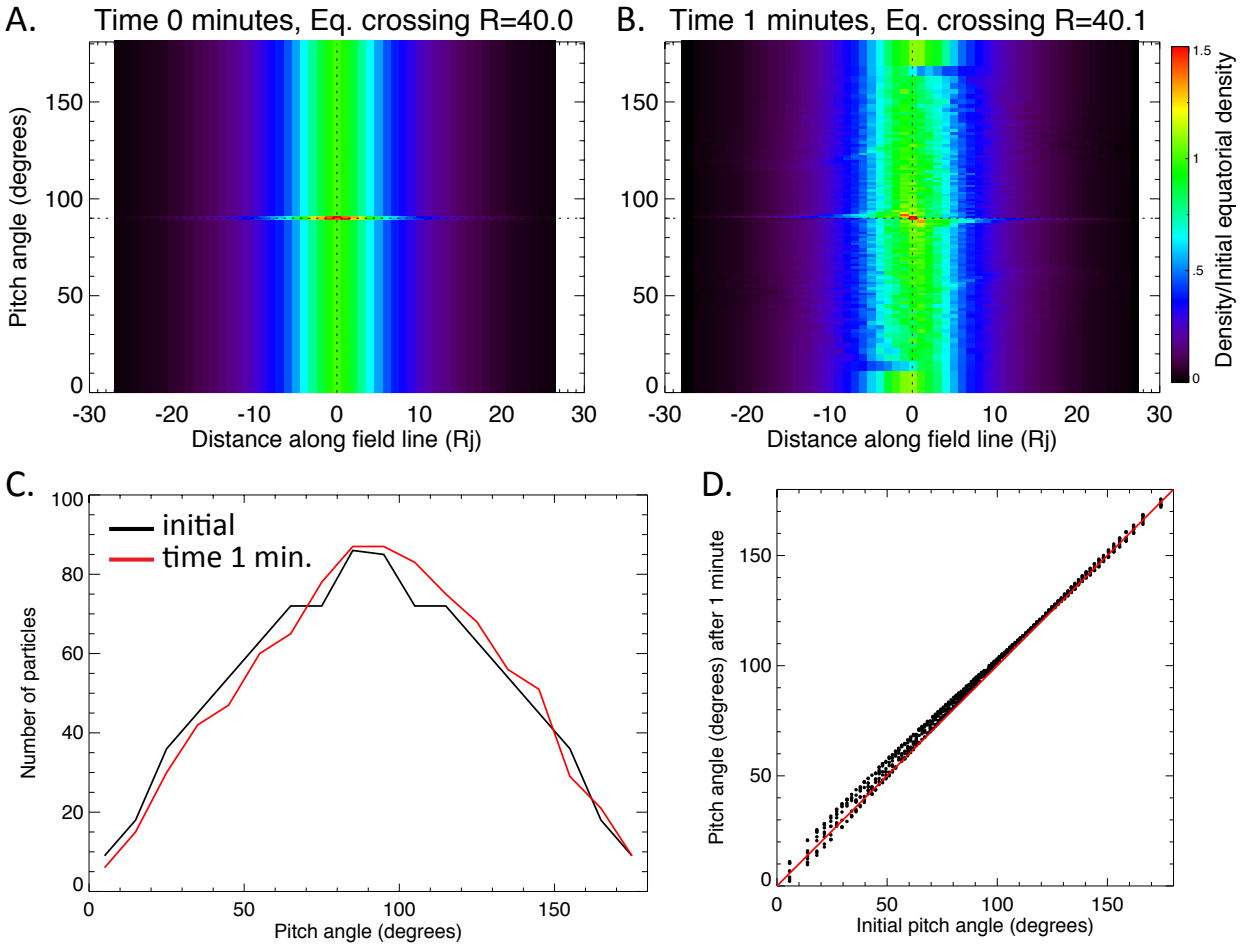

Figure 4.14: Changes to the pitch angle distribution in the first 1 minute of the non-adiabatic stretching case. Panel A: Initial pitch angle distribution. Panel B: Pitch angle distribution after 1 minute for the non-adiabatic stretching case. Panels C and D show the change in the initial pitch angle distribution for particles with equatorial energy of 1 keV, initially located between 1 and 2 R_J along the field line below the equator. Individual particles experience small shifts in pitch angle, but the net effect is that the distribution is shifted toward 180º.

then up along the field. However, as a particle moves up along the field above the equator, its pitch angle will decrease until the particle mirrors at 90º and turns around (moving left in the figure, or back toward the equator), as the pitch angle continues to decrease toward 0º. After the particle passes through the equator, the pitch angle will increase, again going through 90º as the particle mirrors, until the particle returns to its initial position in the upper left quadrant of the

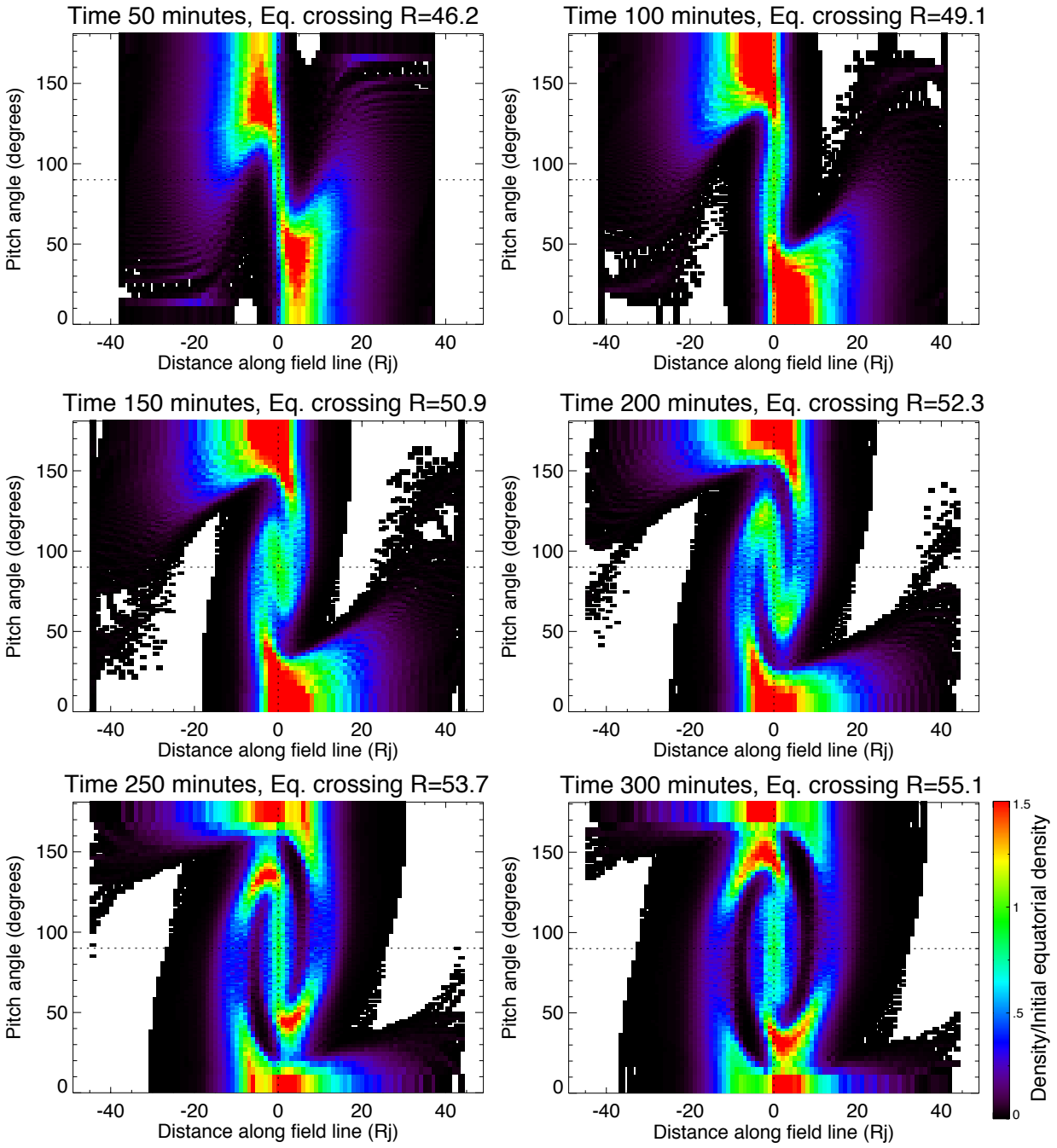

Figure 4.15: As in Figure 4.11, time evolution of the pitch angle distribution, as a function of distance along the field line, but for the rapid stretching case. The initial distribution is shown in Figure 4.14.

figure. This general clockwise swirling pattern can be seen in figure 4.15, and appears to have a periodicity of ~3 hours for half a bounce cycle, which is consistent with the typical bounce periods listed in Table 4.2.

The periodicity seen in the pitch angle distribution is also apparent in the density and energy distributions along the flux tube; the former is plotted in Figure 4.16. As for the adiabatic stretching case, as the flux tube expands, its volume increases, so in general the density along the flux tube will decrease with time, as we observe in the adiabatic case. However, for the non-adiabatic case there are some localized enhancements that can be seen moving along the field. Initially, after 10 minutes, there is an enhanced density at ~10 R_J along the field from the equator, as equatorial particles gain parallel energy and begin to travel to farther distances along the field. After 50 minutes the distribution of low-energy particles and particles with large (near-90º) initial pitch angles returns to the equator, enhancing the density there. Those particles continue their motion along the field line, away from the equator, as is seen by the ~5 R_J off-equator density peaks at time step 100 minutes, and in the pitch angle distribution in Figure 4.15; these density peaks continue moving along the field line through time step 150 minutes, when another equatorial density peak appears, which displays similar motion in the remaining time steps. The energy distribution in Figure 4.17 similarly shows the distribution moving up along the field, with enhancements in the ~2-3 keV energy range at large distances (> 20 R_J) along the field line. Though the peak in the equatorial energy distribution shifts to lower energy as the flux tube moves outward, as occurs in the adiabatic case to conserve μ, equatorial particles are also observed with very large energy (> 12 keV). Overall, the total flux tube energy content is higher for the fast stretching case than for the adiabatic case, as can be seen in Figure 4.18.

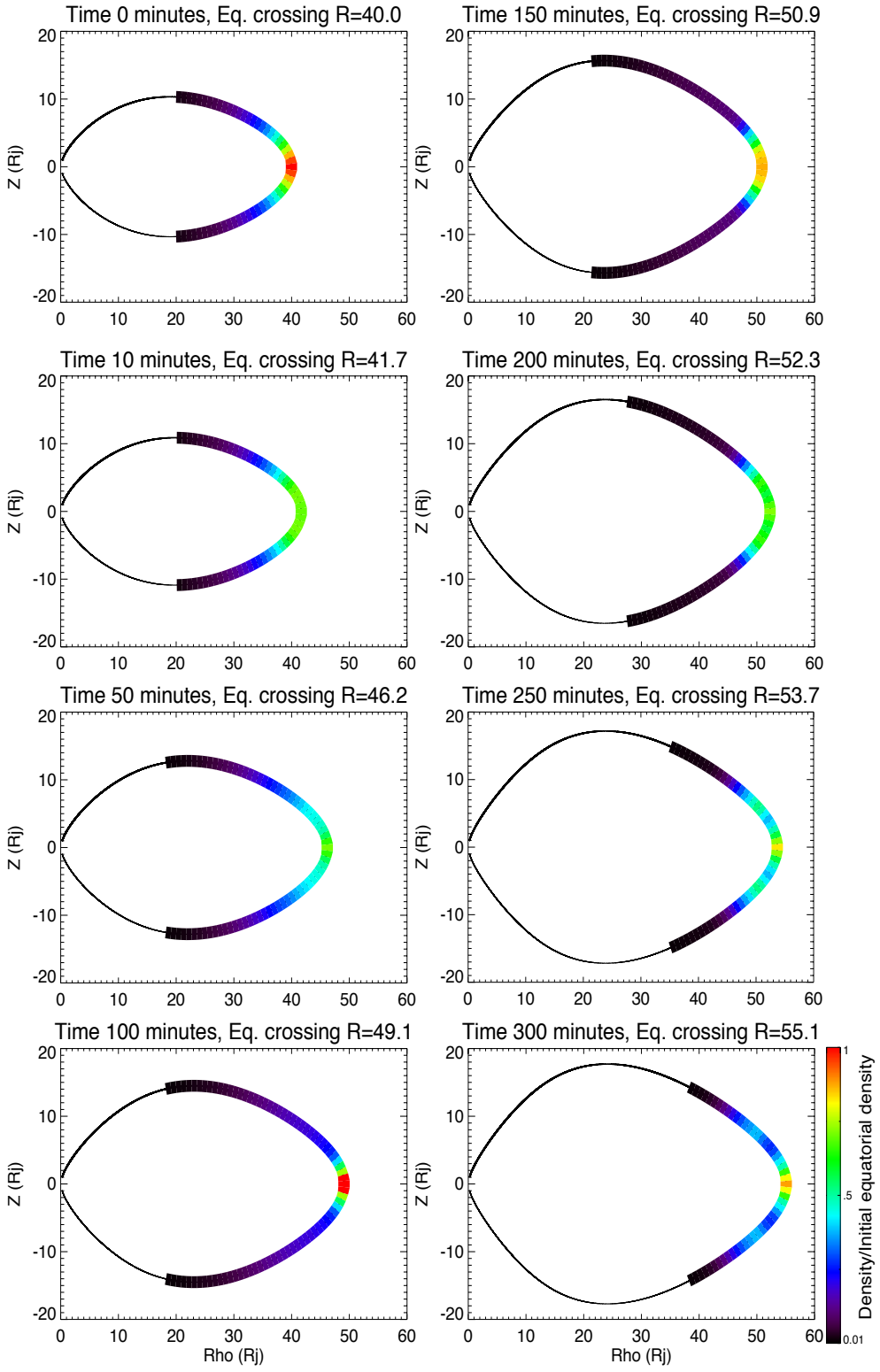

Figure 4.16: As in Figure 4.10, but for the non-adiabatic, or fast stretching, case. Here the field line expansion from 40 R_J to ~55 R_J occurs over only 5 hours.

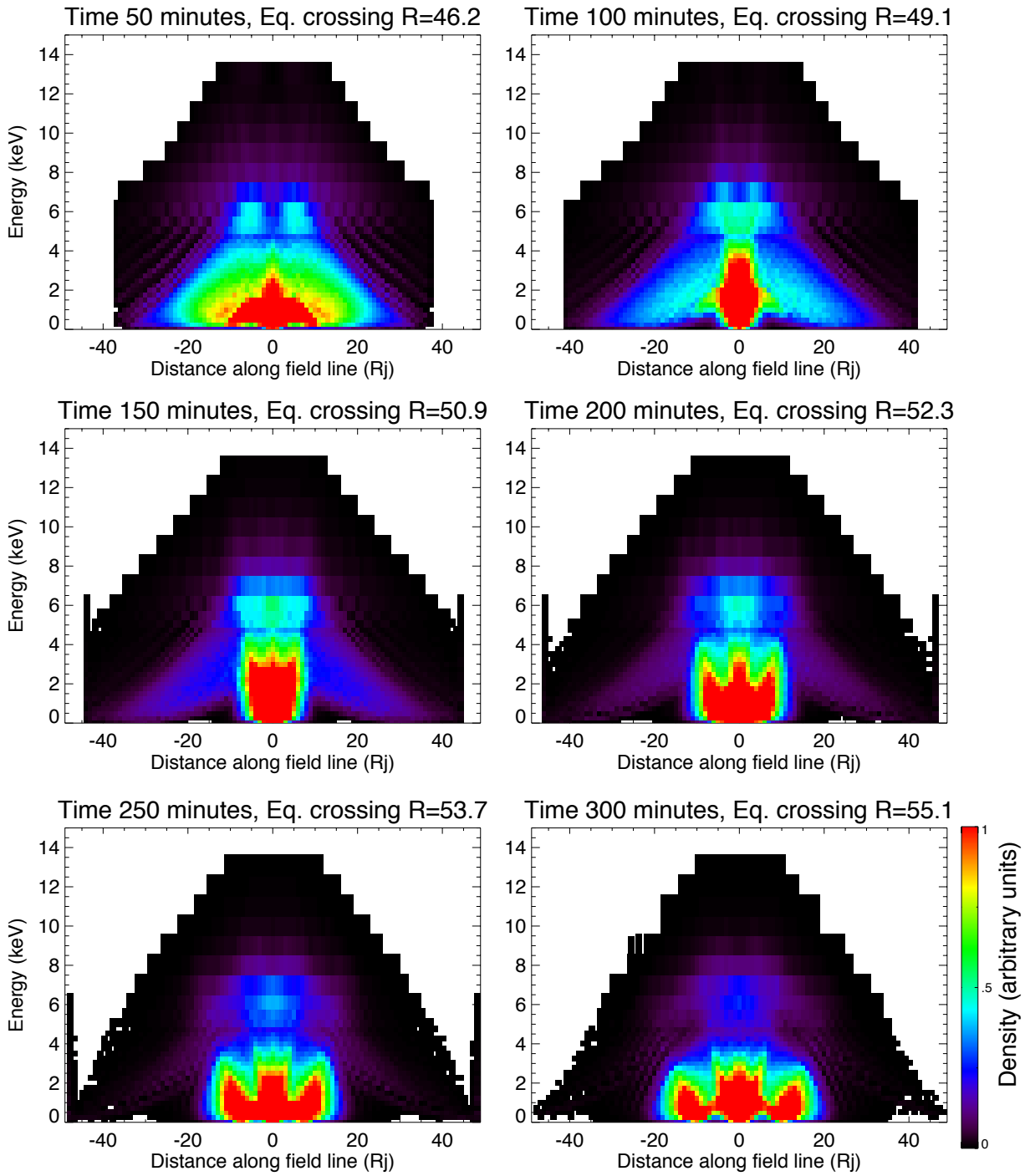

Figure 4.17. As in Figure 4.12, change in density of particles in energy bins as a function of distance along the field line, but for the non-adiabatic case. The initial distribution is the same as in Figure 4.12.

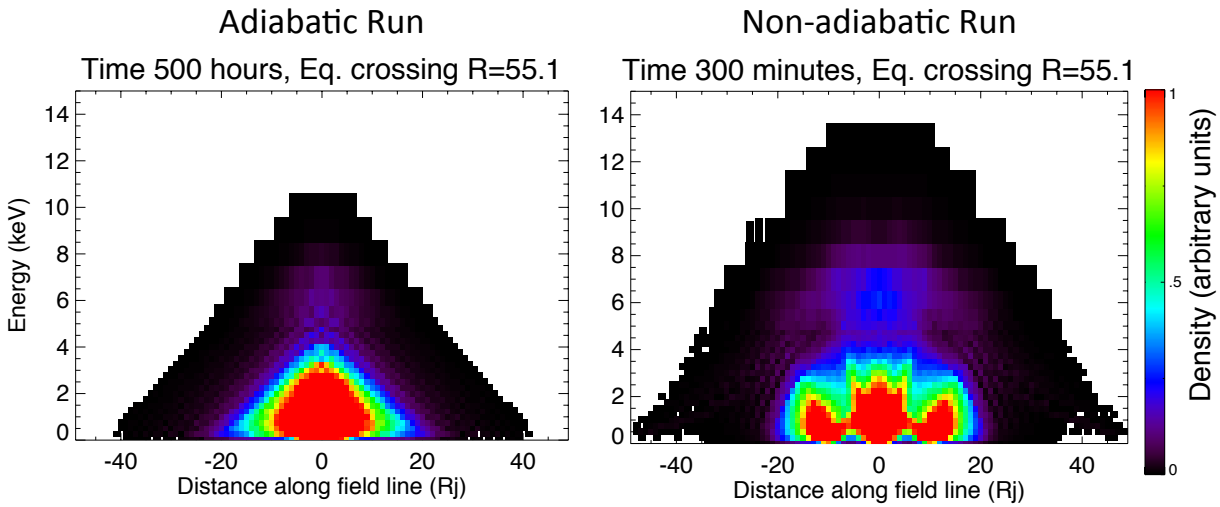

Figure 4.18 Comparison of the final energy distribution for the two simulation runs: adiabatic (left) and fast stretching (right). Compared to the adiabatic case, the fast stretching has more particles at large energies at all points along the field line.

4.6 Discussion

In the previous section we saw qualitatively that rapid, non-adiabatic field line stretching resulted in higher final energy and increased anisotropy compared to adiabatic expansion. But is the relative energy increase enough to produce instability in the plasma sheet and account for the thickening observed from noon to dusk? To answer this question we must examine quantitatively how the total thermal energy evolves for the adiabatic and non-adiabatic cases, and specifically how large an anisotropy develops due to the rapid stretching.

Figure 4.19 compares the evolution of the plasma β, the ratio of the thermal to magnetic pressure, as a function of distance along the field line for the adiabatic and non-adiabatic cases. The initial values, shown in each panel by a dashed black line, peaks near the equator because the density and average thermal energy are highest there and the field magnitude is lowest. We have normalized our particle density such that the initial equatorial β=5, which is consistent with early observations from Jupiter's plasma sheet [*Walker et al.*, 1978; *McNutt et al.*, 1983; *Kane et*

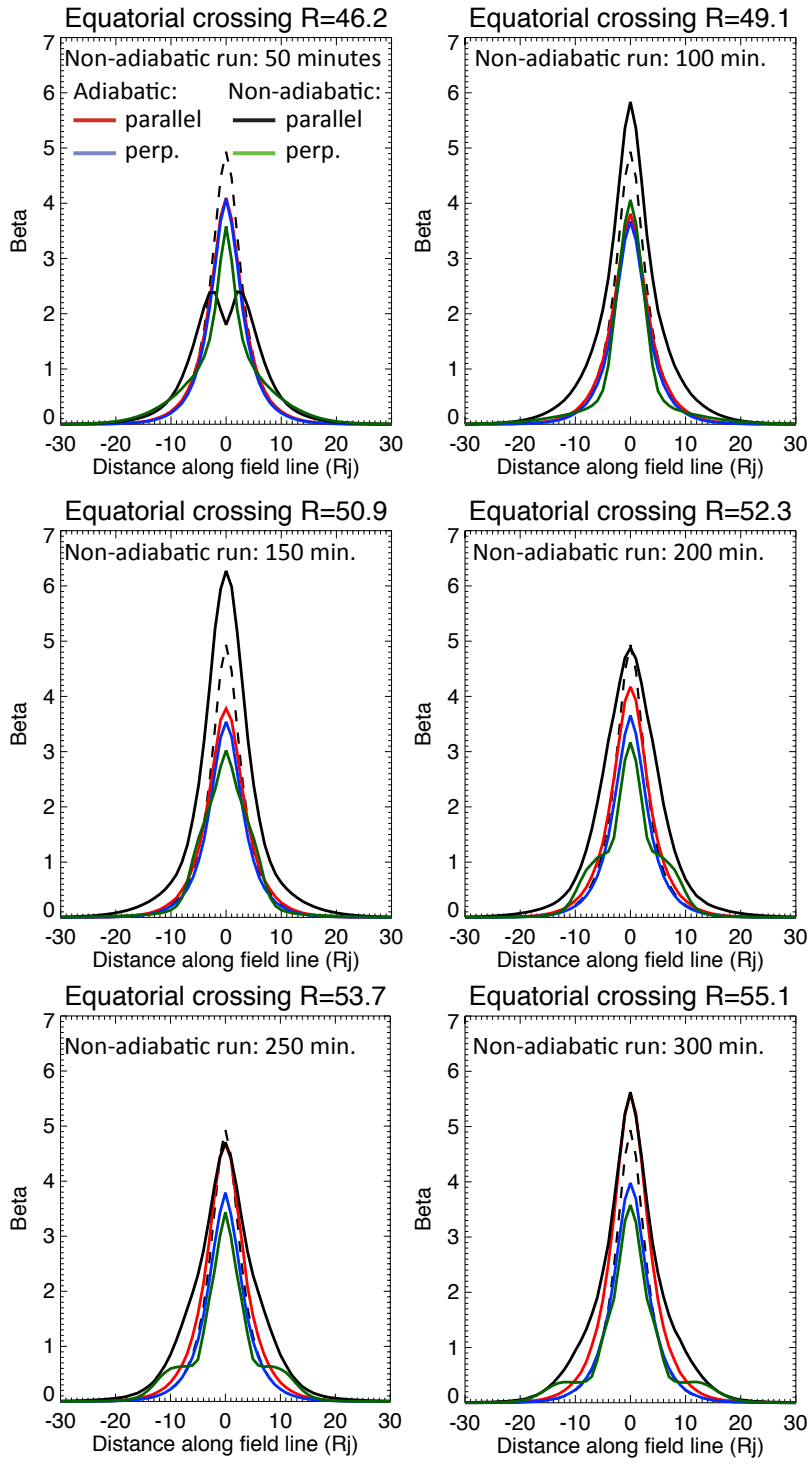

Figure 4.19: $\beta_{//}$ and $\beta_{\perp}$ as a function of distance along the field line. The red and blue lines show $\beta_{//}$ and $\beta_{\perp}$, respectively, for the adiabatic case; the black and green lines show $\beta_{//}$ and $\beta_{\perp}$, respectively, for the non-adiabatic case. The dashed line shows the initial value of $\beta_{//}$ and $\beta_{\perp}$, which were initially equal because we began with an isotropic distribution.

al., 1995], though slightly on the low end of estimates from the Galileo EPD [*Kane et al.*, 1999]. The figure shows that for the adiabatic case, $\beta_{//}$ (red line) initially decreases as the flux tube volume increases, then increases beyond a distance of ~50.9 R_J as the parallel energy increases due to the effects of the centrifugal force. Similarly, for the adiabatic case $\beta_{\perp}$ (blue line) decreases as the flux tube expands to a larger volume, and the perpendicular energy decreases to conserve μ as $|\vec{B}|$ decreases. We showed in section 4.5 that the parallel energy increases much more quickly for the non-adiabatic case than for the adiabatic case, and accordingly, $\beta_{//}$ initially increases (compared to the adiabatic $\beta_{//}$, which initially decreases). After ~150 minutes, the equatorial non-adiabatic $\beta_{//}$ decreases slightly, in part due to the increasing flux tube volume and in part due to particles shifting to higher points along the field line, as evidenced by the relative increase in $\beta_{//}$ at high latitudes. The non-adiabatic $\beta_{\perp}$ decreases at the equator, as expected for conservation of μ and increasing flux tube volume, but decreases more than the adiabatic case does at the equator due to an increase in the number of particles at high latitudes.

What does this tell us about the stability of the plasma sheet? We see that in the latter half of the simulation, equatorial $\beta_{//}$ values are roughly equal for the adiabatic and non-adiabatic cases, but off the equator $\beta_{//}$ is largest for the non-adiabatic case. Compared to the adiabatic case, the non-adiabatic $\beta_{\perp}$ is smaller at the equator and larger at high latitudes; these changes would cause the field to become more dipolar already in early stages of stretching, which is consistent with dipolarization and a thicker plasma sheet. The total energy density increases for the non-adiabatic case compared to the adiabatic case, particularly at high latitudes. Additionally, we can see that the anisotropy, or difference between $\beta_{//}$ and $\beta_{\perp}$, is generally larger for the non-adiabatic case than for the adiabatic case. Returning to the equation for the force density felt by the plasma in the direction perpendicular to the magnetic field,

$$\vec{F}_{\perp} = -\nabla_{\perp}\left[p_{\perp} + \frac{B^2}{2\mu_0}\right] + \left(p_{//} - p_{\perp} - \frac{B^2}{\mu_0}\right)\frac{\vec{R}_C}{R_C^2} + \rho_m\left(\Omega^2\vec{r} - 2\Omega\times\vec{v}\right)_{\perp}. \quad (4.34)$$

As was mentioned in section 4.2.2, force balance requires $p_{//} - p_{\perp} - \frac{B^2}{\mu_0} \approx 0$ because R_C is small at the center of the current sheet, so the second term in equation 4.34 dominates. If the pressure becomes anisotropic such that $p_{//} > p_{\perp} + \frac{B^2}{\mu_0}$, or $\beta_{//} - \beta_{\perp} > 2$, the firehose instability develops. This condition is met as early as ~100 minutes (at ρ ~ 49.1 R_J) for the non-adiabatic case, but is never satisfied for the adiabatic case, where the maximum $\beta_{//} - \beta_{\perp}$ is ~1.8.

Because the simulation did not allow for pitch angle scattering, the relative magnitudes of $\beta_{//}$ and $\beta_{\perp}$ could change, but the fact that the anisotropy is much larger for the non-adiabatic case compared to the adiabatic case suggests that the rapid stretching could contribute to the plasma instability which affects the structure of the plasma sheet and the magnetic field threading it. Additionally, if we had run the simulation self-consistently and allowed the plasma to reisotropize, the pitch angle scattering would transfer momentum from the parallel to the perpendicular degrees of freedom, and $\beta_{\perp}$ would have increased, causing the field to reconfigure at early stages in the simulation.

The observed changes in energy density, $\beta_{//}$, and $\beta_{\perp}$ are all consistent with the non-adiabatic effects leading to field dipolarization, which in turn is consistent with a thickening of the plasma sheet. Our results support the model of *Kivelson and Southwood* [2005] as one plausible explanation for the observed plasma sheet thickening between noon and dusk. One alternate theory was that sunward return flow from tail reconnection at a distance neutral line opposes the dusk corotational flow, causing B_θ to increase and the plasma sheet to thicken. However, we cannot test this idea with our simulation because of certain aspects or assumptions

we made, including a constant azimuthal flow speed, and therefore cannot reject the alternate interpretation.

Finally, we return to our choice for the initial plasma temperature, and what effects that may have on our results here. For both the adiabatic and non-adiabatic runs we launched particles with an initially isotropic Maxwellian distribution with a temperature of 2 keV. While this temperature is consistent with some early observations [*Goertz et al.*, 1979; *McNutt et al.*, 1981], it is much lower than the more recent 4-9 keV [*Frank and Patterson*, 2002] to 40-80 keV [*Kane et al.*, 1999] estimates from Galileo that examined a larger range of particle energies.

Temperature, although properly defined for an equilibrium distribution, typically with a Maxwellian velocity distribution, is a measure of mean energy in a distribution and the term is often used to represent the mean energy. Typically in the magnetospheric plasma, the low energy distribution is Maxwellian and there is a high energy tail; these high energy particles may carry the bulk of the energy density even if they are a small fraction of the number density. The presence of the high energy particles is often handled by introducing a kappa distribution, which is comprised roughly of a low temperature Maxwellian linked to a high energy tail. This allows one to obtain an effective temperature, as defined by the mean energy, that is much higher than that of the temperature that applies to the Maxwellian describing the low energy part of the distribution. The 40-80 keV temperatures given by *Kane et al.* [1999] were calculated from the mean energy of the distribution, and are therefore probably higher than the temperature of the low-energy Maxwellian which is relevant to our analysis.

By selecting an initial temperature of 2 keV and restricting our analysis to particles with initial energies from 25 eV to 12 keV, we have potentially neglected a significant population of high-energy particles. However, in the case of the centrifugal acceleration calculation, the

particles in the high energy tail may make a relatively passive contribution if they react close to adiabatically. In fact, we find that the energy of particles with initial energy of ~12 keV evolve in nearly identical fashions for both the adiabatic and non-adiabatic runs, while particles with initial energies of a few keV or lower show a clear difference between the adiabatic and non-adiabatic runs. This means that in the kappa distribution (whose effective temperature could be ~20 keV), one should focus on the part of the distribution below ~12 keV, which can be approximated as a Maxwellian with a temperature of ~2 keV. By examining how it is affected, we have extracted the important effect of non-adiabatic response to the centrifugal acceleration. In the future we intend to adjust our initial temperature and include higher energies, up to at least 20 keV, in our runs.

4.7 Summary and conclusions

In this chapter we examined the effects of non-adiabatic field line stretching and rapid rotation on pitch angle and energy distributions. We have reviewed how the large spatial scales in Jupiter's magnetosphere and rapid planetary rotation period contribute to the importance of the centrifugal force to particle dynamics. *Kivelson and Southwood* [2005] suggested that these factors are responsible for the thickening of the plasma sheet that occurs as flux tubes expand from noon to dusk, and we have tested this idea with a large scale kinetic simulation.

Following the work of *Northrop and Birmingham* [1982], we have discussed how centrifugal forces affect particle energy and bounce motion, and how energy and pitch angle distributions would evolve under adiabatic expansion in a rotating system. However, a key point in the *Kivelson and Southwood* idea is that bounce periods are long compared to the ~5 hour time scale for field line stretching between noon and dusk, violating the second adiabatic invariant.

We have illustrated how this rapid field line stretching could potentially produce a net increase in energy, but that the answer would depend on the initial energy, spatial, and pitch angle distributions, as well as the stretching time scale and other factors, so we would have to run a simulation.

Through the use of an LSK simulation, we followed a collection of particles as they moved along a rotating, stretching flux tube, and examined the changes to the particle energy and pitch angle distributions. This simulation was meant as a proof-of-principle for the physical processes that occur in Jupiter's magnetosphere between noon and dusk, so we only followed particles beginning on one flux tube. Additionally, the simulation was not done self-consistently, such that we do not allow the plasma to influence the magnetic field geometry nor do we allow the particle distributions to be modified by pitch angle scattering. We ran the simulation with two different field line stretching time scales: once with the realistic but non-adiabatic 5 hours, and once with a 500-hour time scale, which was long enough to conserve the second adiabatic invariant. The adiabatic run provided a baseline to show which changes in the non-adiabatic run were due to the rapid nature of the field line stretching and which were due simply to outward expansion.

Analysis of the pitch angle, energy, and spatial distributions for the two runs showed that the distributions changed as expected under adiabatic expansion: the pitch angle distribution became more field-aligned, particles became further confined to the equator, and the energy decreased. However, under non-adiabatic expansion, the changes were much more complex. Though the pitch angle distribution became more field-aligned, the distribution favored the direction toward the equator. The flux tube energy content decreased but remained larger than for the adiabatic case. Finally, a larger anisotropy developed for the non-adiabatic case than for

the adiabatic case, suggesting that the rapid stretching could contribute to the plasma instability which affects the structure of the plasma sheet and the magnetic field threading it. The observed changes to the pitch angle and energy distributions and energy density in the non-adiabatic case compared to the adiabatic case are all consistent with the idea that the non-adiabatic effects contribute to field dipolarization and plasma sheet thickening. We therefore conclude that the model of *Kivelson and Southwood* [2005] is one plausible explanation for the observed plasma sheet thickening between noon and dusk.

Bibliography

Ashour-Abdalla, M., J. P. Berchem, J. Büchner, and L. M. Zelenyi (1993), Shaping of the magnetotail from the mantle: Global and local structuring, *J. Geophys. Res.*, *98*, 5651-5686.

Bagenal, F., J. D. Sullivan, and G. L. Siscoe (1980), Spatial distribution of plasma in the Io torus, *Geophys. Res. Lett.*, *7*, 17.

Bagenal, F. and J. D. Sullivan (1981), Direct plasma measurements in the Io torus and inner magnetosphere of Jupiter, *J. Geophys. Res.*, *86*, 8447-8466.

Birmingham, T. J. and T. G. Northrop (1979), Theory of flux anisotropies in a guiding center plasma, *J. Geophys. Res.*, *84*, 41.

Frank, L. A. and W. R. Paterson (2002), Galileo observations of electron beams and thermal ions in Jupiter's magnetosphere and their relationship to the auroras, *J. Geophys. Res.*, *107*, 1478, doi:10.1029/2001JA009150.

Frank, L. A. and W. R. Paterson (2004), Plasmas observed near local noon in Jupiter's magnetosphere with the Galileo spacecraft, *J. Geophys. Res.*, *109*, doi:10.1029/2002JA009795.

Gledhill, J. A. (1967), The structure of Jupiter's magnetosphere and the effect of Io on its decametric radio emission, *NASA Tech. Memo. X-55980*, *NASA/GSFC X Doc. 615-67-296*.

Goertz, C. K., A. W. Schardt, J. A. Van Allen, and J. L. Parish (1979), Plasma in the Jovian current sheet, *J. Geophys. Res.*, *6*, 495-498.

Goldstein, H. (1950), *Classical Mechanics*, Addison-Wesley, Cambridge, Mass.

Hill, T. W. and F. C. Michel (1976), Heavy ions from the Galilean satellites and the centrifugal distortion of the Jovian magnetosphere, *J. Geophys. Res.*, *81*, 4561-4565.

Huang, T. S. and T. J. Birmingham (1992), The polarization electric field and its effects in an

anisotropic rotating magnetospheric plasma, *J. Geophys. Res.*, *97*, 1511-1519.

Joy, S. P., M. G. Kivelson, R. J. Walker, K. K. Khurana, C. T. Russell, and T. Ogino (2002), Probabilistic models of the Jovian magnetopause and bow shock locations, *J. Geophys. Res., 107,* 1309, doi: 10.1029/2001JA009146.

Kane, M., B. H. Mauk, E. P. Keath, and S. M. Krimigis (1995), Hot ions in Jupiter's magnetodisc: A model for Voyager 2 Low-Energy Charged Particle measurements, *J. Geophys. Res.*, *100*, 19473-19486.

Kane, M., D. J. Williams, B. H. Mauk, R. W. McEntire, and E. C. Roelof (1999), Galileo Energetic Particles Detector measurements of hot ions in the neutral sheet region of Jupiter's magnetodisk, *Geophys. Res. Lett.*, *26*, 5-8.

Khurana, K. K. (1997), Euler potential models of Jupiter's magnetospheric field, *J. Geophys. Res.*, *102*(A6), 11295-11306.

Khurana, K. K., M. G. Kivelson, V. M. Vasyliūnas, N. Krupp, J. Woch, A. Lagg, B. H. Mauk, and W. S. Kurth (2004), The configuration of Jupiter's magnetosphere, in *Jupiter: the Planet, Satellites, and Magnetosphere*, edited by F. Bagenal et al., Cambridge Univ. Press, New York.

Kivelson, M. G., and K. K. Khurana (2002), Properties of the magnetic field in the Jovian magnetotail, *J. Geophys. Res.*, *107*, 1196.

Kivelson, M. G. and D. J. Southwood (2005), Dynamical consequences of two modes of centrifugal instability in Jupiter's outer magnetosphere, *J. Geophys. Res.*, *110*, A12209, doi:10.1029/2005JA011176.

Krimigis, S. M., J. F. Carbary, E. P. Keath, C. O. Bostrom, W. I. Axford, G. Gloeckler, L. J. Lanzerotti, and T. P. Armstrong (1981), Characteristics of hot plasma in the Jovian magnetosphere: Results from the Voyager spacecraft, *J. Geophys. Res.*, *86*, *A10*, 8227-8257.

Krupp, N., A. Lagg, S. Livi, B. Wilken, J. Woch, E. Roelof, and D. Williams (2001), Global flows of energetic ions in Jupiter's equatorial plane: First-order approximation, *J. Geophys. Res.*, *106*(A11), 26017-26032.

Lanzerotti, L. J., T. P. Armstrong, C. G. Maclennan, G. M. Simnett, A. F. Cheng, R. E. Gold, D. J. Thomson, S. M. Krimigis, K. A. Anderson, S. E. Hawkins III, M. Pick, E. C. Roelog, E. T. Saris, and S. J. Tappin (1993), *Planet. Space Sci.*, *41*, 893-917.

McNutt, R. L., Jr., J. W. Belcher, and H. S. Bridge (1981), Position ion observations in the middle magnetosphere of Jupiter, *J. Geophys. Res.*, *86*, 8319-8342, doi:10.1029/JA086iA10p08319.

McNutt, R. L., Jr. (1983), Force balance in the magnetospheres of Jupiter and Saturn, *Adv. Space Res.*, *3*, 55-58.

Northrop, T. G. (1963), *The Adiabatic Motion of Charged Particles*, Interscience, New York.

Northrop, T. G. and T. J. Birmingham (1982), Adiabatic Charged Particle Motion in Rapidly Rotating Magnetospheres, *J. Geophys. Res.*, *87*(A2), 661-669.

Roederer, J. G. (1970), *Dynamics of Geomagnetically Trapped Radiation*, Springer-Verlag, New York.

Treumann, R. A. and W. Baumjohann (2001), *Advanced Space Plasma Physics*, Imperial College Press, London.

Vasyliūnas, V. M. (1968), A survey of low-energy electrons in the evening sector of the magnetosphere with OGO 1 and OGO 3, *J. Geophys. Res.*, *73*, *9*, 2839-2884.

Vasyliūnas, V. M. (1983), Plasma Distribution and Flow, in *Physics of the Jovian Magnetosphere*, edited by A. J. Dessler, p. 395, Cambridge Univ. Press, New York.

Vogt, M. F., M. G. Kivelson, K. K. Khurana, R. J. Walker, B. Bonfond, D. Grodent, and A. Radioti (2011), *Improved mapping of Jupiter's aurora features to magnetospheric sources*, *J. Geophys. Res.*, *116*, A03220, doi: 10.1029/2010JA016148.

Waldrop, L. S., T. A. Fritz, M. G. Kivelson, K. Khurana, N. Krupp, and A. Lagg (2005), *Planet. Space Sci.*, *53*, 681-692.

Walker, R. J., M. G. Kivelson, and A. W. Schardt (1978), *Geophys. Res. Lett.*, *5*, 799-802.

CHAPTER 5

Summary and Future Work

5.1 Summary

This dissertation has provided new insight into Jupiter's magnetospheric structure and dynamics through three studies: a statistical study of reconnection events observed in magnetometer data in Jupiter's magnetotail; the development of a data-based model to link polar auroral features to their source regions in the magnetosphere; and a large-scale kinetic simulation which examined the effects of Jupiter's rapid rotation and field line stretching on particle energy and pitch angle distributions.

The second chapter characterized the nearly 250 reconnection events identified in magnetometer data from Jupiter's magnetotail. This statistical study provided the first complete survey of reconnection signatures in the magnetometer data. We examined the spatial distribution and recurrence period of the events, as these two properties can provide insight into what drives reconnection at Jupiter. Our events were identified by analyzing the available magnetometer data for signatures of dipolarizations. In comparing our results to studies that used particle anisotropies, we found good agreement between our events and intervals of large radial anisotropies [*Kronberg et al.*, 2005], and that the magnetometer data can be used to infer radial flow direction with a good degree of confidence. In this way, we were able to use our events to infer the location of a statistical separatrix separating inward and outward flow, and found that it qualitatively agrees with work from *Woch et al*. [2002], who studied flow bursts in particle data.

The nearly 250 reconnection events we identified occurred with similar frequency in the pre- and post-midnight local time sectors, with a curious minimum in the event at midnight. From this local time distribution we can infer that reconnection is at least partially internally

driven, since Dungey cycle, or solar wind-driven, reconnection is expected to occur only in the post-midnight local time sector [*Cowley et al.*, 2003]. However, we also analyzed the recurrence period of the events using the Rayleigh power spectrum and found no statistically significant recurrence period that would be representative of the internal processes driving dynamics at Jupiter. This result was somewhat surprising, given that a ~2-3 day period has been observed in flow bursts, reconfiguration events, and auroral polar dawn spots, and is even visually apparently in our events during specific intervals or orbits. Further study is called for, as is discussed in section 5.2.

The third chapter presented an improved model for mapping between Jovian polar auroral features and their magnetospheric sources. Unlike the Earth, where the main auroral oval is associated with the open/closed boundary in the polar cap, Jupiter's main auroral emission is associated with the enforcement of plasma corotation in the middle magnetosphere. Additionally, the available global field models are inaccurate at distances beyond ~30 R_J, so the boundary between open and closed flux in Jupiter's ionosphere is not well-defined, and magnetospheric mapping of polar auroral features is highly uncertain. We took a different approach to our mapping and used a flux equivalence calculation based on the requirement that the magnetic flux through an area in the ionosphere equals the flux through the equatorial region to which it maps. This approach is more accurate than tracing field lines from a model and allowed us to identify the size and location of the polar cap, and the source regions of different auroral features.

The flux equivalence calculation required a model for B_N, the component of the magnetic field normal to the current sheet. We developed a model, based on a fit to the available spacecraft data that accounts for changes with radial distance and local time. The local time dependence was of particular importance for accurately mapping local time asymmetries in the

auroral emissions. We then mapped equatorial field lines from the orbit of Ganymede at 15 R_J, where field models are reasonably accurate, out to 150 R_J in the tail, the farthest limit of available spacecraft observations.

The results showed that the main oval mapping varies with local time, moving outward from ~15-30 R_J near dawn to ~50-60 R_J post-noon. The polar active region, poleward of the main oval and centered on the day side, maps to regions that could plausibly be the dayside polar cusp and that the nearby swirl region is also on open field lines; this mapping is consistent with some earlier predictions. The polar auroral swirl region maps to open tail field lines and is interpreted as the Jovian polar cap. We also showed that dawn and nightside polar spots map to distances inside of a statistical x-line, consistent with the interpretation that they are associated with inward flow from tail reconnection. Finally, in addition to identifying the source region of the polar auroral features, we estimated the size of Jupiter's polar cap and the amount of open flux. Our estimate for the amount of open flux, ~720 GWb, very closely matches the open magnetic flux contained in the magnetotail lobes. We concluded that the size of Jupiter's polar cap is equivalent to a symmetric circle about the pole with an ~11º latitudinal width (though the Jovian polar cap itself is asymmetric).

The fourth chapter described a large-scale kinetic simulation which we developed to test the idea [*Kivelson and Southwood*, 2005] that rapid rotation and non-adiabatic field line stretching between noon and dusk can explain the observed plasma sheet thickening in that local time sector of Jupiter's magnetosphere. We use the LSK simulation to follow a collection of particles as they moved along a rotating, stretching flux tube, and to examine how the particle energy and pitch angle distributions evolved. This simulation was meant as a proof-of-principle for the physical processes that occur in Jupiter's magnetosphere, and was not done self-

consistently. We ran the simulation twice, with different field line stretching time scales but the same initial distributions: once with the realistic but non-adiabatic 5 hours, and once with a 500-hour time scale, which was long enough to conserve the second adiabatic invariant. The adiabatic run provided a baseline to show which changes in the non-adiabatic run were due to the rapid nature of the field line stretching and which were due simply to outward expansion.

Analysis of the pitch angle, energy, and spatial distributions for the adiabatic expansion run showed that the distributions changed as expected for conservation of the first and second adiabatic invariants in the rotating frame: the pitch angle distribution became more field-aligned, particles became further confined to the equator, and the energy decreased. Under non-adiabatic expansion, the changes were much more complex, and though the pitch angle distribution became more field-aligned, the distribution favored the direction toward the equator. The flux tube energy content decreased for the non-adiabatic case but remained larger than for the adiabatic case. A larger anisotropy developed for the non-adiabatic case than for the adiabatic case, suggesting that the rapid stretching could contribute to the plasma instability and subsequent thickening. We concluded that the simulated changes to the energy and pitch angle distributions and the energy density are consistent with the non-adiabatic effects contributing to field dipolarization and plasma sheet thickening, and that our results support the *Kivelson and Southwood* [2005] model as one plausible explanation for the observed plasma sheet thickening between noon and dusk.

5.2 Future work

There are many interesting applications for the findings we have discussed in this dissertation, as well as the potential for further refinement and analysis. Here we briefly review some topics for future study.

In chapter one we discussed the distribution and periodic recurrence of reconnection events observed in Jupiter's magnetotail, and from that, concluded that the results were consistent with both internally-driven and solar wind-driven reconnection, and we do not find strong evidence that one process completely dominates over another. However, further analysis of the mass and flux transported in the events we have identified could give more information about the relative contribution of dayside reconnection and internally driven reconnection in Jupiter's magnetosphere. Estimates of the amount of plasma lost through reconnection suggest that plasmoids cannot account for the ~0.5 ton/s of plasma produced by Io, and that most of the mass must be lost through other processes, such as a diffusive "drizzle" [*Bagenal*, 2007]. It is also possible that the required mass loss could be accounted for through dusk side reconnection and plasmoid release, as proposed by *Kivelson and Southwood* [2005], which would not have been observed if they occurr farther tailward than the duskside orbits of Galileo. As future work, analysis of the observed reconnection events could further confirm these mass transport estimates, and the kinetic simulation described in chapter four could be used to study the diffusive mass loss. Additionally, we could calculate the typical rate of magnetic flux transport from tail reconnection, and compare that to estimates of the rate of flux added to the magnetosphere through dayside reconnection with the solar wind. The relation between those two quantities would directly address the relative importance of solar wind driven versus internally driven reconnection.

The next potential area for future work involves the magnetic mapping model discussed in chapter three, where we employed a flux equivalence calculation to link polar auroral features with source regions in the magnetosphere. In that flux calculation we computed the ionospheric flux using the Grodent anomaly model [*Grodent et al.*, 2008] for the northern hemisphere because it accurately matches the ionospheric positions of the satellite footprints in the northern hemisphere to their orbital distances in the magnetosphere. However, other internal field models are available, each with its advantages and limitation, including VIP4 [*Connerney et al.*, 1998], which we used for the southern hemisphere mapping, and the "VIPAL" model, based on recent work by *Hess et al.* [2011]. The VIPAL internal field model updated the VIP4 model by placing longitudinal constraints on the mapping of the Io footprint, and therefore fits the observed Io, Europa, and Ganymede footprints better than does VIP4. It also predicts a surface magnetic field strength that agrees with the values deduced from observed radio emissions better than the Grodent anomaly model.

Each of the available internal field models has its relative strengths and weaknesses that affect the flux equivalence calculation, but the differences of flux mapping based on the three different field models (VIP4, Grodent anomaly model, VIPAL) has not yet been established. In the future we will compare the previously published mapping results that used the Grodent anomaly model to new results that used the VIP4 and VIPAL models in the flux calculation, placing particular emphasis on any differences in the resulting polar cap size and location or the amount of open flux. Such a comparison will help us understand the degree to which mapping results are model-dependent.

Finally, there are many ways in which we could refine and make further use of the large scale kinetic simulation described in chapter four. This simulation was designed as a toy problem

to test the effect of non-adiabatic flux tube expansion in a rotating system, and we have accounted for those key physical processes. However, the simulation was not run self-consistently, so one way to improve our work would be to begin with a distribution where the particle thermal pressure gradients are consistent with the magnetic forces. Another improvement would be to reisotropize the pitch angle distribution at intermediate time steps, as is likely to happen on relatively short (~1-2 hours) time scales due to pitch angle scattering. Reisotropizing the pitch angle distribution in this way will alter how the density and energy distributions evolve with time. Finally, to address the potential discrepancy between the 2 keV temperature of our initial distribution and some estimates of higher observed temperatures (~tens of keV), in the future we intend to adjust our initial temperature and include higher energies, up to at least 20 keV, in our runs.

Bibliography

Bagenal, F. (2007), The magnetosphere of Jupiter: Coupling the equator to the poles, *J. Atmos. Sol. Terr. Phys.*, *69*, 387–402, doi:10.1016/j.jastp.2006.08.012.

Connerney, J. E. P., and M. H. Acuña (1998), New models of Jupiter's magnetic field constrained by the Io flux tube footprint, *J. Geophys. Res.*, *103*, 11929-11939.

Cowley, S. W. H., E. J. Bunce, T. S. Stallard, and S. Miller (2003), Jupiter's polar ionospheric flows: Theoretical interpretation, *Geophys. Res. Lett.*, *30*(5), 1220.

Grodent, D., B. Bonfond, J.-C. Gérard, A. Radioti, J. Gustin, J. T. Clarke, J. Nichols, and J. E. P. Connerney (2008b), Auroral evidence of a localized magnetic anomaly in Jupiter's northern hemisphere, *J. Geophys. Res.*, *113*, doi:10.1029/2008JA013185.

Hess, S. L. G., B. Bonfond, P. Zarka, and D. Grodent (2011), Model of the Jovian magnetic field topology constrained by the Io auroral emissions, *J. Geophys. Res.*, *116*, A05217, doi:10.1029/2010JA016262.

Kivelson, M. G. and D. J. Southwood (2005), Dynamical consequences of two modes of centrifugal instability in Jupiter's outer magnetosphere, *J. Geophys. Res.*, *110*, A12209, doi:10.1029/2005JA011176.

Kronberg, E. A., J. Woch, N. Krupp, A. Lagg, K. K. Khurana, and K.-H. Glassmeier (2005), Mass release at Jupiter: Substorm-like processes in the Jovian magnetotail, *J. Geophys. Res.*, *110*, A03211, doi:10.1029/2004JA010777.

Woch, J., N. Krupp, and A. Lagg (2002), Particle bursts in the Jovian magnetosphere: Evidence for a near-Jupiter neutral line, *Geophys. Res. Lett.*, *29*, 1138.